UNIVERSITÉ DE GENÈVE
Départment de physique nulcéaire et corpusculaire

FACULTÉ DES SCIENCES
Professeur Allan Clark

Luminosity, Beam Monitoring and Triggering for the CMS Experiment and Measurement of the Total Inelastic Cross-Section at $\sqrt{s} = 7$ TeV

THÈSE

présentée à la Faculté des sciences de l'Université de Genève
pour obtenir le grade de Docteur ès sciences, mention physique

par

Alan James Bell

de la Nouvelle-Zélande

Thèse N^{o} 4516

GENÈVE
Atelier d'impression Repromail
2013

UNIVERSITÉ
DE GENÈVE

FACULTÉ DES SCIENCES

Doctorat ès sciences
Mention physique

Thèse de *Monsieur Alan James BELL*

intitulée :

"Luminosity, Beam Monitoring and Triggering for the CMS Experiment and Measurement of the Total Inelastic Cross-Section at $\sqrt{s}$ 7 TeV"

La Faculté des sciences, sur le préavis de Messieurs A. G. CLARK, professeur honoraire et directeur de thèse (Département de physique nucléaire et corpusculaire), X. WU, professeur associé (Département de physique nucléaire et corpusculaire), A. BALL, docteur, (Physics Department, The European Organization for Nuclear Research, Geneva, Switzerland), R. RUSACK, professeur (School of Physics and Astronomy, University of Minnesota, Minneapolis, United States of America) et de Madame A. DABROWSKI, docteure (Physics Department, The European Organization for Nuclear Research, Geneva, Switzerland), autorise l'impression de la présente thèse, sans exprimer d'opinion sur les propositions qui y sont énoncées.

Genève, le 23 janvier 2013

Thèse - 4516 -

Le Doyen, Jean-Marc TRISCONE

N.B. - La thèse doit porter la déclaration précédente et remplir les conditions énumérées dans les "Informations relatives aux thèses de doctorat à l'Université de Genève".

“An expert is a man who has made all the mistakes which can be made in a very narrow field.”

– Niels Bohr

Acknowledgements

Scientific projects are often carried out by an individual or a small team of people in a laboratory setting in which they design, construct and execute a 'table-top' experiment and analyse their results. This is certainly still true in the fields of Chemistry and Biology. However, physics experiments are more often becoming very complicated and High Energy Physics is possibly the extreme example. The Compact Muon Solenoid experiment brought together a great number of talented and motivated individuals, each of whom contributed to the overall project in some way; be it engineering design, construction, power distribution and cabling, programming or analysis.
Through the four years of this Ph.D project, I have had the good fortune to experience almost every aspect of the kinds of work that is done at CERN. Starting with detector design through to mechanical planning and construction, on to installation and commissioning and finally physics data analysis. In each and every aspect, I required assistance or advice from some of my talented and motivated colleagues in CMS.

I would like the thank the following people whom in some way helped me at various points throughout this thesis . . .

Richard Hall-Wilton, David Stickland and Anne Dabrowski for advice and guidance with the Beam Scintillator Counter (BSC) and Beam Halo Counter (BHC) detector projects and for keeping the pressure on me to complete this thesis. Steffen Müller and Moritz Guntoff for their Fluka simulation results which helped in understanding the particle flux expected in the BSC and BHC regions. Sebastian Viret for his CMSSW simulation datasets which were used in the planning of the BHC detector. Vladimir Ryjov, Martin Ohlerich, Andrey Marinov and Vasil Verguilov for help with programming the VME electronics for the detector readouts. I learned a lot from your techniques; valuable information which is not easy to find. Wolfgang Lange, Wolfgang Lohmann, Elena Castro Carballo and Ringo Schmidt from DESY Zeuthen for their work on the BCM1F which became a useful source of data for testing the operation of the BHC detector. Ianos Schmidt, Randal Rutchi, Yasar Onel, Arjan Heering, Salavat Abdoulline and Edmund Berry for sharing their knowledge of the HF Calorimeters and/or their expertise in detector materials and readout devices. Yen-Jie Lee and Yetkin Yilmaz of MIT for their help in teaching an old, experimental physicist the complicated and sometimes *surreal* ways of CMSSW and ROOT programming. You saved me from banging my head against a wall on more than one occasion! An extra thank you to Yen-Jie for his huge contribution to the commissioning of the BSC detector and making it such a vital component of the 2010 and 2011 Heavy Ion runs. You are the most talented and humble guy I have had the pleasure to work with.

Gabor Veres, Jeremy Gartner and Anna Zsigmond who worked with me on the pp inelastic cross-section measurement. Thank you Gabor for giving me the opportunity to work on the measurement which resulted in a vital analysis component of this thesis; Jeremy Gartner for starting the project as a Technical Student and provided his initial CMSSW code on which the measurement was built on; Anna Zsigmond who worked *extremely* hard on fending off and carrying out the modifications of the analysis paper requested by the ARC, whilst I was off having fun building another detector. A special thank you goes to Tanguy Pierog of The Karlsruhe Institute of Technology, for the rapid production of the improved Monte Carlo model datasets used in the cross-section extrapolation and his invaluable assistance by independently cross-checking the results. Also to Nicolo Cartiglia and Michael Albrow for their clear and detailed explanations of Regge Theory and forward physics and for sharing their knowledge of Monte Carlo generators. Jeroen Hegeman and Stephen Reucroft for their various informative discussions. Austin Ball, Patrice Siegrist, Martin Gastal and David Hay for keeping the CMS cavern from becoming an underground world of chaos and for their integration of the BSC and BHC detector installations in to CMS in a safe and efficient way.

Daniel Marlow and Zhen Xie from the Luminosity Group for their quick and clear answers to my luminosity related questions. Your work has played a central role in every analysis paper that CMS has produced. Edward Wenger for his work in studying the PKAM events with the BSC2 triggers. It was great to see how such a simple device could find so many unforeseen uses such as this! Jonathan Hollar, Ivan Mikulec and Manfred Jeitler for help with HLT and Level 1 trigger advice and implementation. I am very proud to know that my first particle physics detector was responsible for triggering on the first LHC collisions in CMS and was an integral part of CMS for over 18 months thanks to your efforts in integrating it with the trigger systems.

Jean-Paul Chatelain, Dmitry Druzhkin, Roman 'The Master' Stefanovitch and the technicians at The University of Bologna, Italy for manufacturing the pieces of the BHC detector so precisely and quickly and the creativity shown to allow its installation under such tight mechanical limits. I suspect we broke a world record for designing, building and installing a High Energy Physics detector in the shortest time - only 6 months.

Gian Piero Siroli and Marina Giunta, my colleagues on the BHC detector who made it all seem so easy and fun. It was nice to have people to keep the momentum going when my energy and efficiency took a nose-dive. Christian Joram, Adrian Folley and Raphael Dumps for allowing me to use the tools and machines in the scintillator lab. Prof. Philip Butler and Dr. Jenny Williams from the University of Canterbury, New Zealand for sending me to CERN in the first place. Intended initially as a short, 5 week visit to help build the BSC, it has turned in to a highly beneficial 5 year adventure. Marion Picard for helping me with translations and not berating me for my inability to overcome the intricacies of the French language.

I would certainly like to thank my UNIGE supervisor, Allan Clark, who agreed to take me as an external student, meaning that I could commence the Ph.D program with CERN and complete the necessary courses locally with the minimum interruption to an already busy CMS work schedule.

And finally my wife, Rati who agreed to travel to Europe with me for 'just a year or two' and finds herself still here 6 years later, doing her own Ph.D work at a level much higher than that expected or required in many other parts of the world. I know you have found it difficult being so far away from home. But I know you understand that, at the end, we will be much happier and proud of what we have achieved.

Thank you.

Abstract

The Compact Muon Solenoid (CMS) detector, situated on the Large Hadron Collider (LHC) ring is a multi-purpose detector designed to search for new physics phenomena, make precise measurements of known processes at previously untapped energies and look for hints of physics beyond the Standard Model. During the initial low luminosity stages, the Beam Scintillation Counter (BSC) sub-detector was vital in providing accurate and efficient (ϵ ~98%) triggering of beam halo and minimum bias events and helped in the commissioning of the CMS detector. This thesis is given in three parts.

The first section describes the design and implementation of the BSC and the commissioning of the system before and during the early operation of the LHC. Analysis of the technical triggers it provided, using early low pile-up data in shown to demonstrate that the goal of providing an efficient trigger for low luminosities was achieved. Demonstrations of its use beyond its intended design are also shown, which helped drive the need for an upgrade for 2012.

In continuation with the BSC's minimum bias trigger and luminosity monitoring ability, the second section explains the measurement of the proton-proton inelastic cross-section measured at $\sqrt{s}$ =7 TeV using the CMS Hadronic Forward Calorimeters and compares the result with other recent analyses from CMS, ATLAS, ALICE and TOTEM. An extrapolation to the total inelastic cross-section is made with the use of several Monte Carlo event generators with various underlying phenomenological mechanisms. The result shows no large deviation from the steady rise in the pp cross section, indicating that no new physics processes are involved at this high energy.

The third section shows the research and design towards an upgrade of the BSC detector based on knowledge gained so far, resulting in a new halo monitoring detector for 2012. This detector serves to monitor beam backgrounds throughout the LHC fills and will provide useful information towards a more permanent, quartz based sub-detector currently being developed.

Résumé

Le détecteur CMS fonctionne depuis les premières collisions en novembre 2009. Depuis lors il a fonctionné de façon remarquable enregistrant plus de 25 fb^{-1}. Le détecteur a été utilisé par la physique nouvelle afin d'étudier les phénomènes de collisions proton-proton ainsi que d'ions lourds Pb-Pb, mais aussi afin d'affiner les connaissances pre-éxistantes et rechercher des pistes au-delà de la physique du modèle standard. En outre, les études prennent en compte le comportement du faisceau et le bruit de fond pour aider à améliorer la performance, déjà excellente, du LHC. Le sous-détecteur « Beam Scintillator Counter », (BSC), a joué un rôle minime mais essentiel durant les première acquisitions de CMS, contribuant à déclencher de façon efficace l'enregistrement des événements intéressants pendant les premières collisions. Ceci a conduit à de études de topologie et de multiplicité des particules au sein de CMS. Ces thèses décrivent la construction el l'expansion du système BSC, le plaçant parmi l'un des principaux sous-détecteurs déclencheurs durant les dix-huit premiers mois de fonctionnement de CMS.

Par la suite, une importante mesure de la section efficace des collisions inélastiques *pp* a été accomplie. Bien qu'il ait été techniquement possible de réaliser cette mesure avec le BSC, cette analyse a été effectuée par les calorimètres « Hadronic Forward » (HF), en raison de leur plus grande acceptation. La mesure et l'extrapolation aux sections efficaces inélastiques totales effectuée grâce à plusieurs modèles de calculs de Monte-Carlo fournissent d'autres sources d'information intéressantes. L'analyse a donné les résultats suivants:

$$\sigma_{\xi>5\times10^{-6}} = 60.2 \text{ mb } \pm\ 0.2 \text{ mb } (stat.)\ \pm\ 1.1 \text{ mb } (syst.)$$

$$\sigma_{inel} = 68.1 \text{ mb } \pm\ 0.5 \text{ mb } (stat.)\ \pm\ 2.4 \text{ mb } (syst.)$$

Ces données orienteront le développment de simulations futures et de modèles phénoménologiques, dans le but de prédire les caractéristiques d'une myriade de collisions pp à des énergies plus hautes.
Enfin, la conception et la construction de la nouvelle version du sous-détecteur BSC sont également brièvement décrites. Installé au début de l'année 2012, le sous-détecteur « Beam Halo Counter » (BHC), a pour mission d'enregistrer le bruit de fond provenant du halo de faisceau durant le remplissages du LHC. Il fournit actuellement à CMS des don´ees sur les pré-collisions et des mesures du halo de faisceau, utiles au développement en cours d'un futur détecteur plus permanent.

Contents

List of Figures

List of Tables

Chapter 1

Introduction to the LHC

This chapter describes the basic design and important characteristics of the LHC, the injector chain which accelerates and injects particles into the LHC and the mechanisms for controlling the high energy beams, A brief overview of the four main experiments situated at strategic points at the LHC is given along with each of their primary physics goals. The Compact Muon Solenoid (CMS) is described in greater detail in Chapter 2.

In 1994, the CERN council gave their approval for the Large Hadron Collider (LHC) project. The driving forces behind the project were the desire to search for yet undiscovered physics predicted by theory and required within the Standard Model and to further our understanding of particles and interactions already discovered at the Large Electron Positron Collider (LEP), FermiLab and other particle physics experiments internationally. Undoubtedly, the most publicised purpose of the LHC is the search for the Higgs Boson, dubbed the *'God Particle'* by the media. The Higgs mechanism is a key feature of the Standard Model and the discovery of a Higgs Boson would be a strong indication that the Standard Model is on the right track. It alludes to the reasoning behind how particles obtain their masses and is a vital component of the theory in bringing together the Electromagnetic force of Quantum ElectroDynamics (QED) and the Weak force into a single, unified Electroweak force [1]. The discovery of the Higgs Boson is made more difficult as its mass is not predicted by theory, meaning that physicists need to be vigilant over a wide 'field of view' instead of focussing all their combined

efforts into a narrow range of decay paths and kinematics. Equally, the experiments must be designed with a broader range of capabilities in order to detect and measure all possible Higgs decay pathways, should they occur. Many of the Higgs decay signatures are similar to other, more prominent decays and a very large number of Higgs candidates will need to be recorded before physicists can see their existence among the background. For example, $H_0 \rightarrow \gamma\gamma$ is an important decay channel with a clear signature. However, e^-e^+ annihilation contributes a very high background of $\gamma\gamma$ production.
Additionally, the experiments at the LHC will search for answers to the apparent asymmetry between matter and anti-matter, the sources and nature of dark matter which seems to contribute 23% of the mass-energy of the Universe,*
Heavy Ion collisions in the form of lead-lead (Pb-Pb) and proton-lead (p-Pb), will be used for studies of quark-gluon plasma and indications of the existence of super-symmetry (SUSY), a theory which may lead to a unification of all 4 fundamental forces, including Gravity.

1.1 The Large Hadron Collider

The Large Hadron Collider (LHC) [2] is a 27 km circular synchrotron located 50 - 175 m underground on the border between Switzerland and France near the city of Geneva. It is currently the most powerful particle proton-proton (*pp*) accelerator ever built and is expected to reveal new insights beyond our current understanding of particle physics. Initially, the LHC was intended to be constructed in two stages. The first stage aimed to build a proton-proton(*pp*) colliding beam accelerator with a collision energy of $\sqrt{s}$ =10 TeV followed by an upgrade in stage II that would increase the collision energy to $\sqrt{s}$ =14 TeV. However, before completion of stage I, adequate funding and contributions from non-member states such as Canada, Japan, India, Russia and the U.S.A allowed for the immediate construction of the 14 TeV machine [3].

The LHC will take particle physics research to a new energy frontier and closer to the maximum limit of achievable accelerator-based collision energies. Since the 1930's, when Cockcroft and Walton constructed a 800keV accelerator [5], the *effective* collision energy of particle accelerators has increased more than 7 orders of

*Dark Energy contributes around 72%, while normal matter makes up only 4.6%.

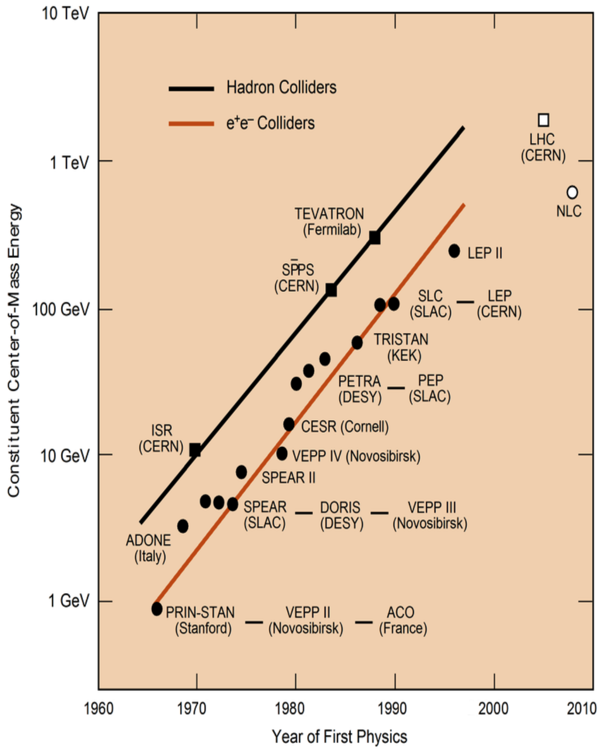

FIGURE 1.1: A Livingston plot of e^+e^- and Hadron colliders in chronological order based on their first year of physics data taking and their center-of-mass, $\sqrt{s}$ collision energy [4].

magnitude [4]. The limiting factor for the energy of proton accelerators like the LHC is the maximum magnetic field required to bend the particles around a ring of manageable size. The LHC itself incorporates approximately 9300 superconducting magnets including 1232 dipole and 858 quadrupole magnets around its circumference for bending and focusing the beams. The field required to bend the two 7 TeV beams within the bending radius of approximately 2.8 km is 8.33 T.[†] The collider tunnel contains two pipes enclosed within these superconducting magnets cooled by liquid helium, each pipe containing a proton beam during the usual proton runs. The two beams travel in opposite directions around the ring and are brought together into a single pipe for 150 m either side of each collision point. Sets of Inner Triplet Magnets are used to focus the beams at four intersection points where interactions between them take place.

There are five experiments positioned at the four interaction points (I.P); ALICE (**A** **L**arge **I**on **C**olliding **E**xperiment)[7], LHCb (**L**arge **H**adron **C**ollidor **b**eauty

[†]The LHC ring is not perfectly circular but has eight long, straight sections (LSS) where the experiments, injectors, services and beam dumps are located.

TABLE 1.1: Some important characteristics of the LHC [6].

	Injection	Collision
Beam Data		
Proton Energy	450GeV	7000GeV
Number of Bunches	2808	
Number of Particles per Bunch	1.15×10^{11}	
Circulating Beam Current	0.582 A	
Stored Energy per Beam	23.3 MJ	362 MJ
Peak Luminosity in IP1 & IP5	-	$1.0 \times 10^{34} \mathrm{cm}^{-2}\mathrm{s}^{-1}$
Geometry & Magnets		
Ring Circumference	26658.883 m	
Number of Main Bends	1232	
Bending Radius	2803.95 m	
B Field at Bends	0.535 T	8.33 T
Revolution Frequency	11.245 kHz	

experiment)[8] and TOTEM* (Total Cross Section, Elastic Scattering and Diffraction Dissociation at the LHC)[9] are three specialized experiments. The Compact Muon Solenoid (CMS) [10] and ATLAS (**A** **T**oroidal **L**HC **A**pparatu**S**) [11] are the two main, multi-purpose experiments positioned at Point 5 and Point 1 of the LHC ring respectively. A more detailed description of CMS is given in Chapter 2.

1.1.1 LHC Layout

The 27 km ring of the Large Hadron Collider is capable of accelerating proton beams to 7 TeV ($\sqrt{s}$ = 14 TeV) and lead nuclei ($^{208}\mathrm{Pb}^{82+}$) to an energy of 2.76 TeV/nucleon and a total center of mass energy of 1.15 PeV. [2]. Figure 1.2 shows the complete path taken by the protons towards the LHC ring. Protons are extracted from hydrogen gas in a Duoplasmatron and injected into a linear accelerator (Linac2) where they are accelerated to 50 MeV. They then pass into the Proton Synchrotron Booster (PSB) where they are accelerated to 1.4 GeV. Next, they are passed into the Proton Synchrotron (PS) itself and again accelerated to 26 GeV. Prior to injection into the Super-Proton-Synchrotron (SPS), the proton beam is de-bunched and recaptured in 40 MHz occupied bunch cavities to create the 25 ns bunch spacing used in the LHC (see section 1.1.2). The bunch lengths are shortened to 4 ns and then injected into the SPS ring. Finally, the

*Totem is situated at Point 5 with CMS.

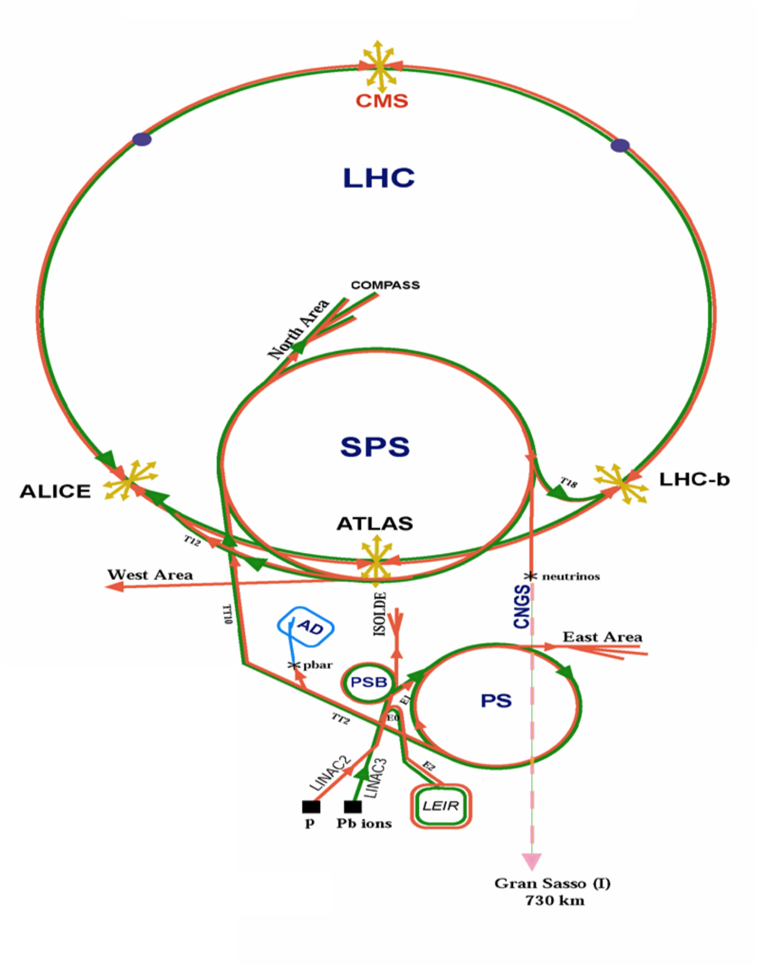

FIGURE 1.2: A schematic of the layout of the injector chain from the LINACs to the LHC at CERN [12].

SPS accelerates these proton bunches from their injection energy of 26 GeV up to 450 GeV before they are injected in groups into the LHC. Within the LHC ring, they are 'ramped up' to the desired collision energy which, to date, stands at 4 TeV ($\sqrt{s}$ =8 TeV.[‡])

During physics operations, the LHC circulates two beams of protons or heavy ions in opposite directions. By convention, beam 1 is in the clockwise direction, passing through the experiments from the plus end to the minus end, whilst beam 2 travels in a counter-clockwise direction. The beams are injected at point 2 (Beam 1) and point 8 (Beam 2). There are eight arcs and straight sections around the LHC. The straight sections, which are approximately 530m long, house either LHC machine

[‡]As of May 2012.

service points (Points 3, 4, 6 and 7) or experimental caverns (Points 1, 2, 5 and 8). The eight 'points' contain the following:

Point 1: The ATLAS Experiment.

Point 2: The ALICE Experiment & Beam 1 Injection.

Point 3: Momentum Cleaning.

Point 4: RF Systems.

Point 5: The CMS Experiment.

Point 6: Beam Dump.

Point 7: Betatron Cleaning.

Point 8: The LHCb Experiment & Beam 2 Injection.

LHCb and TOTEM are designed to run at $\mathcal{L} \approx 1\times10^{32}$ cm^{-2}s^{-1} and $\mathcal{L} \approx 2\times10^{29}$cm^{-2}s^{-1} respectively. ALICE, which is dedicated to Heavy Ion (Pb-Pb) collisions has a design luminosity of $\mathcal{L} = 10^{27}$cm^{-2}s^{-1}. The two 'high luminosity' experiments at the LHC; namely CMS and ATLAS, are designed around a nominal instantaneous peak luminosity of $\mathcal{L} = 10^{34}$cm^{-2}s^{-1} during the proton collision program. For comparison, the Tevatron at Fermilab, saw its highest luminosity (at the time of writing) of $\mathcal{L} = 4.04 \times 10^{32}$cm^{-2}s^{-1}[§] in the CDF experiment [13]. High luminosity is important as it has a direct relation to the number of collision events occurring per second in the experiment which in turn increases the probability of finding rare and interesting physics phenomena within an achievable timespan.

1.1.2 LHC Bunch Structure

The large luminosities demanded by the experiments have strong implications for the LHC machine in terms of beam dynamics, injection schemes and the ability to safely dispose of the beams when necessary. The luminosity due to any pair of bunches which collide in the region of any given interaction point is:

[§]Recorded on April 17, 2010.

$$\mathcal{L}_{bunch} = \frac{f_{rev} N_{b1} N_{b2} S}{4\pi\epsilon\beta^*} \tag{1.1}$$

where, N_{b1} and N_{b2} and the number of protons per bunch, S is a geometry factor based upon the beam profiles and their crossing angles, ϵ is the emittance and β^* is the distance from the I.P at which the width of the beam is double that at the I.P. The revolution frequency f_{rev} is governed by the circumference of the LHC and, to some extent, the energy at which the particles are accelerated. Therefore, to obtain the highest possible luminosity, the number of particles per bunch N and the number of bunches circulating the LHC needs to be maximised, running with the minimum, stable and safe emittance and β^*.

To allow for a sufficient number of bunches, the RF system in the LHC runs at a frequency of 400.8 MHz (λ = 0.7479 m; t=2.5ns). Taking the LHC circumference to be $\approx$ 26659 m, the RF system provides 35640 available 'buckets' into which the proton bunches can be injected. However, the readout limitations of the experiments' detectors must be taken into account and it was decided that the minimum space between colliding bunches will be restricted to 25ns or one in every 10 buckets. With this restriction in place, an entire LHC orbit can be dissected into 3564 usable buckets. During the early phases of LHC commissioning, only a few of these buckets contained bunches. Gradually, throughout 2010 - 2012, more and more bunches were injected. Presently, the LHC is running with 1374 bunches, 1368 of which are colliding in CMS. The remaining 6 bunches per beam are non-colliding and are used for measuring beam backgrounds. The bunches are spaced by 50 ns.

The experiments are interested in the bunch patterns in terms of the colliding and non-colliding bunches. A LHC-wide nomenclature was created to describe the filling scheme in terms of bunches colliding at each I.P and the total number of bunches present. For example:

$$\underbrace{50ns}_{\text{Spacing}} \_ \underbrace{1374}_{N_b} \_ \underbrace{1368}_{\text{IP1,5}} \_ \underbrace{0}_{\text{IP2}} \_ \underbrace{1262}_{\text{IP8}} \_ \text{144bpi12inj.} \tag{1.2}$$

informs the experiments that the bunch spacing is 50ns; there are 1374 bunches present in the LHC, 1368 of which are intended to collide at Points 1 and 5 (ATLAS & CMS), none are to collide at Point 2 (ALICE) and 1262 at Point 8 (LHCb).

Some filling schemes also show the number of bunches per injection (bpi) and the number of injections (inj).

1.2 Experiments at the LHC

There are four large scale experiments at the LHC plus several smaller specialized experiments. ATLAS[11] and CMS[10], described in more detail in chapter 2, are the two largest, general purpose experiments. Both have a rich physics program involving measurements of cross-sections of a wide range of processes, searches for exotic particles and particle resonances, topological measurements of particle production, CP violation, Super Symmetry and of course, the Higgs boson and its possible variants.

ATLAS is the largest detector at the LHC, measuring 44 m in length and having a 25 m diameter. The inner detector, comprised of a Silicon Pixel Tracker, Silicon Microstrip Trackers (SCT) and Transition Radiation Trackers (TRT), is immersed in a 2T field generated by a thin superconducting solenoid. Liquid Argon electromagnetic calorimeters cover the barrel region ($|\eta| < 3.2$)[¶] and a scintillator based hadron calorimeter covers the region $\eta < 1.7$. Liquid Argon forward calorimeters measure electromagnetic and hadronic energy in the pseudorapidity range $1.5 < |\eta| < 4.9$. The entire calorimeter is surrounded by the muon spectrometer which includes triggering chambers with 1.5 - 4ns timing resolution. Three large superconducting endcap toroids arranged in an 8-fold azimuthal symmetry around the calorimeters provide a toroidal magnetic field for muon momentum analysis. ATLAS is a large but open structure, designed to minimize multiple scattering effects which deteriorate the muon momentum resolution. A full, concise description of the ATLAS detector can be found in [11].

Located at point 2, ALICE is the only dedicated Heavy Ion physics detector at the LHC. It is designed to investigate the physics of strongly interacting matter and quark-gluon plasma generated in the collisions of lead (Pb) nuclei. It also operates during the nominal proton-proton (pp) collisions to provide reference data for the heavy-ion program and to search for other strong-interaction processes that will complement data from the other LHC experiments. The ALICE detector dimensions are 16 m$\times$16 m$\times$26 m and has a total weight of approximately 10,000 tonnes.

[¶]See section 6.2 for explanation of pseudorapidity.

The central barrel of ALICE measures hadrons, electrons and photons using an Inner Tracker System made from high resolution silicon pixel detectors, silicon drift detectors, silicon strip detectors, a cylindrical Time-Projection Chamber, Time-of-Flight Ring Imaging Cherenkov, Transition Radiation detectors and finally two electromagnetic calorimeters, providing an impressive array of particle detection, tracking and identification techniques. The forward regions (2.5$\leq |\eta| \leq$4) contain the muon spectrometers which measure the trajectories of pairs of muons, particularly from the decay of J/ψ and ψ'. ALICE employs the use of two magnets. A 0.5 T solenoid magnet houses the central detectors and provides the bending power for momentum measurements of high p_T particles. A separate dipole magnet is located 7 m from the interaction point and forms part of the muon spectrometer, extending the horizontal magnetic field beyond the reach of the solenoid magnet [7].

The LHCb detector is a single-arm spectrometer with a forward angular coverage [8]. Its interaction region is displaced by 11.25 m from the center of the cavern, towards IR7 to allow optimum use of the pre-existing cavern which originally housed the DELPHI experiment at LEP. LHCb is designed to run at a lower luminosity than other experiments with $\mathcal{L} \lesssim 5 \times 10^{32}\text{cm}^{-2}\text{s}^{-1}$ and maintaining the average number of visible collisions per bunch crossing to approximately one. Due to the nature of LHCb's physics goals, the design of the detector was driven by the need for a hardware-based trigger with short latency capable of selecting the decays of b-hadrons. This *b-tagging* method needs to work quickly and is achieved through the use of a silicon vertex detector. A dipole magnet at the center of the LHCb experiment is employed for measuring the momentum of charged particles. Unlike CMS, the magnet design does not use superconducting coils and provides an integrated field of 3.6 Tm over a region of 2.5 - 7.95 m from the interaction region.

Summary

The experiments at the LHC will cover a staggeringly wide range of cutting-edge topics in the field of particle physics research, all of which will have a direct bearing on our understanding of the birth and evolution of the Universe. The physics goals of ALICE will bring a better understanding of the Strong interaction and in-turn explain how nuclei formed in the initial microseconds of the Universe's creation by attempting to extract the quarks and gluons from the colliding nuclei and breaking the apparent rule of confinement. LHCb hopes to uncover new physics in regards to matter/anti-matter asymmetry through yet undiscovered sources of CP violation. Currently known examples of CP violation (eg. $K^0/\bar{K}0$) can be explained by assuming two different interaction pathways, involving weak and strong interaction effects. However, the mechanism cannot account for the magnitude of CP invariance required to cause the observed abundance of matter over anti-matter.

ATLAS and CMS are both targeting a wide range of topics at the leading edge of particle physics including the search for the Higgs Boson, Dark Matter, Dark Energy & Super Symmetry (SUSY). These searches will continue in parallel with countless other analyses which aim to refine and better understand previous measurements.

The experimental discovery and measurements of the underlying mechanisms of these phenomena would have a huge impact on our understanding of particle physics and mark the success of the LHC program. But even if some of these proposals are proven to be incorrect, it would only serve to correct the current course of High Energy Physics and yet again allow physicists to make refinements to the already highly successful Standard Model.

Chapter 2

The Compact Muon Solenoid

In this chapter, we present an overview of the CMS detector layout and the design of the major sub-detector components which allow CMS to make accurate measurements of proton-proton and heavy ion collisions, in the race to new physics discoveries. Using a mixture of well-proven and novel detector materials and designs, CMS is capable of measuring and making track location measurements to within 10 μm and particle momenta to an accuracy of 0.7%.

2.1 CMS Description

The Compact Muon Solenoid (CMS) is one of the two major, general purpose detectors on the LHC; the other being ATLAS. Although CMS and ATLAS are designed to search for the same phenomenon, their designs are drastically different. This was intended so that the results from each detector can be used to confirm the results from the other, reducing the possible systematic effects of particular design features.

CMS is a large scale, general-purpose detector situated under the village of Cessy in France. The CMS design is focussed on simplicity, forming a large, compact, close-ended cylinder around a powerful solenoidal magnetic field, as shown in figure 2.1. The cylinder is segmented for ease of assembly and maintenance. The choice of magnetic field configuration was an important driving factor behind the design and layout of CMS. In order to accurately measure the momentum of charged particles, particularly muons, at the LHC design collision energy $\sqrt{s}$ = 14TeV, a large bending power is required. This led to the choice of using a 3.8T super-conducting magnet at the heart of CMS (See [10] Section 2).

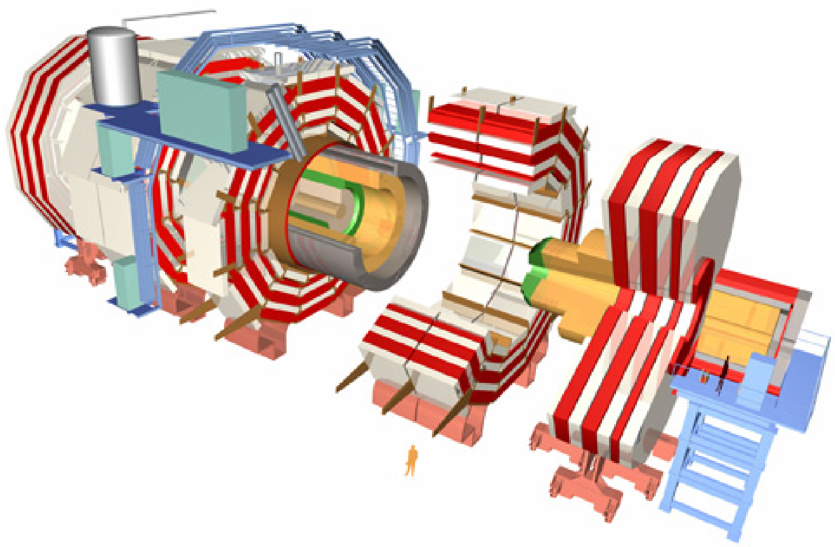

FIGURE 2.1: Diagram of CMS in its open position[10].

2.1.1 CMS Physics Goals

The CMS detector has a wide and varied research program, similar to, and in congenial competition with that of ATLAS. The main physics goals of CMS are to explore physics at the TeV scale including the evolution of cross-sections of many different processes, improve measurements of the W and Z boson masses, search for evidence of Super Symmetry (SUSY) and extra dimensions, study heavy ion collisions and the possibility of the intermediate state of quark-gluon plasma and, of course, search for the Higgs Boson. All publicly available papers can be found on the CERN Document Server [14].

In late 2011, both ATLAS and CMS released tantalising results which, independently pointed to a region of the Higgs mass of 124< m_H <126 GeV/c^2. The CMS analyses looked at five possible Higgs decay modes; $b\bar{b}$, $\tau\bar{\tau}$, $\gamma\gamma$, WW, and ZZ, the latter decaying into four possible combinations of leptons, quarks and neutrinos. Excesses were found in five of these decay channels (with $H \rightarrow ZZ \rightarrow 4l$ in the ZZ channel). The $ZZ \rightarrow 4l$ channel suggested a value of m_H = 119 GeV/c^{-2}

TABLE 2.1: The combined results of the Higgs search analyses presented by the CMS Collaboration[16].

Decay Modes	Combined Significance
$H \to ZZ$ $H \to \gamma\gamma$	5.0σ
$H \to ZZ$ $H \to \gamma\gamma$ $H \to WW$	5.1σ
$H \to ZZ$ $H \to \gamma\gamma$ $H \to WW$ $H \to bb$ $H \to \tau\tau$	4.9σ

while $H \to \gamma\gamma$ suggested a value of $m_H = 124$ GeV/c^2. Combined with all other decay channel results, the best fit converged at 124 GeV/c^2 with a 1σ uncertainty [15]. After gathering further data in 2012, both CMS and ATLAS announced the discovery of a new boson on the 4 July 2012. The combined CMS data for five decay modes gave the results listed in table 2.1. CMS announced a best fit mass value of m_H =125.3±0.6 GeV/c^2 [16].

2.1.2 Detector Layout

The following sections describe the main components of the CMS detector, including the subdetectors used for all physics analysis.

Magnet

With a design for $\sqrt{s} = 14$ TeV collisions, determining the momentum of collision fragments by their bending radius creates a difficult technical issue. The resolution of the momentum is predicted by the Glückstern equation;

$$\frac{\sigma_{p_T}}{p_T} = \sigma_x \cdot \frac{\vec{p}}{0.3\ B\ L^2} \sqrt{\frac{720N^3}{(N-1)(N+2)(N+3)(N+4)}} \tag{2.1}$$

Here, L is the radial length of the detector layers, σ_x is the spatial resolution of the tracking detector and N is the number of space points with which the particle's

TABLE 2.2: A comparison of the transverse momentum resolution of the inner tracker systems of three LHC detectors at $\eta \approx 0$. The combination of the excellent spatial resolution σ_x and the large bending power of the CMS magnet gives the CMS inner tracker an excellent transverse momentum resolution [17, 18].

	ALICE	ATLAS	CMS
Inner Radius [m]	0.039	0.05	0.044
Outer Radius [m]	0.44	1.1	1.1
N° of space points	6	3	3
Avg. Space Point Resolution [μm]	22	130	35
Magnetic Field [T]	0.5	2	3.8
p_T resolution ($\frac{\sigma(p_T)}{p_T}$) at $\mathrm{p}_T = 1$ GeV	6%	1.3%	0.7%

trajectory is measured. To improve the resolution, one could build a much larger detector to measure the trajectory more times or over a larger distance (increase N and L) or one could increase the bending power of the magnetic field B to decrease the radius of the trajectory. Due to geological and financial limitations of building a large underground cavern, the CMS collaboration decided on the latter, employing a 12.5 m long, 6.3 m diameter 3.8 Tesla super-conducting magnet at the core of the detector. Table 2.2 shows a comparison of the inner trackers of three current experiments; ALICE [7], ATLAS [11] and CMS [17].

To achieve such a large magnetic field, the windings are composed of 4 layers carrying a total of 41.7 MAmpere-turns storing 2.6 GJ of energy. This 4-layer winding is made from superconducting Niobium-titanium (NbTi) alloy. More technical information can be found in [10] and [19].

Silicon Pixel and Strip Trackers

At the center of the CMS detector are the silicon pixel and silicon micro-strip trackers. It is these detectors which measure the trajectories of particles emanating from the collisions and allow the vertex position to be reconstructed, along with the decay points of the long lived ($c\tau$ on the order of cm) decaying particles. Through the measurements of energy deposition and measuring the radius of trajectory as the particles bend in the 3.8 T magnetic field, the tracker system yields information on the momenta and particle types for all charged particles produced in every triggered collision. The layout of the pixel and strip tracker system is shown in figure 2.2.

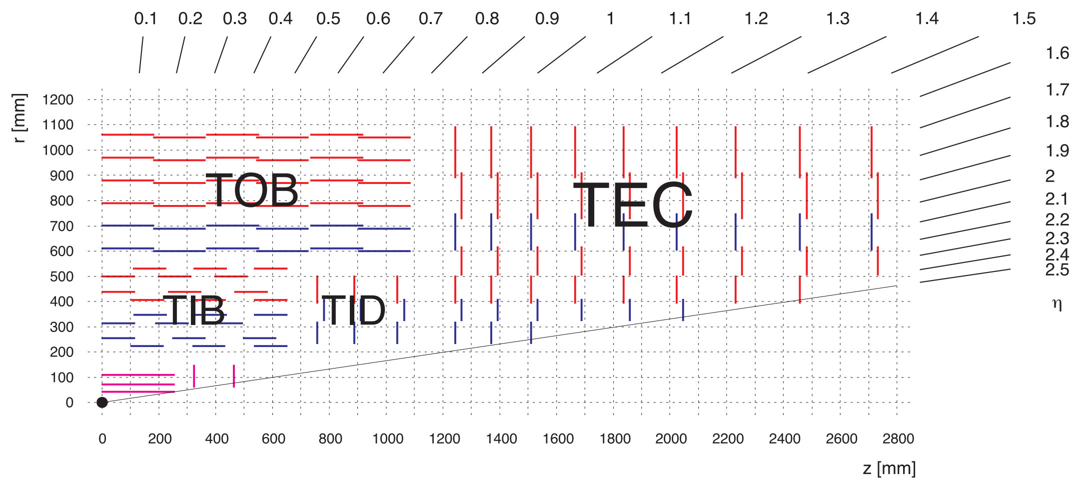

FIGURE 2.2: Transverse (1/4) view of the CMS Pixel and Strip detector [20]. TOB: Tracker Outer Barrel. TIB: Tracker Inner Barrel. TEC: Tracker Endcaps. TID: Tracker Inner Disks. The red lines represent single modules of the strip tracker. The blue lines represent double modules of the strip tracker. The pixel tracker is shown in pink at 0< $|z|$ <260 mm.

TABLE 2.3: The results from the CMS pixel tracker commissioning [21] showing the spatial resolutions in x and z. The resolution in y is the same as in x.

Resolution	Measured	Simulated
$\sigma(x)$	12.7μm $\pm$1.0μm	14.1 μm $\pm$0.5μm
$\sigma(z)$	32.4μm $\pm$1.5μm	24.1 μm $\pm$0.5μm

Pixel Tracker

The CMS Pixel Tracker is designed to measure precisely the trajectories of charged particles from collisions in the interaction region of CMS and to accurately reconstruct the vertices of these collisions. It is composed of three concentric barrel layers from radius $R = 4.4$ cm $-$ 10.2 cm, and two layers of disks on the end caps. The pixel tracker system covers a pseudorapidity range of $|\eta|$ <2.5 with a 2-hit coverage, or $|\eta|$ <2.2 if a more precise 3-hit coverage is required. In total there are 1440 pixel modules with each pixel having dimensions 100 $\times$150 μm^2 providing excellent spatial resolution, shown in Table 2.3. The small pixel sizes also ensure the channel multiplicities, that is, the average number of hits per channel in each collision, is always less than one and each pixel has time to recover in time for the next hit.

Due to its proximity to the beam pipe and its ability to detect patterns of tracks of deposited energy, the pixel tracker was used in the cross-section analysis (Chapter 7) as a way of separating the HF detector noise from beam induced background signals. Data received from the tracker whilst there are only single, non-colliding beams, would show long tracks in the presence of beam background particles generated by protons colliding with gas molecules upstream in the beam pipe.

Pixel Tracker Upgrades

At instantaneous luminosity, $\mathcal{L} = 2\times10^{34}\text{cm}^{-2}\text{s}^{-1}$ with 25 ns bunch spacing, the Pixel detector readout chips have been shown to suffer a data loss of around 15% in the innermost barrel pixel layer. This is due to the limited buffer size and readout speed. The resulting data loss affects the tracking efficiency, damages the performance of the vertex finding algorithms and the b-tagging capability, important for top and bottom quark studies and possible Higgs decay pathways. The new readout chip will have a faster readout implementation to reduce data loss.

An extra pixel barrel layer and disk will be added, encompassing the existing three layers. The ability to obtain 3 space points in the pixel layers increases the tracking efficiency and momentum resolution. A new light-weight structure is being designed to carry the power and cooling requirements of the pixel tracker. It is designed with the aim of reducing the material budget in the region, therefore reducing scattering of particles as they traverse the subdetector.

Strip Tracker

The CMS strip tracker has 9.3 million active elements in 15,148 strip modules and covers an area of 198 m^2 around the CMS interaction region. At design luminosity of the LHC, the collisions will cause $\sim$ 1000 hits per crossing in the tracker, a hit rate density of 1 MHz/mm^2 at R= 4 cm. This is the reason why pixel detectors are employed in the inner-most radius of the tracker. At larger radii, where the hit density is less, these simpler strip detectors can be used.

The strip tracker is divided into sections, shown in figure 2.2. The inner-most section is called the Tracker Inner Barrel (TIB). It contains 4 concentric barrel layers with the strips aligned in z and extending out to a radius of 55 cm. Closing

the ends of the TIB are the Tracker Inner Disks (TID) three layers of disks made of overlapping strip modules with the strips orientated radially.
Encompassing the TIB and TID is the Tracker Outer Barrel (TOB) and Tracker End Caps (TEC) which have 6 and 9 layers of strip modules respectively. The TOB covers a range of $z < 118$ cm and uses 500 μm thick silicon strip modules with a strip pitch of 122 μm - 183 μm. The TEC uses thin (320 μm) silicon strips in order to reduce the material budget and avoid the scattering of low energy particles which would spoil the trajectory before it can be accurately measured. At larger radii, 500 μm strips are used to improve the signal-to-noise ratio. The strip tracker modules have dimensions of 25cm $\times$ 180 μm and a resulting channel occupancy of around 1%. Overall, the CMS Silicon strip tracker provides between 8 and 14 high precisions measurements of the particles' trajectory in a pseudorapidity range $|\eta| <2.4$. The measurement of the CMS strip tracker signal-to-noise (SNR) and efficiency was measured with early LHC data (0.9 TeV and 2.36 TeV). The SNR was of the order of 20 - 25 and the overall efficiency, after accounting for around 2% of modules excluded for technical faults, was 99.8%.
The tracker system and reconstruction plays a major role in reducing the CMS data rate as the tracking information is used in the high level trigger of CMS. First, a track is defined if it creates a line of three pixel hits; one hit per pixel layer. Then, the track finding algorithm tries to reconstruct a track from $\geq$3 hits in the strip tracker, or $\geq$2 hits plus a point of origin from the beam spot or a vertex. With this initial trajectory estimation, the algorithm then searches outwards through the layers to find hits which are compatible with the trajectory. As each hit is found, the space-points are added to the trajectory and the track parameters and uncertainties are updated. This continues until either the outer-most tracker layer is reached or there are no more compatible tracks to be found. Further technical details are available in [10, 21].

Electromagnetic Calorimeter

The Electromagnetic Calorimeter (ECal) of CMS uses over 61,000 lead tungstate ($PbWO_4$) crystals, installed around the central barrel and an additional 7300 crystals in each of the endcaps. It includes a Si-Pb pre-shower counter in the endcaps to reject photons coming from π^0 decays. The ECal barrel covers the pseudorapidity range of $|\eta| < 1.479$. The endcaps extend this to $|\eta| < 3.0$.

Charged particles traversing the $PbWO_4$ crystals induce scintillation light which is detected by Avalanche Photodiodes (APDs) mounted on the ends of the barrel crystals and Vacuum photo-triodes (VPT) on the endcap crystals. The signals from these photo-sensors are pre-amplified and shaped before being converted into a digital signal by a 12 bit 40MHz sampling rate ADC. The data is then transfered to a front-end card which then forms the ECal trigger primitive data before transmitting it to the CMS Level 1 trigger.
The $PbWO_4$ crystal is very dense, 8.3g/cm^3. Ordinary glass used in every day situations such as windows, has a density of only $\sim$2.5g/cm^3. This high density ensures numerous interactions with the charged particles traversing the crystal and therefore a higher scintillation light yield. The energy resolution (σ_E/E) was measured in a test beam in 2004 using 120 GeV electrons and found to be 0.5%. CMS was installed into the underground cavern, a month-long study known as Cosmic Run At Four Tesla (CRAFT) was made. During this time, CMS recorded over 270 million cosmic ray muon events. The energy resolution loss due to non-uniformities, light leakage and calibration inaccuracies was measured to be 0.3%[22], bettering the target resolution of 0.5%.
The $PbWO_4$ crystals are subjected to high particle flux and damage due to radiation was expected. In anticipation of this, a laser calibration system was put in place to allow rapid recalibration of each channel to compensate for the wavelength selective light yield loss. Figure 2.3 shows the ratio of the electron energy E_e, measured with the ECal, to the momentum $\vec{p}_e$, measured in the CMS tracker, as a function of time for the entirety of the 2011 *pp* data and over all ECal channels. The red points show the data before the transparency (radiation damage) correction is applied. Through the period of 2011, ECal experienced around 2.5% light loss due to radiation damage. The green points show the corrected $E/\vec{p}$ data is stable to within 0.2% [23]. Full details are available in [10] and [24].

The electromagnetic calorimeter must be capable of distinguishing between electrons and high energy photons. Electrons can often be associated with the production and decay of W and Z bosons. Furthermore, depending on the mass of the Higgs boson, which was not known or predicted prior to the ECal design and construction, photons may feature in the Higgs boson's decay signatures via $H \to WW* \to \gamma\gamma$ and $H \to t\bar{t}* \to \gamma\gamma$. It is vital that the ECal is capable of distinguishing such *prompt* photons amidst the large backgrounds of photons from π^0 decays.

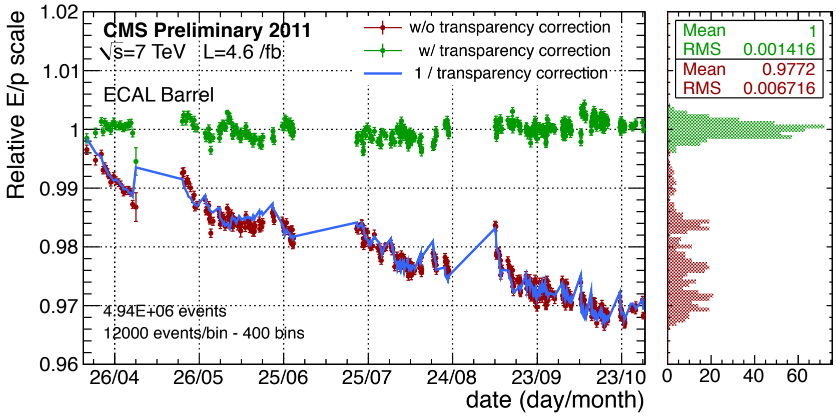

FIGURE 2.3: By the use of the installed laster calibration system, the CMS ECal was able to correct for radiation damage to the $PbWO_4$ crystals to within a 0.2% stability across the entire detector.[23]

Electron identification in the ECal is achieved by searching for electromagnetic clusters with good energy and spatial qualities matching those in the inner tracker. Calibrations were done with early LHC data [25] using electrons produced primarily from W decays ($W^- \to e^-\nu_e$). It has been shown [26] that the electron identification with a range of efficiency cuts from 95% to 80% agreed with Monte Carlo studies to within 3% to 8%.

In pp collisions, isolated final state photons are of interest. Prompt photons produced in collisions through interactions such as $q + g \to q + g + \gamma$ or through the aforementioned Higgs decay paths, are not affected by the magnetic field of the CMS solenoid. Conversely, those produced from hadronic or leptonic interactions, in which the charged particles are bent by the magnetic field, will show a spread in the ECal, thus providing a simple signature from which to identify them. Hence, the shower shape in the ECal, the isolation of energy in neighbouring ECal towers and the ratio of ECal energy and the momentum of the cluster of tracks, as measured in the inner tracker, all give a satisfactory discrimination of prompt photons over those from, for example, π^0 backgrounds. Measurements from 2010 LHC data showed that the CMS ECal is capable of detecting and selecting prompt photons with a >30% signal to background ratio at a 90% signal efficiency [25].

ECal Upgrade

The plans for the ECal upgrade include the replacement of the $PbWO_4$ scintillators with ceramic materials. ECal physicists are currently testing Lutecium Yttrium Aluminium Garnet materials doped with Praseodymium (LuYAG:Pr) or Cesium (LuYAG:Ce) and Yttrium Aluminium Garnet materials doped with Cesium (cYAG:Ce) but without the Lutecium. New light guides, wavelength shifting fibres and GaAs photo detectors are being tested for radiation hardness and light wavelength compatibility to optimise the light yield.

Hadron Calorimeter

Whereas the Electromagnetic Calorimeter aims to measure the momentum of photons and charged leptons, the Hadronic Calorimeter (HCal) is designed to detect and measure the momentum of hadronic jets and neutral hadrons or more exotic particles. HCal is separated into four parts. The HCal Barrel detector (HB), HCal Endcaps (HE), HCal Forward (HF) and HCal Outer (HO). The majority of HB is situated between the ECal (R = 1.77m) and the inner radius of the magnet coil (R = 2.95m). This puts a limit on the amount of material that can absorb the hadronic showers and for this reason, the outer HCal, HO is situated around the barrel, outside of the magnetic coil. The layout is shown in figure 2.4.

The HB Calorimeter uses Bicron BC408 plastic scintillator (identical to that used in the Beam Scintillator Counter (BSC), described in chapter 3) and Kuraray SCSN81 plastic scintillator for their high light yield and moderate radiation hardness. Full details of the Hadronic Calorimeters can be found in [27].

Hadron Forward Calorimeter

The Hadronic Forward Calorimeter (HF) is situated ±11.15m from the I.P and must withstand some of the most severe particle flux. 760 GeV per proton-proton interaction is deposited, on average, into the HF absorbers; nearly eight times more than the rest of the CMS detector. HF covers the pseudorapidity region of $2.9 < |\eta| < 5.2$ and is expected to experience ≈10 MGy over its lifetime. The calorimeter is made from iron absorber layers which are grooved to accommodate

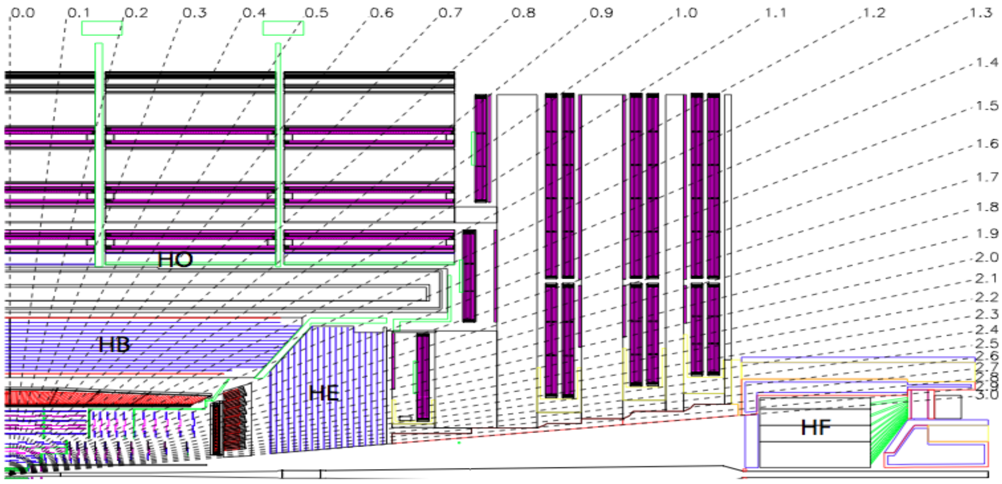

FIGURE 2.4: A transverse view of the HCal layout. The HCal Barrel (HB) is concentric around the beam pipe covering a pseudorapidity range of $|\eta| < 1.3$. The HCal endcaps (HE) and HCal Forward (HF) cover the forward regions ($1.3 < |\eta| < 2.9$ and $2.9 < |\eta| < 5.2$ respectively). The *tail catcher*, HO covers approximately the same η range as HB.

high OH^- Quartz fibers laid along the Z plane. The front face (the location of the BSC1 tiles) is made of 19cm of dense polyethylene. When charged particles above the Čerenkov threshold, E_{thr} pass through the quartz fibers, they generate Čerenkov light. The Ĉerenkov energy threshold for electrons is;

$$E_{th} = m_0 c^2 \left(-1 + \sqrt{1 + \frac{1}{n^2 - 1}} \right)$$

$$\geq 511\text{keV} \left(-1 + \sqrt{1 + \frac{1}{1.45^2 - 1}} \right)$$

$$\geq 190\text{keV}$$

The threshold is dependent on the particle mass. For comparison, muons ($m_\mu =$ 105.658 MeV) require more than 40 MeV to create a signal, while protons (m_p) require 357 MeV. Therefore, the calorimeter is most sensitive to the electromagnetic component of showers. Each calorimeter is formed from 18 wedges, each split into 13 η segments as shown in figure 2.5(a).

The long and short quartz fibers are read out separately by PMTs located in

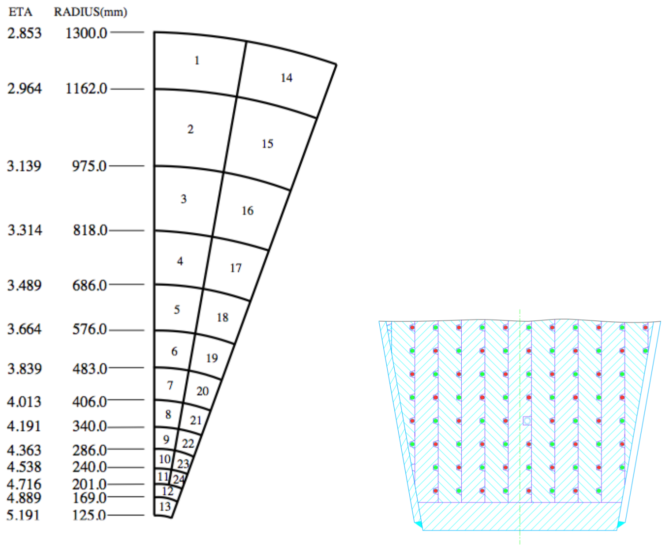

(a) HF Wedge (b) HF Fibers

FIGURE 2.5: (a) One HF Wedge showing the η and ϕ segmentation. (b) One segment of the wedge contains long (EM) and short (Hadronic) fibers.

readout boxes behind the HF calorimeters. The signals from the PMTs are fed into charge integrating analog-to-digital convertors (ADC), the output of which is encoded before being sent to the service cavern via a Gigabit optical link. In the service cavern, the signals are decoded and used to form trigger primitives which feed into the CMS Calorimeter trigger and form a key part of the Level 1 Accept (L1A) decision. The charge integration time of the ADC/Integrator/Encoder, otherwise known as a QIE, is 25ns. The charge from an entire HF tower is summed in η and ϕ prior to being sent to the trigger.

The HF calorimeters are used extensively in the analysis of the inelastic cross-section in Chapter 7. It is important to note that the time granularity of the HF calorimeters is 25 ns, the minimum time between colliding bunch crossings in the LHC. However, many independent *pp* collisions can occur within a single bunch crossing but the HF calorimeters are not able to resolve them. For this reason, data from the early, low luminosity phase of LHC operations was used in the analysis to ensure that the number of simultaneous 'pile-up' collisions is less that one per bunch crossing, on average. Further details of the HCal system are available in [10] and [28].

HCal Upgrade

The planned upgrades for HCal center around the front end electronics. Throughout 2010 - 2012, the HF calorimeter has suffered from problems relating to charge particles interacting with the PMT quartz windows. These events caused very large signals in the PMT which were translated as being sometimes unrealistically high energy deposits in the related HF tower. For this reason, the upgrade of HF includes the replacement of the current PMTs with multi-anode PMTs. Čerenkov light from the quartz fibres illuminates all four photocathodes. By looking for coincidences between the different anodes, a signal can be determined to be real (a signal is seen from two or more anodes) or false (a signal is see by only one anode due to a direct particle hit). This will be a great improvement to the HF calorimeter, especially as the current topological method of signal 'cleaning' is beginning to suffer as the pileup increases.
The HCal Barrel and Endcap calorimeters will be fitted with Silicon Photomultipliers (SiPM) in place of the current Hybrid Photodiodes (HPDs) to improve the signal-to-noise ratio. This will prove to be important as the endcap scintillators begin to show signs of radiation damage. New readout electronics are being developed to provide the ability to control the sampling clock of the QIEs and give a more stable time delay between the occurrence of the event and the production of a triggering signal, which is an important requirement very high luminosities.

RPCs & Muon Chambers

The CMS Muon system plays a vital role in the detection of many interesting events such as the Higgs signature;

$$\mathrm{H} \rightarrow \mathrm{ZZ} \rightarrow 4l \tag{2.2}$$

where $4l$ are muons or electrons, shown in the Feynman diagram of figure 2.6.

The Muon system has a similar layout to that of the HCal. It comprises Drift Tube (DT) chambers in the barrel region that cover $|\eta| < 1.2$ in 4 layers. In the endcap regions, muon rates are higher and the B-field is non-uniform. Here, Cathode Strip Chambers (CSC) are used and cover $0.9 < |\eta| < 2.4$. The magnet return yoke

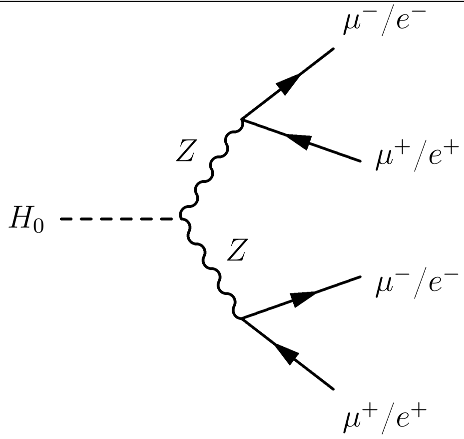

FIGURE 2.6: One of the cleanest decay paths for a SM Higgs. This distinctive signature, with four energetic and isolated final state leptons, was one of the motivations of the CMS design.

comprises of 11 separate elements, including 3 endcap disks per end* and 5 barrel wheels. As well as keeping much of the magnetic field contained, they also act as an hadron absorber for the muon system. Due to the uncertainty of the DT and CSC muon systems being capable of measuring the correct beam crossing time at the full LHC luminosity, a complementary muon detector system, consisting of Resistive Plate Chamber (RPCs), was installed in the barrel and endcap regions. Their speed and high segmentation ensured the availability of an successful and independent muon trigger. The system is shown in the diagram of figure 2.7

Muons lose less energy due to Bremsstrahlung than electrons and are able to penetrate to the outer layers of the CMS detector. The muon system is designed to identify muons, measure their momenta and also provide a Level 1 Muon trigger primitive. It provides a Global Muon Trigger efficiency of >96%. The momentum resolution $\frac{dp_t}{p_t}$ ranges from 0.2% for p_t <100 GeV to 18% in the forward regions. Table 2.4 lists the spatial resolutions achievable by each subsystem.

TABLE 2.4: The spatial resolutions measured in the CMS Muon subsystem when combined with tracking data from the pixel and strip trackers[29].

Location	Hardware	Spatial Resolution (rΦ)	Spatial Resolution (z)
Barrel	DTs	$\sim 100\mu$m	$\sim 150\mu$m
Barrel & End Caps	RPCs	$\sim$ 1 cm	$\sim$ 1 cm
End Cap	CSCs	$\sim$ 74$-$150μm	na

*An extra endcap disk per end is currently being added.

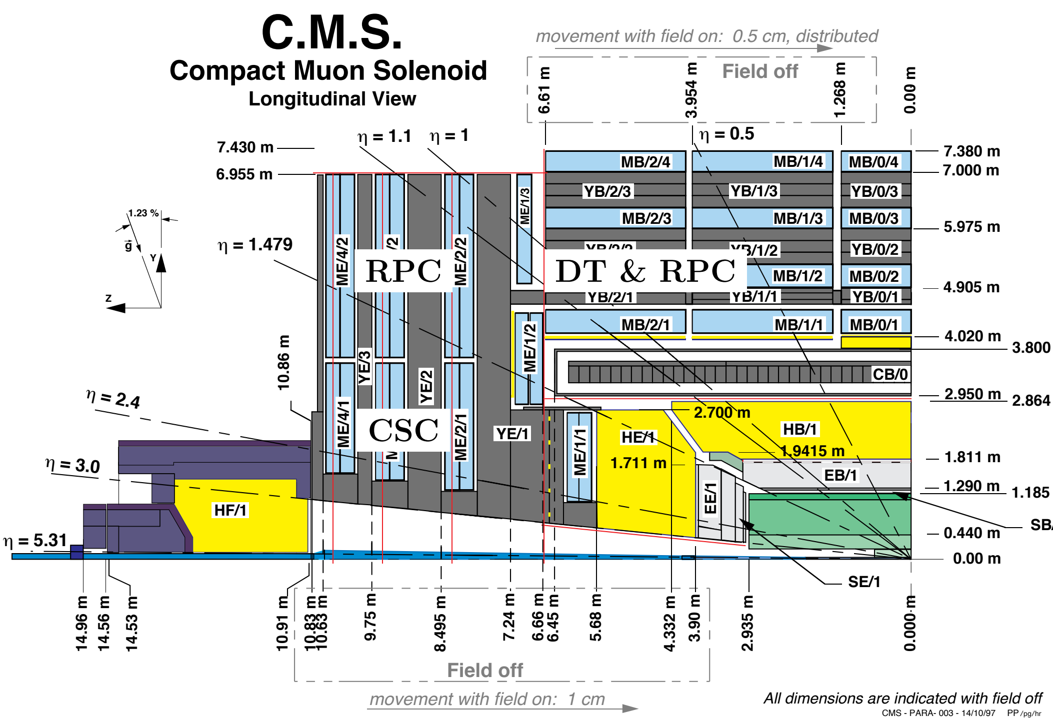

FIGURE 2.7: A side view of the CMS Muon system including the Drift Tubes around the barrel ($|\eta| < 0.8$), the Resistive Plate Chambers ($|\eta| < 1.6$) and the Cathode Strip Chambers ($1.6 < |\eta| < 2.4$) on the end caps.

2.1.3 Triggering System for CMS

The CMS experiment, together with ATLAS, will experience higher luminosity and proton-proton collision rates than any previous experiment. With bunch crossings occurring every 25ns and an aim to obtain a luminosity of up to 10^{34} cm^{-2}s^{-1}, an average of 17 collisions occur at a 40MHz rate. Potentially, there could be $\mathcal{O}(10^9)$ events every second. The CMS trigger system must reduce this colossal amount of data to a more manageable and useful subset, selecting events of interest for further analysis by the High Level Trigger (HLT) algorithms.

Level-1 Trigger

The level-1 trigger is tasked with reducing the vast quantities of data down to a manageable level; less than 100kHz output of the maximum 40MHz input rate. In practice, the output rate is limited to approximately 30kHz to allow a reasonable safety factor [30]. The trigger system runs synchronously at the LHC clock rate

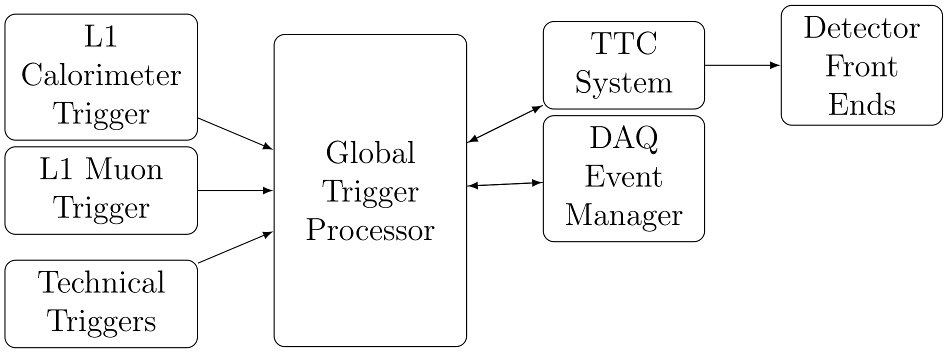

FIGURE 2.8: A block diagram of the CMS Global Trigger (GT) layout showing the input trigger primitives sent from the L1 Calorimeter and L1 Muon trigger and the 64 Technical Triggers (TT) of which the BSC provided 14 triggers[33].

of 40 MHz selecting muons, electrons, photons and jets from the remnants of each collision. For every bunch crossing, the CMS Global Trigger (GT) decides whether to accept or reject a physics event for further analysis. The decision is based on 'trigger objects' which contain information such as energy, momentum, location and quantity of particle hits within the trigger objects. This information comes from the Global Calorimeter Trigger (GCT) and Global Muon Trigger (GMT) which are first synchronised to each other and the LHC orbit clock, then passed to the Level 1 trigger logic module. All events are initially stored in a 3.2μs pipeline, during which time the Level-1 'accept' or 'reject' decision is made every 25ns. The accepted events are moved to a buffer for readout and processing by the High Level Trigger (HLT).

Up to 64 technical triggers are also fed into the global trigger which can be enabled to accept or reject events. These enter the final OR to trigger or veto an event [31, 32]. Their purpose is to provide minimally-biased triggers for off-line physics and trigger analysis, allowing physicists to understand the conditions in CMS for any particular event. For example, Technical Trigger Bit 0 (`BPTX plus AND minus)` flags when the two proton or heavy ion bunches are entering the CMS detector simultaneously, which must be the case for any chance for a collision event to occur. The technical triggers are hard-wired and cannot be combined in logic with any other triggers. Figure 2.8 shows a block diagram of the layout of the Level-1 Global Trigger (GT).

The GT system also allows for another 64 trigger inputs which, unlike the technical triggers, can be logically combined with other triggers to provide useful analysis triggers. These are referred to as 'External Conditions Triggers' or 'Extra-Algo Triggers' and are constructed in software by configuring Field Programmable Gated Arrays (FPGA). They enter the final OR with the technical triggers.

During 2009 - 2011, the BSC provided both technical triggers and Extra-Algo triggers to the GT. These triggers were intended for use in online event selection and off-line physics analysis, allowing physicists to select events based on the kinematic selectivity they provide. Further details of the BSC triggers and analysis of their performance in 2010 is given in Chapter 4.

The Higher Level Trigger

The CMS Higher Level Trigger (HLT) is capable of accepting a Level-1 output rate of up to 50kHz. It is tasked with reducing this data rate down to a maximum rate of only 300 Hz for permanent storage. With current safety limits in place, the storage rate is not expected to be more than 200 Hz. The HLT trigger hardware comprises approximately 1000 commercial CPUs making up the 'Event Filter Farm'. The software filtering works by taking the input from the Level 1 trigger 'seed' and carrying out increasingly complex reconstruction algorithms and applying kinematic cuts at each stage. The HLT trigger algorithms can be divided into the following categories;

Muon Trigger: Reconstruction of μ trajectories using the Drift Tubes (DT), Cathode Strip Chambers (CSC) and Resistive Plate Chambers (RPC). The μ trajectories are then combined with charged particle tracks, reconstructed from the central tracker in what is termed 'Level 3 reconstruction'.

Photons & Electrons: The Level 1 e/γ trigger, based on information from ECAL, seeds the HLT e/γ algorithms. Reconstruction algorithms are based on ECAL clusters and HCAL energy.

Jets & missing E_T: Important for QCD dominated physics processes, the HLT trigger uses iterative cone algorithms based around the HCAL towers and ECAL crystals. Certain threshold requirements must be satisfied.

Hadronic τ decay: Important for Higgs and SUSY searches. The τ decays hadronically 65% of the time, producing τ jets. As these jets do not contain leptons which would pass the corresponding Level 1 trigger, special trigger algorithms are implemented in both the L1 and HLT. More details of these algoritms can be found in [34].

b-Jets: For selecting exotic physics channels, this trigger requires a b-tagged jet in the HLT path. The b-Jet HLT trigger can be further sub-divided into a b-lifetime trigger and a $b \rightarrow \mu$ trigger. Further details are available in [34].

Combined objects: This trigger combines two or more trigger objects to make more specialised triggers focussed on certain processes. For example, the Higgs boson may decay indirectly, by $H_0 \rightarrow \tau + \nu_\tau$ with the τ in turn decaying into e/μ or a τ-jet. The HLT Combined trigger can select events based on the combination of the τ-jet and e/γ triggers.

2.2 Beam & Radiation Monitoring for CMS

In relation to the protection and the requirement of stringent beam monitoring of CMS, it is worth mentioning the beam dump system located at point 6 of the LHC. The purpose of the beam dump system is to extract the two beams quickly and safely and is usually a planned action, initiated towards the end of a fill when the bunch intensities have been depleted. Occasionally, however, the control of the beams may be lost due to vacuum failures, triggering of magnet quench protection systems or a multitude of other reasons [35]. The beam dump system involves horizontally deflecting fast-pulsed magnets (‘kicker’ magnets) and vertically-deflecting septum magnets. A $3\mu s$ gap is incorporated into the bunch structures of both beams. These ‘abort gaps’ are created so that the kicker and septum magnets can turn on as the gaps pass the beam dump, directing the entire bunch train safely into absorber material outside of the LHC tunnel. This is known as a ‘synchronous beam dump’. There is, however, the possibility of a system failure resulting in an ‘asynchronous beam-dump’ where the kicker magnets turn on while the high energy proton beams are still passing, disturbing the momentum of the particles and causing large beam losses. In the event of such an occurrence, CMS is in danger of being showered with high energy, heavily ionising particles

TABLE 2.5: A list of the BRM sub-detectors in CMS with their primary functionality, location and time resolution.

Detector	Location	Purpose	Sampling Time
Medipix	z = 15 m, x = 12m	Dose Monitoring & Particle Identification	1 minute
BCM1F	Pixel Volume. Z = $\pm$1.8 m	Beam Monitoring	$\sim$ns
BCM1L	Pixel Volume. Z = $\pm$1.8 m	Beam Monitoring & abort	5μs
BCM2	TOTEM T2. Z = $\pm$14.4 m	Beam Monitoring & abort	40μs
BSC	Z = $\pm$10.9 m & TOTEM T2, Z = $\pm$14.4 m	Beam Monitoring & Triggers	$\sim$ns
BPTX	Z = $\pm$175 m	Beam Monitoring & Triggers	$\sim$ps

which could damage the delicate silicon tracker (see section 2.1.2) and other sub-detectors [36]. It is extremely important that the monitoring of the beams and the radiation environment in CMS is done in such a way to protect the detector and allow for post-mortem analysis of dose and particle flux should an unplanned beam dump occur.

The CMS Beam & Radiation Monitoring (BRM) group have installed several subdetectors which are designed to detect and limit the damage due to sudden beam losses while allowing for quick post-mortem analysis should a large loss occur. Additionally, many of these subdetectors play further roles in CMS in the form of beam monitoring for normal running periods or triggering on minimum bias and zero bias events, as was the case with the BSC and the BPTX. Table 2.5 gives a list of the BRM sub-detectors in terms of their functionality, time resolution and location.

Medipix

The Medipix2 detectors are a collection of 256$\times$256 pixel detectors measuring 1.4 cm^2 and with pixel dimensions of 55μm^2. The active 300μm silicon layer is covered by various conversion layers, assembled by the Czech Technical University in Prague. Figure 2.9 shows a photograph of the Medipix2 ASIC mounted on its readout board. Figure 2.10 shows an X-ray image from the Medipix chip taken through the various conversion layers. Table 2.6 lists the purpose of the various conversion layers.

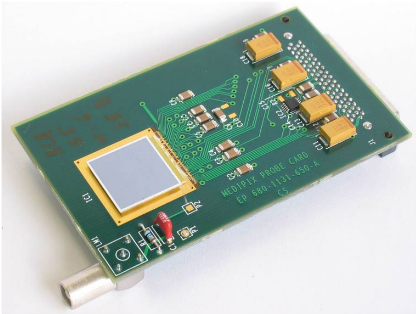

FIGURE 2.9: A photograph of the Medipix2 ASIC on its readout board similar to those installed in the CMS experimental cavern.

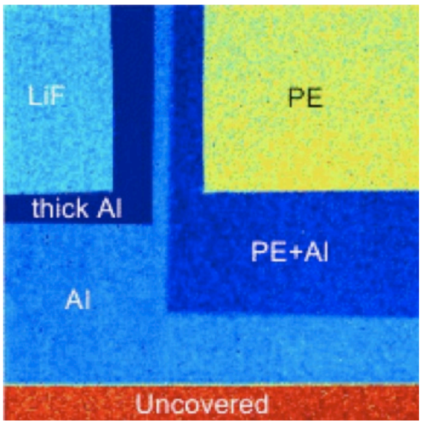

FIGURE 2.10: An x-ray image taken with the Medipix2 ASIC showing the various conversion layers.

TABLE 2.6: The various conversion layers glued to the silicon surface of the Medipix2 devices installed in CMS act to optimize small regions of the ASIC to certain particle fluxes and energies. The installation of these layers was done by a team lead by S. Posposil at the Czech Technical University in Prague.[37]

Layer	Material	Purpose
Al	Aluminium	Beam hardening. Removal of low energy electrons.
PE	Polyethylene	Fast neutron conversion to protons.
LiF	Lithium Fluoride	Thermal neutrons to α particles.
Al + PE	Aluminium + Polyethylene	Remove low energy electron signal from neutron signal.
Thick Al	Aluminium	More aggressive beam hardening.

Three Medipix devices were installed† on the walls of the CMS cavern and collected data throughout 2010 to compare particle fluence with those of Monte Carlo simulations[37].

2.2.1 BCM1F

The Beams Condition Monitor 1 - Fast (BCM1F)[38] is a single-crystal diamond based monitor located ± 1.8 m from the nominal interaction point at a radius of only 4.5 cm. There are four diamonds (5 cm $\times$ 5 cm $\times$ 500μm) on each end positioned in the $\pm x$ and $\pm y$ locations and running in pulse counting mode. The

†Installed by A. J. Bell (2009). System improved and calibrated by D. Pfeiffer (2010).

BCM1F is used to detect and diagnose problematic beam conditions which result in beam losses over a very short time period. Through 2010 - 2012, the BCM1F has been developed to measure the real-time luminosity and gate on colliding and non-colliding bunches to search for vacuum pressure spikes and beam gas events. This work was carried out by physicists from the *Deutsches Elektronen-Synchrotron* (DESY) in Zeuthen.

2.2.2 BCM1L

The Beams Condition Monitor 1 - Leakage Current (BCM1L) is a polycrystalline diamond system located alongside the BCM1F ($|z| = 1.8$ m, $r = 4.5$ cm). Each diamond is $10\times10\times0.4$ mm^3 and orientated parallel to the z direction. Unlike the BCM1F, which detects individual quanta of beam losses, the diamonds of the BCM1L run in *leakage current* mode in which the longer term beam losses cause a proportional current. A threshold value is applied to the integrated current measurement, over which, a hardware beam abort signal can be generated and transmitted to the LHC control via the Beam Interlock System. This causes the beams to be dumped within 3 orbits. Lower threshold levels can be set at which, should the leakage current cross, will send a hardware signal to the CMS sub-detectors to initiate a voltage ramp down.

2.2.3 BCM2

The BCM2 subsystem is virtually identical to the BCM1L subsystem in technicalities. The BCM2 uses poly-crystal diamonds and is located at ±14.4 m from the I.P. It comprises of 12 diamonds per end; 4 inner diamonds ($r = 5$ cm) which are in a direct line-of-sight to the I.P, and 8 outer diamonds ($r = 29$ cm). The readout system uses standard LHC Beam Loss Monitor electronics and data processing [39] running at a 40μs sampling time. Like the BCM1L, the BCM2 leakage current is proportional to the beam losses and thresholds are applied at which the system will trigger a hardware beam abort via the interlock system. This system was the responsibility of Karlsruhe Technical University, Germany and installed by Steffen Müller and the CMS BRM group.

2.2.4 BPTX

The Beam Position and Timing (BPTX) subdetector comprises of 2×2 electrostatic detectors with picosecond timing resolution located at ±175 m from the CMS interaction point. These are the same devices used throughout the LHC for the beam position monitors. At ±175 m, the LHC beams are in separate beam pipes and the electrodes are positioned to pick-up the charge of only the incoming beams. The readout is achieved through a commercial 5 GigaSamples/second oscilloscope. Comparisons of the relative timing from the electrodes allows the BRM group to display the collision offset with respect to the nominal $z = 0$ position with ∼200 ps precision (6 cm), ensuring that the data taken comes from collisions very close to the I.P. The coincidence of the BPTX signals acted as a zero bias trigger in many analyses, including the pp cross section analysis of Chapter 7. It also provides the non-colliding gating signals used in the BCM1F beam gas monitoring and Beam Halo Counter (BHC) system for triggering on bunches without collisions to allow a better measurement of the beam muon halo background.

Chapter 3

Design of the Beam Scintillation Counter

The Beam Scintillation Counter (BSC) was designed to be a monitoring and triggering sub-detector for CMS during the very early phases of the 2009 - 2010 LHC commissioning. Over two years later, the system was still operating, providing accurate minimum bias triggers during the low luminosity or low energy re-start runs, as well as during the Heavy Ion runs. It provided full-time beam monitoring for CMS from the LHC injection and ramps, continuing through the entire fill, enabling CMS operators to determine if conditions were safe to turn on the more fragile sub-systems like the Cathode Strip Chambers (CSC) and the Silicon Tracker. Furthermore, it was used as an online luminosity monitor for the heavy ion program. It was made primarily from parts reclaimed from the OPAL endcaps and its acceptance was limited due to the available quantity of materials. With a greater acceptance, the BSC could have been an excellent detector for the measurement of the *pp* inelastic cross-section (See Chapter 7) and other forward physics analyses, as were the equivalent Minimum Bias Scintillator Counters (MBSC) of ATLAS. This chapter describes the BSC system. More information of the installation can be found in [40].

3.1 Purpose of the BSC

The BSC detector was constructed with two primary goals in mind. First, it had to provide short to mid-term beam monitoring capabilities for CMS particularly for low bunch intensity LHC fills where other Beam & Radiation Monitoring (BRM) detectors were not expected to be capable. The second aim was to provide various triggers to the CMS Level-1 trigger system which would aid in timing in all other CMS trigger inputs, provide minimum-bias detection at low luminosity and improve the zero-bias trigger selection in offline analysis. The BSC had to utilize tried and trusted technologies as it was a vital component of CMS for the start-up phase.

3.2 Layout of the BSC

A schematic overview of the BSC system is shown in figure 3.1 and a photograph of the installed BSC1 tiles is shown in figure 3.2, which was done during 2008 - 2009 [40]. The BSC1 scintillator tiles were situated on the front of the Hadron Forward calorimeters (HF) at a nominal distance of $\pm$ 10.9 m $\pm$5 cm from the I.P. There were two additional tiles per end, known as the BSC2, located behind the HF calorimeter and inside the wheels of the Beam Condition Monitor (BCM2) at a nominal distance of 14.36m $\pm$5cm. The pseudo-rapidity ranges are shown in figure 3.3 and in table 3.1. The η values for the outer BSC1 tiles are approximate due to the trapezoid shape of these tiles. All of the front-end components of the BSC were obtained from the endcaps of the OPAL experiment [41] at LEP.

The basic operation was as follows. Charged particles interacted with the tile material causing scintillator light. This scintillator light was collected by wavelength shifting fibers and transmitted down clear polystyrene/PMMA optical fibers to banks of 10-dynode photomultiplier tubes (PMT), located above the calorimeter and partially shielded from the magnetic field by the iron bulk of the HF. The PMTs were supplied with high voltage (typically between 700V - 1500V) from a CAEN power crate situated in the Underground Service Cavern (USC) at the S1 level. The PMT output signals were carried up to this location by 50Ω impedance co-axial cables where they entered the NIM based and VME based readout systems.

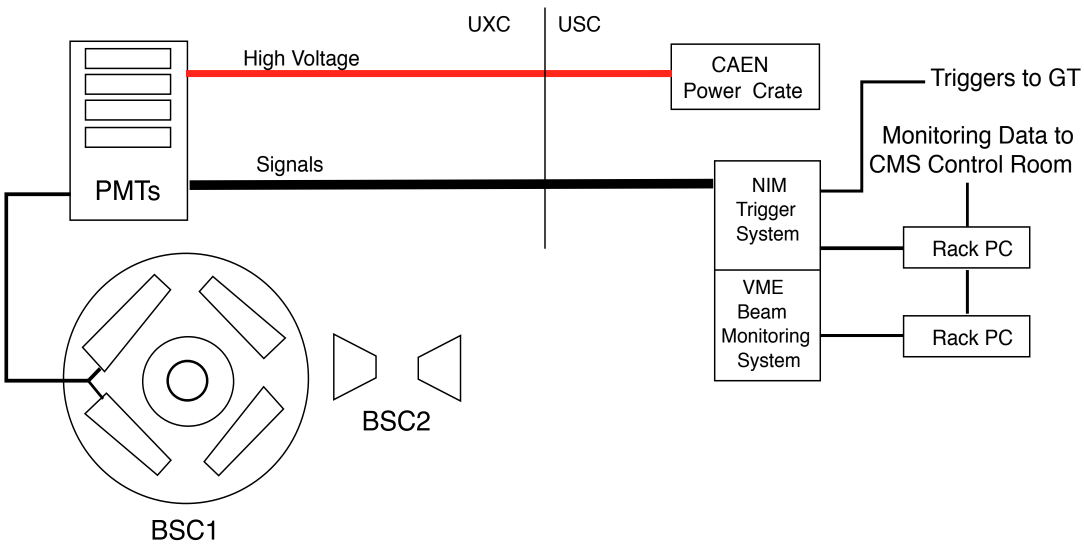

FIGURE 3.1: Schematic diagram of the BSC layout

FIGURE 3.2: A photograph of the installed BSC1 tiles on the HF calorimeter. The work was carried out in 2008 - 2009. More details can be found in [40].

TABLE 3.1: The locations and pseudo-rapidity ranges of the BSC1 and BSC2 tiles.

Tiles	z position	R	$\Delta\eta$
BSC1 Inner	10.9m	0.186m - 0.306m	4.26 - 4.76
BSC1 Outer	10.9m	0.399m - 0.509m	3.75 $\sim$ 3.99
BSC2	14.4m	0.054m - 0.264m	4.69 - 6.25

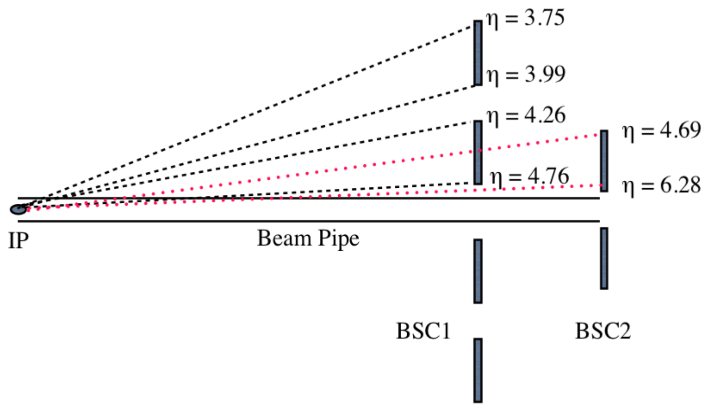

FIGURE 3.3: The pseudo-rapidity ranges of the BSC1 and BSC2 tiles.

The NIM system created all of the triggers from the BSC signals and passed them on to the Level-1 Global trigger via a NIM-LVDS level convertor. The VME system performed the monitoring by way of Scalar modules, a Time-to-Digital Convertor (TDC) and four Analog-to-Digital Convertors (ADC). The control of the VME modules and the storage and transmission of the data was carried out by two rack PC's via PCI-Express optical links.

Visualisation of the monitoring data was taken care of in one of the CMS node computers and sent to screens in the CMS control room. Information of the triggers enters the CMS data stream via the Global trigger and was recoverable using various software tools; CMSSW, NanoDST or OpenHLT as explained in Chapter 4.

3.3 Front End Detector

The BSC front end was made from simple, yet robust materials which would withstand the first year or so of LHC operation without the need for repeated complicated calibration and would reduce the probability of technical failure. There were 36 channels in total. 16 channels were located on the front of each HF calorimeter forming the 'BSC 1'. A further 2 channels were mounted behind each HF calorimeter within the frame of the BCM2 sub-detector at a nominal distance of $\pm$ 14.36m from the I.P. The tiles were made from BC408 [42] polyvinyl-toluene with polystyrene wavelength shifting fibres embedded into grooves etched into the surface. The wavelength shifters converted the $\lambda_{\text{peak, scint}}=$ 425 nm light to $\lambda_{\text{peak, WLS}}=$ 495 nm to increase the conversion efficiency at the green sensitive PMT photo-cathode. The FWHM of the output signal from the PMT was measured using cosmics to be 12 ns $\pm$4 ns and the number of photo-electrons from cosmics was measured to be between 8 and 15, depending on the tile. The variation is thought to stem from the quality of the optical coupling between the scintillator and the wavelength shifting fibers.

3.4 Optimization of the BSC channels

In order to produce an efficient triggering system, it was vital that each of the individual channels of the BSC were set up correctly so the signals from either end arrive in time with similar channels and the voltages were such that they are able to resolve the entire spectrum of pulse heights expected from minimum ionising particles (MIPs). A full description of the BSC trigger system is given in section 3.5.

3.4.1 BSC Pulse heights

The first step in setting up the individual channels was to get the optimum voltage so that the maximum amount of the MIP energy spectrum possible was resolved. The minimum threshold level achievable by the trigger logic was -30mV, so it was important that the majority of the signal spectrum overcomes this level. The energy loss in the BSC scintillator tiles was expected to follow a Landau distribution.

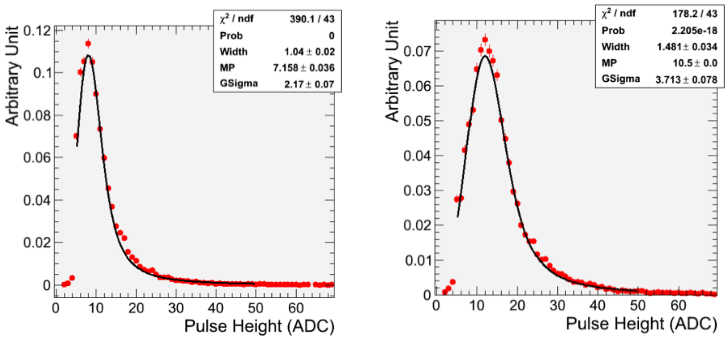

FIGURE 3.4: Two examples of the Landau distribution in pulse heights from the BSC channels during circulating beam.

If the voltage to the PMT was too low, some of the Landau peak would fall below the -30 mV threshold resulting in a loss of single channel efficiency (See figure 3.4 Left). If the voltage was too high, there is a possibility that PMT noise could overcome the discriminator threshold, or pulse pile-up could occur as the filling schemes advanced. Both would severely influence the trigger logic and monitoring of the BSC system.

The ADC channels were first calibrated using a signal generator to ensure the digitised readout correctly represented the analog signal input. Calibration factors for each channel were applied to correct for any discrepancy. Groups of 8 channels were connected to a CAEN V1721 ADC and the peak pulse heights measured using single bunch circulating beam. Histograms of the pulse heights in volts were made for each channel and an extrapolation to zero volts made to determine what fraction of the distribution fell below -30 mV in each channel. Figure 3.4 shows the distributions for two of the BSC channels in terms of ADC units, where 1 ADC unit $= -4$ mV. On this scale, the -30 mV lies at 7.5 ADC units. The initial single channel efficiencies, based on approximate plateau curve measurements in the lab, ranged between $79\% - 98\%$. The PMT high voltage supplies were adjusted and the MIP peak analysis repeated to attain an average MIP detection efficiency of 97% ±2% across all 36 BSC channels.*

*This work was carried out with the help of Dr. Yen-Jie Lee (MIT, Boston USA) and Dr. Gabor Veres (University of Budapest, Hungary).

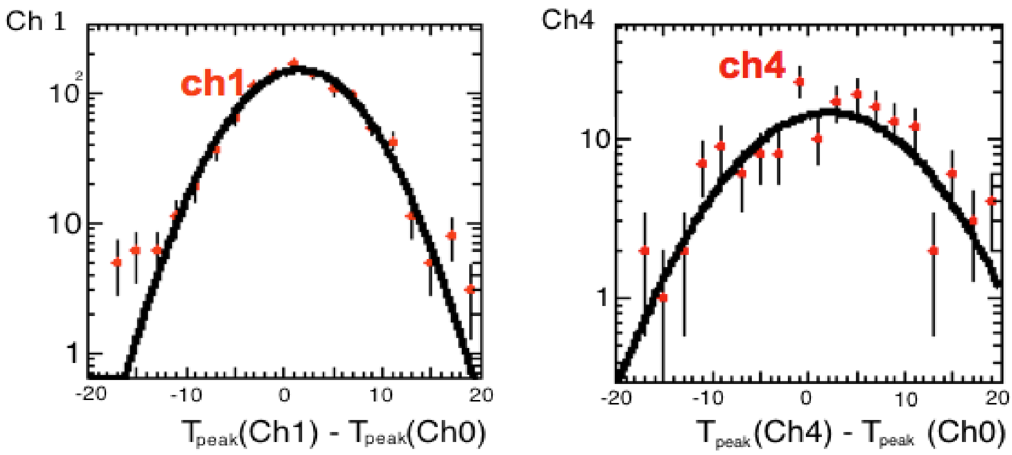

FIGURE 3.5: The average arrival time of signals on Channel 0 of the ADC were artificially set at $T_{\text{Ref}} = 0$ ns. The timing of other channels were compared to Channel 0. On the left, Channel 1 required negligible delay adjustment. The diagram on the right showing a larger Δt in the average timing peak for Channel 4 which was corrected by adding 4 ns Lemo cables.

3.4.2 Signal timing

During installation, the cables from the BSC front end were cut to length so that all channels from each detector end (+Z or -Z) had similar propagation delay times. Once connected and during times of circulating beam in the LHC, more accurate measurements of the timing were made using the ADC. The ADC was set to trigger on the orbit clock (11.2kHz) and the timing of the signal peak relative to the reference clock was read out and recorded for each channel. Channel 0 of the ADC was used as the 'reference' channel with the other 7 channels of the 8 channel ADC showing some positive or negative time offset. Figure 3.5 shows this for ADC channel 1 (BSC Channel 1NBSC1D1) and ADC channel 4 (BSC channel 1NBSC1D4) for one set of such measurements. Data were gathered over a period of several minutes using circulating beam with single bunches and the time of arrival for signals from each channel were plotted in a histogram. A clear peak in the timing spectrum formed, signifying the average signal arrival time for that channel.

The largest timing offset encountered was -10ns and the nominal time offset was of the order of $\pm$3ns. These timings discrepancies were corrected by adding short Lemo cables of the relevant propagation time to those channels which arrived early. In cases where the cable length resulted in a signal delay on more than 3ns, the cables were shortened to bring the timing into a Δt range of $\Delta t_{avg} = 0 \pm 1$ns. A timing distribution from each channel with σ = 5 - 10ns was inevitable due to the variations in pulse shapes and propagation times through the scintillator tiles and PMTs.

3.4.3 Background analysis

To ascertain how much the beam or cosmic background may influence the BSC during the LHC start up and CMS commissioning, a method was devised to measure the quantities of LHC particles and background based on their arrival times. This was achieved using a single pilot bunch (BX = 1) circulating beam in the LHC as a trigger whilst monitoring each individual channel with a CAEN V1721 ADC. Channel 0 of the ADC was used as a trigger and timing reference from one BSC channel, defining the center of a $\pm$20 ns window in which the remaining channel signals must fall in order for their amplitudes to be measured. Additionally, the peak amplitudes of background signals, arbitrarily defined as those falling between $400 - 440$ ns from the initial signal, were measured and subtracted from the true signal, shown in figure 3.6. The independent trigger ensures that the measured signals from the tiles were not subject to a minimum discriminator threshold value and the entire signal height spectrum could be measured. In figure 3.6, one can see the results from one of the BSC channels in which the full signal height spectra, including backgrounds is shown in black. The signals which fell in the t_0+(400−440) ns window and deemed to be due to noise are shown in red.

A negligible amount of signals ($\ll$1%) capable of passing the 30 mV thresholds of the readout logic discriminators are due to background noise. As the trigger logic required stringent coincidence between multiple channels, the background rate propagating through the BSC triggers was deemed to be negligible during test runs of one circulating bunch.

BSC Optimization Summary

During the first days of the LHC operation, the BSC system was calibrated in terms of the signal timing and pulse heights to ensure an optimum triggering performance. Optimization of the single channel efficiency through measurements of

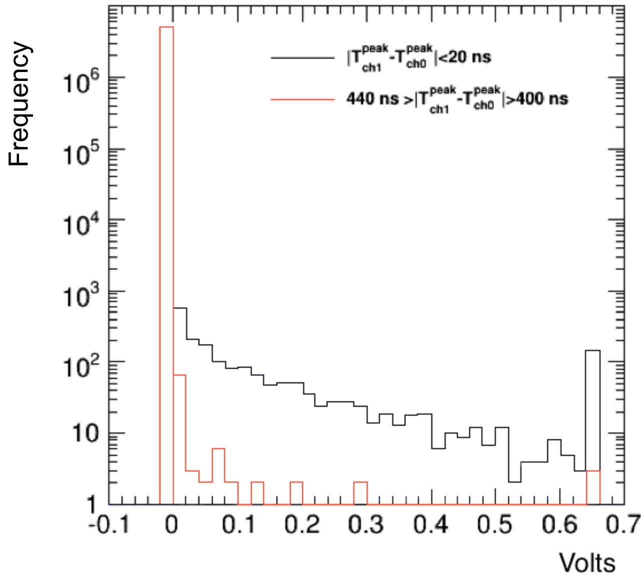

FIGURE 3.6: The pulse height spectrum from BSC Channels shows the contribution from background (cosmic rays, scattered particles and thermionic emissions of the PMT) and from LHC beam particles.

the MIP peak distributions and appropriate adjustments of the high voltages supplying the PMTs resulted in a highly efficient detector (ϵ_{avg} = 97%±2%), critical for triggering and monitoring during the first collisions of the 2010 LHC start-up. Equalising the timing from all channels (+Z end and -Z end separately) maximised the coincidence efficiency in the triggering logic, establishing the maximum overlap between any combination of NIM pulses coming from the discriminators. This in turn ensured that the construction of the trigger logic, based on the expected time-of-flight of Minimum Bias and Beam Halo particles, was simplified and functioned exactly as expected without the need to further correct for channel-by-channel timing differences.

3.5 NIM Based Triggering

The 36 signals from the BSC arrived in the S1 room of the Underground Service Cavern (USC). Due to the layout of the USC cavern relative to the Underground Experimental Cavern (UXC), the cables from the +Z end of the detector were, on average, 16 m longer than those from the -Z end. This resulted in an average difference of propagation time of 61 ns which had to be accounted for in the set up of the minimum bias and beam halo trigger logic.

3.5.1 Brief Description of BSC Triggers

Full details of the BSC trigger system are available in a CMS detector note [43]. Because the high efficiency and robustness of the BSC detector, it was able to provide many important triggers to the CMS Global Trigger (GT) and constantly monitor the activity in CMS even before the declaration of stable beams. Tables 3.2 and 3.3 give the trigger 'bit' numbers as they appear in the Level 1 trigger menu. The Technical Triggers are hardwired. Their bit numbers can be used to identify the trigger allocated to them. The 'External-Condition' bit numbers however, are set up in software and can be changed to suit the needs of the HLT trigger. The tables are followed by a brief technical overview of each of the trigger logic.

Two additional triggers, namely the BSC2_plus and BSC2_minus, were not input into the Level 1 technical trigger but only into the software based 'External-Conditions' trigger. These two triggers were created to provide a trigger input to veto the readout of CMS in the presence of a large energy depositing beam-gas event (PKAM)[†], as explained in section 3.5.1.

Minimum bias triggers

From an experimental point of view, minimum bias events are those events which exhibit non-diffractive dissociation. They have a high cross-section, estimated to be between 55 and 68 mb at $\sqrt{s} = 14$ TeV [44] and distribute hadronised, colourless parton states throughout the detector. As the luminosity in CMS increases, such minimum-bias events become more common, causing pile-up in the detector and complicating the reconstruction of more interesting physics events.
A sensitive and reliable minimum bias trigger was vital for aiding in the understanding of these non-diffractive events which are useful in tuning the Monte Carlo

[†]Due to the massive amount of energy deposited in CMS when a proton collides with a gas molecule in the long straight section, Beam Gas events became known as Monster events. With the concern that the term 'Monster' may strike fear into the hearts of the general public, the term 'PKAM event' was adopted: 'Previously Known As Monster' event.

TABLE 3.2: Table of BSC Technical Trigger bit numbers and a brief description of each.

Tech Bit	Algo Bit	Name	Description
31	12	L1Tech_BSC_minBias_inner_threshold1.v0	Req's one or more inner BSC1 channels to fire on both ends of the detector within 40 ns.
33	13	L1Tech_BSC_minBias_inner_threshold2.v0	Req's two or more BSC1 channels to fire on both ends of the detector within 40 ns.
34	14	L1Tech_BSC_minBias_OR.v0	Req's any one BSC1 channel to fire.
35	3	L1Tech_BSC_HighMultiplicity.v0	Req's all 32 BSC1 channels to fire within 40 ns.
36	32	L1Tech_BSC_halo_beam2_inner.v0	Req's one or more BSC1 inner channels to fire with a $\Delta t_{-\to+}$ of 73 ns $\pm$ 20 ns.
37	33	L1Tech_BSC_halo_beam2_outer.v0	Req's one or more BSC1 outer channels to fire with a $\Delta t_{-\to+}$ of 73 ns $\pm$ 20 ns.
38	34	L1Tech_BSC_halo_beam1_inner.v0	Req's one or more BSC1 inner channels to fire with a $\Delta t_{+\to-}$ of 73 ns $\pm$ 20 ns.
39	35	L1Tech_BSC_halo_beam1_outer.v0	Req's one or more BSC1 outer channels to fire with a $\Delta t_{+\to-}$ of 73 ns $\pm$ 20 ns.
40	28	L1Tech_BSC_minBias_threshold1.v0	Req's one or more BSC1 channels to fire on both ends of the detector within 40 ns.
41	29	L1Tech_BSC_minBias_threshold2.v0	Req's two or more BSC1 channels to fire on both ends of the detector within 40 ns.
42	30	L1Tech_BSC_splash_beam1.v0	Req's two or more channels on the +Z end of the detector to fire. Timed in for out-going beam.
43	31	L1Tech_BSC_splash_beam2.v0	Req's two or more channels on the -Z end of the detector to fire. Timed in for out-going beam.

TABLE 3.3: Table of BSC 'External Conditions' Trigger bit numbers and a brief description of each.

Algo Trig Bit	Name	Description
24	BSC_BSC2_plus.v0	Required one or both BSC2 channels on the +Z to fire. Timed in for incoming beam.
25	BSC_BSC2_minus.v0	Required one or both BSC2 channels on the -Z to fire. Timed in for incoming beam.

detector simulations to real data. They were particularly important during the low luminosity and low energy phases of the LHC as most other detectors were not designed to run optimally in this regime. With the use of the BSC minimum bias triggered datasets, general properties of the pp collisions, such as the distribution of particles produced in the collisions, $\frac{dN}{d\eta}$ and the distribution of energy deposition, $\frac{dE}{d\eta}$ could be studied prior to the higher energy and luminosity era of the LHC and before the rare and interesting physics events are to occur.

The BSC NIM readout system produced 5 minimum bias triggers as follows:

- Minimum Bias based on inner channels only. One or more channels per end fired simultaneously.
- Minimum Bias based on inner channels only. Two or more channels per end fired simultaneously.
- Minimum Bias based on all channels. One or more channels per end fired simultaneously.
- Minimum Bias based on all channels. Two or more channels per end fired simultaneously.
- A logical 'OR' of all channels.

A block diagram of the minimum bias trigger logic is shown in figure 3.7. The trigger logic used Lecroy modules obtained from the CERN ESS department and delay units manufactured by the CERN electronics workshop. The logic was set up to correct for the time of flight (TOF) for particles originating at the I.P and for the propagation time for the corresponding signals to arrive at the USC. Ideally, particles originating at the I.P will hit the BSC scintillator tiles at each end of CMS simultaneously. However, due to differing cable lengths, there is a difference of 61 ns in the signal arrival time at the readout electronics with the -Z end signals arriving ahead of the +Z signals, as shown in figure 3.8. This propagation time was corrected for in the minimum bias logic bringing the signals from the two ends back into coincidence. An additional feature of the minimum bias logic was to create two triggers based on the number of channels that are hit on each end. This was achieved by summing the NIM signals from each channel after the discriminators and setting $\frac{1}{2}$ NIM amplitude (-450mV) and $1\frac{1}{2}$ NIM amplitude (-1.3V) on the subsequent discriminators, therefore providing minimum bias triggers based on one or more hits per end, and two or more hits per end, shown in figure 3.9. This was done to allow some adaptation in the event that the HF Calorimeters become overly activated causing the minimum bias trigger to fire randomly. Studies into the performance and efficiency of the BSC minimum bias triggers for *pp* and Heavy Ion collisions are given in Chapter 4.

BSC ‘OR’ trigger

The BSC OR trigger was also created in the logic shown in figure 3.7. This was achieved by taking the logic-OR of all the +Z and -Z signals. If any one of the 32 BSC1 channels fired, the BSC OR trigger registered the hit. This trigger was very useful for showing the beam activity in CMS and was often the first indication of beam passing through the experiment. Due to its high sensitivity, the BSC OR trigger was used extensively in CMS data analysis in conjunction with the BPTX coincidence trigger (`BPTX_plus_AND_minus`) for filtering data.

Figure 3.10 shows the different minimum bias event filtering achieved by using only the BSC OR trigger (Grey), only the BPTX Coincidence trigger (Red) and the BSC OR and BSC Coincidence combined (Blue). The number of events with no vertex (empty events) is reduced by approximately 40%, saving unnecessary processing time of any physics analysis without placing an overly stringent cut on the event selection.

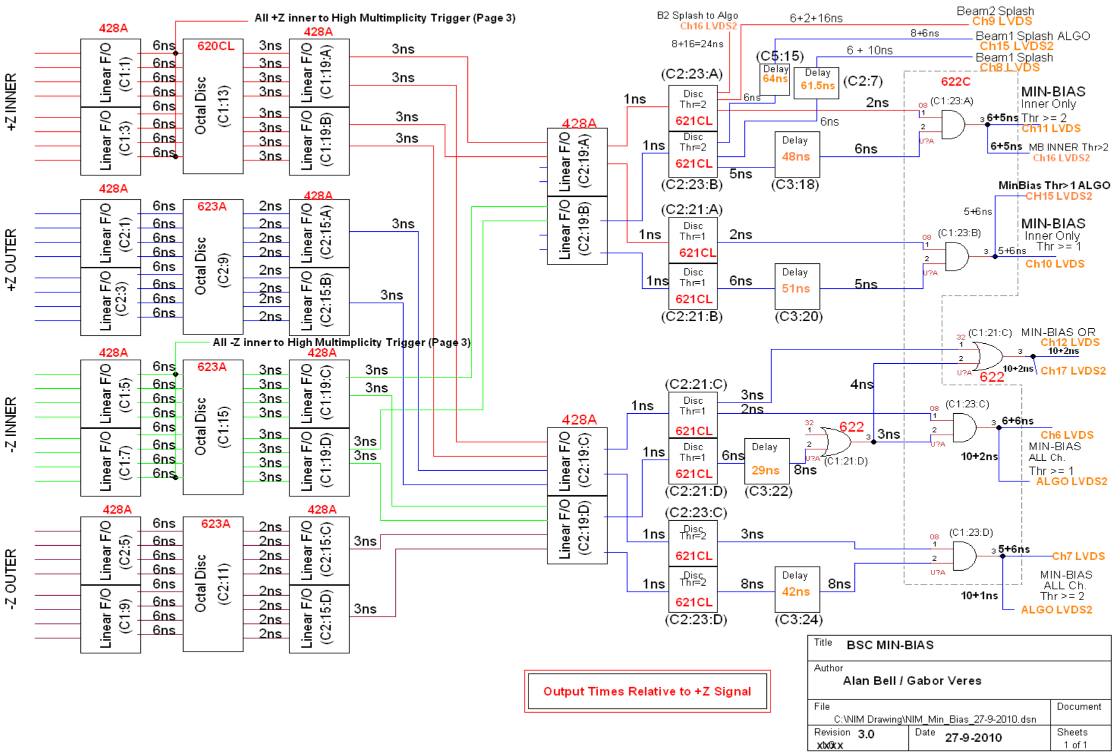

FIGURE 3.7: Diagram of the BSC Minimum Bias & OR Trigger Logic. Discriminator thresholds of -30mV were set to reduce the noise propagation from the front end detectors and the output signal width is set to 20 ns. Thresholds of > 1 and > 2 channels firing per end were achieved by the use of linear fan in/ fan outs and discriminators.

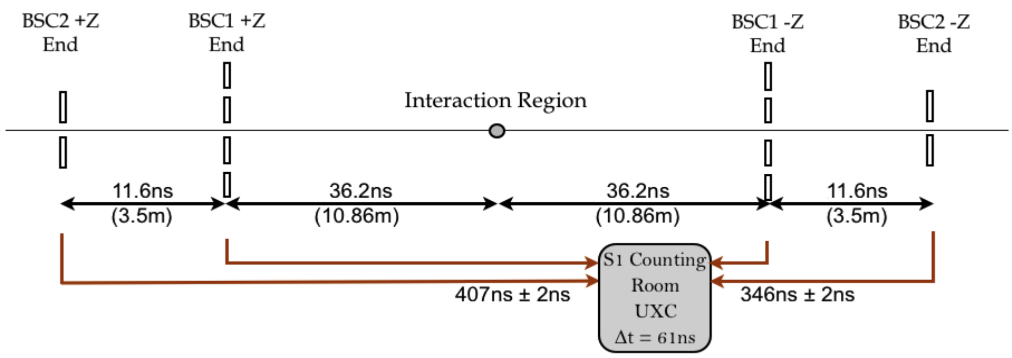

FIGURE 3.8: Diagram of the time-of-flight of particles from the interaction region to the BSC1 and BSC2 stations. The brown arrows represent the coaxial cables from the front end PMTs to the UXC counting room, with their propagation times shown.

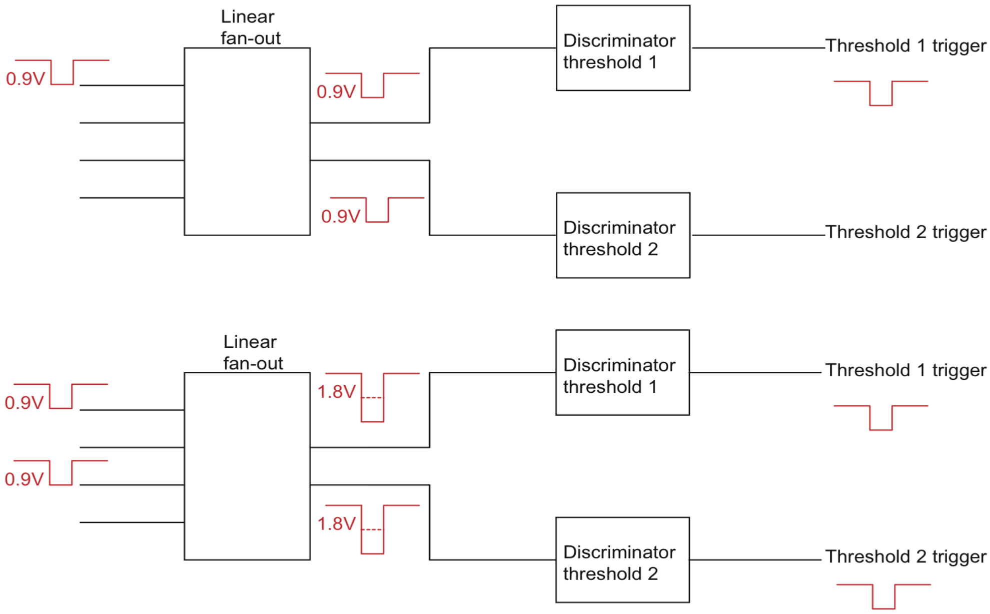

FIGURE 3.9: Diagram showing how the Minimum Bias threshold levels were achieved in the NIM based trigger logic.

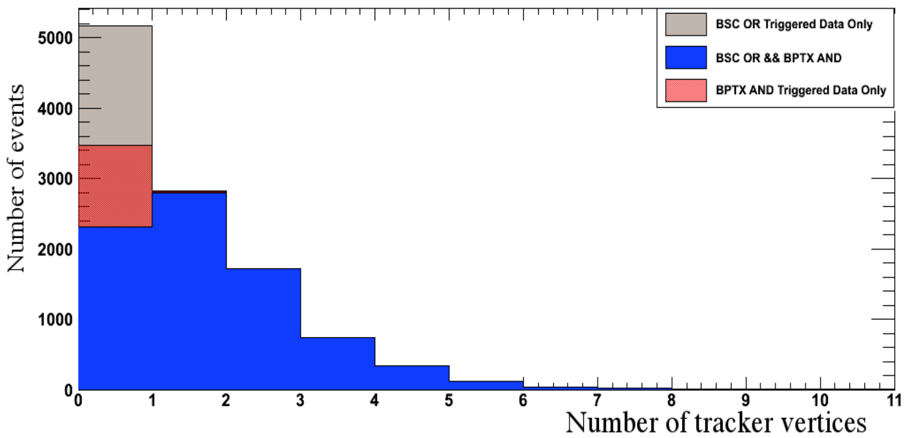

FIGURE 3.10: Using the number of tracker vertices as a measure of the usefulness of any given event data, the use of the BPTX coincidence trigger in conjunction with the BSC OR trigger removes much of the non-interesting events.

Beam halo triggers

Beam muon halo occurs in the LHC when off-momentum protons are 'cleaned' from the beam by the collimators to protect the LHC magnets or when a beam proton meets a relatively stationary gas molecule in the long straight section and arcs upstream of the experiments' interaction points. The proton-nucleon interactions, $p + N$ cause a shower of pions and kaons which decay into $\mu^+ + \nu_\mu$ or $\mu^- + \bar{\nu}_\mu$

either directly ($\pi^{\pm} \to \mu^{\pm}$ branching ratio: $\approx$99.99%, $k^{\pm} \to \mu^{\pm}$ branching ratio: $\approx$63.43%) or indirectly ($k^{\pm} \to \pi^{\pm} \to \mu^{\pm}$). As a consequence of relativistic time dilation, the lifetime of the muons in the lab frame can be of the order of 50 μs, allowing them to travel long distances and through the detector leaving long tracks in the central tracker and causing electron showers as they interact with the dense materials in the experiment.
The BSC Beam Halo triggers were designed to trigger on background particles that travel through CMS approximately in time with the *pp* beams. The rate of hits with $\Delta t_{+z\to -z}$ and $\Delta t_{-z\to +z}$ represent the amount of beam muon halo traveling with Beam 1 and Beam 2 respectively. The time-of-flight between opposite ends of the BSC detector of the beam background or halo is 73 ns. The trigger logic was configured to bring into coincidence, the signals generated by particles passing through the opposite ends of the BSC with a Δt of 73 ns $\pm$20 ns. As in the Minimum Bias logic, the beam halo trigger logic must account for the differences in signal propagation time within the cables between the +Z and -Z ends of the detector.

The BSC NIM readout system produced 4 beam halo triggers as follows:

- Beam 1 halo based on inner channels only.
- Beam 2 halo based on inner channels only.
- Beam 1 halo based on outer channels only.
- Beam 2 halo based on outer channels only.

The raw photomultiplier tube signals entered the linear fan-in/fan-outs (Lecroy 428A) and were passed through octal discriminators (Lecroy 623A).

From here, the beam halo signals and the minimum bias signals took different routes. Figure 3.11 shows the block diagram of the beam halo logic. The signals from +Z (-Z) inner and outer tiles were put through logic fan-in/fan-out modules which act as 8-input AND logic units. The outputs were brought into coincidence using delay units to correct for the time-of-flight of halo particles (Δt = 73 ns) and the difference in cable propagation time (Δt = 61 ns) and fed into 2-input coincidence units. The outputs were in-turn delayed so that they would arrive at the Global Trigger at the same time within a single event window; a requirement set by the L1 trigger PSB board [32].

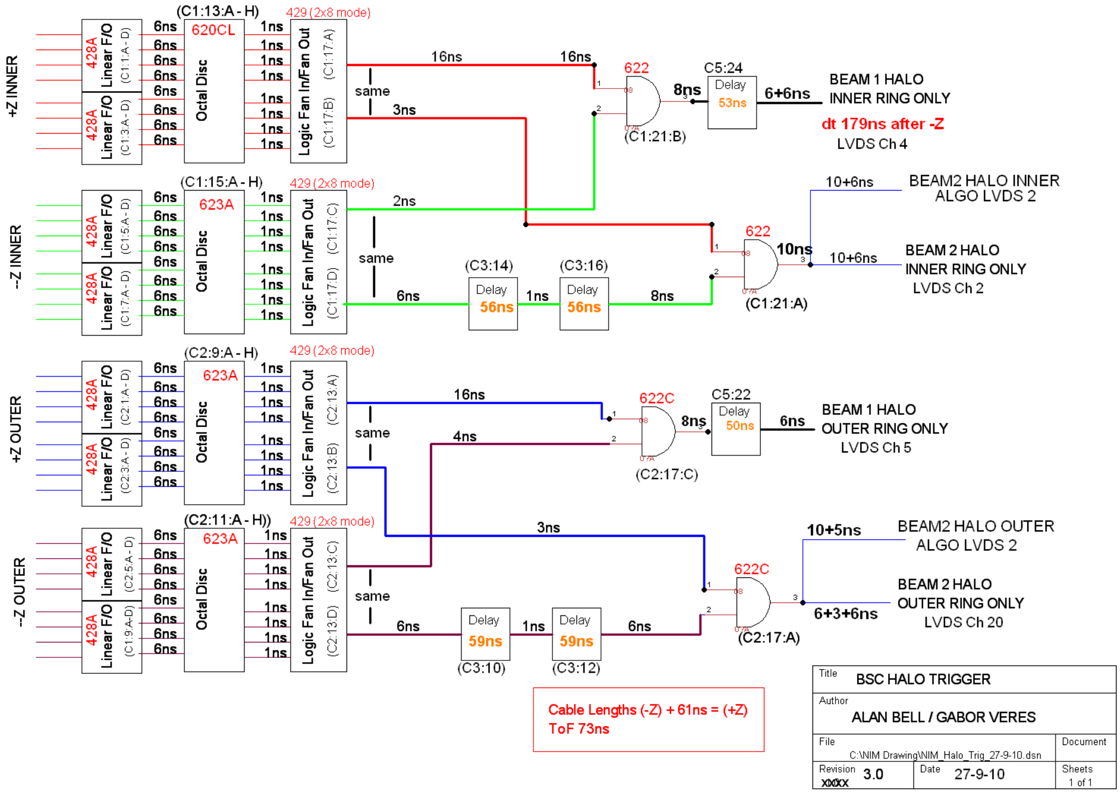

FIGURE 3.11: Diagram of the BSC beam halo trigger logic. The linear fan-in/fan-out and octal discriminators on the left are the same modules as for the minimum bias logic. After the octal discriminator however, the beam halo logic took a different route.

Splash triggers

Running the LHC machine is a delicate procedure and great care was taken during the 2009 start-up phase to ensure every operation was completely understood. Achieving a complete revolution of a single bunch of protons was done in several small steps where the bunch was injected and allowed to go part way around the LHC before hitting a set of closed collimators prior to each experimental area. A 450 GeV bunch of protons hitting the tertiary collimators causes a cascade of secondary and tertiary particles, mainly muons, to shower the CMS detector. The Splash triggers were designed to detect these cascades, confirming to CMS and the LHC Control Room that the bunch had completed its intended journey without unexpected losses elsewhere. A Splash trigger was fired when two or more BSC1 inner channels on the same end were hit within the 20 ns window set by the discriminator output signal width in the trigger logic. The Splash1 trigger

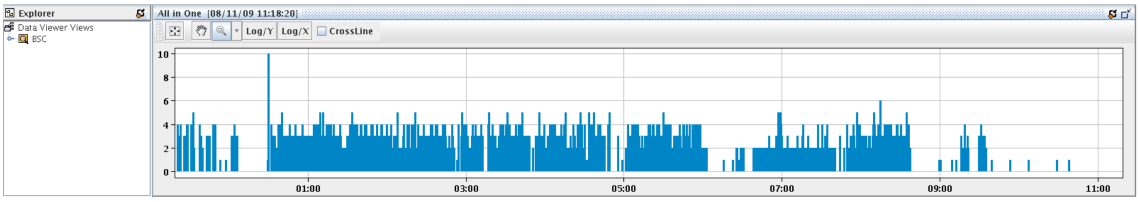

FIGURE 3.12: The BSC Splash triggers were used to monitor the beam splash events in CMS during the LHC commissioning phase in the form of a rolling histogram. Time is on the x-axis.

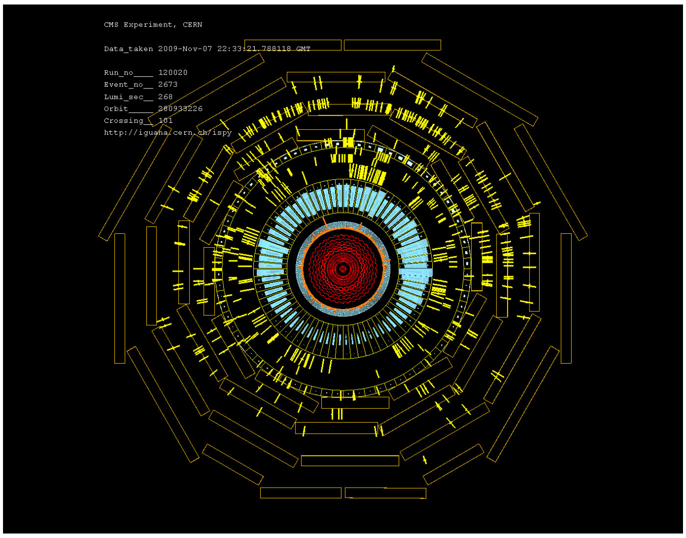

FIGURE 3.13: An example of the 'beam splash' events in CMS prior to the first full revolution of protons in the LHC. Hits can be seen in the inner tracker with energy deposition described by the outward radiating bars in the inner tracker, electromagnetic calorimeter (ECal) and muon chambers. These early 'test' events were triggered by the BSC Splash triggers.

signified an event on the Beam 1 outgoing (-Z) end of CMS, and a Splash2 trigger signified an event on the Beam 2 outgoing (+Z) end of CMS. The threshold of 2 or more channels was achieved in the same way as for the Minimum Bias triggers. Once the LHC operators were confident of their ability to send the proton bunch this far, the collimators were opened to eventually allow the first ever full revolution of protons around the LHC on 20 November 2009. Figure 3.12 shows the BSC beam splash display. Figure 3.13 shows the resulting 'Fireworks' Software display of a typical beam splash event.

High Multiplicity trigger

The high multiplicity trigger was implemented in order to help understand the trigger efficiency in *pp* events and for use in studies by the QCD and Heavy Ion groups [45]. It was also intended as a back-up option for the minimum bias triggers if the albedo or HF activation became too great for the less selective trigger logic. Albedo refers to the fraction of reflected radiation from the materials of the CMS detector due to short-lived activation and the effect causes the effects of the collisions at the I.P to arrive at the BSC detector channels several bunch-crossing later. For less selective triggers, the albedo could cause fake triggers to be sent to the CMS GT.

BSC2 triggers

The BSC2 tiles were installed at $\pm$ 14.36 m where the time between incoming halo and outgoing collision products is greater (20.7 ns) than at the BSC1 location of $\pm$ 10.9 m (2.6 ns) at nominal 25 ns bunch spacing[40]. However, they proved to be very useful as a beam-gas trigger during 2010 and aided in the studies of highly energetic beam-gas events which were seen frequently in CMS during the LHC phase II commissioning and risked damaging the sensitive CMS tracker.

The BSC2 triggers were exceptional among the BSC triggers in that they were timed into the event by the upstream channels. i.e The timing was set such that the beam-gas particles collide with the BSC 2 tiles *before* they pass the I.P. as is the case for the BPTX. All other BSC triggers are timed-in for outgoing particles tagged to the previous collision. The subsequent trigger signal fired in time with the bunch-crossing at the I.P indicating the possibility of a beam gas event being seen in the data. Studies into the PKAM events were carried out using the BSC2 trigger in coincidence with the usual BPTX triggers [46][‡]. The results showed that the BSC2 triggers were capable of selecting 26% $\pm$5% of the events containing PKAM-like signatures. This relatively low selection efficiency was in some part due to the small geometrical acceptance of BSC2 tiles, making up only $\sim$29% of the azimuthal coverage, as well as non-optimised trigger timing into the CMS Global Trigger. The selection of events with and without the BSC2 triggers is shown in figure 3.15(a) and 3.15(b) respectively. Each event was tested for the

[‡]Studies carried out by E. Wenger, MIT.

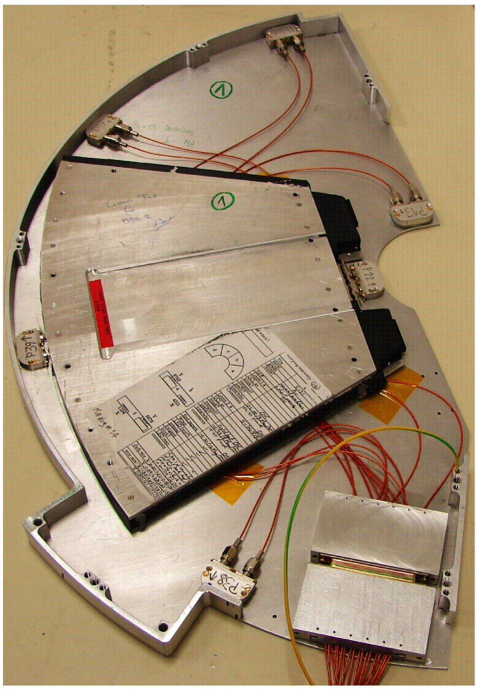

FIGURE 3.14: Photograph of the BSC2 tiles inside the BCM2 wheels before installation.

compatibility between the pixel cluster shapes and the Z positions of the primary vertices. As the diagram of figure 3.16 shows, events detected in the CMS pixel tracker that originate at, or close to the nominal interaction point, will result in small length clusters of energy deposits in the pixels of the tracker.

As the Z-vertex position moves away from the I.P, the cluster length, in the Z-direction increases. Ultimately, a PKAM-like event will deposit large amounts of energy over many pixels, resulting in a very long cluster. The Pixel Cluster Compatibility (PCC) value was calculated as the ratio of the number of events that fall within the expected range of cluster lengths for their respective Z-vertex location, and those which fall outside this expected range. For runs with mostly true *pp* events originating from the I.P region, the PCC should be a large value. For runs with many PKAM events, the PCC value approaches ∼1. [47].

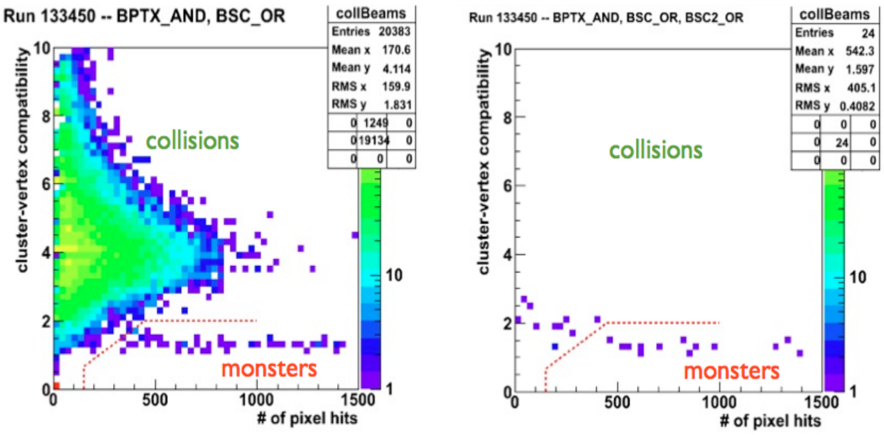

(a) PKAM events without filtering (b) PKAM events with BSC2 trigger filtering

FIGURE 3.15: Filtering out the PKAM events for further study was achieved using the BSC2 triggers. (a) Events seen in HF without the BSC2 veto triggers. (b) Events seen in HF after the BSC2 triggered veto.

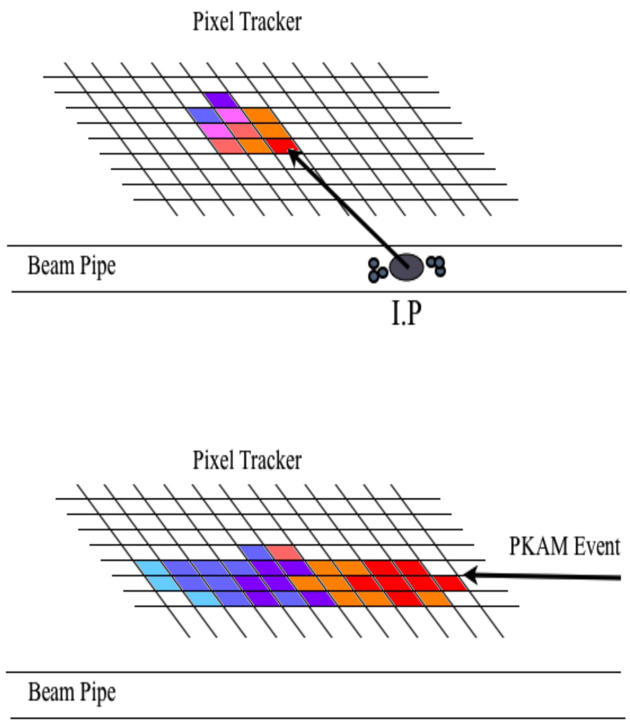

FIGURE 3.16: The number of pixels registered in pp events stemming from the I.P (top) is less than those from PKAM events which originate at large distances from the nominal collision point. The length of the pixel cluster gives a method of identifying the PKAM events.

3.6 VME Based monitoring

The VME monitoring system tracked the rates, timing and amplitudes of all the signals and triggers. Comprising of three scalers (V650N [48]) a 128 channel 0.78 ns resolution TDC (V767 [49]) and four fast ADCs (V1721 [50]) the VME readout monitored nearly all aspects of the trigger logic and raw channel rates for fast system debugging.

3.6.1 Scalers

The three scalers monitored the Inner BSC channels, the Outer BSC channels and the Triggers. The analog signals from the inner and outer BSC channels were passed through the NIM discriminators with the minimal -30mV threshold. The scalers were readout at a rate of 1Hz and the absolute counts and the differential counts (number of counts per second) were stored to disk. The differential counts were also published to DIP, a data exchange protocol developed at CERN for exchanging small amounts of data in approximately real-time [51]. The raw signal inputs were separated into *Inner* and *Outer* with the +Z and -Z sides of the BSC detector going into the same module. This allowed for an easy like-for-like comparison between the +Z side channel rates or the -Z side channel rates which is more useful than comparing inner and outer rates from each side separately. The Trigger scaler monitored the four BSC2 channels and 12 trigger rates.

Time-to-Digital Convertor

A CAEN V767 TDC provided signal timing information with respect to the LHC orbit clock. The orbit clock is a pulse of 11.246 kHz locked to the passing of the first LHC bunch (BX 1). The TDC monitored the timing of several important triggers providing fast, easy access to information for system calibration and debugging. Also monitored were the four BSC2 channels which, being only ± 5 cm from the beam-pipe at their closest point, were very sensitive to particle detection. With the aid of the TDC, the presence of particles in the 3 μs abort gap could be seen.

A software flow diagram is shown in figure 3.17. The V767 TDC contains a 32K deep 32-bit FIFO buffer [49] which stores the inputs from 4 TDC integrated circuits. A threshold on the number of words held by the buffer can be set by a register setting. Another register can be polled to check if the buffer has reached this threshold. If is has, the entire buffer can be read out as a block. Each word contains 4 status bits which identifies its content. The content can be either a header containing the event number; Datum containing either Start information or Event information; End-Of-Block information or Invalid data. By polling the status bits, the relevant information can be extracted from the 32-bit output buffer word, compressed and stored in a text file for post-processing. In the case of invalid data, an error message is written to a separate status log file.

During the early, low-luminosity phases of the LHC, the TDC acquisition ran constantly. As the luminosity increased, the data rate from the TDC became too great and so an easily adjustable, non-synchronous pre-scale was applied so the frequency of data written to disk could be reduced to 1 Hz without biassing the acquisition to any part of the LHC orbit.

Figure 3.18 shows an example of the TDC acquisition during the first Heavy Ion runs of November 2010. The presence of 'albedo' is clearly visible (see figure 3.19) after the colliding bunches. During the H.I runs, the amount of albedo was greater due to the greater particle multiplicities experienced in Pb-Pb collisions compared to *pp* collisions. However, the spacing between *pp* colliding bunches has gradually been reduced down to 50 ns and albedo poses a serious problem to the HF based luminosity measurements and beam background measurements in CMS.

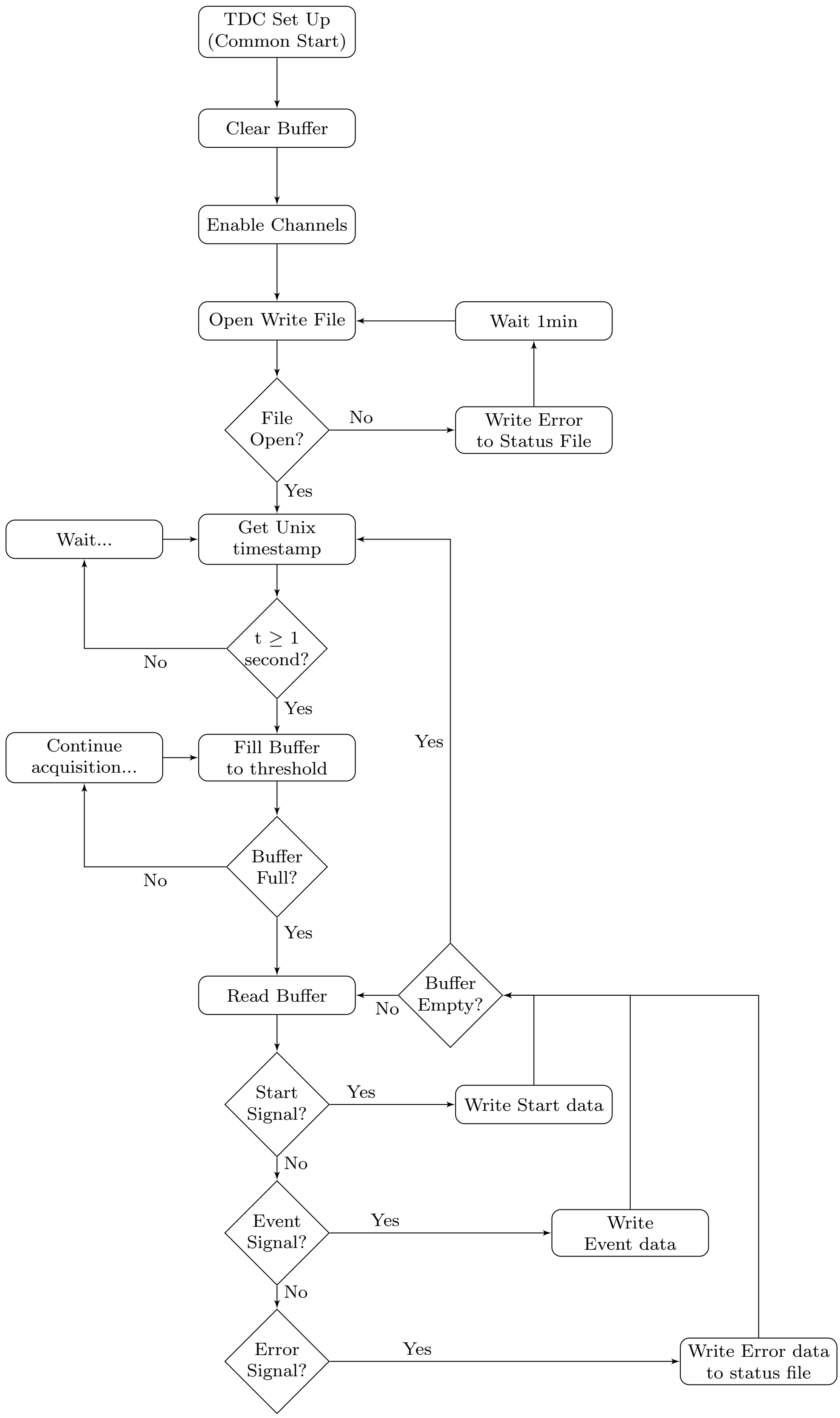

FIGURE 3.17: A flow diagram of the TDC acquisition software. To limit the vast quantity of data gathered, the TDC acquisition had to be pre-scaled at higher luminosities.

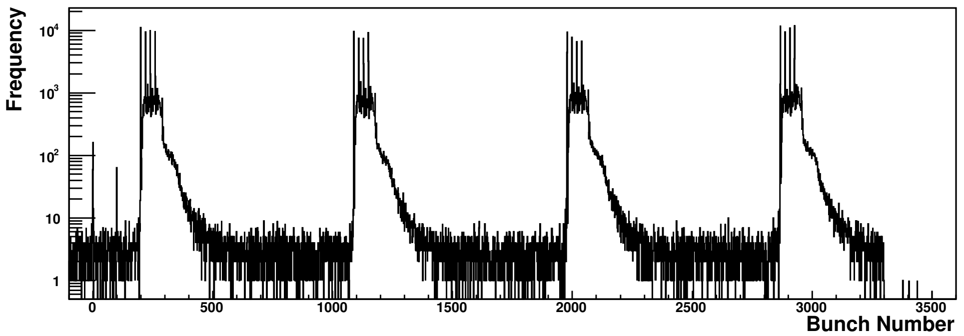

FIGURE 3.18: An example of the BSC 2 signal timing during the Heavy Ion runs of November 2010.

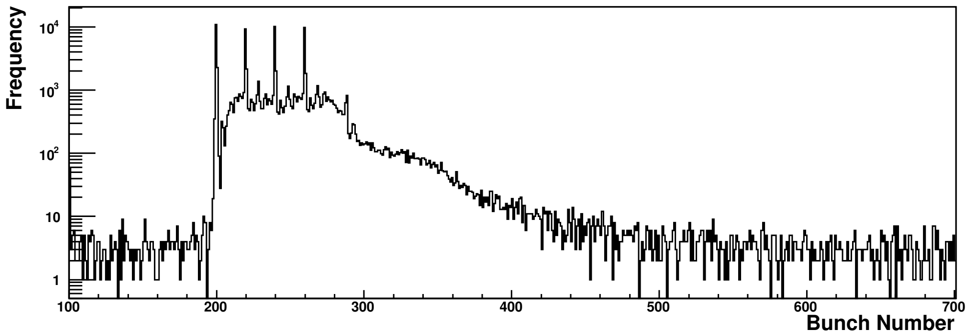

FIGURE 3.19: A closer view clearly shows the presence of 'albedo' following the train of collisions.

3.7 Monitoring Displays

The data from the BSC VME system was displayed in the CMS control room, providing information on the beam conditions at all times. The pre-collision rates gave an indication of the beam background so that the decision of turning on sensitive detectors, such as the CSCs and the Tracker could be made with a level of confidence. The displays were generated by a Java-based software framework and showed live data from all BRM sub-detectors, BSC minimum bias and OR trigger rates updated at 1 Hz and a 24 hour summary plot updated every 10 minutes. The displays were made available outside of the `.CMS`network via the Web Based Monitoring (WBM) page [52].

During collisions, the beam background rates detected by the BSC were overshadowed by the collision rates and the task of background monitoring is taken over by the BCM1F, BCM1L and BCM2 detectors, described in Chapter 2. These systems use diamonds as the detector medium and have a much smaller active area than the BSC. However, the BSC was ideal for monitoring the beam luminosity as the LHC fill progresses and also gave immediate indication of short-term beam losses due to vacuum problems.

BSC Design Summary

The BSC was a vital component of the 2009 and 2010 LHC start up phases and continued to play a roll in event triggering until mid-2011 and monitoring until the end of 2011. The triggers it provided were extensively used in filtering events for off-line analyses which resulted in several interesting papers [45, 53–55, 55–61]. The design of the BSC was limited by both time and funding, relying heavily on obtaining reusable materials from the OPAL detector [41] for the front end and available readout hardware to produce a CMS commissioning detector that would be both reliable and adaptable. Through supplying 14 technical triggers and on-line monitoring of beam conditions throughout 2010 and early 2011, the BSC has surpassed expectations in many ways. As beam conditions pushed the limits of the sub-detector, its design ensured that channels could be quickly tuned and adapted so that the integrity of the beam monitoring functionality continued, albeit at the cost of triggering efficiency.

Chapter 4

BSC Trigger Performance During 2010 - 2011 LHC Running

This chapter explains in detail the analysis of the BSC triggering performance in terms of efficiency and timing and provides some understanding of the needs of CMS for which the design and functionality of the future upgrade detector will be built.

The operation of the LHC during 2010 saw the LHC and experiments rapidly progress in terms of delivered luminosity, increased bunch filling schemes and the longevity of stable beams. The BSC, intended only for use during the very early, low luminosity phases for CMS triggering and monitoring, operated as a minimum bias trigger for luminosities below $4{\times}10^{32}\mathrm{cm}^2\mathrm{s}^{-1}$ and was used in offline analysis in several important CMS papers [45, 53–55, 55–61]. These triggers have shown to be an essential component for CMS operations and monitoring for the following reasons;

- All BSC channels are sensitive to single minimum ionising particles (MIPS).
- Independent of CMS readout. 100% Operational.
- Rapidity coverage of $3.23 < |\eta| < 4.65$.
- A very low minimum energy threshold which would otherwise bias the kinematics.

- Complementary and superior to the Forward Hadronic Calorimeter minimum bias trigger during low beam intensity phase due to its MIP sensitivity and adaptability for varied degrees of luminosity.

The BSC detector was the first CMS sub-detector to register collisions in CMS on November 23, 2009. Figure 4.1 shows the resulting event display after reading out all CMS physics detectors, triggered with the aid of the BSC minimum bias trigger. During the start-up period of the *pp* and Heavy Ion physics runs, the luminosity was much lower than many of the CMS subdetectors were designed to operate with. During this time, the average number of collisions in each bunch crossing was very low and it was not sensible to read-out the CMS detector on every bunch crossing. It was during these phases when the BSC minimum bias triggers were most important, as well as throughout the heavy ion running when event pile-up was typically $\mathcal{O}(10^{-3})$. The selection of minimum bias data has an importance for physics analysis in terms of understanding the backgrounds which mask many interesting *pp* events and for tuning Monte Carlo simulations to the true CMS data. The first heavy ion runs of November 2010 concentrated on measurements of charge multiplicities, transverse energy and other properties of particle production which rely on minimum bias data samples [62] and the BSC was configured and employed as the primary HI minimum bias trigger for this reason. The BSC OR trigger, as mentioned, also played a role in reducing the amount of data processed in the early Minimum Bias datasets by acting as an additional filter on *pp* events in which no activity was seen in the BSC and therefore, not an inelastic event.
It is therefore imperative that the BSC trigger performance is well understood and optimised. By looking in detail at data from the Level-1 trigger records, it is possible to see how the BSC triggers performed during the progression of the LHC operations.

4.1 Level-1 BSC Trigger Analysis

Several hardware and software tools were developed to analyse the BSC triggers and the Level 1 triggers in general. These are;

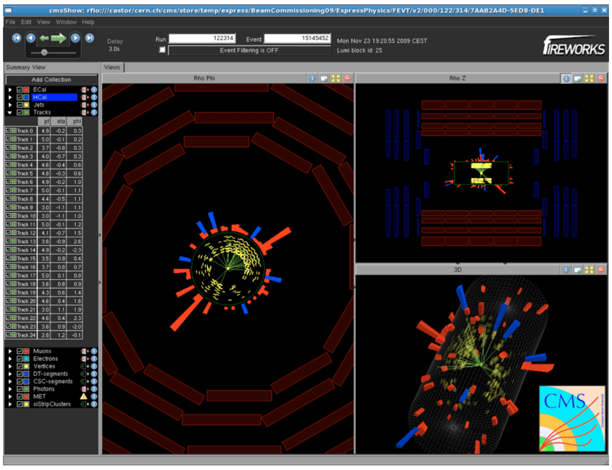

FIGURE 4.1: The first collisions in CMS were triggered with the sensitive BSC Minimum Bias trigger. This shows the resulting display of the triggered event readout.

CAEN V560N Scaler. Three VME Scaler hardware modules [48] are installed in the BSC readout crates to monitor all 36 channels and all 12 triggers. They provide absolute and differential counts at a readout rate of 1Hz.

NanoDST Framework. NanoDST is a framework written by the CMS trigger group. A special subset of data called 'Level1Accept' is recorded for most runs. These data are processed using the CERN Analysis Framework (CAF) and the Worldwide LHC Computing Grid (WLCG), (here on referred to simply as 'the Grid') to provide special NanoDST ROOT [63, 64] nTuples. In turn, these nTuples can be reduced down to a required subset using a purpose written macro, allowing the user to analyse the timing performance of the triggers of interest.

OpenHLT Framework. Similar to NanoDST, OpenHLT processes data from the HLT as well as the 'Level1Accept' data to produce a ROOT TTree containing all HLT trigger paths as well as L1 Technical Trigger states for 'good' events plus a pre-scaled subset of zero-bias events.

CMSSW. The Software framework of CMS has evolved to include level 1 trigger information before and after pre-scales and masking. It also allows the comparison of the level 1 trigger response with that of other parts of the CMS detector.

4.2 Evolution of minimum-bias trigger timings in the pile up era

Reading out all the channels of a vastly complex detector such as CMS is not a trivial task as it requires the synchronous transfer of a very large amount of data. The timing of any given trigger must correspond to the correct bunch crossing so that the event of interest may be processed by the HLT algorithms. During the CMS commissioning phase, all the triggers were 'timed-in' to collisions from single pilot coincident bunches (one bunch in beam 1 colliding with one bunch in beam 2). In 2009 and early 2010, the bunch intensities and luminosities were low, typically $mathcalL \approx 10^{27}\mathrm{cm}^{-2}\mathrm{s}^{-1}$ and proton-proton collisions were infrequent ($\mathcal{O}(0.1\%)$). These infrequent collisions, triggered on by the BSC, were used to time-in the many CMS sub-detector channels. To understand how well the BSC triggers performed during and after the commissioning phase, NanoDST was used to make studies of the BSC trigger timing and overall performance.
A selection of runs starting from Run 143727 (23 August, 2010) were recorded in the form of Level-1 Accept (L1A) data. Every one in ten events passing the L1A was recorded and written into a special stream which contained only minimal information, including Global Trigger (GT) information. These data allow CMS experts to look back at how various triggers performed and to debug problems such as over-firing and post-firing. The Muon Trigger, Calorimetry Trigger, Technical Triggers and Algo Triggers (see figure 4.2) can all cause a readout of CMS if they detect an 'interesting' event. Many of the technical triggers, such as the BSC minimum bias triggers had to be pre-scaled at the GT to prevent CMS being read-out at an unsustainable rate.

After the commissioning phase, the BSC triggers were combined with the BPTX coincidence trigger to ensure the most accurate trigger timing relative to the bunch crossing. Using NanoDST, it was possible to see when the triggers fired within a 5 bunch-crossing window centred on the event defined by the BPTX timing. Any trigger which fired and initiates a Level-1 Accept signal is, by definition put in the centre, (BX = 0) of the readout window. Any subsystem which fires later will show up in BX = +1 or BX = +2 of the readout window. Figure 4.3 shows a graphical representation of this. The triggers that appear in BX = -1 or BX = -2 appear because they fired out of time of the BPTX coincidence and therefore, no

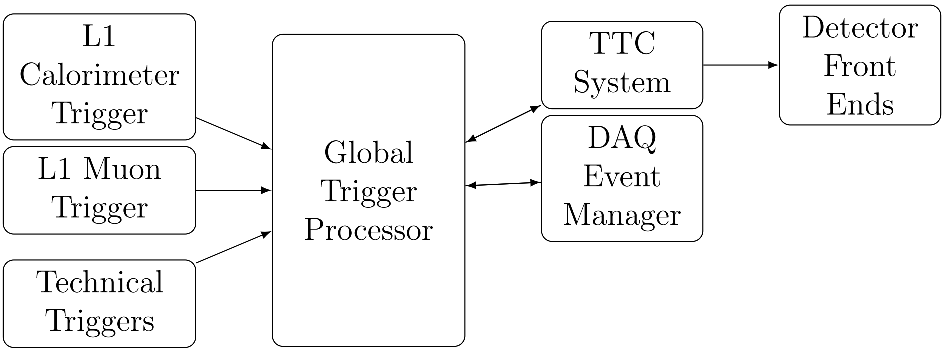

FIGURE 4.2: A block diagram of the Global Trigger layout showing the input trigger primitives sent from the L1 Calorimeter and L1 Muon triggers and the 64 Technical Triggers (TT) of which the BSC provides 14 triggers.

L1-Accept signal was produced, or because the L1-Accept signal was veto'd to limit the readout rate of the CMS detector.

During the commissioning phase, the BSC triggers were used in a stand-alone fashion, with no reliance on the BPTX gating. During this regime, it was vital that the BSC trigger latency was well defined to read out the correct bunch crossing.

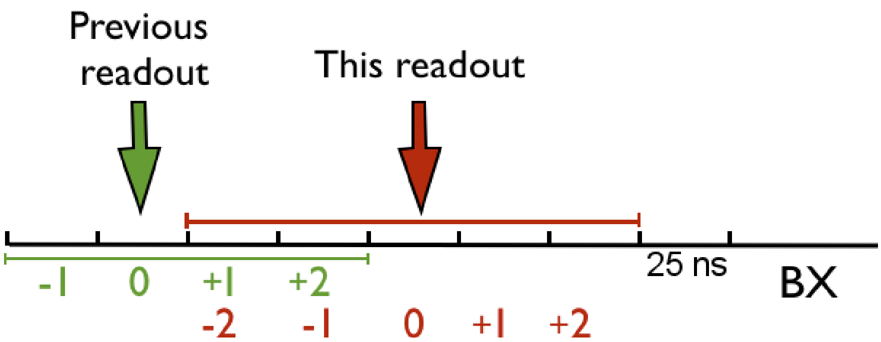

FIGURE 4.3: A diagram of the NanoDST readout window. L1A initiating triggers define the central bin of the 5 bin window. Triggers which occur after an L1A signal fall into bins 1 or 2. Triggers which occurred after the previous L1A signal may fall into bins -2 or -1.

Level-1 Accept data were processed using the CAF and the Grid in order to create ROOT tables in the form of NanoDST formatted 'ntuples'. Fill numbers were chosen to give a broad selection of LHC luminosities and bunch spacing examples. The CMS Data Base Server (DBS) was searched to locate the necessary /L1Accept/ data. Once located, a `.json` file and CRAB configuration file were written. The `.json` file tells the configuration file which run numbers and luminosity section numbers to process, where a luminosity section is $\approx$ 23 seconds of data.

Using a purpose-written macro, the timing distributions for selected runs through 2010, for *pp* runs and November for Heavy Ion runs, were plotted to ascertain the accuracy and purity of the BSC triggers as the luminosity increased.

As an example, figure 4.4 shows a section of the orbit (Bunches 1000 - 1350) where the BSC OR trigger fired. It can be seen that, on average the BSC OR actually fired on time or one bunch crossing late. This is because the BSC OR trigger was set up with a wider output pulse to compensate for the inherently large ($\sim$ 15ns) spread in trigger latency and increase the likelihood of coincidence with the BPTX. This greatly improved the triggering efficiency of the OR trigger for physics analysis. Conversely, the BSC Minimum bias threshold 2 trigger, shown in figure 4.5, is much more selective and fires on the correct bunch crossing with very few offset triggers.

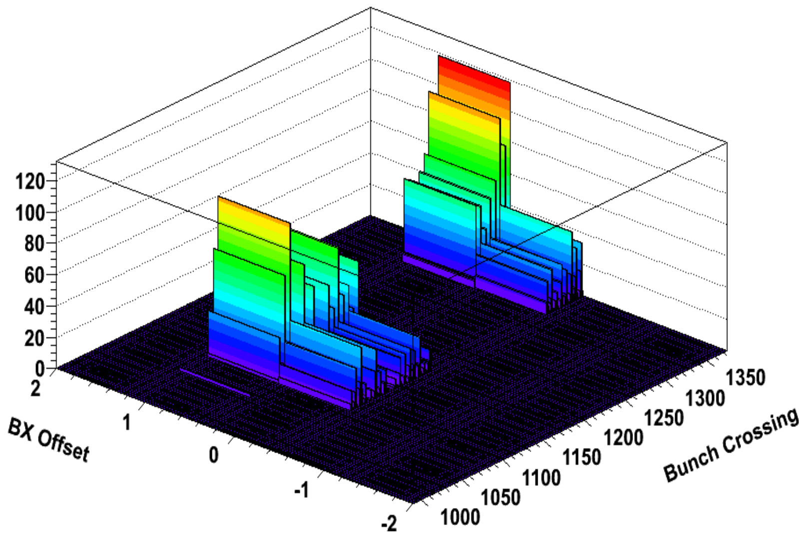

FIGURE 4.4: A graphical view of the information gathered through the NanoDST framework. Here we see an example of the BSC OR trigger timing, zoomed into bunch crossings 1000 - 1350 for clarification. On the left axis are the bunch crossing offsets. The BSC OR was designed to fire on time (Bunch Offset 0) and one bunch crossing later (Bunch Offset 1) to increase its coincidence efficiency with the BPTX.

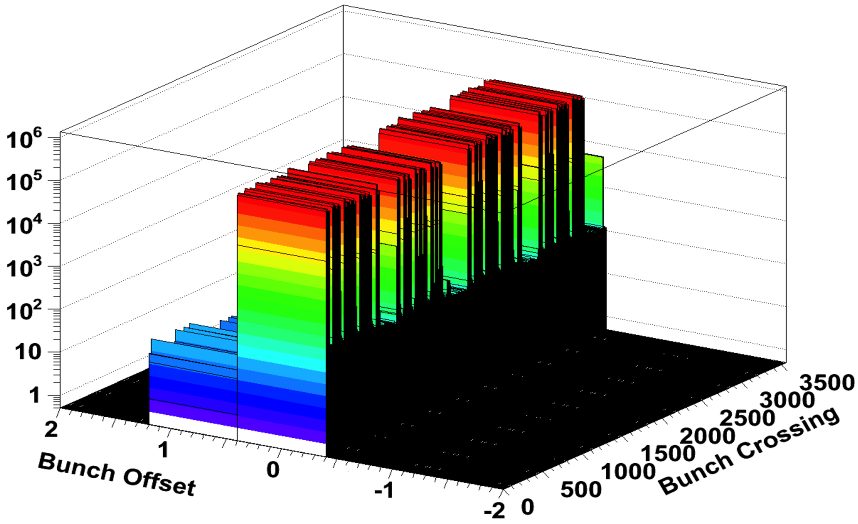

FIGURE 4.5: An example of the Minimum Bias threshold 2 timing performance. The more selective MinBias 2 trigger predominantly fired on the correct bunch crossing (Bunch Offset 0). Note that the z-axis is shown in $\log_{10}$ scale.

To measure the timing accuracy of the BSC triggers, the number of pre-firing (BX = -2 and BX = -1), post-firing, (BX = +1 and BX = +2) and on-time firing (BX = 0) triggers were counted for runs taken from August - October 2010 when the luminosities and the bunch occupancy increased. Ideally, the minimum bias and high multiplicity triggers should only fire in time with the colliding bunches and all similar triggers in the CMS detector. The beam halo, high multiplicity and OR triggers are expected to fire predominantly in time with the bunch crossing, but beam halo particles typically arrive with some time spread, causing triggers to occur in-time with, or after the collisions. Additionally, the rates of the halo triggers depends on the beam-pipe vacuum conditions which may change between runs. Table 4.1 lists the percentage of pre, post and on-time triggers for runs with increasing filling schemes and decreasing bunch spacing. More details of the runs used in the timing analysis are given in table 4.3. The recorded luminosities and estimated pile-up values were provided by the CMS Luminosity Group.

The timing accuracy of the BSC Minimum Bias Threshold1 trigger performed at ∼90% during runs with less bunches and greater inter-bunch timing. With greater numbers of colliding bunches in the LHC, the more sensitive Minimum Bias Threshold1 trigger timing became less accurate with more late arriving triggers from the previous L1 Accepted event occurring when the bunches were 125 ns apart. This was caused by an effect referred to as 'Albedo', generated by short-term activation of the CMS bulk materials which causes a delayed arrival of particles which, in-turn trigger the Minimum Bias Threshold1 trigger. The Minimum Bias Threshold2 trigger was not as susceptible to these backgrounds, requiring two channels per end to fire and its timing accuracy remained above 90% even during the higher luminosity runs.

The highly stringent High Multiplicity trigger performed exceptionally well in regards to timing jitter with >99% of triggers firing on the bunch crossing. This trigger is not susceptible to the effects of albedo or beam background suggesting that the timing drifts of the other BSC technical triggers are due to real beam dynamics and albedo rather than flaws in the detector readout or coincidence logic.

TABLE 4.1: Minimum bias, OR and, High Multiplicity L1 triggering contributions for selected runs through August - October 2010. 'On-time' triggers are wholly or partly responsible for initiating a L1A signal and a subsequent CMS readout. The 'on-time' OR trigger accuracy shown includes only those triggers which appeared in BX = 0 of the NanoDST nTuples and does not account for the acceptance of the BX = -1 contribution.

Run/Fill	Scheme	BX Spacing ($\times$25ns)	% Previous L1A Late	% On Time	% Late
		Minimum Bias 1			
146436/1364	16 Colliding	5	22.5	71.8	5.7
146431/1364	16 Colliding	5	24.1	70.4	5.5
143955/1303	32 Colliding	40	1.5	91.3	7.2
143727/1299	36 Colliding	50	1.4	92.0	6.5
		Minimum Bias 2			
146436/1364	16 Colliding	5	6.6	91.4	2.0
146431/1364	16 Colliding	5	7.5	90.5	2.0
143955/1303	32 Colliding	40	0.9	97.2	1.96
143727/1299	36 Colliding	50	3.05	94.80	2.15
		OR			
146436/1364	16 Colliding	5	40.3	44.6	15.1
146431/1364	16 Colliding	5	40.6	44.2	15.2
143955/1303	32 Colliding	40	22.8	56.2	21.0
143727/1299	36 Colliding	50	22.4	57.0	20.5
		High Multiplicity			
146436/1364	16 Colliding	5	0.0	99.87	0.13
146431/1364	16 Colliding	5	0.0	99.85	0.15
143955/1303	32 Colliding	40	0.009	99.67	0.32
143727/1299	36 Colliding	50	0.0	99.69	0.31

Table 4.2: Halo L1 triggering contributions for selected runs through August - October 2010. The Halo triggers were not included in the L1Accept decision making algorithm. Additionally, the timing of beam halo may be smeared around the nominal timing of the *pp* beams.

Run/Fill	Scheme	BX Spacing ($\times$25ns)	% Previous L1A Late	% On Time	% Late
		Beam 1 Halo			
146436/1364	16 Colliding	5	43.18	34.36	22.46
146431/1364	16 Colliding	5	43.29	34.33	22.38
143955/1303	32 Colliding	40	7.12	61.78	31.10
143727/1299	36 Colliding	50	35.97	39.47	24.55
		Beam 2 Halo			
146436/1364	16 Colliding	5	24.35	41.37	34.28
146431/1364	16 Colliding	5	24.37	41.30	34.33
143955/1303	32 Colliding	40	4.81	45.77	49.41
143727/1299	36 Colliding	50	20.90	41.94	37.17

Figures 4.6 to 4.8 show the BSC minimum bias trigger firing for each bunch crossing (BX) in runs with increasing bunches. The Minimum Bias trigger timing correctly reconstructs the filling scheme used for the fills.

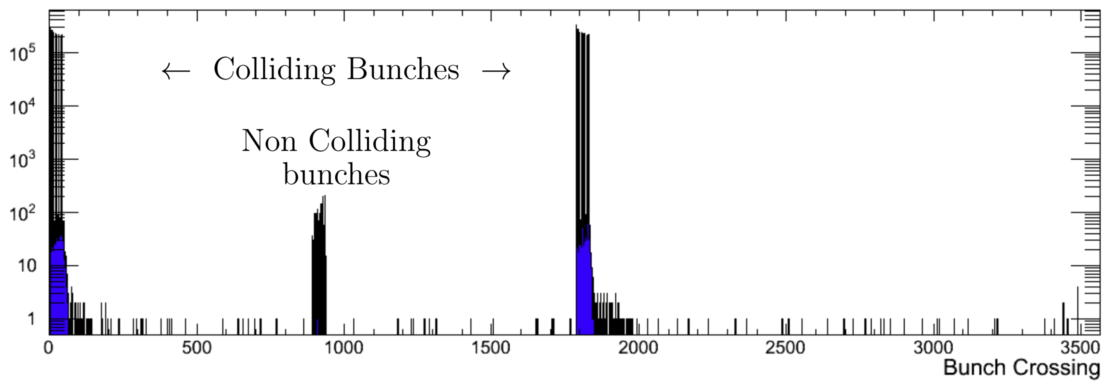

Figure 4.6: BSC Minimum bias trigger (Bit40) data taken from run 146436 (Fill 1364) in which there were 2×8 colliding bunches (150ns spacing) and 16 non-colliding bunches (75ns spacing).

TABLE 4.3: Luminosity and pile-up estimates for the analyzed runs in table 4.1.

Run/Fill	Date	Average $\mathcal{L}_{rec}$/LS	$\mathcal{L}_{inst}$	Estimated Pile-up
146436/1364	22.09.2010	77.7 μb	3.35μb s^{-1}	1.33
146431/1364	22.09.2010	86.1 μb	3.74μb s^{-1}	1.52
143727/1299	23.08.2010	180.7 μb	7.86μb s^{-1}	1.40
143955/1303	26.08.2010	191.7 μb	8.33μb s^{-1}	1.68

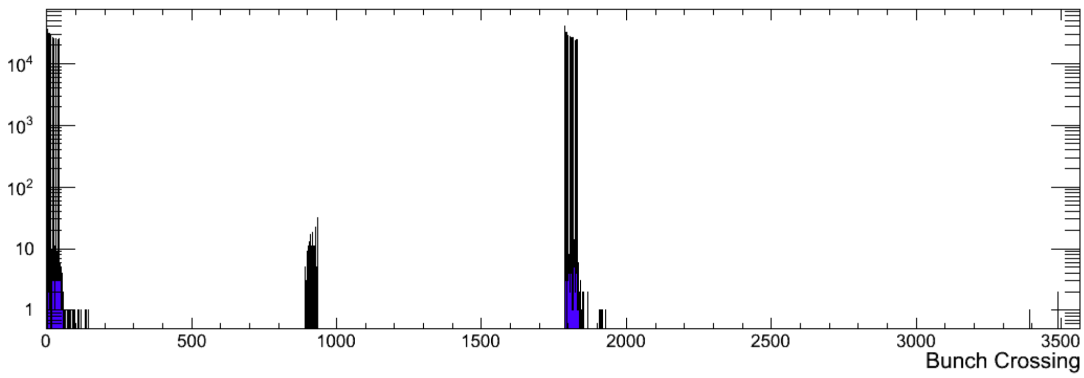

FIGURE 4.7: BSC Minimum bias trigger (Bit40) data taken from run 146431 (Fill 1364) in which there were 2×8 colliding bunches (150ns spacing) and 16 non-colliding bunches (75ns spacing).

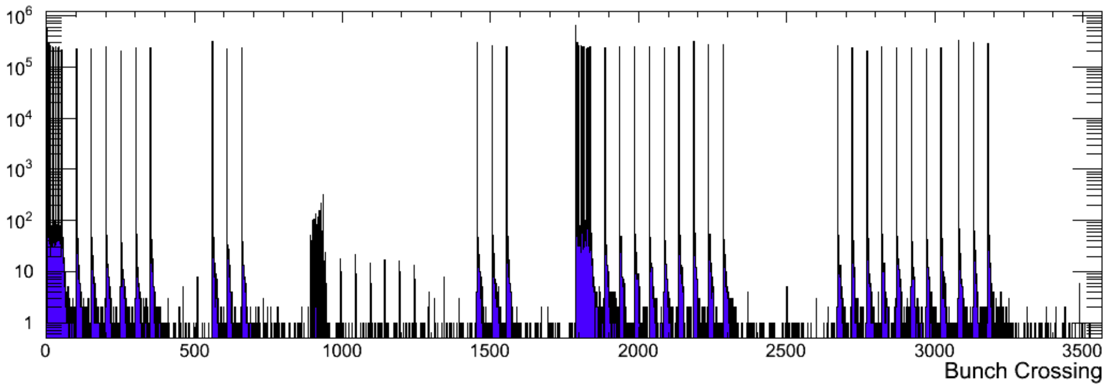

FIGURE 4.8: BSC Minimum bias trigger (Bit40) data taken from run 143727 (Fill 1299) in which there were 36 colliding bunches and 24 non-colliding bunches. Note the presence of a decay in the rates after the colliding bunches caused by *albedo*.

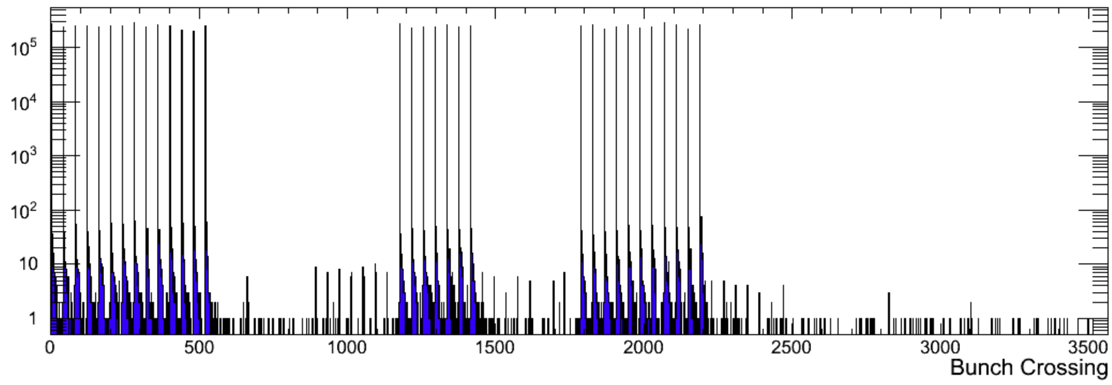

FIGURE 4.9: BSC Minimum bias trigger (Bit40) data taken from run 143955 (Fill 1303) in which 32 colliding bunches were observed.

As the luminosities delivered by the LHC increased, the 'albedo' effect became more important in regards to the behaviour of the more sensitive triggers, such as the BSC OR, Minimum Bias1 and Beam Halo triggers. Coincidences of the albedo particles caused a very small fraction of late triggers from the BSC as shown in figure 4.10. One of the Level 1 trigger rules masks any L1 trigger from firing on the following two bunch-crossing, prohibiting the vast majority of the albedo particles from causing fake triggers.

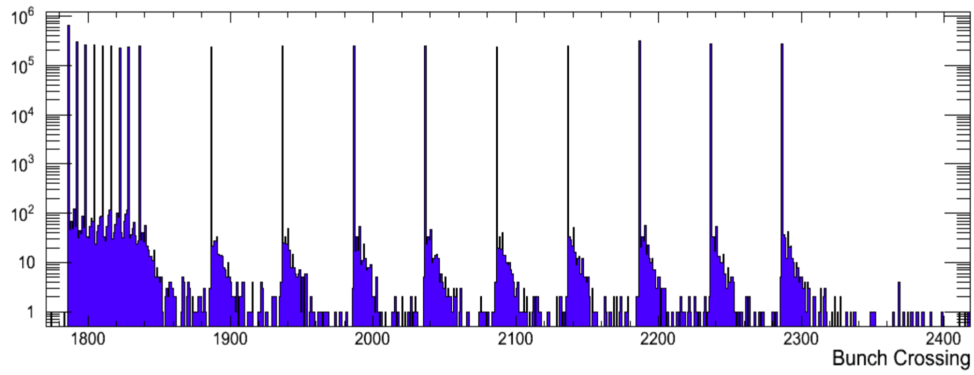

FIGURE 4.10: BSC Minimum Bias trigger (threshold1) for run 143727 showing the effect of 'albedo' reflections within CMS on the triggering. As the luminosities increased, the late arrival of reflected particles contributed to additional and undesirable Minimum Bias triggers.

BSC trigger timing analysis summary

The results of the NanoDST timing analysis of the BSC triggers showed that they performed exceptionally well over a large range of instantaneous luminosities and filling schemes. The minimum bias threshold 1 trigger, perhaps the most important signal sent from the BSC to the Global Trigger, fired in-time with >90% of the Level-1 accepted events until the bunch spacing was reduced to 5BX (125ns) when the rate of albedo particles incident on the detector caused a degradation in the timing accuracy of the trigger. The minimum bias threshold 2 was much more stable over the increased luminosity range but possibly at the expense of triggering efficiency. The efficiencies of the triggers are studied in section 4.3 using the CMSSW framework.

The BSC OR trigger, which fires when one of more single channels detects a particle, was set up such that the output pulse to the GT was 2 bunch-crossings (50ns) long. This was to improve the coincidence efficiency with the BPTX AND. Further studies of this highly sensitive trigger must be done with the BPTX in order to get any quantitative information about its efficiency.
The High Multiplicity trigger was close to 100% accurate in its timing of triggering L1A events, creating very few (<1%) late triggers and has therefore provided an excellent tool for selecting high multiplicity events as well as providing a way of confirming the timing of the BSC triggers with the correct bunch crossing time, provided from the BPTX.
The beam halo triggers aimed to trigger on beam background and ideally, should show a very low contribution within the L1A dataset but is dependent on the amount of halo in the LHC and the timing is dependent on the nature and origin of the beam halo. As can be seen in table 4.1, the halo triggers fire 30 - 60% in the center of the readout window and 20 - 50% in the following two bunch crossings. The beam halo triggers were not enabled in the L1 accept path and appear here only if they fired within an event which was triggered by some other means.

4.3 BSC Minimum Bias Trigger Turn On Curves

The BSC trigger data is recorded with all other technical and Extra-Algo triggers into the CMS data stream via the GT. Each recorded event contains a vast amount of information from all CMS sub-detectors. Exploiting this fact, the following plots show how the BSC minimum bias triggers performed during early-mid 2010 running. Figure 4.11 compares the BSC minimum bias threshold 1 and threshold 2 triggers and the equivalent HF minimum-bias trigger, the HF_COINCIDENCE trigger which requires the detection of at least one particle over 4 GeV in a single tower in both calorimeters simultaneously. The trigger efficiencies were calculated as a function of the number of tracks in the inner tracker with events selected by the zero-bias trigger. The number of pixel tracks scales linearly with luminosity and therefore, a low number of tracks can be considered as a typical low luminosity event, whereas many pixel tracks can be equated to a typical event seen at higher luminosity. *pp* runs from May - July 2010 were processed during which time the initial luminosity rose from $3.11 \times 10^{28}\text{cm}^{-2}\text{s}^{-1}$ to $9.6 \times 10^{29}\text{cm}^{-2}\text{s}^{-1}$ ($\mathcal{L} = 31.1\ \text{mb}^{-1}\text{s}^{-1}$ - $960\ \text{mb}^{-1}\text{s}^{-1}$) and a $\sqrt{s}$ energy range from 900 GeV to 7 TeV.

For an event to be deemed *minimum bias*, a BPTX coincidence (AND) trigger was required as well as ≥ 1 track in the inner tracker. For each event passing this cut, the values of the BSC minimum bias triggers and the HF coincidence trigger were checked to see if they fired on the event. The efficiency was calculated by the ratio;

$$\epsilon = \frac{N_{\text{Triggers}}}{N_{\text{Cut}}} \tag{4.1}$$

where N_{Cut} is defined as events in which the `BPTX_plus_AND_minus` trigger fired and with ≥ 1 track seen in the tracker. N_{Triggers} is defined as those events which satisfy the cut and also were fired by the BSC Minimum Bias trigger or HF Minimum Bias trigger. Beam background is excluded by the requirement that the `BPTX XOR` trigger, which signals the arrival on non-colliding beam, is false.
Although the geometrical coverage of the BSC tiles is smaller than that of the HF, the BSC minimum bias triggers out performed the HF coincidence trigger for low multiplicity events, which are common at low enegies (900 GeV) and luminosities ($<10^{30}\text{cm}^{-2}\text{s}^{-1}$). The 4 GeV lower energy threshold and broad energy resolution at low energies restricted the HF Calorimeter's ability to act as an efficient trigger during the start-up phase of the LHC, which is where the BSC system excelled.

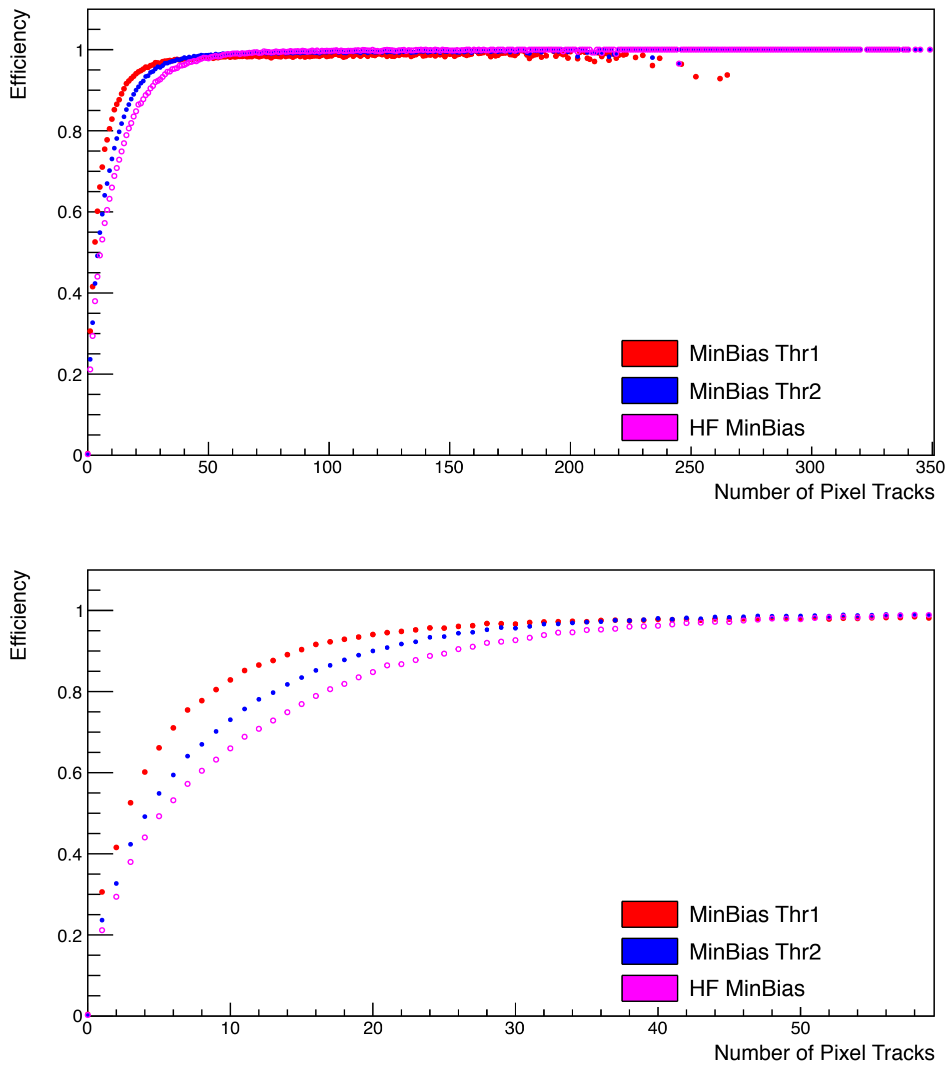

FIGURE 4.11: Calculations of the detection efficiency of the BSC minimum bias triggers (threshold 1 & threshold 2) for increasing number of tracks recorded by the CMS tracker provides insight into the turn on performance of these triggers relative to the HF Minimum Bias trigger. Data from runs 136035 - 141881.

4.4 BSC trigger status report for 2011

The BSC Minimum Bias and OR triggers performed exceptionally well over a wide range of luminosities. However, the limiting factor of the BSC triggering performance in 2010 was the bunch spacing and channel multiplicities (the number of particles interacting with each of the scintillator tiles). As the time between bunches approached 5 bunch crossings (125ns), the effectiveness of the BSC minimum bias and OR triggers declined. The underlying causes for this were the presence of albedo and the occurrence of pulse pile-up in the individual channels where each signal is unable to return to the baseline before the following bunch arrives. This caused a drop in the baseline below the -30mV discriminator threshold and some triggers failed until the baseline was restored. This problem was able to be compensated for by reducing the high voltages to the PMTs, restoring the signal amplitudes and reducing the time required for the signals to return to their normal zero volt baseline as shown in the photographs of figure 4.12. However, this reduction in PMT voltage also decreases the efficiency of the individual channels and therefore, the efficiency of the trigger. At the beginning of 2011, it was decided to inform the CMS collaboration the BSC triggers were no longer operating at the required efficiency during nominal running and the system was configured to operate primarily as a beam monitoring detector.

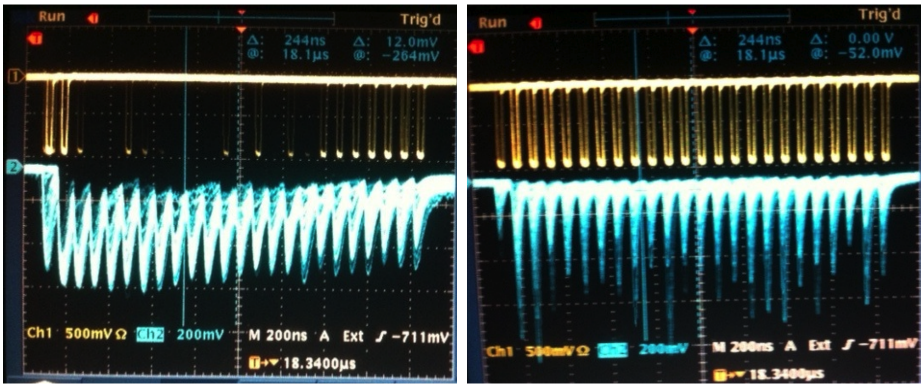

FIGURE 4.12: Effects seen in the BSC due to pulse pile-up during April 2011. (Left) The bunch spacing is 3BX (75ns). The analog signals were unable to return to zero volts before the next pulse arrived, resulting in a drop in the baseline below the −30mV discriminator threshold. (Right) Adjustment of the high voltages by ∼ 20 - 40V temporarily solved the problem at the cost of single channel efficiency. The adjustments needed to be repeated as the LHC luminosity and bunch occupancy increased.

As the LHC filling schemes developed to bring the experiments up to full design luminosities, the BSC was no longer be able to cope either as a trigger, nor as a meaningful monitoring device. It's large channel size lead to a large channel occupancy and large quantity of energy deposited in each tile per collision. In turn, this resulted in large amplitude signals which were unable to recover in less than the 25 ns or even 50 ns between bunches. The simplicity of the design also meant that it was impossible to filter out background noise due to 'albedo' and HF activation. An upgrade of the BSC must be capable of filtering out such random signals if it is to provide accurate triggers. The design of an upgrade depends very much on the requirements of CMS. Intended as a monitoring detector capable of providing commissioning triggers, the BSC became a primary triggering detector. Many of the triggering needs are now supplied by other CMS subdetectors such as the HCal and Muon systems. Minimum bias triggering is no longer required at a time when the LHC delivers high luminosities resulting in dozens of events with each colliding bunch. Beam timing measurements are currently done by the BPTX whilst the monitoring of beam losses is carried out by the BCM1L, BCM1F and BCM2. The only tasks not well covered by any BRM subdetector are the monitoring beam backgrounds during collisions and online measurements of luminosity in CMS. It is feasible that the BSC upgrade could fulfil one or both of these tasks.

Chapter 5

Luminosity Studies & Monitoring

The luminosity of a colliding beam experiment is a measure of how well the particle beams collide which is directly related to the rate of production of all physics events. In order for experiments to search for extremely rare physics processes among the vast amount of background, a high luminosity is of great importance. Knowledge of the luminosity during the experimental run-time is difficult to achieve as direct measurement of the beam profiles easily disturbs the beams and reduces the luminosity.
This chapter describes the methods of measuring the luminosity in the CMS experiment and explores the possibility of the BSC upgrade providing online luminosity measurements for nominal LHC intensities.

During the early LHC running the absolute luminosity ($\mathcal{L}_0$) was measured in CMS by means of Van der Meer scans (VdM). This method provides an absolute physical measurement, independent of the underlying physics processes. The VdM technique works on the principle of sweeping one beam across the other whilst measuring the rate of collisions, measuring the size of the luminous region formed by the overlap of the two beam profiles[65, 66].

The number of events per second is given by:

$$\frac{dN_{event}}{dt} = \mathcal{L}\sigma_{event} \tag{5.1}$$

where σ_{event} is the total cross-section for the event under study; proton-proton inelastic collisions, in the case of the CMS. The pp total cross-section is not *a priori* known at LHC energies, thus simply measuring the event rate N does not determine the value of the luminosity.

The absolute luminosity, $\mathcal{L}_0$ is dependent on several beam parameters. Assuming a Gaussian beam distribution, the absolute luminosity without beam displacement is given by:

$$\mathcal{L}_0(\mathrm{cm}^{-2}\mathrm{s}^{-1}) = \frac{N_1 N_2 f_{rev} N_b}{2\pi\sqrt{(\sigma_{1x}^2 + \sigma_{2x}^2)(\sigma_{1y}^2 + \sigma_{2y}^2)}} \tag{5.2}$$

where, N_1 and N_2 are the bunch intensities or particles per bunch, N_b is the number of bunches per beam (maximum of 2808 in the LHC), f_{rev} is the revolution frequency of the bunches around the LHC, 11.246 kHz. σ_{nx}^2 and σ_{ny}^2 are the standard deviations of the Gaussian beam profile shape in the x and y directions respectively, for beam n = 1 and similarly for beam n = 2. As a function of beam displacement u, the luminosity varies as:

$$\mathcal{L} = \mathcal{L}_0 \; exp\left[\frac{-\delta u^2}{2(\sigma_{1x}^2 + \sigma_{2x}^2)(\sigma_{1y}^2 + \sigma_{2y}^2)}\right] \tag{5.3}$$

Measuring and optimizing $\mathcal{L}$ whilst scanning the beams finds the optimal displacement value $u = 0$, allowing the determination of the maximum achievable collision rates [66] and therefore allows for the cross section of any given process to be determined by:

$$\sigma_{vis} = \frac{dN_{(u=0)}}{dt}\frac{1}{\mathcal{L}_{u=0}} \tag{5.4}$$

where $\frac{dN_{(u=0)}}{dt}$ is the *visible*, or *detectable* count rate of the process at zero beam displacement.

Although precise results are obtained, measuring and optimizing the luminosity in this way is not practical for every new fill as it takes considerable time and greatly increases the possibility of large beam losses. The official CMS Luminosity values are calculated using the HF calorimeters by the CMS Luminosity Group [67]*. The results of the VdM scans were used to provide a calibration factor for the HF based calculations.

The luminosity is not constant but decays over time as the protons or heavy ions

*As of 2012, a technique of counting pixel clusters was developed to overcome non-linearities of the HF method at high luminosities, $\mathcal{O}(10^{34}\mathrm{cm}^{-2}\mathrm{s}^{-1})$.

collide, reducing the beam intensities. For an initial peak proton luminosity of $\mathcal{L} = 10^{34}\mathrm{cm}^{-2}\mathrm{s}^{-1}$, the CMS and ATLAS experiments will experience a luminosity decay time $\tau \approx 44.85h$ under ideal conditions [2]. To track the true luminosity decay during an LHC fill, an online, non-intrusive method of monitoring must be achieved.

5.1 CMS Luminosity Calculation

As the LHC luminosity has increased, the methods of measuring the luminosity in CMS have had to evolve. The VdM scans described cannot be used for every fill due to the time it takes as well as the risks of losing the beam and the effects it has on the luminosities of other experiments on the LHC. 'Standard candle' events like W and Z production could not be used at the low luminosities seen in 2010 because these cross sections were too low and were not precisely determined at the LHC collision energies. This section describes the methods used in 2010 and 2011 for measuring the luminosity in CMS.
Full credit for this work goes to CMS Luminosity Group.

5.1.1 2010 On-line Methods

Several techniques were developed in CMS to measure the luminosity *online* without interrupting the beams. The BSC counted events where signals from the +Z and -Z tiles occurred in coincidence within ±20 ns. The rate of these coincident signals was converted to a luminosity value using a factor calculated from data collected during runs in which VdM scans had been made.
The BRAN (Beam RAte for Neutrals) ionisation chambers situated at ±140 m from the IP counted high energy neutrons emanating from the collisions, the rate of neutrons being proportional to the luminosity. However, the official online and offline methods of measuring the luminosity employed by CMS involved the HF calorimeters. Two methods were developed; one using a method of *zero counting* of towers in the HF calorimeters, whereas the other method sums the transverse energy E_T. In order to derive *online* luminosity information from the HF, a dedicated mezzanine board called the HF luminosity transmitter (HLX) is mounted

on each HF trigger and readout board. It takes in the raw data and produces histograms of the ΣE_T and channel occupancy for the 3564 bunch crossings.

Zero Counting of HF Towers

From mid-2010 onwards, the relative luminosity in CMS was monitored using on-line measurements from the HF Calorimeters [10] employing a technique based on *zero counting*, as described in [67, 68]. The basic idea is as follows.

The average number of HF towers registering a 'hit' (energy deposit) within a time dt is proportional to the average luminosity in that time. The average number of events over many bunch crossings is known to follow Poisson statistics and therefore, so does the number of events detecting a hit in the HF calorimeters measured over many bunch crossings.

Let $P(n, \mu)$ be the Poisson probability of a HF tower being 'hit', where n is the number of towers being hit and μ is the Poisson mean of the samples taken over 1 second.

$$P(n, \mu) = \frac{e^{-\mu}\mu^n}{n!} \tag{5.5}$$

When $n = 0$;

$$P(0, \mu) = \frac{e^{-\mu}\mu^0}{0!} \tag{5.6}$$

$$= e^{-\mu} \tag{5.7}$$

Inverting this we obtain;

$$\mu = -\ln P(0) \tag{5.8}$$

where $P(0)$ is the average of the fraction of zero towers recorded over a specified time interval. Finally, using a theoretically calculated minimum-bias cross-section value of 71.3 mb, derived from the extrapolation of historical pp cross-section results to the current $\sqrt{s}$ collision energy, CMS obtains an online luminosity value by:

$$\mathcal{L} \approx \frac{f_{rev}\ \mu}{71.3\ \text{mb}} \tag{5.9}$$

where f_{rev} is the orbital frequency of 11.246 kHz. A more robust off-line method, accounting for beam backgrounds and detector noise, measured from empty bunch

crossings is used to determine the official luminosity figures for CMS.
For low values of n, there is an almost linear dependence of the luminosity on the number of channels hit. The *zero counting* method was expected to be capable up to luminosities of the order of $10^{34}\text{cm}^{-2}\text{s}^{-1}$ without displaying serious non-linearities. As the luminosity increases, the method suffers from an effect termed 'zero starvation' where almost all the towers are being hit, as well as saturation where any single tower may be hit multiple times within a bunch crossing. Multiple, simultaneous hits within one tower cannot be distinguished. Hence, the non-linearity of the higher luminosity measurement will be accompanied by a large uncertainty.

Online Corrections

Corrections in the HLX algorithms minimised the sensitivity to pedestal shift or gain changes of the HF photomultiplier tubes and QIEs. To improve the linearity of the measurement, only four azimuthal (2π) rings are used in two pairs covering the ranges $3.49 < |\eta| < 3.84$ and $3.84 < |\eta| < 4.2$. This avoids non-linearities stemming from averaging over η rings that have very different probabilities of being hit in any given bunch crossing. Additional corrections needed to be applied as the LHC bunch structure became more occupied. The after effects of collisions take the form of PMT after-pulsing and albedo which can remain for many bunch crossings. The amount of after-pulsing and albedo signals is proportional to the luminosity and is handled through a recalibration using a dedicated VdM scan.

E_T summing

As the luminosity increases, so too does the event rate. In turn, the HF calorimeters will experience greater instantaneous energy deposits. Therefore, by summing the transverse energy, E_T over all the HF towers, one can get a value which is proportional to luminosity and normalisable to the luminosity measured during a previous VdM scan. After comparing this method with the method of zero counting, it was shown that zero counting gave more stable results and the E_T summing method was not pursued further as an online luminosity measurement tool.

5.1.2 2010 Offline Methods

Two offline methods were tested for the low luminosity era of CMS. One measured the ΣE_T deposits, similar to the online method briefly described above. However it was improved to remove HF detector noise. The other method used the pixel and strip tracker to look for zero bias triggered events containing one-or-more two-track vertices and applying the zero counting method similar to that of the HF online method.

E_T summing offline

For 2010, a method using ΣE_T was developed to check and improve the online luminosity measurement. It involved summing the E_T for hits coincident in the HF within an 8 ns timing cut. Even though the time slices of the HF calorimeter are limited to 25 ns by the integration time of the QIE's, it was possible to look at the energy temporal distribution between consecutive 25 ns bins and gain some approximate timing information from the distributions. This method could only work whilst the event pile-up was <1. The sum of E_T was then normalized with a correction factor gained from VdM scans such that $\mathcal{L} = f_{corr} \frac{\Sigma E_T}{\mathcal{L}_{VdM}}$. An additional requirement of at least one vertex reconstruction was implemented to enhance the beam background and detector noise rejection.

Vertex zero counting

This method used the CMS tracker system to look for zero bias (coincident incoming beams) triggered events which contained at least one two-track vertex at ± 15 cm from the nominal I.P. To remove any trigger inefficiencies or complexities due to trigger pre-scaling, where one in N triggers is counted, a new dedicated trigger, based only on the known LHC filling scheme for colliding bunches (N_{BX}) was used. The luminosity was calculated by:

$$\mathcal{L} = \frac{\mu f_{orb} N_{BX}}{\sigma_{eff}}$$

where μ is calculated from the mean number of interactions without a two-track vertex and assuming a Poisson probability of interactions so that, $\mu = -\ln P(0)$, where $P(0)$ is the fraction of bunch crossings with no vertex, or HF hits, in the case of the HF zero counting method. The effective cross section σ_{eff} was calculated using Monte Carlo minimum bias simulations and is the generator level minimum bias cross section multiplied by the ratio of MC events passing the cut and all MC events. f_{orb} is the LHC orbital frequency (11,246 Hz). A 10% difference in the ratio was found between the HF based measurement and the vertex based measurement.

5.1.3 2011 Luminosity Measurements

In 2011, the HF zero counting method continued to be employed as the primary luminosity measurement in CMS. The LHC saw an increase in the number of bunches and luminosity in the experiments. It was noted that luminosity readings from the HF were higher than expected by an amount proportional to the instantaneous luminosity per bunch. The cause was thought to be either the vertex finding efficiency falling off at high luminosity due to vertex merging or the luminosity measurement became non-linear and overestimated at high luminosities. Analysis showed that, with increased luminosity the effects of albedo and PMT after-pulsing became more important. Collectively labeled 'afterglow', these resulted in increased count rates in bunch crossings following a previous collision. The effects could be corrected for using results from minimum bias simulation studies.

Offline Corrections

The offline calculations of the luminosity typically take 24 hours to process before the results are made available to the CMS community. This is due to the corrections applied to both the online measurement data and to the calibrating VdM scans to ensure the most accurate luminosity value possible, which is vitally important for practically all physics analyses. Table 5.1 lists the main corrections applied to the CMS luminosity measurement in 2010 and 2011.

The major change in the uncertainty of the overall luminosity measurement from CMS came from the increased accuracy and understanding of the bunch current measurements of the FBCTs, starting at a very conservative 10% in 2010 and

Table 5.1: The list of corrections and their uncertainties of the CMS HF based luminosity measurement in 2010 and 2011. Well explained details of each correction can be found in [68–70].

Uncertainty	Description	Value (%) 2010	Value (%) 2011
Beam Background	Use non-colliding bunches to remove beam induced noise.	0.1	
Non-Linearity	Non-linearity of the HF detector response at high luminosity.		2.5
Afterglow	Albedo and PMT ringing contributions		0.7
Beam Shape	Correct for emittance increase from time of (normalizing) VdM scan.	3.4	0.3
Fit Systematics	Fitting of the VdM beam widths.	0.5	
Length Scale	Uncertainty of Δx,Δy movement during VdM scans.	1.2	0.5
Zero Point	Unknown hysteresis effects in the beam separation magnets.	1.5	1.1
Beam Current	Uncertainty of Fast Beam Current transformers (FBCTs).	10	3.1
Crossing angle	Uncertainty of the precise crossing angle during the VdM scans and runs	1.0	
HF detector	Detector noise, pedestal shifts & long-term gain fluctuations	1.0	1.5
	Total	11	4.5

reduced to 3.1% in 2011. This resulted in a total uncertainty reduction from 11% in 2010 to 4.5% in 2011. Luminosity values from pre-May 2011 were required to have a correction factor of 1.007 applied and all luminosity values had an overall uncertainty of 4.5%.

5.2 BSC as a Luminosity Monitor

During the low-luminosity phases of the LHC operation, including the Heavy Ion runs, there was the desire to have an independent method of monitoring the luminosity to act as a cross check to the HF based system. Throughout most of 2010 *pp* running and subsequent Heavy Ion runs, the BSC was capable of providing another independent measurement by using the minimum bias triggers. However, in its current form, this capability was limited due to the fact that there were only 16 channels at each end of CMS (BSC1) and rates from the large and sensitive scintillator tiles quickly saturated. Above some value of luminosity, signals were produced in every channel in every bunch crossing. Before saturation, the event rate in the BSC detector increased with luminosity. Assuming a detection efficiency of ϵ_{det}, the rate of events detected per second is given by;

$$R_{events} = \mathcal{P} N_{bb} f_{orb} \epsilon_{det} \tag{5.10}$$

where R_{events} is the minimum bias trigger rate in Hz, N_{bb} is the number of colliding bunches, f_{orb} is the LHC orbit frequency and $\mathcal{P}$ is the average number of pp collision events occurring simultaneously, known as the pile-up fraction ($0 \leq \mathcal{P} \leq 1$).

The event rate, R is also related to the luminosity by;

$$< R_{\text{ events}} >= k\sigma_{pp}\ \mathcal{L}_{inst} \tag{5.11}$$

where $< R_{events} >$ is the mean number of events, assuming Poisson statistics, σ_{pp} is the pp minimum bias cross-section†,$\mathcal{L}_{inst}$ is the instantaneous luminosity per second and k is the correction factor accounting for the detector efficiency and geometrical acceptance.

Therefore, by monitoring the rate of the minimum bias trigger and applying a suitable factor, it is possible to obtain a relative luminosity value from the BSC, provided that the average number of collisions within a single bunch crossing (the pile-up) is $\leq$1.

Minimum bias trigger rates and CMS instantaneous luminosity were compared for the months of August - October 2010 to obtain a relationship between the minimum bias trigger and the luminosity during this early phase of pp running. It should be noted that the luminosity was increased throughout September and October bringing the instantaneous luminosity beyond the design luminosity of the BSC, $\mathcal{L} \approx 10^{32}\text{cm}^{-2}\text{s}^{-1}$ [40]. Figures 5.1(a), 5.1(b) and 5.1(c) show the normalized BSC Minimum Bias rates (Red) and Instantaneous luminosity (Blue) for August, September and October respectively.

The signals from the BSC were used to monitor the luminosity online during the Heavy Ion (H.I) runs, temporarily replacing the HF Zero Counting method. The

†The elastic and many of the diffractive collisions will not be detected by the BSC due to kinematic considerations. The minimum bias trigger is fired mainly by non-diffractive and double diffractive events. See chapter 6

BSC channels did not reach saturation due to the lower minimum bias rates during these runs. The minimum bias trigger rates of the BSC closely followed the CMS instantaneous luminosity in September ($\mathcal{L}_{inst}$ <30 μb^{-1}s^{-1}). A single, empirically derived conversion factor ($\approx$71000μb), required to convert the BSC minimum bias trigger count rates (Hz) to an instantaneous luminosity measurement (μb^{-1}s^{-1}) was sufficient. In late September, there was the first significant increase in luminosity ($\mathcal{L}_{inst} = 3.5 \times 10^{31}$cm^{-2}s^{-1} = 35$\mu$b^{-1}s^{-1}), when it was observed that the BSC minimum bias trigger was triggering at a rate $\sim$ 10 $-$ 20% lower than expected. Inspection showed that the increase in bunch intensity lead to excessive signal amplitudes from the front-end PMTs. Such large signals caused oscillations to be produced by the tube base electronics (typically by the dynode bypass capacitors) with amplitudes capable of crossing the discriminator thresholds (see figure 3.7), causing secondary firing of some triggers. When these oscillations occurred within the 20 ns output pulse width of the discriminators, it had the effect of prolonging the output pulse, effectively increasing the dead-time of the corresponding channel. Adjustments to the discriminator thresholds and high voltages were made to accommodate these increased signal amplitudes which, together with a new conversion factor, restored the linearity of the BSC minimum bias triggers with the instantaneous luminosity values, as shown in figure 5.1(b).

Through 28 September to 18 October, the luminosity in CMS was increased from $\mathcal{L}_{inst}$ = 30μb^{-1}s^{-1} (3$\times$10^{31}cm^{-2}s^{-1}) to $\mathcal{L}_{inst}$ = 180μb^{-1}s^{-1} (1.8$\times$10^{32}cm^{-2}s^{-1}) pushing beyond the limit of the BSC performance as a luminosity monitor without adjusting the sensitivity and triggering efficiency. Figure 5.1(c) shows the point at which the BSC minimum bias trigger rate saturated at $\sim$40μb^{-1}s^{-1}. The HF based luminosity calculations, explained in [67] are not susceptible to saturation due to pile up until at least $\mathcal{L} = 5 \times 10^{34}$cm^{-2}s^{-1} (50 nb^{-1}s^{-1}). However, the HF luminosity monitor does not function well for low luminosities which is where the BSC excels.

Summary

The BSC detector operated as a relative luminosity monitor during the low luminosity phases of the LHC. During these phases, in which the BSC tiles were able to operate at $\approx$95% efficiency without suffering from excessive signal heights or

saturation, it was possible to convert the minimum bias trigger rates into luminosity values by a single, empirical conversion factor.
As the luminosities and particle flux increased, the signal amplitudes from each channel became excessively large, causing signal ringing and overlapping pulses on the arrival at the readout electronics. This had the effect of increasing the dead-time of the trigger system, reducing the efficiency of counting the minimum bias rates. The effect could be corrected for by fine tuning thresholds of the first level of discriminators in the readout and tuning the high voltages to the PMTs to reduce the signal heights and prevent excessive pulse amplitudes due to the increase in particle flux.
Further increases in luminosity during October signaled the limitation of the BSC sub-detector as a luminosity monitor. Because of the simplicity of the design, the BSC did not provide adequate timing or topological information to help distinguish and account for multiple events occurring simultaneously. The larger number of particle interactions with the BSC tiles pushed the BSC front end to its operational limits. Even after reducing the high voltage and single channel efficiency, the minimum bias trigger rates reached a plateau when the luminosity reached $\sim 40\mu\mathrm{b}^{-1}\mathrm{s}^{-1}$.
However, it had been shown that, with the aid of VdM scans, the BSC was capable of providing online luminosity information throughout the 2010 and 2011 H.I runs. The functionality of a H.I and low *pp* luminosity monitor was one consideration when determining the requirements of the upgrade system.

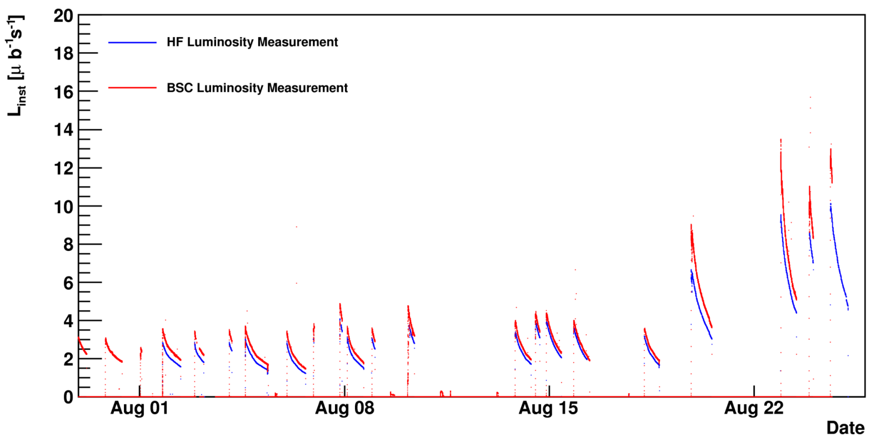

(a)

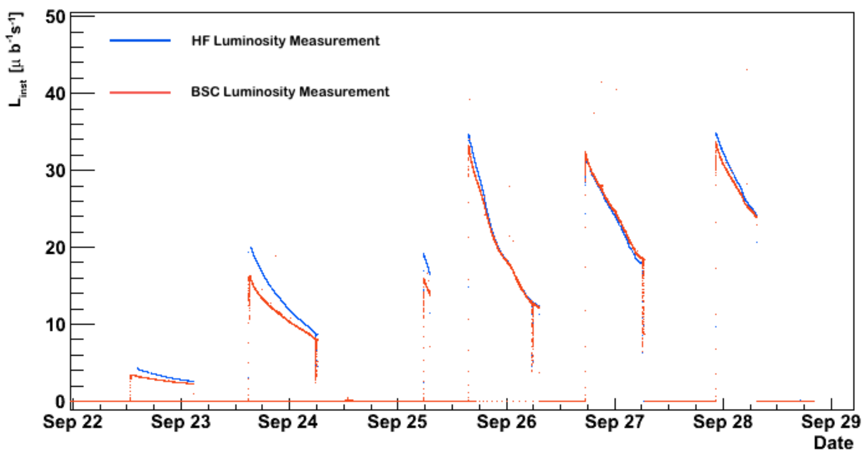

(b)

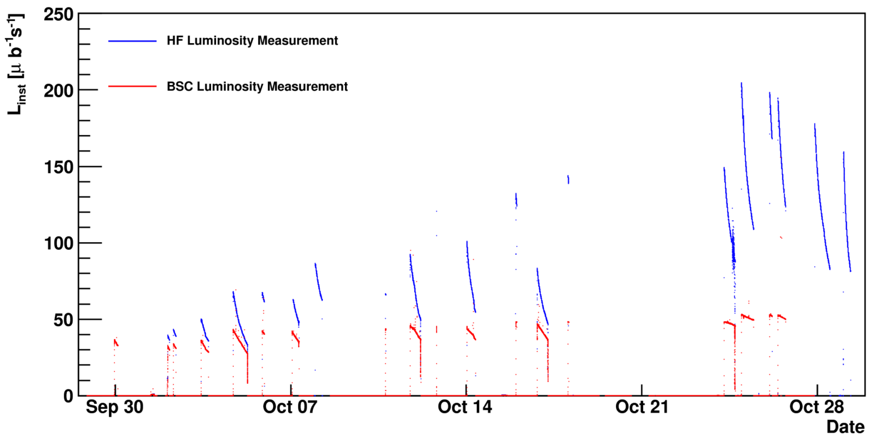

(c)

FIGURE 5.1: Trigger and luminosity data throughout (a) August, (b) September and (c) October 2010. BSC luminosity monitoring is shown in red. The official CMS off-line luminosity measurements are shown in blue.

Chapter 6

Forward Physics

This thesis investigates the performance of the BSC in terms of its triggering efficiency, particularly for minimum bias events, and subsequently, the capabilities for such a detector to perform as an online luminosity monitor should such a device be required by the BSC upgrade. Chapter 7 also describes the measurement of the inelastic cross-section for pp collisions at $\sqrt{s} = 7$ TeV. All of these require some understanding of the theory and mechanisms behind high energy hadronic interactions. This chapter provides an overview of the Standard Model followed by the current theory of elastic, inelastic and diffractive hadronic interactions.

6.1 The Standard Model

The Standard Model of particle physics is undoubtedly one of the greatest achievements in the history of science, accurately describing three of the four known fundamental interactions in nature and the particles that participate in these interactions.

The entirety of *normal* matter in our universe is made from a surprisingly small set of 'building blocks'; six Leptons and six Quarks with their interactions governed by 4 gauge bosons. The leptons, the electron (e), muon (μ) and tau (τ) each with its corresponding neutrino; (ν_e, ν_μ and ν_τ), make up the three generations of leptons. The six flavours of quarks similarly come in three *families* with the rather whimsical names of *up* and *down*, *charm* and *strange*, and *top* and *bottom*. All the leptons and quarks are classed as *fermions*, particles which have an intrinsic *spin angular momentum* equal to $\pm{}^1\!/_2\hbar$ [71].

To accompany these 12 fermions, 4 gauge bosons (spin $= 1\hbar$) are so far known to exist which convey the interactions between the fermions resulting in three of the four known forces; namely the Electromagnetic force (*EM*), the Weak force and the Strong force. The gravitational force is far too weak compared to the others and as such, has not been studied to the extent where it can be included into the Standard Model. Figure 6.1 shows the list of known elementary particles. Table 6.1 shows the relative strengths of the four known forces.

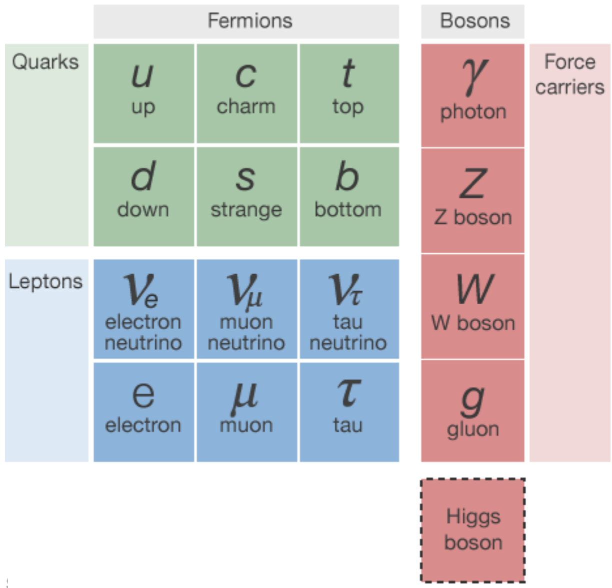

FIGURE 6.1: The elementary particles of the standard model. The Higgs Boson was tentatively declared as 'discovered' on 4th July 2012 by the CERN Director General, Rolf Heuer after presentations by the CMS Collaboration and the ATLAS Collaboration.

TABLE 6.1: The relative strengths of the fundamental forces, normalised to the Strong force.

Force	Mediating Boson	Relative Strength	Range
Strong Force	g	1	2 fm
ElectroMagnetic Force	γ	$\sim 10^{-2}$	∞
Weak Force	$W^{\pm}, Z^0$	$\sim 10^{-14}$	10^{-3} fm
Gravitation Force	Not Found	$\sim 10^{-39}$	∞

6.1.1 Electromagnetic Force

The Electromagnetic force (EM) is responsible for all interactions between charged particles. EM Interactions are described *very* accurately through the framework of Quantum Electrodynamics (QED), a field theory which incorporates a U(1) gauge symmetry on the particle field, Ψ. Gauge symmetries can be either global or local. Global gauge symmetries (Eq. 6.1) predict the existence of a conserved quantity. In the case of $U(1)_{em}$ gauge symmetry, the conserved quantity is *Charge*. By imposing a *local* symmetry (Eq. 6.2) requirement, one is forced to introduce a new gauge field. The new field produces the *gauge boson(s)* that interact with these charged particles. In QED, the gauge boson is the photon, γ.

$$\Psi \rightarrow e^{i\alpha}\Psi \tag{6.1}$$

$$\Psi \rightarrow e^{i\alpha(x)}\Psi \tag{6.2}$$

6.1.2 Weak Force

The Weak Interacting force is involved in β decay, $n \rightarrow p + e^- + \bar{\nu}_e$ and in the decay processes of many meson particles, such as $\pi^\pm \rightarrow \mu^\pm + \nu_\mu$, which is seen as beam halo background in the experiments.

Weak interactions were postulated to explain the long lifetimes of some particles such as the muon ($\tau \approx 2.2 \times 10^{-6}$ sec) and the neutron ($\tau \approx 960$ sec)[72]. The evolution of the theory of Weak interactions is an interesting example of the entwined nature of theory and experimental results. Initially, Weak interactions were formulated by E. Fermi as a *four fermion interactions* theory, described diagrammatically in figure 6.2 with the amplitude given in equation 6.3 [73].

$$\mathcal{M} = -\frac{G_F}{\sqrt{2}}[\bar{p}(x)\gamma_\lambda n(x)][\bar{e}(x)\gamma^\lambda \nu_e(x)] \tag{6.3}$$

However, it was subsequently noted in experiments involving *Kaons* that the decay of K^+ can result in two different final states each with opposite parities. In the case of $K^+ \rightarrow \pi^+\pi^-$, *Parity* = -1, whereas for $K^+ \rightarrow \pi^+\pi^+\pi^-$, *Parity* = +1. This led to the suggestion that Weak interactions do not conserve parity, as EM and Strong

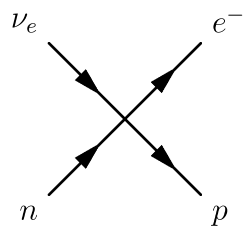

FIGURE 6.2: The vector formulation by Fermi postulated that all the interaction takes place the same space-time point.

interactions do [74]. Experimental evidence quickly confirmed this suggestion [75], leading on to the theory of a vector minus axial vector form ($V - A$) of the charged Weak current; one which violates Parity *maximally.* As a result, charged Weak interactions only couple to left (right) handed fermions (anti-fermions). The $V - A$ formulation of a charged Weak current described the phenomenology of Weak interactions very well. But it did not include *neutral* currents which were eventually discovered in 1973 at the Gargamelle bubble chamber at CERN [76]. Additionally, the $V - A$ theory was non-renormalisable and also violated unitarity. A new theory had to be found which incorporated all the good properties of $V - A$ theory but was also renormalisable, described neutral currents and the relative weakness of the Weak force.
The final amendment to the Weak theory is known as the *Intermediate Vector Boson* (IVB) theory. This theory assumes that the Weak currents are mediated by massive vector bosons (spin = 1). The charged Weak currents involved, for example, in β decay, are conveyed by the W^+ and W^- bosons. The interactions involved in the interaction $\nu_\mu e^- \rightarrow \nu_\mu e^-$ seen in Gargamelle can *only* happen via the neutral weak current, shown in figure 6.3. The boson responsible for neutral current weak interactions, the Z^0 boson, was discovered at CERN in 1983 at the UA1 and UA2 [77] experiments shortly after the discovery of the $W^\pm$ bosons.

The confirmation of the existence of the $W^\pm$ and Z^0 bosons as predicted by theory, solidified the understanding of Weak interactions. As well as predicting the three Weak vector bosons, the theory included the photon γ of *EM* and unified the $U(1)_{em}$ theory of QED with the $SU(2)$ theory of weak interactions into a single $SU(2)_L \times U(1)_Y$ theory of ElectroWeak interactions.

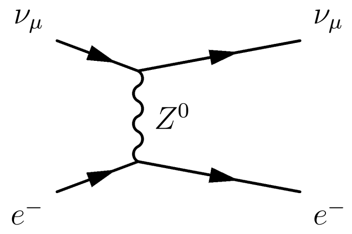

FIGURE 6.3: The interaction seen in Gargamelle (CERN) can only proceed via the Weak neutral current. Strong interactions are excluded as all particles involved are leptons. The presence of the neutrinos excludes *EM* interactions. Finally, no charge transfer takes place, excluding the involvement of $W^{\pm}$ bosons.

Electroweak Unification

The Standard Model of Glashow, Weinberg and Salam unifies the Electromagnetic force (with its U(1) symmetry), and the Weak force (SU(2) symmetry) to form an $SU(2)_L \times U(1)_Y$ symmetry group. Here, the subscript L refers to the charged weak coupling to left handed fermions. The subscript Y refers to the more fundamental quantum number of the weak hypercharge. The electronic charge Q is a linear combination of this hypercharge and the conserved quantity of the z component of the weak isospin, T_z.

$$Q = T_z + \frac{1}{2}Y \tag{6.4}$$

Both T_z and Y are conserved currents and therefore, electronic charge is also conserved. This is different to the $U(1)_{em}$ symmetry group where Q was conserved directly as a consequence of imposing global gauge invariance. The $SU(2)_L$ symmetry group has 3 generators, $W^{\mu}_{1,2,3}$ while the $U(1)_Y$ has one, B^{μ}.
The Lagrangian for the EW theory of the standard model can be written as:

$$\mathcal{L}_{SM} = \mathcal{L}_f + \mathcal{L}_G + \mathcal{L}_{SBS} + \mathcal{L}_{YW} \tag{6.5}$$

where $\mathcal{L}_f$ is the fermion Lagrangian and $\mathcal{L}_G$ is the Lagrangian of the gauge fields.

$$\mathcal{L}_f = \Sigma_f \bar{f} i\gamma D_\mu f$$

$$\mathcal{L}_G = -\frac{1}{4}W^i_{\mu\nu}W^{\mu\nu}_i - \frac{1}{4}B^i_{\mu\nu}B^{\mu\nu}_i + ...$$

where;

$$W^i_{\mu\nu} = \delta_\mu W^i_\nu - \delta_\nu W^i_\mu + g\epsilon^{ijk} W^j_\mu W^k_\nu$$

$$B_{\mu\nu} = \delta_{mu} B_\nu - \delta_\nu B_\mu$$

The last two terms of equation 6.5 are the Spontaneous Symmetry Breaking Lagrangian, required to introduce masses to the gauge bosons in a gauge invariant way, and the Yukawa Lagrangian to give masses to the fermions. The physical gauge bosons, $W^\pm_\mu$, Z_μ and A_μ are formed from these electroweak eigenstates by:

$$W^\pm_\mu = \frac{1}{\sqrt{2}}(W^1_\mu \mp iW^2_\mu)$$

$$Z_\mu = \cos\theta_w W^3_\mu - \sin\theta_w B_\mu$$

$$A_\mu = \sin\theta_w W^3_\mu + \cos\theta_w B_\mu$$

where θ_w is the weak mixing angle of the neutral components, Z_μ and A_μ. This forms the $W^\pm$, Z and photon of the weak and electromagnetic forces. However, none of these bosons have mass as expected of the short range weak force. The Higgs Mechanism is the simplest method of introducing mass terms without spoiling the gauge invariance of the local symmetry.

Higgs Mechanism

A method of bestowing mass to the $W^\pm$ and Z bosons while leaving the U$(1)_{em}$ photon massless needs to be done in an way which still leaves the Lagrangian invariant. The simplest way to do this is to introduce a complex scalar doublet field:

$$\Phi = \begin{pmatrix} \Phi^+ \\ \Phi^0 \end{pmatrix} = \frac{1}{\sqrt{2}} \begin{pmatrix} \Phi^+_1 + i\Phi^+_2 \\ \Phi^0_1 + i\Phi^0_2 \end{pmatrix} \tag{6.6}$$

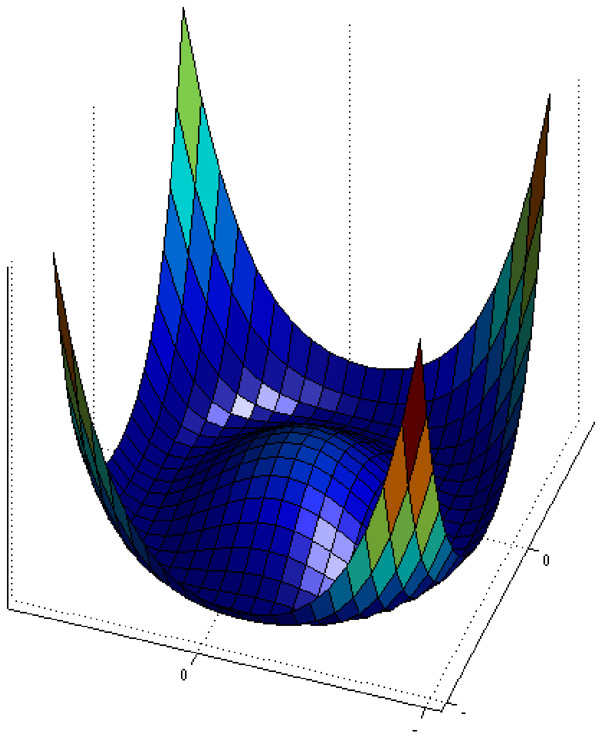

FIGURE 6.4: The traditional 'wine bottle' potential of the Higgs field. There are infinite number of degenerate minima states after spontaneous symmetry breaking. Shifting one of these states to the zero point of the vacuum *hides* the broken symmetry and the previously massless Goldstone Bosons acquire mass.

and a vacuum potential term:

$$V(\Phi) = \mu\Phi^\dagger\Phi + \lambda(\Phi^\dagger\Phi)^2 \tag{6.7}$$

where μ and λ are constants with $\lambda >0$ so the vacuum potential is bounded from below [78]. When $\mu <0$, the vacuum potential has a non-trivial zero value, as seen in figure 6.4. The degenerate set of zero values are found at a magnitude $v_0 = \sqrt{\frac{-\mu}{2\lambda}}$. Choosing one of these possible minima - traditionally the one laying on the $\mathbb{R}e(\Phi)$ axis - breaks the symmetry.

Performing small perturbations around the newly chosen vacuum state* results in mass terms for all the gauge vector bosons as well as a massless scalar boson for each, known as *Goldstone Bosons*. Additionally, one also obtains a massive scalar field, the *Higgs Field*. By applying a carefully chosen gauge transformation,

* Small perturbations around the vacuum are excited states which, in Quantum Mechanics are interpreted as particles.

known as the *unitarity gauge*, these non-physical massless Goldstone bosons can be 'rotated' away and in their place we gain the longitudinal polarisation of the massive SU(2) vector bosons.
However, the vacuum is invariant under simultaneous $\mathrm{SU}(2)_z$, U(1) rotations of ϕ and $\frac{1}{2}\phi$ respectively (see equation 6.4). It is this part of the gauge group which remains massless and provides the required massless photon.

6.1.3 Strong Force

Strong interactions are described within the framework of Quantum Chromodynamics (QCD), a non-Abelian theory with $\mathrm{SU}(3)_c$ symmetry. Here, c denotes '*colour*', the name given to the charge involved in strong interactions, much like electronic charge Q. The strong force affects only quarks and gluons. Leptons ($e^{\pm}, \mu^{\pm}, \tau^{\pm}$) and their neutrinos ($\nu_{e,\mu,\tau}$) do not have the colour charge and thus do not couple to the strong force. The colour charge comes in three possible flavours; red, green and blue and their anti-matter counterparts ($\overline{\text{red}}, \overline{\text{green}}, \overline{\text{blue}}$). Being an SU(3) symmetry, the strong interactions are governed by 3^2-1 $=$ 8 gauge bosons, namely the Gluons, which also carry the colour charge and are therefore self-interacting. An important feature of the strong force is that of *colour confinement* in which all coloured quarks can only appear as colour neutral entities. This results in hadronic (quark containing) particles only being seen in 2-quark (meson) or 3-quark (baryon) bound states in which the 2-quark states contain quark-anti-quark pairs. e.g. the $\pi^+ = u_r\bar{d}_{\bar{r}}$ in which the quark may be red while the anti-quark is $\overline{\text{red}}$, and the 3-quark states contain 3 quarks, one of each colour. e.g. The proton, $\mathrm{u}_r\mathrm{u}_g\mathrm{d}_b$.
Another important feature of the strong colour charge is that, unlike the electromagnetic or weak forces, the strength, α_s increases with separation. At small separation (high energies) the strength of $\alpha_s \lim_{x\to 0} = 0$ and the quarks and gluons behave as free particles, an effect known as *asymptotic freedom* [79].
Conversely, as separation x increases, current QCD models predict that the energy density between the quarks increases to such an extent that new pairs are produced from the vacuum ensuring the original entities appear as colour neutral mesons. This concept is exploited in the Lund string model of hadronisation used in many high energy physics Monte Carlo generators.

6.2 Proton Interactions

Hadronic interactions can reveal information about the properties of the strong interactions allowing the further development of models of how the quarks and gluons within the hadrons behave.The interactions can occur in several ways, namely *elastic scattering*†, *inelastic* or *Non-Diffractive scattering* and *diffractive scattering*, which in-turn can be divided into Single Diffractive and Double Diffractive‡. Together, these processes account for almost all of the total cross-section of *pp* interactions. The approximate cross-section values expected at the LHC for each process are given in table 6.2 [80, 81].

TABLE 6.2: The approximate cross-sections, σ for elastic and inelastic processes at $\sqrt{s}$ = 14 TeV [80, 81].

Process	Description	Cross Section
Elastic	pp→pp	∼30 mb
Non-Diffractive	pp→ N	∼65 mb
Single Diffractive	pp→ p + X_p	∼10 mb
Double Diffractive	pp→ X_p + X_p	∼7 mb

From the point of view of quarks or gluons (often referred to as 'partons') in the collision of hadrons, the coming together of these partons causes a redistribution, or polarisation, of the colour charge. The partons may be only slightly influenced and continue in their original direction as in the case of elastic scattering. Others may form into new, colourless hadrons due to the energy transfer and excitation provided during the collision, resulting in an inelastic collision. Or in a *quasi-elastic* event, an incident hadron may be excited but recombine into the same hadron, in which case, this 'leading particle' appears as the incident hadron with slightly reduced momentum. Diffractive scattering events, which are thought to involve the exchange of a multiple-gluon colourless singlet state, as described in section 6.2.4, are characterised by large gaps in the distribution of the outgoing

†There is some confusion in the literature with some authors defining diffractive scattering as a sub-category of elastic scattering, while others define it as a sub-category of inelastic scattering. As both protons do not exit a diffractive collision intact, one could define the event as inelastic. However, one could define elastic events as the *ultimate* diffractive event with the maximum possible rapidity gap!

‡Other processes such as Centrally Diffractive and Multi-Pomeron exchange have only small contributions and will be ignored

particles.

To aid in the discussion of these collisions, we introduce some useful variables. The rapidity, which can be thought of as the relativistic-invariant measure of the longitudinal velocity [82] and the Mandelstam variables which are invariant quantities describing 2-body scattering processes of the form $AB \to CD$.

Rapidity & Pseudo-rapidity

A useful kinematic variable in hadronic collisions is the Lorentz invariant *rapidity*, y defined as,

$$y = \frac{1}{2}\ln\frac{E + p_L}{E - p_L}$$

where p_L = p $cos\theta$ and θ is the angle of deflection between the incoming and outgoing particle. For situations where the particle mass is negligible and θ is not very small, y can often be replaced by the more usual quantity of *pseudo-rapidity*, η.

$$\eta = -\ln\,\tan(\theta/2)$$

The experiment sub-detectors are usually referred to in terms of their η coverage. However, in the case of elastic scattering, the emerging particles leave the detector inside or very close to the beam pipe and at very small θ. Thus, for elastic scattering, $\eta \to \infty$ for $\theta \sim 0$ and y is a more useful quantity.

Mandelstam Variables

Assume two particles, A and B interacting as shown in figure 6.5. p_A, p_B, p_C and p_D are the 4-momenta of the particles, (E, px, py, pz). Due to energy-momentum conservation, $P_A + P_B = P_C + P_D$. The Mandelstam variables are defined as,

$$s = (P_A + P_B)^2 \simeq \quad 2P_A \cdot P_B$$

$$t = (P_A - P_C)^2 \simeq -2P_A \cdot P_C$$

$$u = (P_A - P_D)^2 \simeq -2P_A \cdot P_D$$

where the approximations are made when dealing with energies much greater than the mass-energy of the particles involved. In the LHC, where the particle beams are made to collide head on, the particles have equal and opposite momenta. $P_A = (E, \mathbf{p})$ and $P_B = (E, -\mathbf{p})$. Thus, s becomes,

$$s = (E_A + E_B, \mathbf{p_A} - \mathbf{p_B})^2 = (E_A + E_B)^2$$

In other words, s is the square of the colliding beam total centre of mass energy. Similarly, the variable t (and u) is equal to the square of the momentum transfer from P_A to P_C (P_A to P_D) or equivalently, from P_B to P_D (P_B to P_C).

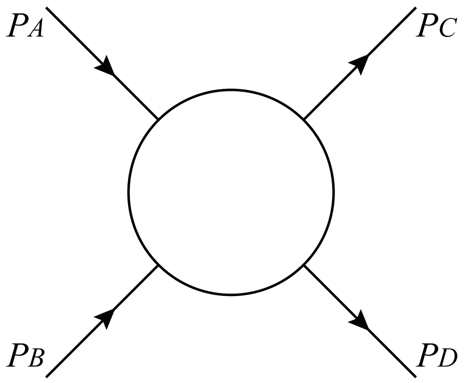

FIGURE 6.5: A 2-body interaction diagram of the type $AB \to CD$ where P represents the particle 4-momenta of the particles.Time flows in the horizontal direction.

The Froissart bound

In the 1960, M. Froissart [83] showed that the rise of the total cross-section of hadronic interactions has an upper limit.

$$\sigma_{tot}(s) \leq ln^2\left(\frac{s}{s_0}\right) \tag{6.8}$$

where s_0 is a scaling factor which is undefined but typically taken to have the value of ≈1 GeV^2. The interaction between the two hadrons is mediated by the exchange of bosons. This is possible, according to Heiseberg's Uncertainty principle, but only over very short time intervals and the effect decreases exponentially as the shortest distance between the hadrons, known as the *impact parameter* **b**, increases. Beyond a certain impact parameter, the interaction between two particles becomes negligible. What Froissart showed is that the impact parameter is determined by the natural logarithm of the collision energy. The cross section cannot increase faster than $\mathbf{b}_0^2$. Thus, the cross section rise is limited by $\ln^2 s$.

Invariant Mass of the diffractive system

The invariant mass of a particle or system of particles is a characteristic of their energy and momentum which is the same in all reference frames related by Lorentz transformations. For pp elastic scattering, the mass of the protons, of course remains unchanged. For inelastic diffractive scattering, the mass of the final state particles is not the same as the original proton mass. The final state system X must contain at least one baryon in order to conserve baryon number, and has absorbed energy and momentum during the interaction. Assuming one is dealing with pp collisions, this implies the $M_X > M_p$, where M_p is the mass of the proton, 938.27 MeV. The invariant mass of a single particle is calculated from Einstein's Energy-Momentum relation;

$$E^2 = m^2c^4 + \mathbf{p}^2c^2 \tag{6.9}$$

$$= m^2 + \mathbf{p}^2 \tag{6.10}$$

where $\mathbf{p} = [p_x, p_y, p_z]$ and the second line is using 'natural' units where $c = 1$. Thus, for a single particle, the invariant mass is simply

$$m = \sqrt{E^2 - \mathbf{p}^2} \tag{6.11}$$

In inelastic and diffractive scattering, the system, X is made of many partons. One needs to sum the energy and momentum of these individual partons to obtain the invariant mass;

$$M_x = \sqrt{\Sigma E^2 - \Sigma \mathbf{p}^2} \tag{6.12}$$

$$= \sqrt{\Sigma E^2 - (\Sigma p_x^2 + \Sigma p_y^2 + \Sigma p_z^2)} \tag{6.13}$$

6.2.1 The Pomeron Model

Further to assist in the discussion of hadronic interactions, a brief description of Regge theory [84] and an associated pseudo-particle called the *Pomeron*, $\mathcal{P}$ is required. Regge theory was conceived in the 1960's (prior to pQCD) to describe the behaviour of high energy, soft (small $|t|$) elastic and diffractive scattering. The traditional idea of nucleon-nucleon interactions being mediated by meson exchange or resonances (collectively named *Reggeons*) gives an scattering amplitude,

$$A(s,t) = \frac{s^{\alpha}}{t \, - \, m^2} \tag{6.14}$$

where s is the square of the collision energy, α is the Reggeon spin ($\alpha \, = \, 0{,}1{,}2{,}3...$), t is the square of the momentum transfer and m is the Reggeon mass. Therefore, exchanges of Reggeons, with higher spins result in dramatically higher amplitudes, and subsequently higher cross-sections. The cross-section evolution based on the idea of individual meson exchange would therefore violate the Froissart Bound as $s \rightarrow \infty$ [85] (See also section 6.2).
Experimental results of pp cross-section measurements, as shown in figure 6.6, demonstrated that the total cross section initially falls at low $\sqrt{s}$ ($1 - 10$ GeV) at a rate of approximately $s^{-0.5}$. The cross section, $\frac{d\sigma}{ds}$ then becomes constant over an energy range of $10 \sim 100$ GeV before increasing, approximately as $\ln^2(s)$ as $\sqrt{s}$ further increases. This behaviour could not be explained by the exchange of individual mesons.

Regge theory suggested that the observed energy dependence is due to a combination of particles and resonances which contribute together in the t-channel. Each Reggeon is considered to be part of a family of mesons and resonances with increasing spin angular momentum and mass. In fact, the Reggeon spin and squared mass are proportional, and when plotted as $\alpha(t)$ (or equivalently $\alpha(m^2)$), the families lie on a straight line, or *trajectory*. Figure 6.7 shows one such trajectory of the ρ and f_2 mesons and ω and ρ resonances.

It can be seen that the mesons and resonances lie on a trajectory described by $\alpha(t) \, = \, \alpha_0 + \alpha'_t$ where α_0 is the point of intercept of the trajectory on the $m^2 \, = \, t \, = \, 0$ axis. In the example ρ trajectory of figure 6.7, $\alpha(0) \approx 0.5$. It was

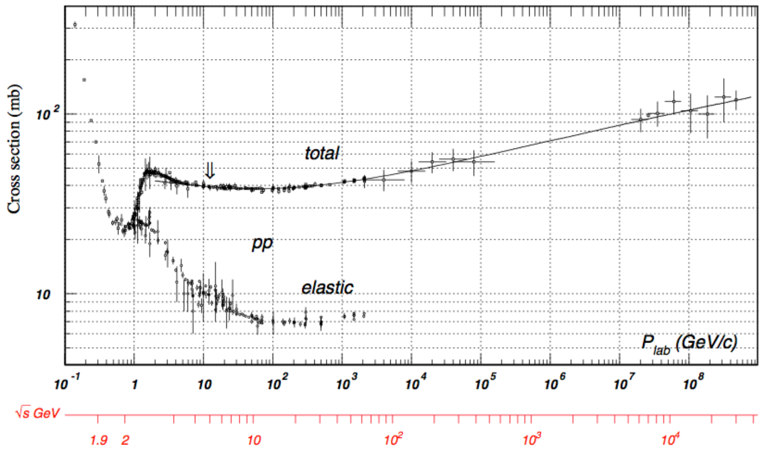

FIGURE 6.6: Results from past measurements of the pp total cross section, collected by the COMPAS group on behalf of the PDG [72], show the initial fall-off of the cross section at low energies (1< $\sqrt{s}$ <10 GeV) is replaced by a logorithmic-like increase as $\sqrt{s}$ increases.

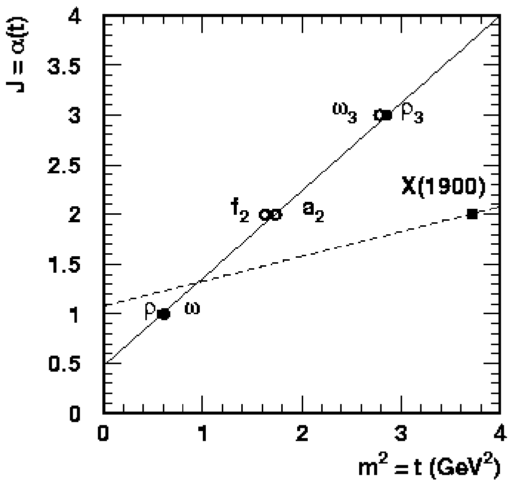

FIGURE 6.7: A Chew-Frautschi plot showing an example of a Regge Trajectory (ρ trajectory) depicted by the solid line. The dashed line represents the 'Pomeron' trajectory[86].

found that the total cross section at a given $\sqrt{s}$ behaves as,

$$\sigma_{total} \propto s^{\alpha(0)-1} \tag{6.15}$$

The low energy cross section behaviour shown in figure 6.6 can be explained if one assumes the ρ trajectory is involved in the t-channel exchange of the pp interactions. With $\alpha(0) \approx 0.5$ for the ρ trajectory, equation 6.15 predicts,

$$\sigma_{total} \propto s^{-0.5}$$

in agreement with the low energy, $1/\sqrt{s}$ behaviour seen from experimental results. However, no such trajectory has been discovered that explains the slowly rising nature of the total cross section at higher $\sqrt{s}$. For this, a trajectory with an $\alpha(0)$ intercept slightly greater than 1 must exist so that $(\alpha(0) - 1)$ of Eq. 6.15 is greater than one. Fits to the data suggest a trajectory with an intercept value of ≈ 1.08 would predict the higher energy behaviour of σ_{total}. Unfortunately, no such particles on the required trajectory have been found to exist. To *fill in* the gap until such a trajectory was really discovered, the *Pomeron* trajectory was conceived [87]. This hypothetical trajectory is also shown in figure 6.7 as the dashed line.

An additional characteristic required of the Pomeron(s) is that it must be a colourless entity with the quantum numbers of the vacuum in order to explain the large rapidity gaps seen in the distribution of diffractively scattered particles and the equal rise in the cross section for both pp and $p\bar{p}$ scattering at high energies. If the Pomeron transfered colour charge during diffractive scattering interactions, hadronisation of the partons would occur more rapidly, suppressing the existence of the rapidity gap. Only a Pomeron trajectory with $\alpha(0) \approx 1$ produces rapidity gaps [88].

The simple Pomeron model was found to only work for 'soft' diffraction (small momentum transfer, $|t|$) but failed when applied to semi-hard diffractive reactions with $|t|$ larger than $\mathcal{O}(1\text{ GeV})$, unless additional Pomerons were introduced. Nevertheless, the concept of the Pomeron is still useful as it makes reasonable predictions of forward scattering seen in diffractive interactions, and also scattering interactions at very high energies. It also provides a simple parameterisation of the evolution of the total cross-section (see Eq 6.17)

After the development of perturbative QCD (pQCD) and the quark-gluon model of strong interactions, the concept of the Pomeron was replaced with a colourless pair of interacting gluons (a colourless singlet state), often referred to as a 'glueball' [89–91]. Again, no colour charge is exchanged during the interaction, and so no hadronisation of outgoing partons occurs which would otherwise be detected in the form of *jets* or the absence of the diffractive event defining rapidity gap. To achieve a colourless exchange in the fabric of QCD, two or more gluons must take part[92]. The Pomeron model was advanced further within QCD with the BFKL[§] approach in which the self-interaction of the gluons was taken into account and also expanded to include the mechanisms of triple-gluon exchange and hard Pomeron exchange [93].

In the same way that none of the particles on the Pomeron trajectory have been observed, there has so far been no conclusive experimental evidence of the existence of glue balls. Although the theoretical models can make predictions of the cross-section value at a given $\sqrt{s}$, there is little phenomenological understanding of the processes involved in high energy, small-|t| scattering. Therefore, Monte Carlo models used to evaluate these events can have vastly different outcomes and large uncertainties.

6.2.2 Total Cross-sections

Above $\sqrt{s} \approx 10$ GeV, the total cross-sections of pp and $p\bar{p}$ interactions rise with increasing collision energy. The impact picture model [94, 95] and the Donnachie-Landshoff (DL) model, based on Regge Theory, make different predictions for the rate of the rise. The impact picture model predicted a rise proportional to $\ln^2 s$ while the DL model which predicted a rise proportional to $s^{\alpha(0)-1}$. Augier *et. al* applied a fit to historical cross-section data including that of the CERN ISR and the Tevatron (5< $\sqrt{s}$ <546 GeV) and found that $\ln^2 s$ followed the data more precisely[96]. The fits to the data and different predictions are shown in figure 6.8.

The total cross-section of proton-proton interactions can be divided into two parts. The elastic cross-section (σ_{el}) in which both protons remain intact and no energy is lost to other processes or particle production, and inelastic scattering (σ_{inel}), in which one or both protons fragment. Inelastic scattering can be further divided into single diffractive (SD), double diffractive (DD), non-diffractive (ND) and centrally diffractive (CD) processes. σ_{el} makes up approximately 20% of the total cross-section with σ_{inel} making up the remaining 80%.

$$\sigma_{tot} = \sigma_{el} + \underbrace{\sigma_{ND} + \sigma_{SD} + \sigma_{DD} + \sigma_{CD}}_{\text{inelastic components}} \tag{6.16}$$

[§]named after the authors, Balitsky, Fadin, Kuraev & Lipatov

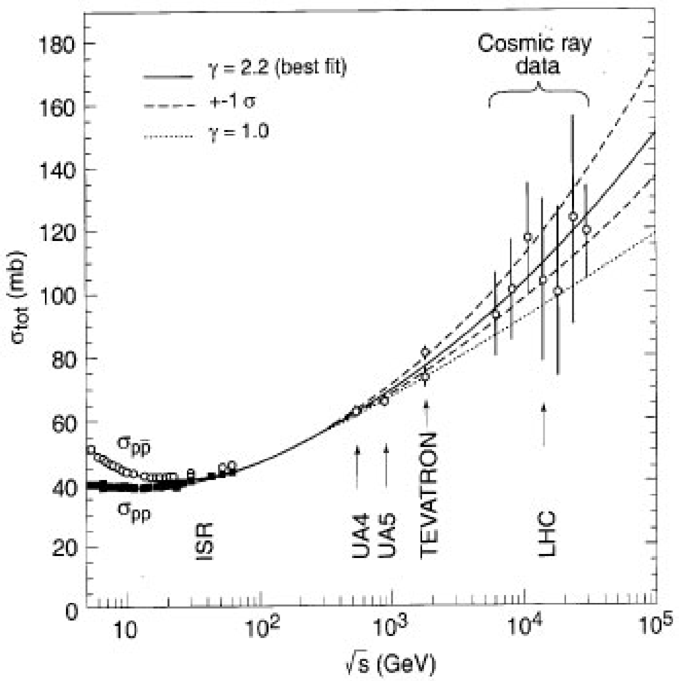

FIGURE 6.8: Historical pp and $p\bar{p}$ cross-section data showing the $(\ln s)^{\Gamma}$ dependence with $\Gamma = 2.2$ (solid line). The dotted line shows the with $\Gamma = 1$. The dashed lines mark the region of uncertainty[96, 97].

The optical theorem (See Appendix F) relates the total cross section (σ_{tot}) for a pair of scattering hadrons, A and B to the amplitude $T_{AB}\ (s,t)$ for elastic scattering. When $\sqrt{s}$ is large, one gets:

$$\sigma_{tot} \approx s^{-1}\mathrm{Im}\ T^{el}_{AB} \quad (s, t = 0)$$

6.2.3 Elastic Scattering

Elastic pp scattering provides a method of probing the proton's internal structure. In elastic scattering, the incoming particles remain intact and no secondary hadrons are produced. This can happen when the collisions are 'soft' and the momentum transfer t is small. Increasing $|t|$ means looking deeper into the proton structure and the amplitudes of different scattering processes contribute to the differential cross-section, $d\sigma_{elastic}/dt$ [98]. For instance, referring to figure 6.9, at very small momentum transfer ($t \lesssim 6.5{\times}10^{-4}$ GeV^2), the interaction proceeds by photon exchange (Compton Scattering). The outgoing particles undergo a very small deflection from their initial directions, leaving the detector region at very high rapidities.

At higher values of $|t|$, the mechanism involving Pomeron exchange takes over and the elastic differential cross-section falls away rapidly as $e^{-B|t|}$ [99]. (where B is a parameter whose value is dependent on the collision energy, $\sqrt{s}$). Increasing $|t|$ further, the process reaches a diffractive minimum before rapidly increasing again. The cause of this local minimum, which was predicted by Chou & Yang many years before the experimental confirmation, involves the interference of two competing processes. On the left side of the dip, Pomeron exchange with charge parity $C = +1$, dominates. On the right hand side of the dip, a Pomeron with $C = -1$ becomes more dominant. In the context of QCD, the $C = +1$ Pomeron is a 2-gluon exchange that has net zero colour. The $C = -1$ Pomeron is considered to be a 3-gluon exchange, again with net zero colour. The latter Pomeron is referred to as an *Odderon* due to its odd parity. The $|t|$ value of this minimum decreases

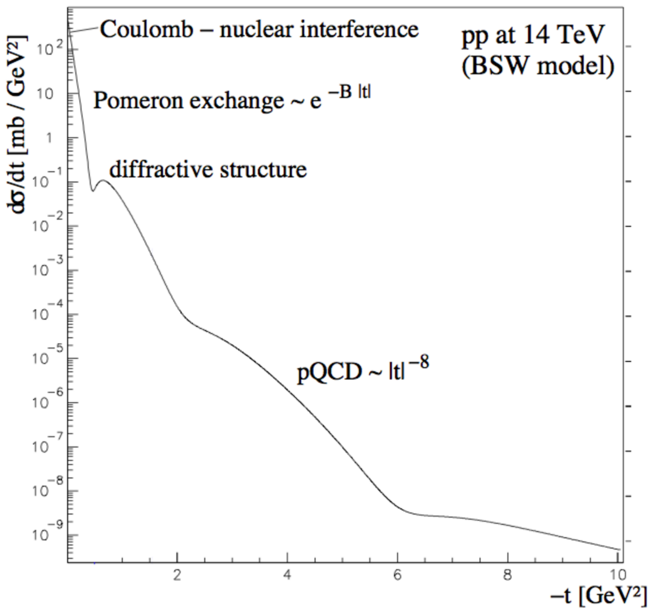

FIGURE 6.9: The expected pp elastic and diffractive scattering at the LHC at $\sqrt{s} = 14$ TeV [80].

very slightly as $\sqrt{s}$ increases, suggesting that the cross over from single Pomeron to multi-Pomeron exchange is almost independent on the collision energy. Beyond this local minimum, the measurements can only be described by including perturbative QCD and multi-Pomeron exchange. The cross-section continues to fall as $|t|^{-8}$ [80].

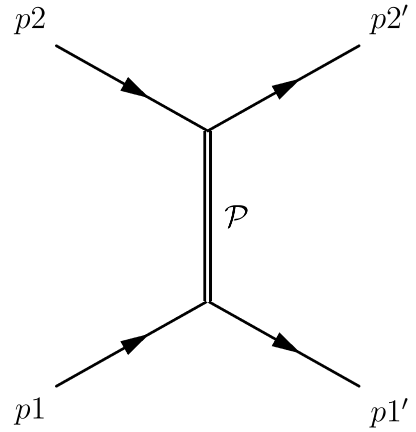

FIGURE 6.10: A Feynman diagram of pp elastic scattering. The momentum transfer is carried by the virtual photon at low $\sqrt{s}$ energy but is replaced by a colourless gluon singlet state called the Pomeron, $\mathcal{P}$ at higher energies. Time is on the horizontal axis.

FIGURE 6.11: A sketch of the distribution of particles in η and ϕ from elastic collisions. The majority of outgoing particles undergo very small deflections and leave the interaction in the very forward direction and large η. The dashed lines represent $|\eta| = 5.2$, the limit of Forward Calorimeter acceptance.

Figure 6.10 shows a Feynman diagram of the hadronic elastic interaction with the single Pomeron exchange. Figure 6.11 symbolises the particle positions in ϕ and η from such inelastic collisions with the dots representing the outgoing particles. The dashed lines represent the $|\eta| = 5.2$ limit of the CMS detector (excluding CASTOR and TOTEM).

6.2.4 Diffractive Reactions

Diffractive processes are not well understood and the models and theory are still developing based on new data from accelerators such as the Tevatron and the LHC. Diffractive physics investigates the elastic and inelastic interactions that contain large rapidity gaps and where one or both protons emerge intact [82].

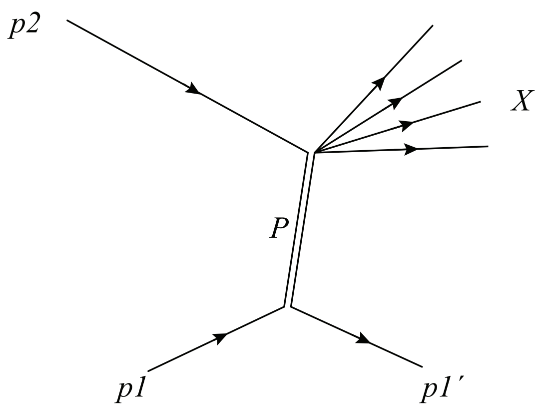

FIGURE 6.12: A Feynman diagram of *pp* SD scattering. One of the two protons dissociates, causing a cascade of colourless mesons and light baryons to emerge asymmetrically from the interaction.

The following sections briefly describe the two main types of diffractive scattering interactions. More information can be found in [80, 82, 99–101].

Single Diffractive Scattering

Single diffractive (SD) scattering involves Pomeron (or colourless glue-ball) exchange, causing one of the incident protons to be scattered while the other forms a diffractive system X, as shown in figure 6.12. The event is signified by a one-sided distribution of outgoing partons and one incident proton emerging at very high y (or η) as shown in figure 6.13 in which the distribution of particles from a single diffractive event of the type AB→AX (a) and AB→XB (b) is predicted by PYTHIA 6. At $\eta \approx \pm$ 10, there is a peak due to the 'leading proton' which has been elastically scattered but is outside the acceptance of the CMS detector.

Most SD events are within the acceptance of CMS, mostly depositing energy in the HF calorimeters. It is shown in Chapter 7 that the HF calorimeter acceptance extends as far as the invariant mass of M_x ~15.6 GeV/c^2 with an 80% detection efficiency for SD interactions.

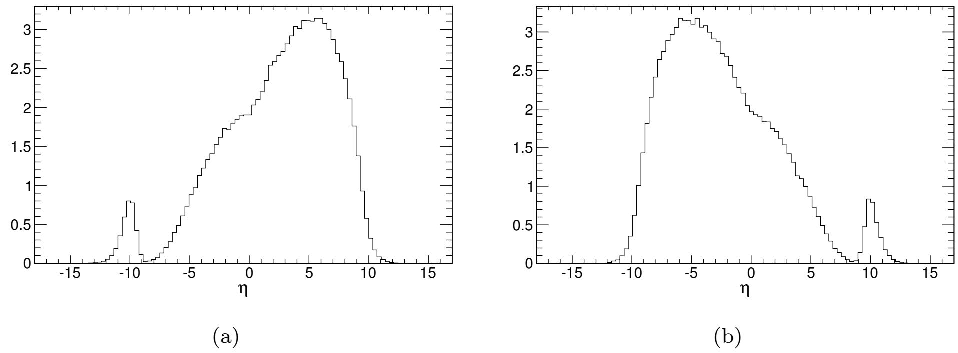

FIGURE 6.13: A sketch of the distribution of particles in η from SD events as predicted from PYTHIA 6 Monte Carlo generator. (a) AB $\rightarrow$ XB and (b) AB $\rightarrow$ AX. The peak at $\eta = \pm 10$ is from the outgoing protons and inelastic (soft) diffractive events.

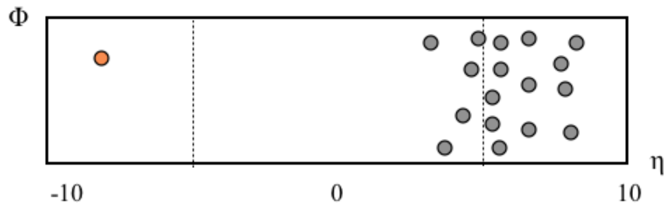

FIGURE 6.14: A sketch of the distribution of particles in η and ϕ from single diffractive (SD) collisions. One of the protons dissociates, its partons of colourless mesons and baryons (mostly pions) to emerge over a wide range of η in one direction only. The other proton proceeds in a very forward direction. The dashed lines represent $|\eta| = 5.2$, the limit of Forward Calorimeter acceptance.

Double Diffractive Scattering

Double Diffractive (DD) interactions occur when both incident protons undergo diffraction, as shown in figure 6.15. Here, the two incoming protons exchange one or more Pomerons in the t channel. The momentum transfer is large enough to cause the protons to disassociate into two forward clusters. Again, a signature *rapidity gap* can be seen in the distribution of the partons as represented in figures 6.16 and 6.17.

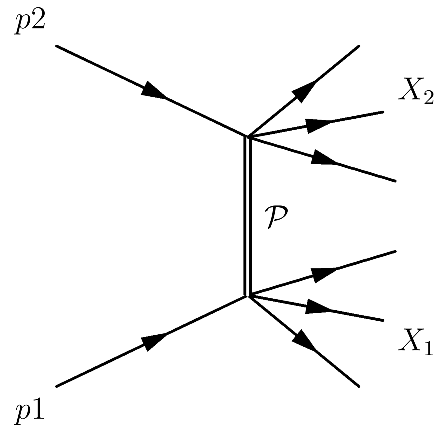

FIGURE 6.15: A Feynman diagram of pp double diffractive scattering.

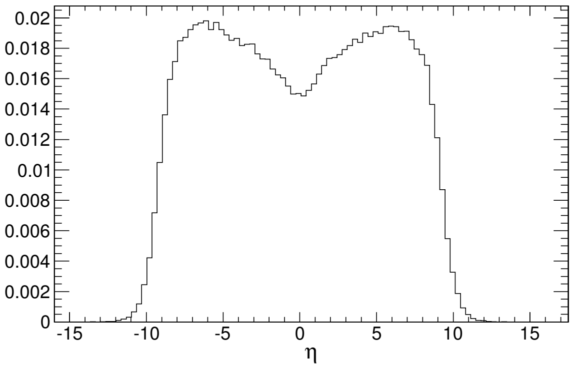

FIGURE 6.16: The distribution of particles in η from double diffractive events as predicted from PYTHIA 6 Monte Carlo generator.

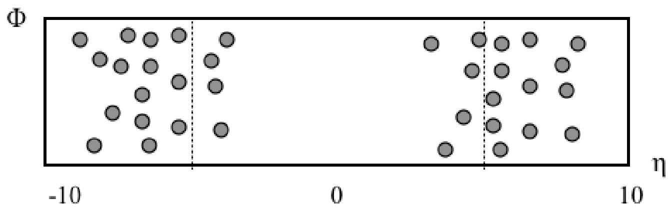

FIGURE 6.17: The distribution of particles in η and ϕ from double diffractive (DD) collisions. One of the protons dissociates, its partons rapidly hadronising causing jets of particles to emerge over a wide range of η in one direction only. The other proton proceeds in a very forward direction. The dashed lines represent $|\eta| = 5.2$, the limit of Forward Calorimeter acceptance.

Non Diffractive Scattering

Non-diffractive (ND) events, often referred to in experiments as 'minimum bias' events, are the result of parton collisions; i.e. low $|t|$ interactions between the constituant quarks and gluons. These collisions dominate the pp events at the LHC and are a major source of the backgrounds, obstructing the detection of rare physics processes. In ND scattering, the incident hadrons each acquire colour by the exchange of a quark or gluon and break apart. Though precise definitional boundaries are not clear, the distinguishing feature of ND scattering compared to diffractive scattering is the absence of a rapidity gap, as shown in figure 6.19.

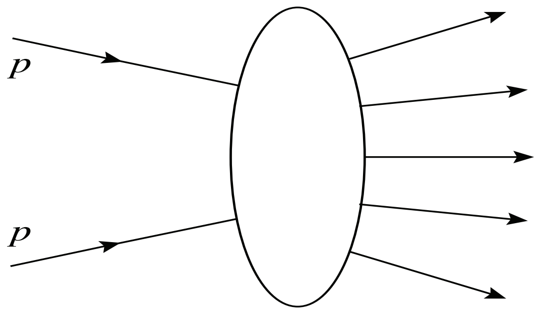

FIGURE 6.18: A Feynman diagram of pp non-diffractive scattering. The ellipse represents one of many possible interactions involving some form of colour exchange, either by gluons, quarks or both.

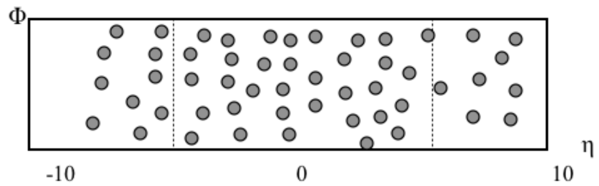

FIGURE 6.19: The distribution of particles in η and ϕ from non-diffractive collisions. The dashed lines represent $|\eta| = 5.2$, the limit of Forward Calorimeter acceptance.

Non-diffractive events account for the majority of the pp total cross-section ($\sigma_{total} \sim 111.5$ mb ± 1.2 [80], $\sigma_{ND} \sim 65$ mb) and together with some contamination from double diffractive events, are the major source for minimum bias trigger selection in the experiments.

6.3 Comparison of Monte Carlo Models

There are many Monte Carlo event generators available in high energy physics each with its strengths and weaknesses and a focus on a particular family of physics processes. For example, PHOJET [102] was not explicitly developed for Standard Model physics analysis, although it is capable of making reasonable predictions of LHC data. QGSJET [103] is tuned to very high energy cosmic ray data in an attempt to predict lower energy data from the Tevetron and the LHC. PYTHIA 6 and PYTHIA 8 [104, 105] employ a different phenomenological model from PHOJET and QGSJET. The following sections explain some of the differences between the three official models used in CMS; PYTHIA 6, PYTHIA 8 and PHOJET. These models were used in conjunction with the full GEANT4 detector simulation in the cross-section analysis of chapter 7.

6.3.1 PYTHIA 6

The model behind PYTHIA 6 aims to combine perturbative Quantum Chromo-Dynamics (pQCD) of hard scattering the phenomenological model of Regge theory for soft scattering to provide a complete description of pp collisions. The total cross section is made up of elastic and inelastic components (Refer to Eq.6.16). The Regge theory model tries to predict the total cross section σ_{tot} whilst the diffractive cross sections, σ_{SD} and σ_{DD} are predicted from pQCD. The Centrally diffractive cross section σ_{CD} is not included in the PYTHIA 6 model. The elastic cross section σ_{ND} is then calculated from $\sigma_{tot}-(\sigma_{ND}+\sigma_{SD}+\sigma_{DD})$. The total cross section of Hadron-Hadron interactions is calculated using the parameterisation developed by Donnachie and Landshoff [93] which appears as a sum of a Pomeron term and a Reggeon, or meson term;

$$\sigma_{tot}^{AB}(s) = \overbrace{X^{AB}s^{\epsilon}}^{\text{Pomeron term}} + \overbrace{Y^{AB}s^{-\eta}}^{\text{Reggeon term}} \tag{6.17}$$

where s is the centre-of-momentum energy squared ($s = E_{cm}^2$), X^{AB} and Y^{AB} are parameters which depend on the exchanged field and ϵ and η are the Pomeron and Reggeon intercepts at $\alpha(t = 0)$ respectively. The Pomeron trajectory has an intercept $\epsilon = (\alpha_P(0) - 1) \approx 0.081$ while the Reggeon trajectory intercept η is $\alpha_K(0) \approx 0.5$. It can be seen from equation 6.17 that as s increases, the Pomeron term dominates and the Reggeon term becomes negligible, resulting in the rise in the total cross section.

PYTHIA 6 includes multi-parton interactions where the number of interactions is the ratio of the hard scattering cross section, σ_{hard}, and the non-diffractive cross section.

$$N_{int} = \frac{\sigma_{\text{hard}}}{\sigma_{ND}} \tag{6.18}$$

σ_{hard} can become greater than the total cross section. N_{int} is characterised as two overlapping density distributions (the protons). These distributions are double Gaussian, the widths and relative fractions of which are tuneable parameters.
After generating the initial collision, the branching of outgoing partons is modeled by a parton shower approach in which a shower is a repetitive sequence of 1→2 branchings. For hadronic collisions, these might be $q \to qg$, $q \to q\bar{q}$ or $g \to gg$, where q and g represent quarks and gluons respectively. The branching probabilities are given by the DGLAP equations. Energy and momentum are conserved at each branching step. The diffractive cross sections are described by a model by Schuler and Sjöstrand[106].
The elastic cross section σ_{el} is approximated by a simple exponential, as long as the momentum transfer $|t|$, is not too large. The optical theorem gives:

$$\sigma_{el} = \frac{\sigma_{tot}^2}{16\pi B_{el}} \tag{6.19}$$

with $B_{el} = 2b_A + 2b_B + 4 \cdot s^{0.0808} - 4.2$ and $bA = b_B = 2.3$ for protons.[104].
Hadronisation, the mechanism by which quarks remain colour confined by the creation of, and binding with other quarks to produce colourless mesons and light hadrons, is done using the *Lund* model[107]. It describes the evolution of initial state scattered partons to final state hadrons by String Fragmentation in which new $q\bar{q}$ pairs are created from the vacuum as a result of the increasing energy stored in the colour field between the original quarks as the distance between them increases.
Full details of the PYTHIA 6 physics generator can be found in [104]

6.3.2 PYTHIA 8

PYTHIA 8 is a C++ version of the Fortran based PYTHIA 6 and as such, shares many common features. It is the preferred generator for LHC studies. PYTHIA 8 has been developed with a focus on pp and $p\bar{p}$ collisions as well as $l\bar{l}$ annihilation. It includes multi-parton interactions which are important for predicting the total cross section. Hadronisation is again based solely on the *Lund* string fragmentation model.

Diffractive hadron-hadron interactions are modeled as in PYTHIA 6 (Pomeron and Reggeon model) but with additional Pomeron flux parameterisations beyond the Schuler and Sjöstrand model, namely *Bruni and Ingelman*[108], *Berger et. al.*[109] and *Donnachie and Landshoff* [85]. Some useful information on PYTHIA 8 can be found in [110].

6.3.3 PHOJET

PHOJET uses the Dual Parton Model (DPM) which provides a full phenomenological description of soft processes. Soft processes, in which the strong coupling constant α_s is large, cannot be analysed using perturbative methods. DPM is a non-perturbative approach to modeling strong interactions consisting of performing a topological expansion of the interaction (forming cyclinders, toroids, spheres etc) and applying unitarity considerations¶ and Regge field theory. More complicated topologies become important at higher energies but in each case, the topology represents the partonic nature of the interaction from which the momentum distributions of valance and sea quarks can be inferred. Detailed information can be found in [111]. PHOJET is a two component model with smooth transition between soft and hard interactions. The results from the DPM methodology have been confirmed at the ISR $p\bar{p}$ experiment, UA4 [44] and in heavy ion collisions at RHIC. The phenomenological model underpinning PHOJET suppresses the triple-Pomeron exchange at higher energies, which was the largest contributor to the differences in cross section and rapidity distributions seen between PHOJET and PYTHIA 6. Through the inclusion of the additional Pomeron flux parameterisations in PYTHIA 8, these differences have be reduced, making PYTHIA 8 results closer to those of PHOJET. However, PHOJET includes central diffractive (CD) events which PYTHIA 8 does not. Although the cross section σ_{CD} is small, it is not negligible and the PYTHIA authors plan to include the mechanism in subsequent versions. Figure 6.20 shows the inelastic cross section evolutions with $\sqrt{s}$ predicted from each model and demostrates the increasing diversions of the models at higher energies. The measurement from CDF [112] and the measurements of E710 [113] and E811 were expected to help in determining the correct model of pp interactions at higher energies. However, the σ_{total} measurements disagreed by

¶Unitarity states that the total probability of an interaction cannot exceed 1

2.6σ with CDF preferring a $\ln^2(s)$ fit, while E710 and E811 results preferred a $\ln(s)$ fit [97], leading to an increase in the uncertainty for higher energy extrapolations.

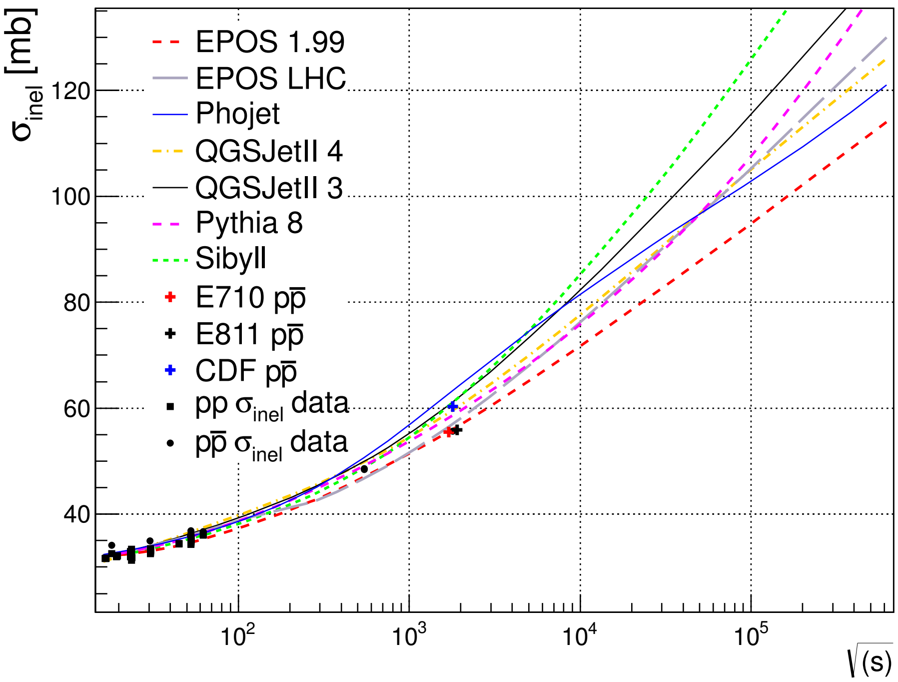

FIGURE 6.20: Predictions of σ_{inel} for increasing collision energy from several MC models including those used in the σ_{inel} measurement of chapter 7.

Figure 6.21 shows the η distribution and the number of particles per event from each Monte Carlo generator used in the cross-section analysis. For the η distribution of non-diffractive events, all generators are in good agreement. This is to be expected as ND events are the most abundant and have been extensively studied in experiments. The models differ in their topology of SD events, with some models, such as PHOJET showing a tendancy towards the central regions (-3$\lesssim \eta \lesssim$3), while others such as EPOS LHC and QGSJETII 4 produce stable outgoing particle trajectories towards the more forward regions, beyond $|\eta| \approx$5. EPOS LHC in particular, has been tuned to LHC data, resulting in a modification of the mass distribution parameter which, in turn, produces lower mass, higher momentum (more forward going) particles [114]. These features play a role in the extrapolation to σ_{inel} in the following chapter.

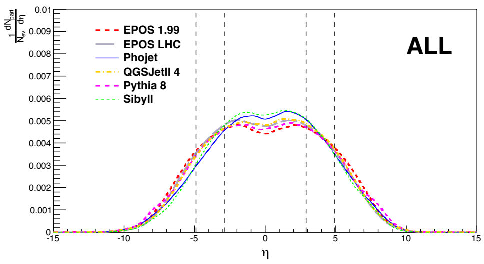

(a) $\frac{dN}{d\eta}$ All Events

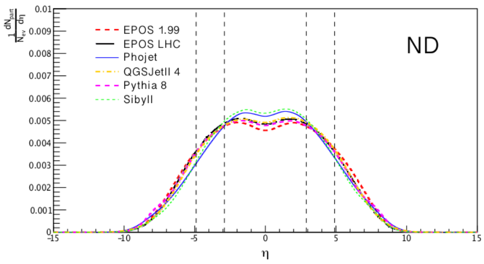

(b) $\frac{dN}{d\eta}$ ND Events

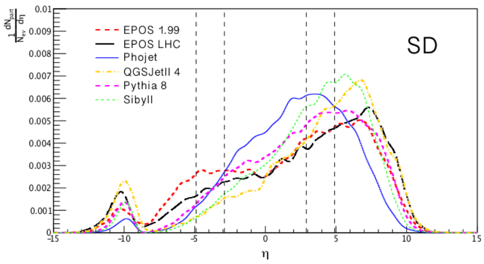

(c) $\frac{dN}{d\eta}$ SD Events

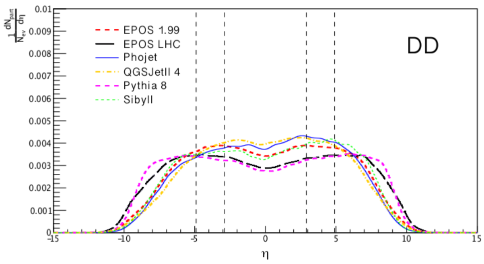

(d) $\frac{dN}{d\eta}$ DD Events

FIGURE 6.21: The particle distributions for All, Non-Diffractive (ND), Single Diffractive (SD) and Double Diffractive (DD) events as predicted by the six MC generators used in the inelastic cross-section measurement.

Chapter 7

Measurement of the Inelastic Cross-section at $\sqrt{s} = 7$ TeV

The BSC was used as a highly efficient minimum bias trigger during the low-pileup phase of LHC operations and as an online luminosity monitor during low intensity *pp* and 2010 H.I running. Knowledge of luminosity and event rates goes some way to determining the proton-proton total cross-section. Unfortunately, despite its high channel-by-channel efficiency, the acceptance efficiency of the BSC was too low to be used in a cross-section measurement. Additionally, only the inelastic processes can be 'seen' by the CMS forward detectors, such as the Hadron Forward (HF) calorimeters. Therefore, data from the HF calorimeters were used in the measurement of the inelastic cross-section at $\sqrt{s} = 7$ TeV. This chapter comes from the CMS Physics Analysis Summary (PAS), authored in collaboration with Gabor Veres, Jeremy Gartner, Anna Zsigmond and Albert de Roeck and approved in February 2012 (QCD-11-002).

Introduction

The cross sections of hadronic collisions are important fundamental quantities in high energy particle, nuclear and cosmic-rays physics and have been studied in the last 40 years in experiments covering many orders of magnitude in center-of-mass energies [95, 115–117]. It is surprising that the underlying mechanisms of *pp* and

$p\bar{p}$ interations at high energy and low momentum transfer are not well understood, leading to the inability to calculate the pp (and $p\bar{p}$) total inelastic cross section from perturbative calculations of quantum chromodynamics (QCD).
Various phenomenological approaches based on unitarity and analyticity [99] exist that describe the experimental results. Even though the phenomenological description of the lower center-of-mass energy cross section data is quite precise, there are large uncertainties on the extrapolation to higher (LHC) energies. The present measurement is an input to these phenomenological models and provides crucial information for the fine tuning of hadronic Monte Carlo generators [102, 104, 105, 118]. The cross section values are also used in luminosity estimates at accelerators [119], they are relevant for high energy cosmic ray physics [120], and play an important role in the characterisation of collision centrality of heavy ion collisions (e.g. in the Glauber model [121]).

This chapter presents the measurement of the inelastic proton-proton cross section at $\sqrt{s} = 7$ TeV with the CMS detector at the LHC. The data were collected in early 2010 during the commissioning phase of the LHC operation with 3.5 TeV colliding beams, with an integrated luminosity of 2.76 μb^{-1}. The analysis uses the Hadron Forward Calorimeters (HF) which are sensitive to most of the inelastic cross section except for the fraction coming from diffractive processes where the dissociated systems have a small invariant mass, M_X (See chapter 6). The HF acceptance cut was chosen to match the acceptance cut used in a recent publication by the ATLAS Collaboration [122] and corresponds approximately to values of the fractional momentum loss of the scattered proton of $\xi \equiv M_X^2/s > 5 \times 10^{-6}$, equivalent to $M_X > 16$ GeV/c^2. Thus the measurement presented here focuses on this restricted kinematic range. In order to compare the results with measurements at lower energies, the inelastic cross section is extrapolated from the above restricted ξ range to the full ξ range ($\xi > M_p^2/s$).

7.1 Experimental apparatus

The Compact Muon Solenoid has been described in detail in Chapter 2. One can refer to the sections on the Hadronic Forward Calorimeter and the Pixel Tracker for information on the sub-detectors pertaining to this analysis.

7.2 Method

In order to measure the inelastic cross-section in CMS, the HF calorimeters were used to count the number of inelastic events N_{inel} in which a collision was detected over a given amount of luminosity, $\mathcal{L}$. A simplified form of the calculation is given in equation Eq. 7.1.

$$\sigma_{inel} = \frac{N_{inel}}{\mathcal{L}} \tag{7.1}$$

However, one must also account for the efficiency of the detector which is not capable of detecting all collisions, especially those which deposit small amounts of energy or are outside the geometrical acceptance of the detector. To obtain an estimate of these losses, one must use Monte Carlo simulations of the detector response to estimate the fraction of events counted, compared to the total number that occurred. The HF calorimeter is able to resolve energy deposits down to approximately 4 GeV. Below this level, the inherent detector noise interferes with the measurement. The detector efficiency for detecting inelastic events is denoted ε_{inel} and is calculated from Monte Carlo with full detector simulation as the ratio of the number of events over a given energy cut and the total number of events. In this analysis, two energy cuts of 4 GeV and 5 GeV were used to test the stability of the measurement in terms of HF energy mis-calibration between runs. In this chapter, the 5 GeV threshold is referred to as the 'energy cut'. More details of the ε_{inel} correction factor are given in section 7.4.1.

One must also account for the possibility that some small fraction of the events in N_{inel} actually contained more than one pp collision*, but were only counted once. A correction factor, F_{pileup} must therefore also be applied to Eq. 7.1.

These efficiency and counting corrections modify Eq. 7.1 into the form of Eq. 7.2.

$$\sigma_{inel} = \frac{N_{inel} F_{pileup}}{\varepsilon_{inel} \mathcal{L}} \tag{7.2}$$

The ε_{inel} correction factor can only be derived from Monte Carlo simulations combined with full detector simulations (provided by GEANT 4). There are many Monte Carlo generators available with different underlying phenomenology and

*Multiple, simultaneous *pp* collisions are known as *pile-up*

parameters. Consequently, no two Monte Carlo simulators will give identical results, especially in the forward ($|\eta|$ >3) region where diffractive scattering events occur.
To minimize the dependence of the measurement on any one Monte Carlo model, a kinematic region can be chosen in which all the models practically agree. In this analysis, a kinematic cut of $\xi > 5 \times 10^{-6}$ has been chosen, where $\xi \equiv M_x^2/s$. M_x^2 is the invariant mass of the outgoing system of particles and s is the square of the collision energy. The calculation for the (approximately) model independent measurement of the cross-section is given by Eq. 7.3.

$$\sigma_{(\xi>5\times10^{-6})} = \frac{N_{inel}F_{pileup}}{\varepsilon_{(\xi>5\times10^{-6})}\mathcal{L}} \tag{7.3}$$

One further correction factor, which will be explained in section 7.4.3, aims to account for the fraction of events detected by the HF calorimeter but were actually below the ξ cut. This factor, $f_{(\xi<5\times10^{-6})}$, as will be shown, is typically of the order of 1 - 2%.

7.3 Event Selection

To reduce the probability of multiple, simultaneous *pp* collisions, or pile-up, within an event, runs with low bunch intensities were chosen for the analysis. The runs had an average pile-up, λ, of between 0.07 and 0.12. These values were obtained from a script written by the CMS Luminosity Group but were measured again from the data in order to correct for the small, but non-negligible probability that more that one collision did occur. This is explained in detail in section 7.4.5. Table 7.1 lists the runs used in this analysis.

The luminosity values for these runs were obtained on the basis of Van der Meer scans. The luminosity measurements carried a 4% normalisation uncertainty [70], which dominates the uncertainties in the present analysis.
The data for each run contains a vast amount of information, not just records of collision events. Events can be divided into three categories. In the first case, the data contains detector read-out information recorded during *potential* collisions, in which the two LHC beams crossed the interaction point simultaneously. This

TABLE 7.1: A list of the run numbers used in this analysis and their effective luminosities.

Run No.	Effective $\mathcal{L}$
132599	228.9 mb^{-1}
132601	501.0 mb^{-1}
132602	27.4 mb^{-1}
132716	151.3 mb^{-1}
133874	223.3 mb^{-1}
133877	323.8 mb^{-1}
135175	724.7 mb^{-1}
135575	751.4 mb^{-1}
137027	26.9 mb^{-1}

data was selected by the use of the BPTX $+Z$ and $-Z$ *Coincidence* trigger. The second case involves detector read-out information recorded when only one beam was passing through CMS. This data was selected using a trigger composed of an exclusive-OR combination from the BPTX $+Z$ and $-Z$ beam pick-ups, which fired only when B1 or B2 was present, but not both. The trigger is referred to as the 'Single Bunch' trigger. This data is useful for analysing the beam induced background signal in the HF detector. The third case involves the periods in which no beam is passing through CMS. The Level 1 trigger menu includes a *Random* trigger which pseudo-randomly selects bunch crossings which do not fall within the first two categories. The data selected by this trigger allows the detector noise to be analysed and statistically removed from the data pertaining to true events. The three triggers were pre-scaled. i.e. Only data from a well-defined fraction of all events were recorded. These pre-scale values must be accounted for when comparing data from the three triggers.

7.4 Measurement of the Cross-Section

The method of counting inelastic events in the HF calorimeters involved searching the data, event-by-event, for those in which an energy deposit above the energy threshold occurred. The HF data is read out in a 'bundle' called a *recHit*. These recHit contain the energy information as well as course position information in terms of η and ϕ. The entire data from each of the chosen runs were processed using each of the three aforementioned triggers. Only events which passed the energy cut were counted. Table 7.2 shows the number of events counted using each of the three triggers. The number of triggers demonstrates the differences in trigger pre-scaling.

Table 7.2: The number of events in the data (all runs) selected with each of the three triggers described.

Trigger	No. of Triggers	4 GeV	5 GeV
Coincidence	9244011	239782	191654
Single Bunch	1097292	8883	3291
Random	27759	254	89

To account for the pre-scaling, the number of counted events from the Single Bunch and Random triggers were scaled to the number of Coincidence triggers. Table 7.3 shows these normalised number of events for each trigger.

The events that pass the Single Bunch or Random triggers as well as the HF energy threshold, have their origin in beam background and detector noise respectively. There may also be beam background and noise present in the data collected using the Coincidence trigger. There are two beams present in the Coincidence triggered data and only one beam present in the Single Bunch triggered data. Assuming both beams to be equal, one would need to double the beam background contribution found in the Single Bunch triggered sample to estimate the beam background noise that is merged with the collision data in the Coincidence sample. Table 7.3 shows that the number of normalised events from the Random trigger, which selects detector noise, is approximately equal to the number of events from the Single Bunch trigger, suggesting that the majority of background contamination in the Coincidence triggered sample originates from detector noise, rather than from beam related effects. To test this hypothesis, the activity in the inner tracker,

Table 7.3: The number of events in the data (all runs) selected with each of the three triggers described. The Single Bunch and Random values have been normalised to the number of Coincidence triggers. Statistical uncertainties ($\sqrt{N}$) are shown.

Trigger	No. of Triggers	4 GeV	5 GeV
Coincidence	9244011	239782±490	191654±438
Single Bunch	9244011	74834 ±794	27725±483
Random	9244011	84584 ±5307	29638±3141

during events selected with the Single Bunch trigger, was inspected. Any beam background travelling approximately parallel to the beam pipe would leave long tracks in the inner tracker. As none were found, it was concluded that the vast majority of the contribution to the background events was due to detector noise in the HF detector, which is expected to be constant, irrespective of beam presence. Therefore, beam gas contributions were neglected and all events selected by the Single Bunch trigger were treated as being due to detector noise, thus providing a larger 'detector noise' dataset as well as eliminating the need to double their contribution.

The HF towers were studied individually to ensure that they all detected events at rates similar to the nearest neighbouring towers and that no one tower was over or under represented due to poorly calibrated pedestal levels. A few specific towers were found in which the number of reconstructed recHit over the energy threshold were much larger than the global average, even without beam presence. Further investigations with the HF group resulted in the conclusion that the pedestal settings for several towers had drifted and the worst towers should be excluded from the event counting [123]. The number of events was counted with the noisy towers included and excluded. The exclusion caused a 0.4% difference in the result, which is included in the final systematic uncertainty.

7.4.1 HF Detector Efficiency

The HF calorimeters cover a pseudo-rapidity range of 2.9< $|\eta|$ <5.2 and have a minimum energy threshold of 4 GeV. Due to these limitations, not all inelastic events can be detected. In particular, many low mass ($M_x \approx M_{\text{proton}}$) events will pass through the HF calorimeter at $|\eta|$ >5.2. In addition, there was some doubt about the calibration and performance of the inner most η ring of the detector during the early operations when the data for this analysis was recorded. Therefore, only the rings covering the η range of 2.9< $|\eta|$ <4.9 were used. To get an estimate of the efficiency of detecting inelastic events, Monte Carlo models were used in conjunction with the full CMS detector simulation. The detector simulation is provided by GEANT 4 and contains an accurate geometry and tuned readout simulation of the entire CMS detector. At the time of this analysis, the Monte Carlo generators of PYTHIA 6, PYTHIA 8 and PHOJET were officially integrated with the CMS full simulation. Figure 7.1 shows the M_x distributions from the three models. The left hand figures show the generated distributions (white) with the distributions of events detected in the HF calorimeters which are over 4 GeV (light blue patterned area) and 5 GeV (plain red shaded area). The region corresponding the ξ cut is shown as the dark shaded area and excludes the regions in the models which disagree the most. The right hand figures show the efficiencies of each energy cut along the ξ distribution.

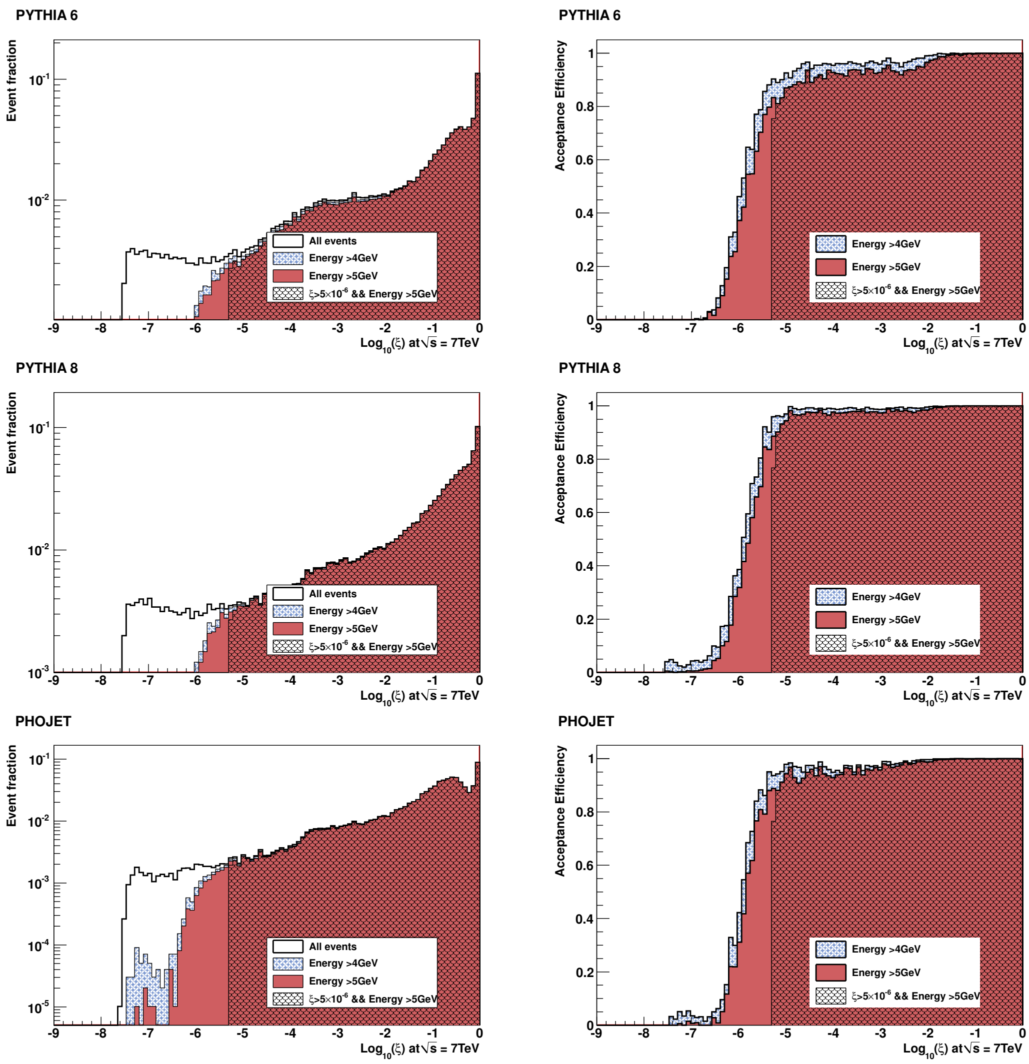

FIGURE 7.1: Left: Generated ξ distributions for inelastic events according to PYTHIA 6 (top), PYTHIA 8 (center), PHOJET (bottom), normalised to unity over the full ξ range. Events that fulfil the 4 and 5 GeV energy requirements in the HF calorimeters, using the CMS detector simulation, are represented by the coloured histograms. Right: Efficiency of the event selection, for the two thresholds of the energy deposited in the HF calorimeters. The ξ threshold at 5×10^{-6} is also shown.

Table 7.4 lists the HF detector efficiencies of detecting inelastic events, estimated from each of the three Monte Carlo simulations.

TABLE 7.4: The ε_{inel} efficiency values estimated from the three full simulation models.

Energy cut	PYTHIA 6	PYTHIA 8	PHOJET
E>4 GeV	94.0%	94.2%	97.3%
E>5 GeV	93.8%	94.1%	97.2%

7.4.2 Detection Efficiency over the ξ cut

Table 7.4 demonstrates the differences of ε_{inel} between the three models. To reduce the dependency of the result on the variation in the models, the analysis focuses on the region in which they mostly agree. Referring to figure 7.1, a cut on $\log_{10}(\xi)$ needed to be chosen. In their analysis of the inelastic cross-section, the ATLAS collaboration had selected a ξ cut of $5{\times}10^{-6}$ ($M_x > 15.6$ GeV), so the same cut was used in this analysis to give a directly comparable result.
The calculation of the efficiency of detecting events over the ξ cut follows the same principle as the ε_{inel} estimation. The difference is that now, only the number of events over the HF energy cut and with a $\xi > 5 \times 10^{-6}$ are counted and divided by the total number of generated events above the ξ cut. Table 7.5 lists the efficiencies, ε_{ξ}, for the restricted kinematic range using the PYTHIA 6, PYTHIA 8 and PHOJET models.

TABLE 7.5: The ε_{ξ} efficiency values estimated from the three full simulation models.

Energy cut	PYTHIA 6	PYTHIA 8	PHOJET
E>4 GeV	98.7%	99.7%	99.4%
E>5 GeV	97.5%	99.3%	99.1%

One can see that the differences in detection efficiency have been reduced, compared to those in table 7.4. These efficiencies are used to calculate $\sigma_{\xi>5\times10^{-6}}$.

7.4.3 'Contamination' Factor correction

Referring to the distributions of figure 7.1, one can see that the HF calorimeters are capable of detecting events down to $\log_{10}(\xi) \approx -6$. This corresponds to an ξ

value of approximately $\xi \approx 1 \times 10^{-6}$, which is below the imposed ξ cut. The very small fraction of these 'contamination' events need to be removed from N_{inel} to further reduce the model dependency of the result. ξ is purely a Monte Carlo based cut and cannot be implemented experimentally. The fraction of 'contamination' events within the HF acceptance can be estimated from the ratio,

$$f_{(\xi<5\times10^{-6})} = \frac{N^{HF}_{(\xi<5\times10^{-6})}}{N^{HF}} \tag{7.4}$$

where N^{HF} is the number of simulated events passing the HF energy cut and are therefore within the HF acceptance. Table 7.6 lists the f_ξ contamination correction factors from each full simulation model.

Table 7.6: The 'contamination' factors f_ξ obtained from the three full simulation models.

Generator	f_ξ	
Energy Threshold	4 GeV	5 GeV
PYTHIA 6	0.0234	0.0200
PYTHIA 8	0.0256	0.0205
PHOJET	0.0143	0.0118

To remove these events from N_{inel}, one must multiply by a factor $(1 - f_\xi)$. The final modification to Eq. 7.3 gives,

$$\sigma_{(\xi>5\times10^{-6})} = \frac{N_{inel}(1 - f_\xi)F_{pileup}}{\varepsilon_{(\xi>5\times10^{-6})}\mathcal{L}} \tag{7.5}$$

The methods of removing background events from N_{inel} and accounting for the pile-up of two or more simultaneous events with $F_{\text{pile up}}$ are described in the following sections.

7.4.4 Background Subtraction

As mentioned previously, a fraction of the events counted as collisions may actually be due to detector noise. To first approximation, the number of inelastic collisions can be obtained by subtracting the number of events selected by the Single Bunch trigger, from the number selected by the Coincidence trigger.

$$N_{inel} \approx N_{\text{coinc.}} - N_{\text{single bunch}} \tag{7.6}$$

However, events containing both detector noise and collision signals should not be subtracted. To take account of this, an estimate of the rate of these overlapping events must be made. The probability that an event contains both noise and collisions can be estimated from the ratio,

$$\mathcal{P}_{noise} = \frac{N_{\text{single bunch}}}{T_{\text{single bunch}}} \tag{7.7}$$

where $N_{\text{single bunch}}$ and $T_{\text{single bunch}}$ are the number of Single Bunch selected noise events over threshold and the number of Single Bunch triggers respectively. The estimate of the number of true collision events which were over-subtracted in Eq. 7.6 is the probability of noise ($\mathcal{P}$) multiplied by the raw number of collision events N'_{inel}, i.e before background subtraction. The equation for correcting the over-subtraction is,

$$N_{inel} = \frac{N'_{inel} - N_{\text{single bunch}}}{1 - N_{\text{single bunch}}/T_{\text{single bunch}}} \tag{7.8}$$

7.4.5 Pile-up correction

As previously mentioned, even in *pp* runs with low beam intensities, there is a possibility that the HF calorimeters time resolving limitations would lead to missed events which happened simultaneously within the same bunch crossing. The low intensity runs were chosen to minimise such events as much as possible. Since the number of particles per bunch is approximately uniform and the interactions are uncorrelated, it follows that the number of collisions per bunch follows a Poisson distribution. Due to the long tails of the Poisson distribution, the number of simultaneously interacting events ($\geq$ 2) cannot be neglected. This is shown in figure 7.2. The calculation of a Poisson distribution (Eq. 7.9) with a mean 'pile up' value of 0.12 shows that whilst most events contained no collisions at all, and approximately 11% of events had a solitary collision, there is a small (0.6%) probability of an event containing two collisions. The probability of 3 or more collisions rapidly falls away.

$$P(i, \lambda) = \frac{\lambda^i e^{-\lambda}}{i!} \tag{7.9}$$

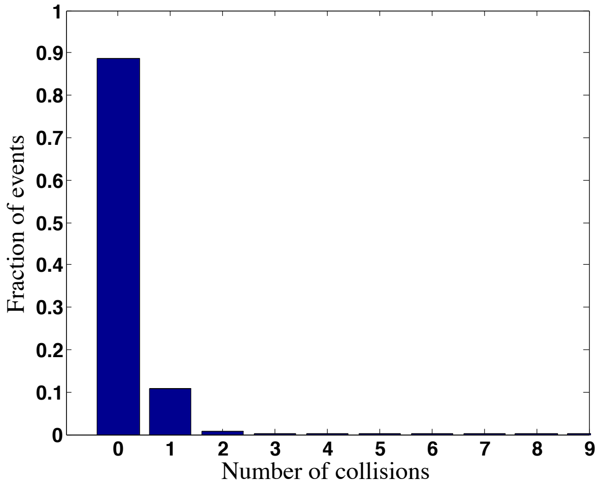

FIGURE 7.2: A calculation of the Poisson distribution of the number of events for an average 'pile-up' estimate of 0.12 shows that there is a non-negligible number of events with two or more collisions. The F_{pileup} factor corrects for these missed events.

The CMS Luminosity Group provided a script which could estimate the average number of events per bunch crossing over the entire run. However, a more accurate estimate of the pile up can be calculated from the data by,

$$\lambda = \frac{N_{inel}}{\varepsilon_{inel} T_{\text{Coincidence}}} \times F_{\text{pile up}} \tag{7.10}$$

where $F_{\text{pile up}}$ is a correction factor which accounts for the missed, simultaneous events. $F_{\text{pile up}}$ relies on the average pile up, λ and the corrected λ relies on $F_{\text{pile up}}$. Therefore, an iterative calculation is required. Taking into account the detector efficiency, $F_{\text{pile up}}$ can be calculated by,

$$F_{\text{pile up}} = \frac{\Sigma_{i=1}^{\infty} iP(i,\lambda)}{\Sigma_{i=1}^{\infty}(1-(1-\varepsilon_{inel})^i)P(i,\lambda)} \cdot \varepsilon_{inel} \tag{7.11}$$

$$= \frac{\varepsilon_{inel}\lambda}{\Sigma_{i=1}^{\infty}(1-(1-\varepsilon_{inel})^i)P(i,\lambda)} \tag{7.12}$$

$$= 1 + \frac{1}{2}\lambda\varepsilon_{inel} + \frac{1}{12}\lambda^2\varepsilon_{inel}^2 + \mathcal{O}(\lambda^3) \tag{7.13}$$

where the numerator sums over the probabilities of i events occurring. The expectation value λ replaces $iP(i,\lambda)$ (see Appendix B). ε_{inel} appears to keep the definition of λ consistent (Eq. 7.10). The denominator accounts for the detector efficiency of detecting those events. Substituting Eq. 7.13 into Eq. 7.10, one obtains,

$$\lambda = \frac{N_{inel}}{\varepsilon_{inel}T_{\text{Coincidence}}}F_{\text{pile up}} = \left(1 + \frac{N_{inel}}{2T} + \frac{N_{inel}^2}{3T^2}\right) + \mathcal{O}\left((N_{inel}/T)^4\right) \tag{7.14}$$

where $T_{coincidence}$ is written as T on the right hand side, for brevity. Inserting the estimated pile up factor provided from the Luminosity group for each run, and taking N_{inel} and T from data and ε_{inel} from the Monte Carlo models, equation Eq. 7.14 produces a new value of λ which, in turn is inserted back in to $F_{\text{pile up}}$. The equation quickly converges to a stable λ value after 2 - 3 iterations. Table 7.7 shows the pile up estimates from the luminosity group compared with the measurement of the pile up as described. Finally, a value of $F_{\text{pile up}}$ for each run is shown. ε_{inel} was taken from the Pythia 6 D6T tune with the 5 GeV energy cut.

The estimated and measured pile up values agree to within 2% for most runs. The estimate for run 137027 was much higher than the measured value. Further investigation suggested an error in the processing of this run by the luminosity group.

TABLE 7.7: Pile up estimates from the luminosity group and from the method described in the text. Also shown is the $F_{\text{pile up}}$ value obtained from Eq. 7.14

Run No.	Pile up est	Measured Pile up	Correction Factor $F_{\text{pile up}}$
132599	0.89%	0.82±0.006%	1.0039
132601	0.74%	0.68±0.005%	1.0032
132602	0.67%	0.64±0.004%	1.0030
132716	0.71%	0.65±0.004%	1.0031
133874	4.02%	3.55±0.02%	1.0168
133877	2.24%	1.84±0.01%	1.0087
135175	11.9%	10.6±0.07%	1.0510
135575	10.2%	8.93±0.06%	1.0429
137027	8.26%	4.94±0.03%	1.0235

7.4.6 Comparing full simulation and generator level efficiencies

In the CMSSW framework, the simulated events are available at particle level and at detector reconstruction. The detection efficiency can be defined at both levels as the ratio of number of *detected* inelastic events above the ξ cut, and the number of generated inelastic events above the ξ cut. The difference is in the definition of the declaration of an event as being *detected*. At the reconstruction level, as described previously, an event is 'detected' if there is a reconstructed hit (recHit) in the HF calorimeter simulation data, with energy greater than the energy cut. At the generated particle level, an event is declared detected if there is a stable particle in the HF acceptance, 2.9< $|\eta|$ <4.9 with energy greater than the energy cut.

Table 7.8 shows the calculated efficiencies with the two different definitions from the three fully integrated (i.e. generator through to full detector simulation) Monte Carlo models. The differences between the two methods are quite small ($\leq$2%) This justifies the use of the generator level efficiencies in the extrapolation to the total inelastic *pp* cross section. The motivation is that, at generator level, even models which are not fully integrated in to the CMS full simulation could be included in the extrapolation.

TABLE 7.8: Comparing the inelastic detection efficiencies (ξ >5×10^{-6}) defined at generated particle level and detector reconstruction level.

Single-arm	3 GeV		4 GeV		5 GeV	
Generator	full sim.	generator	full sim.	generator	full sim.	generator
PYTHIA 6	99.4%	99.8%	98.7%	99.7%	97.5%	99.5%
PYTHIA 8	99.9%	99.9%	99.7%	99.9%	99.3%	99.9%
PHOJET	99.7%	99.8%	99.4%	99.7%	99.1%	99.7%

7.4.7 Luminosity

The value of the total recorded luminosity is provided by the CMS Luminosity Group via their offline method. In early 2010, when the data used in this analysis was taken, many runs were proceeded by VdM scans which provided an accurate, direct luminosity value at the beginning of each run to which the HF luminosity measurement could be calibrated to. The integrated luminosity used in the analysis was $\mathcal{L}$ = 2.76 μb^{-1}± 4%.

7.5 Results

The results for the inelastic cross-section with the applied ξ cut of $\xi > 5 \times 10^{-6}$ are presented here based on the 5 GeV energy cut. The calculations were made separately for groups of runs based on their pile-up. i.e. runs with similar measured pile up values were processed as a larger, single run. To demonstrate the stability of the result in terms of HF energy mis-calibration, table 7.9 lists $\sigma_{\xi>5\times10^{-6}}$ for both the 4 GeV and 5 GeV energy cuts from the largest dataset, run number 135575 ($\mathcal{L}$ = 751.4 mb^{-1}). The results are given separately for each of the ε_ξ values obtained from PYTHIA6, PYTHIA8 and PHOJET.

TABLE 7.9: The results of the reduced model dependent $\sigma_{(\xi>5\times10^{-6})}$ calculation for each full simulation model and for the two energy cuts. The example shown here is of data from the $\mathcal{L}$ = 751.4 mb^{-1} run 135575.

Model	4 GeV	5 GeV
PYTHIA 6	60.3 ±0.4	60.8±0.3
PYTHIA 8	59.5 ±0.4	59.6±0.3
PHOJET	60.4 ±0.4	60.3±0.3

The result for each run (or collection of runs with similar pile up values) was calculated as the average of the results from the three models. In the case of the example run in table 7.9, $\sigma_{(\xi>5\times10^{-6})} = 60.2$ mb^{-1}.
Averaging over the cross-section results (with the 5 GeV cut) of all the runs listed in table 7.1, one obtains a final result for the $\sigma_{(\xi>5\times10^{-6})}$ cross-section. The result includes the 4% uncertainty of the luminosity and statistical and systematic uncertainties, which are explained in section 7.7.

$$\sigma_{(\xi>5\times10^{-6})} = 60.2\text{mb} \pm 0.2\text{mb(stat.)} \pm 1.1\text{mb(syst.)} \pm 2.4\text{mb(lumi)}$$

7.6 Extrapolation to σ_{inel}

The measurement of the inelastic cross-section within the ξ cut was an important step and provided a measurement which could be directly compared with the result from ATLAS [122] (60.3 mb ±0.5 (stat.) ± 0.5 (syst.)) However, σ_{inel} is the important physical quantity one wishes to derive. To achieve this, Monte Carlo models must again be employed to extrapolate over the invisible region where the CMS detector was unable to measure†.
Additional Monte Carlo models were used for the extrapolation from the restricted ξ range to the total inelastic cross section. As the models were not able to be combined with the full CMS detector simulation, the extrapolation was made by using the models at the generator level to determine their ξ distribution and acceptance. This has already been shown in table 7.8 to be an acceptable compromise as the differences between the full simulation and generator level efficiencies were within 2%.
Six additional models were considered: PYTHIA 8 [105], PHOJET [102], SIBYLL 2.1 [124], EPOS 1.99, EPOS LHC [125], and QGSJET-II 4 [103, 126]. The models use various phenomenology and tunings for the hard parton-parton and for the diffractive scattering cross sections [127], and can be considered to be aimed at modelling either collider physics processes (PYTHIA, PHOJET) or high-energy cosmic ray interactions (SIBYLL, QGSJETII). EPOS claims to be capable of modelling

†The TOTEM and CASTOR detectors are located at higher η than the HF. However, acquiring their data in the CMS framework was not possible.

both scenarios.

The diffractive mass distribution in EPOS 1.99 was known to be too large. This has been corrected in EPOS LHC [114]. QGSJET-II 4 has been shown to predict the data from TOTEM quite closely[128]. PYTHIA 8 is one of the recommended generators for LHC physics. The other generators have not been tuned to data at LHC energies but have been included in order to provide a broad sample of varying models. Figure 7.3 shows the predictions of the visible cross section from the six Monte Carlo generators employed in this analysis. Also shown are the measurement results and model predictions of those results, from the CMS paper FWD-11-001 [119], in which the inner tracker ($|\eta|$ <2.4) was used to count tracks with p_T >200 MeV/c, shown as the red squares.

The predicted results of this analysis are shown as the left-most points (upper plot) and were calculated by counting generated events over the ξ and energy cuts. The same correction factors as used in reaching the measured $\sigma_{\xi>5\times10^{-6}}$ result were calculated from each of the generators and applied in the same way. The remaining points are taken from FWD-11-001. The lower plot shows each Monte Carlo predicted value normalized to the relative measurement value. As clearly shown, EPOS LHC (blue crosses) gives the closest predictions to the CMS data. For this reason, EPOS LHC has been chosen as the primary model in this analysis.

In section 7.4, a ξ cut was applied to the data to reduce the effects of the variations seen between the Monte Carlo models. The equation used for calculating the ξ value was:

$$\xi = \frac{M_x^2}{s} \tag{7.15}$$

where,

$$M_x^2 = \left((\Sigma E)^2 - ((\Sigma p_x)^2) + (\Sigma p_y)^2) + (\Sigma p_z)^2)\right) \tag{7.16}$$

In the alternative CMS measurement of the pp inelastic cross-section (FWD-11-001), the calculation of ξ was made by equation 7.17.

$$\xi = \frac{(\Sigma E + \Sigma p_z)}{\sqrt{s}} \tag{7.17}$$

In order to be sure one can compare the MC predictions and results of FWD-11-001 and the MC predictions and result of the current analysis, both ξ calculations were made and compared for equivalency. The ξ distributions of inelastic events

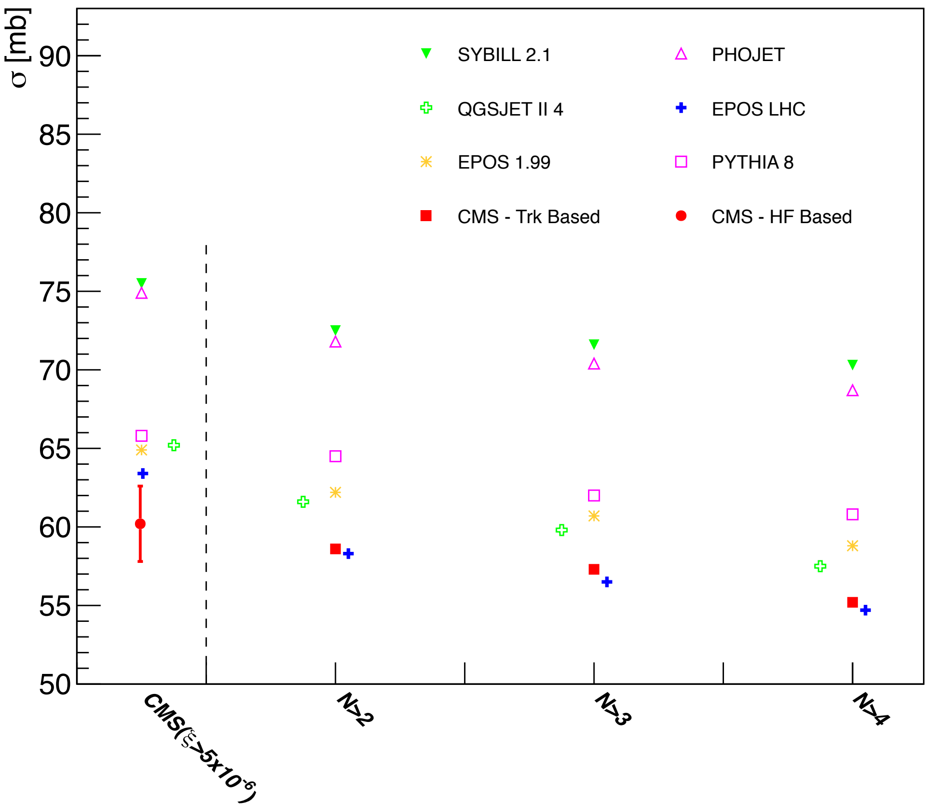

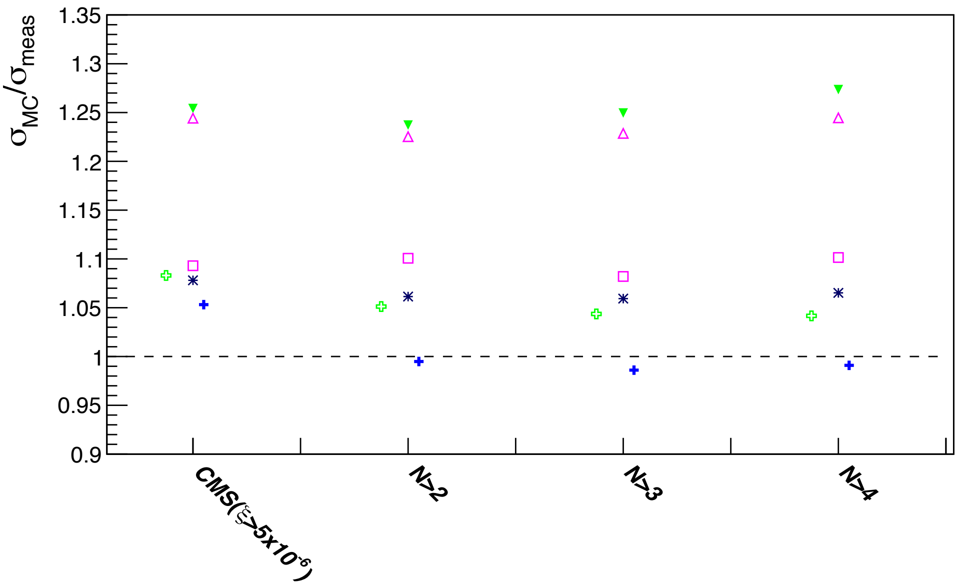

FIGURE 7.3: (Top) Monte Carlo model predictions of the $\sigma_{(\xi>5\times10^{-6})}$ measurement in this analysis and the track counting analysis detailed in FWD-11-001 [119]. (Bottom) Each Monte Carlo prediction normalised to its repective measurement result.

from the generator level calculations are shown in figures 7.5 - 7.6. An example of the direct comparison of the results from the two ξ methods is shown in figure 7.4. The two distributions agree very closely with only a small deviation at very low masses ($\xi < 6$). The comparisons for all models are shown in Appendix C.

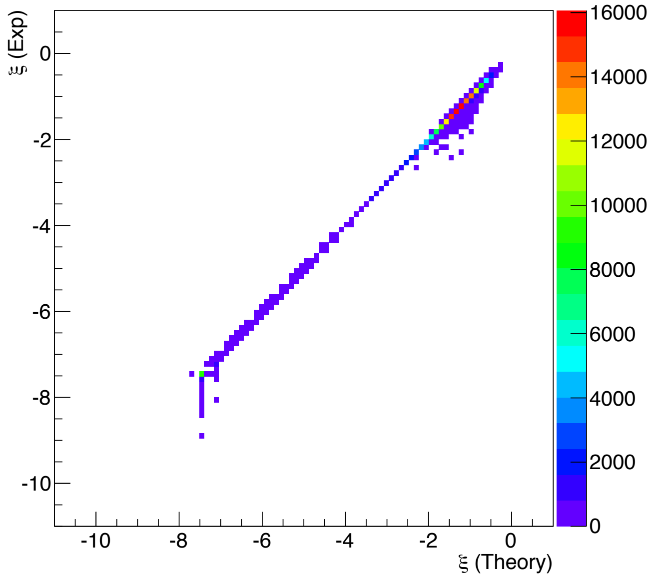

FIGURE 7.4: An example from EPOS LHC of the conformity between the two possible ξ calculations. The choice of calculation has a $\ll$0.1% effect on the outcome of the extrapolation prediction of each model.

The detection efficiency to inelastic events (ε_{inel}), the efficiency to detecting events above the ξ cuts (ε_{ξ}) and the fraction of selected events below threshold, (f_{ξ}), were calculated from each model and together, provided six extrapolation factors which are shown in table 7.10.

$$\text{Extrapolation Factor} = \epsilon_{\xi}/(1 \ - \ f_{\xi})\epsilon_{\text{inel}}$$

The extrapolated cross-sections from each model are also shown in table 7.10. Dividing the σ_{inel}^{total} cross-section of each model by the extrapolation factor gives the $\sigma_{(\xi>5\times10^{-6})}$ value as predicted by the models. Figure 7.7 shows these values with the $\sigma_{(\xi>5\times10^{-6})}$ measurement made in this analysis (red dot).

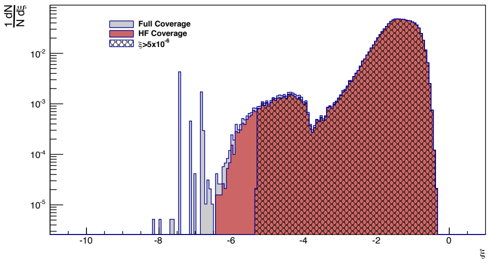

(a) EPOS 1.99 Calculation based on Eq. 7.15.

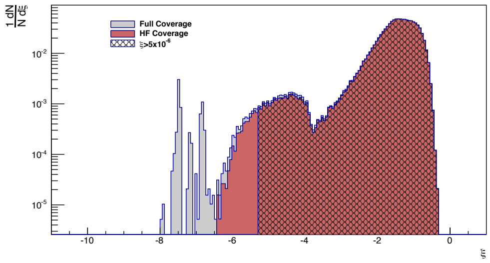

(b) EPOS 1.99 Calculation based on Eq. 7.17.

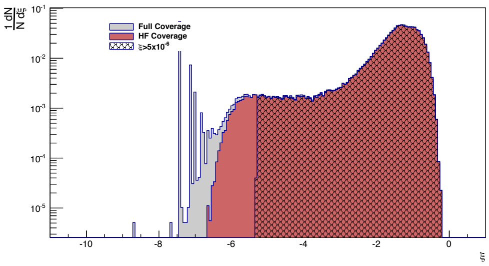

(c) EPOS LHC Calculation based on Eq. 7.15.

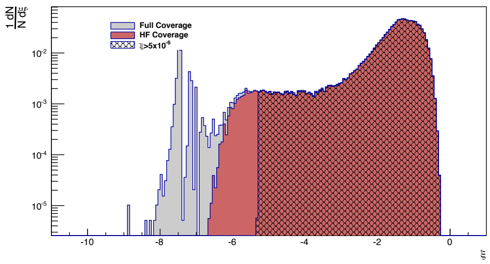

(d) EPOS LHC Calculation based on Eq. 7.17.

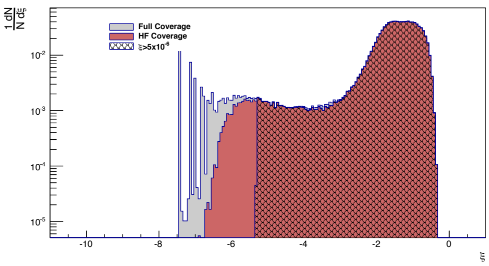

(e) QGSJETII-4 Calculation based on Eq. 7.15.

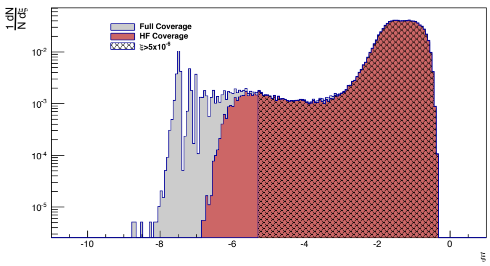

(f) QGSJETII-4 Calculation based on Eq. 7.17.

FIGURE 7.5: Generator level ξ distributions of inelastic events in the different models used for extrapolation.

TABLE 7.10: Efficiency and 'contamination' correction factors and the extrapolation factor derived from each Monte Carlo generator. The differences in the results from ξ calculation of FWD-11-001 (Eq. 7.15) and from Eq. 7.17 are negligible ($\ll$0.1%). Numbers are calculated from 200,000 events from each MC generator.

Model	σ_{inel}^{total} [mb]	$\varepsilon_{inel} \pm 0.2\%$	$\varepsilon_{\xi} \pm 0.2\%$	$f \pm 0.2\%$	extr. factor	$\sigma_{inel}^{extr.}$ [mb]
EPOS	67.9	0.955	0.995	0.0052	1.047	63.0
EPOS LHC	71.32	0.897	0.988	0.027	1.131	**68.1**
Phojet	77.52	0.972	0.996	0.009	1.035	62.3
Pythia 8	71.5	0.929	0.991	0.019	1.087	65.4
QGSJetII-04	73.11	0.904	0.992	0.021	1.121	67.5
Sibyll	79.61	0.959	0.998	0.012	1.054	63.5

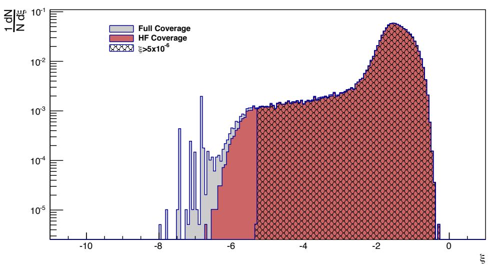

(a) PHOJET CALCULATION BASED ON EQ. 7.15.

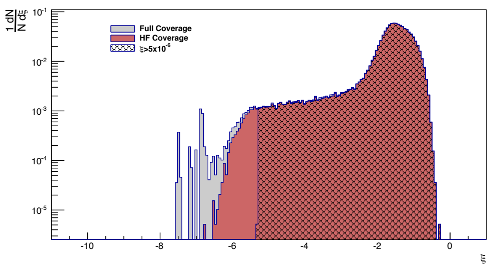

(b) PHOJET CALCULATION BASED ON EQ. 7.17.

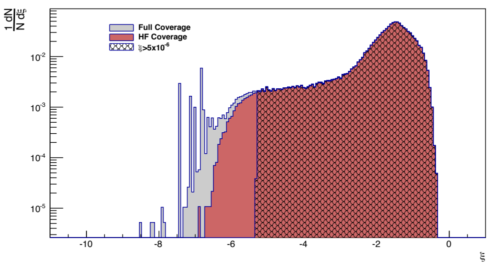

(c) PYTHIA CALCULATION BASED ON EQ. 7.15.

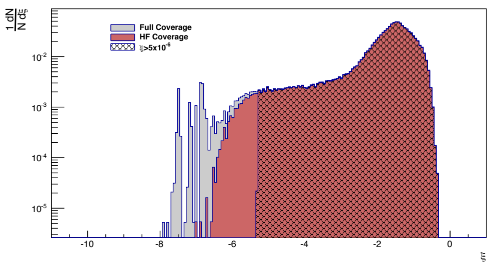

(d) PYTHIA CALCULATION BASED ON EQ. 7.17.

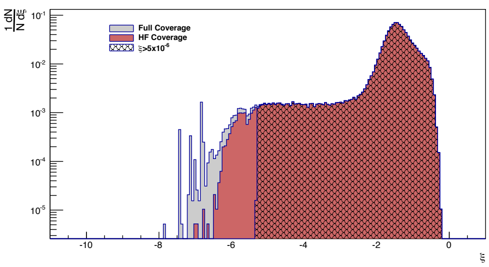

(e) SIBYLL CALCULATION BASED ON EQ. 7.15.

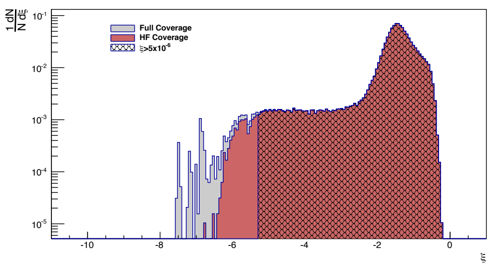

(f) SIBYLL CALCULATION BASED ON EQ. 7.17.

FIGURE 7.6: Generator level ξ distributions of inelastic events in the different models used for extrapolation (continued).

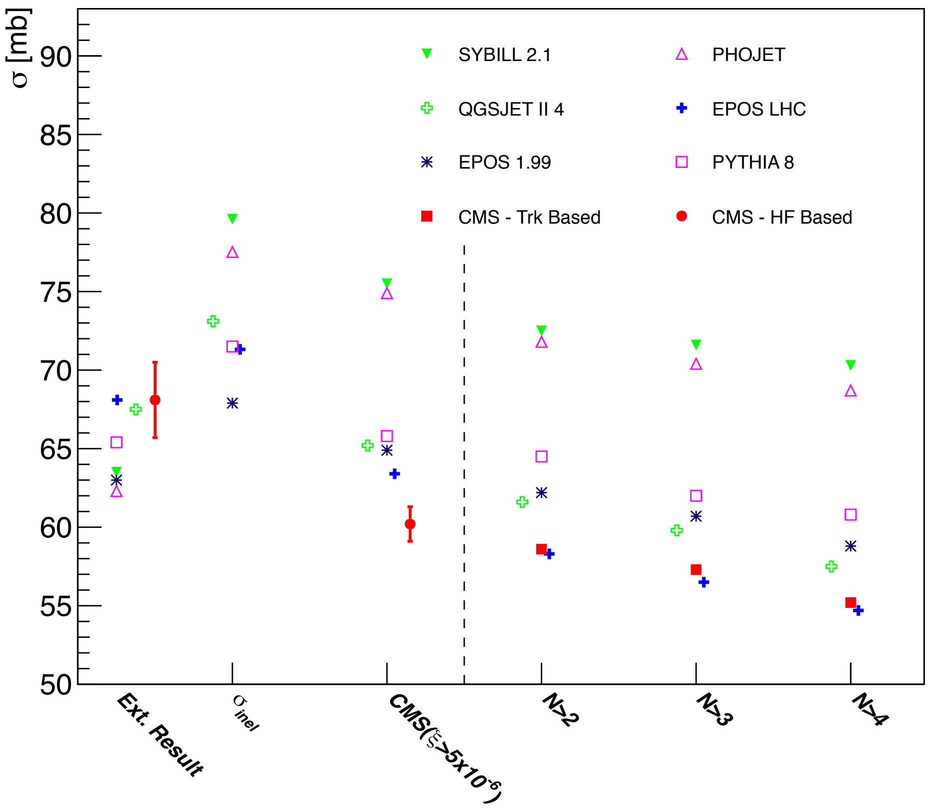

FIGURE 7.7: Comparison between the Monte Carlo model predictions of the σ_ξ and $\sigma_{(N\ \mathrm{tracks})}$ measurements done in this analysis and FWD-11-001. The left-most points show the extrapolation from each model based on the $\sigma_{(\xi>5\times10^{-6})}$ measurement of 60.2 mb. Note that the values from FWD-11-001 have not been recalculated in this analysis.

The primary model of EPOS LHC gives and extrapolation factor of 1.131 and an extrapolated cross section result of 68.1 mb ±0.5 mb (stat). When combined with the systematic uncertainties of the restricted cross section measurement and the 4% uncertainty in the luminosity, one obtains the inelastic *pp* cross section result, based on the EPOS LHC generator:

$$\sigma_{inel} = 68.1 \text{ mb} \pm 0.5 \text{ mb(stat.)} \pm 2.4 \text{ mb(syst.)} \pm 2.7 \text{ mb(lumi)}$$

7.7 Uncertainties

Statistical uncertainties

The statistical uncertainty of the restricted ξ range cross-section measurement $\sigma_{(\xi > 5\times 10^{-6})}$ comes from the statistical error of the number of detected events. As the events are are independent of each other, the statistical error on counting N events has been taken as $\sqrt{N}$. This applies independently to the number of events passing the selection cuts in both the *Coincidence* triggered sample and the normalised *Single-Bunch* triggered sample. The combined uncertainty is calculated by,

$$\boldsymbol{\sigma}_{stat.} = \sqrt{N_{\text{coinc.}} - k^2 N_{\text{Single-Bunch}}} \tag{7.18}$$

where k is the normalisation factor used to scale the number of Single-Bunch triggered events to the number of Coincidence triggered events. This results in an uncertainty of 0.2 mb.
The extrapolation carries a statistical uncertainty stemming from the number of generated events (20,000), providing a $1/\sqrt{N}$ uncertainty of 0.5 mb.

Systematic uncertainties

The systematic uncertainty is dominated by variations in the parameters of Eq. 7.5 which was calculated for each run and the average value taken. The variations between runs is taken as an additional uncertainty, providing a 0.8 mb uncertainty to the $\sigma_{(\xi>5\times10^{-6})}$ result. Variations in the Monte Carlo derived detection efficiencies and low-ξ 'contamination' factors provide a further 0.6 mb and 0.2 mb uncertainty respectively. The exclusion of the noisy HF towers due to incorrect pedestal settings adds 0.2 mb of uncertainty and the HF threshold energy scaling between 4 GeV and 5 GeV provides another 0.2 mb.

The extrapolation to the total inelastic cross section relies completely on the EPOS LHC Monte Carlo model and, as such, carries no uncertainties due to detector effects.
The systematic uncertainties of the restricted cross section result are propagated through to the σ_{inel} result and provide a 1.2 mb systematic uncertainty. Table 7.11 lists the systematic and theoretical uncertainties of the measurement and the extrapolated result.

TABLE 7.11: List of the systematic and theoretical uncertainties on σ_ξ and σ_{inel}. The luminosity contributes an additional 4% to the uncertainty.

σ_ξ result	
Run-by-Run variations	$\pm$0.8 mb
Detection Efficiency	$\pm$0.6 mb
$\xi < 5 \times 10^{-6}$ contamination	$\pm$0.2 mb
HF tower exclusion	$\pm$0.2 mb
HF energy threshold	$\pm$0.2 mb
Quadrature Total	$\pm$1.1 mb
σ_{inel} result	
$\sigma_{(\xi>5\times10^{-6})}$ uncertainty propagation	$\pm$1.2 mb
Standard deviation of MC models	$\pm$2.1 mb
Quadrature Total	$\pm$2.4 mb

Finally, applying the 4% luminosity uncertainty gives an additional $\pm$2.4 mb and $\pm$2.7 mb uncertainty on the $\sigma_{(\xi>5\times10^{-6})}$ and σ_{inel} results respectively.

7.8 Comparing the results with other measurements

The final results for the inelastic *pp* cross section at $\sqrt{s} = 7$ TeV are shown in Figure 7.8 together with results from other analyses. The CMS result for the *pp* inelastic cross section with the ξ threshold compares well with the measurement of the ATLAS Collaboration for the same ξ cut and with the preliminary results for visible *pp* cross section obtained by event pile-up counting in CMS. Table 7.12 lists the various cross sections obtained in this work compared with other recent LHC cross section measurements.

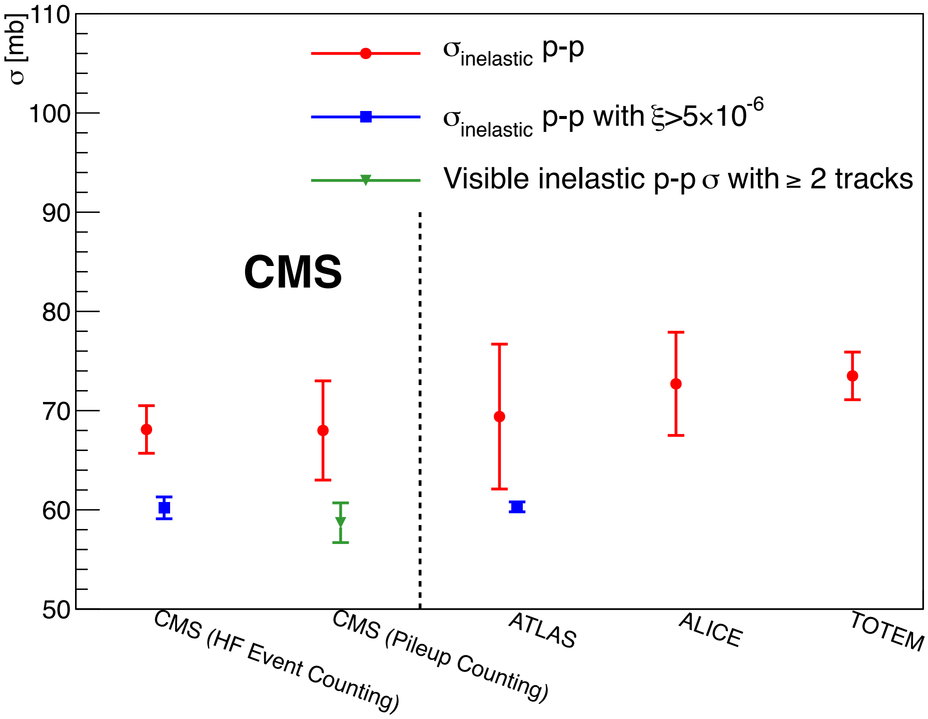

FIGURE 7.8: Comparison of the *pp* total inelastic cross sections (red circles) and the inelastic cross section with the $\xi > 5 \times 10^{-6}$ selection (blue squares) from CMS, ATLAS, the CMS (via pileup counting), ALICE and TOTEM. The leftmost points are the results of the present measurement. The error bars do not contain the common (4%) uncertainty of the measurement of the absolute scale of the LHC luminosity.

The final results for the inelastic *pp* cross section are shown in Fig. 7.9 together with the results from the ATLAS Collaboration [122], the CMS pile-up counting method [119], ALICE [129], TOTEM [130] and the values of previous *pp* and $p\bar{p}$ cross section measurements at lower energies taken from the PDG database [72].

TABLE 7.12: Comparison of the inelastic *pp* cross section results from different analyses. All results are shown in mb. The quoted σ_{inel} experimental uncertainty includes the sum of statistical and systematic uncertainties.

	$\sigma_{\mathrm{inel}}[mb]$ $(\xi > 5 \times 10^{-6})$	$\sigma_{\mathrm{inel}}[mb]$ ($\geq$2 tracks)	$\sigma_{\mathrm{inel}}[mb]$
CMS present analysis	60.2 ± 0.2(stat.) ± 1.1(syst.)		68.1 ± 0.5(stat.) ± 2.4(syst.)
ATLAS	60.3 ± 0.05(stat.) ± 0.5(syst.)		69.4 ± 2.4(stat.) ± 6.9(syst..)
CMS pile-up counting		58.7 ± 2.0(syst.)	68 ± 3(stat.) ± 4(syst.)
ALICE			72.7 ± 5.2
TOTEM			$73.5^{+2.4}_{-1.9}$

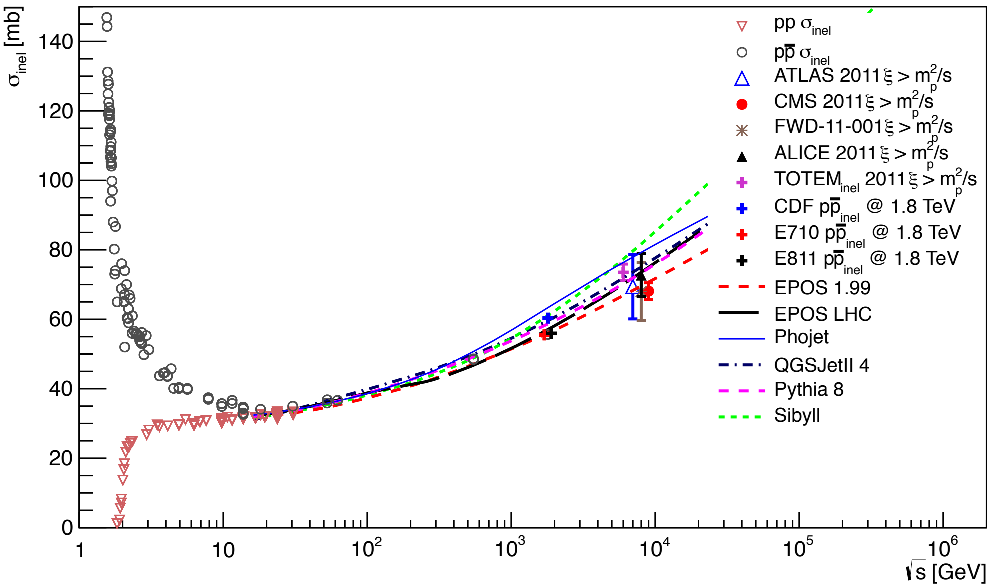

FIGURE 7.9: The results from the present CMS inelastic cross section analysis at $\sqrt{s} = 7$ TeV (red square) compared with the results from ATLAS [122], CMS (via pile-up counting) [119], ALICE [129], TOTEM [130] and lower energy pp and $p\bar{p}$ data from PDG [72].

ATLAS Result

The measurement of the inelastic cross-section by ATLAS was carried out in a similar way to that described above. Where CMS used the Hadron Forward calorimeter the ATLAS measurement used the Minimum Bias Trigger Scintillators, MBTS ($2 < |\eta| < 3.8$) and tuned the PYTHIA 6, PYTHIA 8 and PHOJET simulations to the data. The same kinematic ξ cut was used and detector efficiencies derived from the full GEANT4 detector simulations. The major difference comes in the extrapolation from $\sigma_{(\xi > 5\times10^{-6})}$ and its uncertainty. In the method described in this chapter, CMS extrapolated from $\xi_{(f_{\xi<5\times10^{-6}})}$ to $\xi_{(m_X \leq m_p)}$ by using the acceptance values provided by QGSJETII-4, PYTHIA 8 and EPOS LHC at the generator level. These were compared with PHOJET, EPOS 1.99 and SIBYLL, also at the generator level - albeit in the raw `.LHE` format - to further examine the uncertainties implicit within the generators.

The extrapolation method of the ATLAS analysis, calculated the acceptance efficiency of the $\xi > 5 \times 10^{-6}$ cut from various models. An average ε_ξ acceptance efficiency of 87% was found and applied to the measurement result to obtain

σ_{inel} =69.4 mb. As the ATLAS data was based on a single run with an estimated pile-up of 1%, no $F_{\text{pile up}}$ correction was made to account for the possibility of multiple collisions within an event. Also, due to the small geometrical acceptance of the MBTS, no 'contamination' correction was required to account for the fraction of data which fell below the ξ cut.

TOTEM Result

The measurement of the inelastic cross-section by TOTEM was achieved by Measuring the *elastic* differential cross-section down to $|t| = 2 \times 10^{-2}\text{GeV}^2$, then extrapolating to $|t| = 0$ assuming the function

$$\frac{d\sigma_{el}}{\mathrm{d}t} = \frac{d\sigma_{el}}{\mathrm{d}t}|_{t=0} e^{-B|t|} \tag{7.19}$$

where B describes the slope of the fit of the data over the complete $|t|$ range, having a value of 20.1 ± 0.5 GeV^{-2}. Assuming the slope B to be constant, the total elastic differential cross-section at $t = 0$ was determined, then integrated over $d\theta\ d\phi$ to obtain a total elastic cross-section (24.8 ±1.4 mb).

Using the optical theorem, the total proton-proton cross-section was calculated from the total elastic cross-section by:

$$\sigma^2_{tot} = \frac{16\pi(hc)^2}{1+\rho} \frac{\mathrm{d}\sigma_{el}}{\mathrm{d}t}\bigg|_{t=0} \tag{7.20}$$

which gives a value of 98.3 $\pm 0.2(\text{stat})^{+2.8}_{-2.7}(syst)$ mb. In Eq. 7.20, ρ is the ratio of the real and imaginary parts of the *pp* forward elastic scattering amplitude, with a value of $\rho = 0.14^{+0.01}_{-0.08}$, arrived at by the COMPETE Collaboration by averaging over all available measurement data.

Subtracting the elastic cross-section from the total cross-section gave a value for the total inelastic cross-section of 73.5 $\pm 0.6^{(stat)}\ {}^{+1.8}_{-1.3}\ {}^{(syst)}$ mb, shown in the comparison plot of figure 7.8 and the results summary of figure 7.9.

Because the extrapolation from measured elastic cross-section to the total elastic cross-section ($|t| = 0$) is based simply on a well founded assumption of a parameter fit ($B|_{t=0}$) which, in turn is extrapolated to the total cross-section through the use of the well defined *optical theorem*, the uncertainties in arriving at the value of the total inelastic cross-section are small, relative to those of ATLAS, ALICE and CMS which all rely heavily on Monte Carlo models.

CMS Vertex Counting Result

The analysis outlined in this chapter is complementary to the measurement of the visible part of the inelastic cross section based on pile-up counting [119] as the acceptance of the two analyses is very different. In each analysis, there are possible events which can escape detection. Most single and double diffractive events are detected by the HF calorimeter but fail to hit the pixel tracker region. Similarly, central exclusive events, $pp \rightarrow ppX$ in which the two protons exit the detector in the very forward direction and the system X interacts with the pixel tracker but not with the forward calorimeters, as shown in figure 7.10.

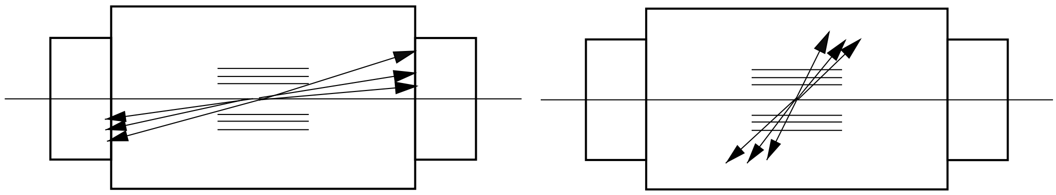

FIGURE 7.10: When counting events, the topology of those events can lead to counting inefficiencies. (Left) In the case of low p_T diffractive events, only the forward detectors register a hit. (Right) In central exclusive events, the incident protons remain intact, losing a small fraction of their longitudinal momentum. A central system is produced and detected by the CMS tracker (shown as the parallel lines). Because the outgoing protons remain close to the beam pipe, the forward calorimeters do not see such events.

The extrapolations of these two analyses to the value of the total inelastic cross section differs both numerically and in the nature of events. The recent measurement of the total, elastic and inelastic cross section by the TOTEM collaboration [130] and the results presented here may indicate that the invisible part of the inelastic cross section is underestimated by a wide range of models. However, improvements to EPOS LHC and QGSJETII-4 which place more emphasis on central diffractive events, show substantial improvements in their $\frac{dN}{d\xi}$ evolution, compared to their predecessors.

7.9 Conclusions

A measurement of the inelastic cross section for pp collisions at $\sqrt{s} = 7$ TeV has been made with CMS using the Hadronic Forward Calorimeters (HF). The inelastic events were counted requiring the detection of one particle above the 4 GeV or 5 GeV energy threshold in at least one side of the HF. The efficiencies for inelastic events using this counting mode were estimated by Monte Carlo simulations using PYTHIA 6 (D6T tune), PYTHIA 8 and PHOJET. To mitigate the model dependence, a selection of $\xi > 5 \times 10^{-6}$ was used in determining the detection efficiency values. This value was specifically chosen to give a visible inelastic cross-section result which would be directly comparable to that of the ATLAS collaboration.

Over 9.2 million events were processed in the dataset with low pile-up data, corresponding to an integrated effective luminosity of 2.76 μb^{-1}. Data from runs with pile-up ranging from ∼7% to ∼12% were processed with the corresponding pile-up correction factors applied.

The value of the *pp* cross section was calculated as the result of the analysis using the selection $\xi > 5 \times 10^{-6}$ and a 5 GeV HF energy threshold. An extrapolation was carried out to determine the total inelastic cross section using additional generator level Monte Carlo models. The final results are in good agreement with the results independently obtained recently by CMS (via event pileup counting) [119] and ATLAS [122], and follow the $\ln^2(s)$ increasing trend established by previous measurements at lower energies.

The results presented here improve upon those of the original paper QCD-11-001 by the use of updated Monte Carlo generators, particularly EPOS LHC and QGSJETII-4. As most models over-estimated the number of events detected in the forward calorimeters above the ξ cut, it is possible that Centrally Diffractive events play a more important role in the total cross section at higher $\sqrt{s}$. This is predicted in theory [131] but not accounted for in most of the MC models. This would result in a greater number of MC events with particle trajectories in the central, tracker region. Alternatively, if the Monte Carlo modelled M_x distributions err towards larger masses, the result would be a greater number of simulated events passing the ξ cut, as well as the p_T cut in the analysis of FWD-11-001. Figure 7.11 shows the η distribution of the number of particles per event. One can see that the models with a tendancy to scatter at higher η (stemming from smaller produced M_x particles) have a better agreement with the measurement of $\sigma_{(\xi<5\times10^{-6})}$, shown in 7.7.

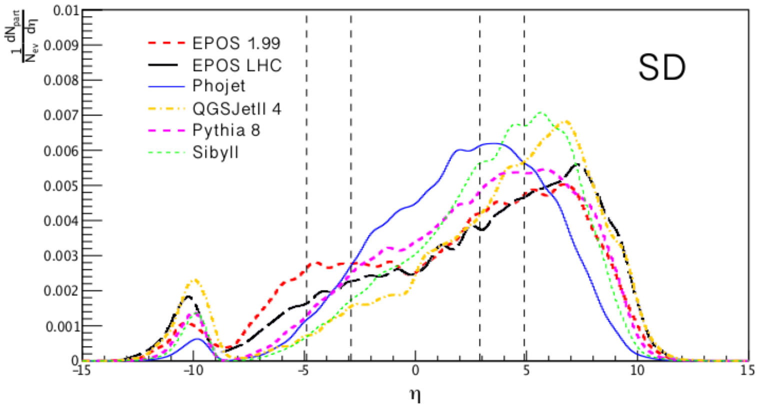

FIGURE 7.11: The η distribution of single diffractive events from each of the Monte Carlo models used in the analysis. The models with the more forward (higher η trends have a closer agreement with the restricted cross section measurement.

The recently modified EPOS LHC model gives excellent results for the prediction in the central region analysis of FWD-11-001 and gives the best agreement with the current analysis. The modifications to the diffractive mass distributions of EPOS LHC resulted in lower mass, more forward going partons, compared to the other models. It is hoped that the combination of this analysis with that of FWD-11-001 and TOTEM will provide an important tool for tuning the topologies, event fractions and mass distributions of soft hadronic collisions in Monte Carlo models. Although, currently this does not provide a true theoretical understanding of the phenomonolgy unpinning such events, Monte Carlo models which are able to predict the evolution of hadronic cross sections with increased collision energy will be vital in designing detector upgrades to LHC experiments and future, higher energy colliders.

Chapter 8

Future Functionality Of The BSC Upgrade

The Beam Scintillator Counter (BSC) has proven to be a vital component during the early commissioning phases of the LHC and CMS. It not only fulfilled its design goals as a beam monitoring device but also provided important trigger information when beam intensities and stabilities were insufficient for other triggering systems to function efficiently and safely. This ability continued throughout 2010 for both proton-proton (p-p) and Heavy Ion (HI) physics but diminished in early 2011. It was suggested that an upgrade of the BSC system should be planned to fulfil a need where other sub-detectors may not be sufficient or where such an upgraded detector could greatly improve the operation of CMS in some way. This chapter reviews the limitations of the BSC detector, outlines the functions that the system performed and defines a proposal for the functionality of the detector upgrade based on the experiences of 2009 - 2011.

8.1 Limitations of current design

The BSC was ideally suited to the early phases of proton-proton and heavy ion LHC operations. Its large individual channel acceptance, >95% efficiency and its location in the more active forward regions (3.23< $|\eta|$ <4.65) resulted in the BSC being the first CMS sub-detector that responded to collisions, often with no ambiguity. The robustness of the front end system and the relatively easy accessibility for repairs allowed for the BSC to operate 100% of the time without worrying about damage due to large beam losses. However, there are several limitations of the design at higher luminosities.

Luminosity Limit of the BSC system

During early 2010, luminosity related problems were first observed in the BSC trigger rates. These problems manifested themselves as a reduction in trigger rates. In June 2010, a high luminosity VdM scan was done in CMS. The two beams were scanned across each other over a period of ∼20 minutes, reaching an instantaneous luminosity of $\sim 8\times10^{32}$ cm^{-2}s^{-1}. The scan served the purpose in finding the maximum luminosity at which the BSC could operate. During the scan, the voltages to the PMTs was already greatly reduced to combat the effects of pulse pileup. Figure 8.1 shows the instantaneous luminosity in red and the rates from one of the inner BSC channels (1FBSC1D3) during the scan.

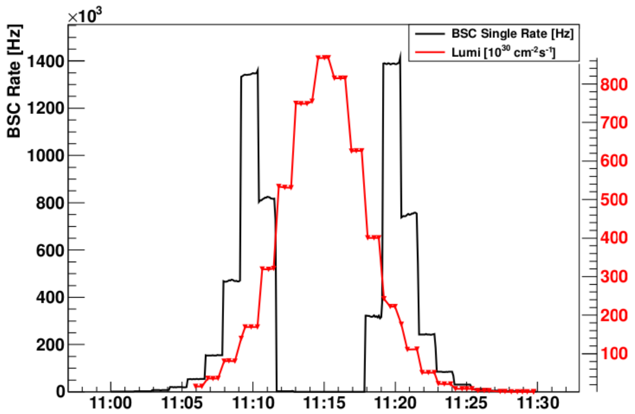

FIGURE 8.1: The BSC single channel rate luminosity limit was found to be $\mathcal{O}(3-4\times10^{32}\mathrm{cm}^{-2}\mathrm{s}^{-1})$. Data recorded in June 2011.

On average, the flux of particles emerging from the I.P is proportional to the instantaneous luminosity and the single channel rates should increase and decrease with the luminosity. One can see that, initially the BSC rate increases inline with the luminosity during the beginning of the scan. But as the luminosity increases beyond 300 - 400 $\times10^{30}$ cm^{-2}s^{-1}, the BSC rate suddenly drops to zero and only returns once the luminosity reduces below $\sim$ 400×10^{30} cm^{-2}s^{-1}. This therefore defines the luminosity limit of the BSC as being in the region of $\sim 4{\times}10^{32}$ cm^{-2}s^{-1} (400 μb^{-1}s^{-1}). The luminosity limit plots for all channels is given in Appendix A.

Pulse Pileup

When the voltages were set at optimal efficiency, at instantaneous luminosities above $30{\times}10^{30}$cm^{-2}s^{-1} ($30\mu b^{-1}$s^{-1}), the effects of pile-up could be seen in the minimum bias trigger as shown in figure 8.2. The flux of particles through each tile increases with luminosity therefore creating signals of larger amplitude. Combined with the decreased time between consecutive bunches, the output from the PMTs was unable to return to the baseline before the next bunch arrived. The effect could initially be prevented by reducing the high voltage supply on the PMTs, thus reducing their gain and sensitivity. However, as the CMS luminosity further increased, no measures could be taken to prevent the pulse pile-up and the BSC reached the end of its useful operations for proton-proton collisions.

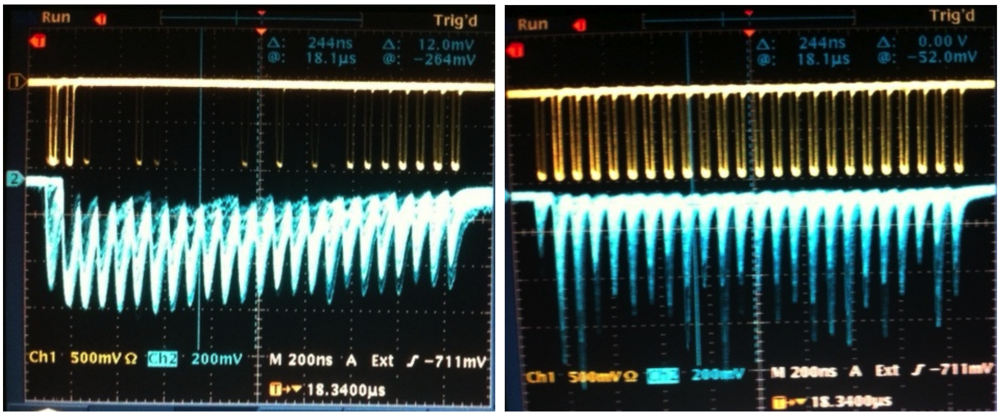

(a) (b)

Figure 8.2: The effects of pulse pileup was seen in all channels as the luminosity increased throughout September and beyond during *pp* running. The voltage to the PMTs were reduced to restore the baseline of the signal. However, this also reduced the efficiency of the BSC, preventing its use as a triggering detectors.

Albedo

As seen in section 4.2, the BSC triggers were strongly affected by the presence of Albedo, particle reflections and short-term activation of materials in the vicinity of the BSC tiles. As a trigger or as a beam monitor, it is important that the BSC upgrade is able to filter out these backgrounds without placing overly stringent requirements on the detection of true collision or beam background signals.

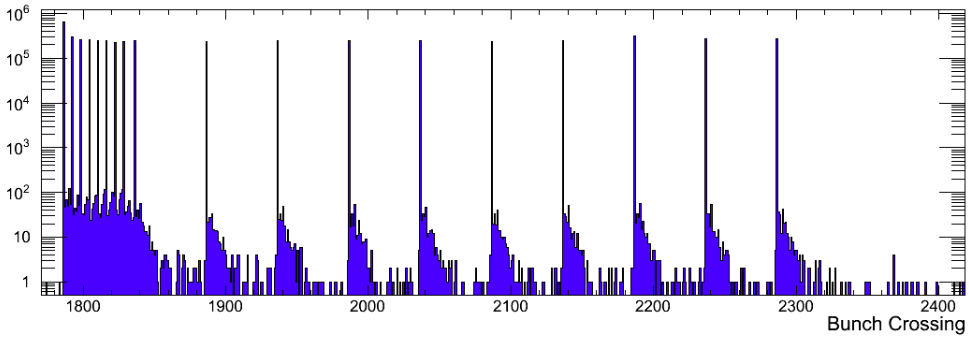

FIGURE 8.3: BSC Minimum Bias trigger (threshold1) became contaminated by the effects of albedo as luminosities approached $\mathcal{L} \approx 10^{29}\text{cm}^{-2}\text{s}^{-1}$.

8.2 Proposed functionality of the BSC Upgrade detector

The BSC subdetector performed several important roles during the start-up and commissioning phases of the LHC and CMS. The following lists the uses of the BSC during 2009-2011 as well as the limitations of continuing with these roles.

Online luminosity monitor: Limited by the excessive flux per channel and 25 ns time resolution of the minimum bias trigger used to monitor the luminosity. In future, the Pixel Luminosity Telescope (PLT), Pixel tracker and HF calorimeter will fulfil the function of measuring the instantaneous luminosity online.

Minimum Bias Trigger: At $\mathcal{L} = 10^{34}\text{cm}^{-2}\text{s}^{-1}$, there will be approximately 14 collisions per bunch crossing during proton-proton physics runs. Additionally, the topology of minimum bias events in CMS is now well understood.

For these reasons, a minimum bias trigger for *pp* events is no longer required. The situation for Heavy Ions is different with $\mathcal{O}(10^{-3})$ beam crossings resulting in a minimum-bias event. There is a continued requirement for a minimum bias trigger for HI runs.

Physics triggers: The BSC triggering efficiency surpassed that of the HF for low multiplicity, and therefore low luminosity fills. This may still be important if the LHC returns to low luminosity runs due to technical problems or after a long shutdown. However, it is not viable to build a detector upgrade solely for this purpose.

Centrality measurements: During the first HI run, the BSC was used as a crude measure of the H.I event centrality by looking at the amplitudes of signals from each channel using the CAEN ADCs. No such alternative exists, the HF calorimeter having a ∼4 GeV lower energy threshold. An upgrade detector for this purpose would need to have high granularity and a moderate acceptance ($3.2 \leq \eta \leq 5.2$) to provide a high quality measurement of event centrality. However, such a detector is not within the remit of the CMS Beam & Radiation monitoring group.

Beam monitor: The monitoring of beam losses for the safe operation of CMS requires a subdetector with elements close to the beam and is able to respond quickly to sudden changes in flux which could signal an imminent loss. The CMS BRM group already run and maintain three detectors which monitor the beam status; namely the BCM2, BCM1F and BCM1L.

8.2.1 Luminosity Monitor.

Luminosity studies in CMS currently use the HF Calorimeter, normalised to the absolute Van der Meer scans (VdM). The Pixel Luminosity Telescope (PLT) is planned for installation and testing in 2012 which will provide a more accurate and online measure of luminosity. However, it is feasible that a new, multichannel subdetector could provide a back-up relative-luminosity measurement by monitoring the minimum-bias rate in the forward regions. Channel areas must be determined such that they will be able to detect single or multiple particle hits (by measuring pulse heights, for instance) without saturating at high luminosities.They must be fast enough so that pulse pile-up will not occur even between incoming and outgoing bunches (Δ t $\approx$ 3ns at the HF front face). As a dedicated luminosity monitor is planned for installation, this functionality from the BSC upgrade would only be a secondary feature rather than the main goal. The BSC upgrade does, however afford the opportunity to improve the HF calorimeter and its ability to provide accurate luminosity measurements.

8.2.2 Minimum Bias Trigger for *pp* & H.I runs.

The LHC is now reasonably well understood meaning that clean, stable p-p beams are more easily delivered with a minimal risk of large beam losses. The CMS detector is also under control in terms of sub-detector and trigger performance. This implies that many of the BSC triggers are slowly becoming unnecessary for *pp* beams. Minimum bias events occur every bunch crossing in *pp* collisions. Such a trigger will not serve to reduce the amount of data taking and filter out the 'good' events at the L1 trigger level, although it may still act as a tool for verifying other minimum-bias triggers and for providing triggers during HI runs. There is also a possibility that a *pp* minimum bias trigger could be useful immediately after a long shutdown period or in the event of a LHC magnet replacement, but this functionality should ideally be a by-product of a more meaningful purpose, rather than a main design aim.

8.2.3 General L1 Triggering.

Many of the triggers that the BSC provided in 2009 - 2011 are no longer required. The HF calorimeter is also intended to provide more advanced triggers but has been shown to be non-optimal during low luminosity runs and HI runs. From discussions within CMS, there is still a need for a beam-gas and PKAM veto trigger to aid in the removal of background contaminated collision events in the wide range of physics analysis. The ability to select or mask particular bunch crossings was also requested as this would allow for detailed and clean studies into the effects of backgrounds.

8.2.4 Centrality Trigger & Measurements of Heavy Ion running.

Centrality measurements of heavy ion collisions were achieved at PHOBOS (RHIC) using a detector not dissimilar to the current BSC [132]. In CMS, the majority of the H.I centrality measurement requirements are to be provided by the HF (as a trigger) and the tracker (off-line analysis). To study the properties of PbPb collisions, it is often desirable to record only a well defined subset of the data for detailed analysis. PbPb collisions with a small impact parameter (referred to as *central* collisions) provide the most useful information on the collisions. A well designed centrality trigger should be capable of determining these central collisions in a well defined way and should be read out in parallel with the minimum bias trigger [133]. If the BSC upgrade is designed with small granularity that can detect *pp* min-bias and beam halo spatial distributions with channel-by-channel information (see sections 8.2.3 and 8.2.5), performing online centrality triggering and measurements for PbPb collisions may be an additional, yet natural extension of functionality.

8.2.5 Background & Beam Monitoring.

Beam monitoring and background monitoring are vitally important for CMS. Although many of the nominal running conditions will be monitored sufficiently by existing detectors (BCM2, BCM1F, BCM1L and BPTX) these detectors lack a complete ϕ coverage and have a relatively small acceptance but are still capable of monitoring the beam dynamics very well. However, there are no dedicated subdetectors capable of monitoring beam halo background whilst there are also collisions, which is important for providing real-time feedback to the LHC control.

8.2.6 Conclusion

It is proposed that the BSC upgrade aims at providing online, full-time beam background monitoring even whilst the beams are colliding. For this, the detector either needs to be insensitive to particles coming from the I.P or designed around a geometry that favours the detection of the beam halo as much as possible. The detection of beam background is technically challenging due to the much larger quantity of particles emanating from collisions.

Figures 8.4a-e show the relative flux for various particle types for collisions and from background calculated from Fluka Simulations [134]. Typically, there is a $\mathcal{O}(10^5)$ greater collision related flux than background related flux over the entire region of the current BSC position. This is generally true for all positions along the beam pipe within the CMS cavern, meaning that either the detector needs to be very well shielded from the I.P, insensitive to the collision fragments due to their direction or optimised for the acceptance of beam halo whilst keeping the acceptance of collisions products to a minimum through using the relative timing of the two.

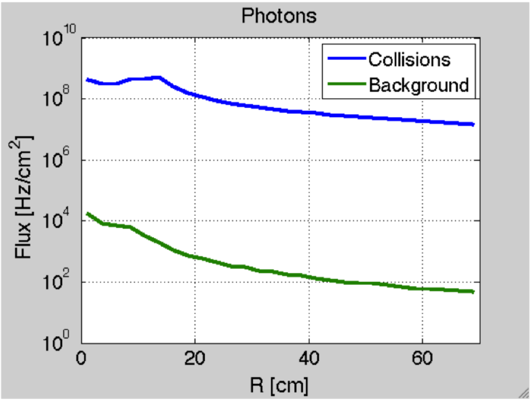

(a)

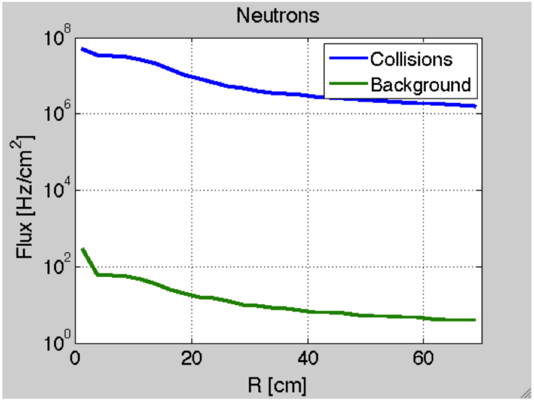

(b)

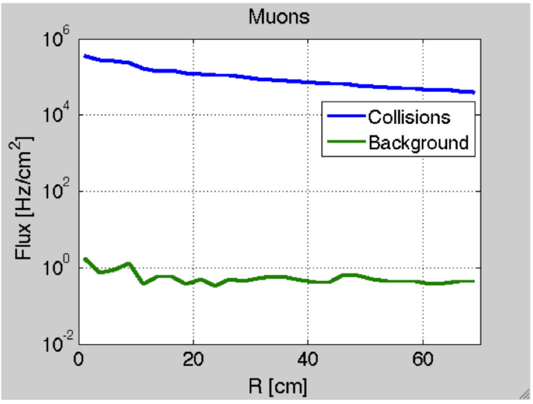

(c)

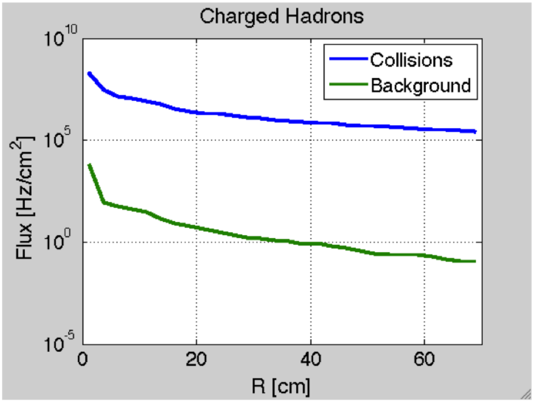

(d)

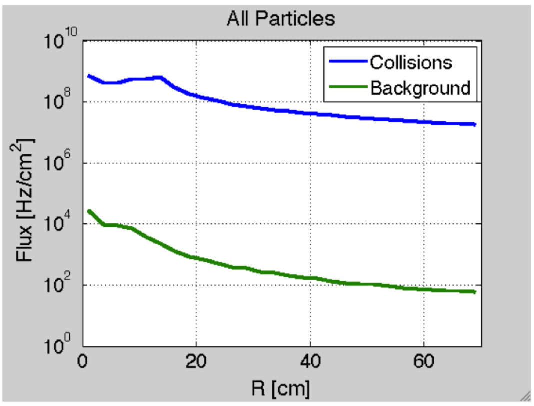

(e)

FIGURE 8.4: Particle fluxes at the current BSC location (±10.86 m) [134].

Chapter 9

Design Of The Beam Halo Counter

The BSC was used for many tasks beyond its intended purpose such as luminosity monitoring and many Level 1 triggers. As the luminosity increased, other detectors were capable of providing this information and the BSC was no longer useful during *pp* running due to the excessive rates. As of late 2011, the CMS Beam & Radiation Monitoring group did not have a satisfactory method of monitoring beam backgrounds such as beam halo and beam gas events. Triggering on them either to veto the event or to allow studies of these backgrounds will be useful for improving the operation of CMS and the LHC. The Beam Halo Counter (BHC) aims to provide a high quality trigger of beam backgrounds around CMS during both the proton-proton and heavy ion physics programs. This chapter outlines the concepts, calculations and simulations for the BHC, a set of small scintillator tiles and time of flight logic timed to detect beam halo and beam gas events.

The important aspects considered in the design were the following:

- Detection of the relatively small amount of beam background amongst the collision products. Simulations have shown [135] that the ratio of particles produced at the collision and the beam background particles is $\mathcal{O}(10^5)$.
- Intrinsic signal width is important. Detector media that provide large light outputs are typically slow, having long signal tails many tens of nanoseconds

long. These long tails limit the maximum frequency which the channels can handle before the onset of pulse pileup.

- Occupancy and frequency of hits to each detector channel must be limited. Each channel must be small enough to avoid being hit and producing a signal in every bunch crossing, thus allowing enough recovery time for the signal to return to zero prior to the next bunch crossing. Detector materials with shorter signals (faster recovery times) will handle higher luminosities and multiplicities than slower detector materials.

- Radiation hardness. As the upgrade will be located in one of the harshest radiation environments in CMS, the materials used should be able to withstand the conditions for a number of years without a significant loss of signal.

- Cost. Several factors must be considered when determining the cost of the system. A plastic scintillator system would be cheaper per channel than say, a silicon based system and each channel could be replaced during technical stops or shutdowns when the radiation damage becomes too great. However, due to the large light output and relatively slow signals, each channel must have a smaller area which leads to the need for significantly more channels to cover the same η, ϕ range.

9.1 Available Locations

The BHC has been designed with the aim to monitor the beam background in CMS, ignoring the activity from collisions that currently overwhelm the background rates. The current system monitors the background exceedingly well up to the point of collisions. Figure 9.1 shows the longitudinal view of CMS and the various subdetectors that run along the beam pipe. On the left is the inner pixel tracker (barrel and endcaps) as well as the Beams Condition Monitors, BCM1L and BCM1F (0 m - 3.1 m). Moving right, along the beam pipe, there is a cone (**1**) through the middle of the electromagnetic calorimeter (ECAL) and Hadronic Calorimeter (HCAL) endcaps providing a space of ~4.3 m in front of the TOTEM T1 detector (7.4 m). This region is very difficult to access and provide services to. Behind the TOTEM T1 subdetector is the current BSC1 location (10.9 m) and the HF calorimeter (**2**). The rear of the calorimeter ends at 13.8 m (**3**) after which TOTEM T2 and CASTOR (one side only) are situated. Beyond this point (∼15 m) is the rotating shielding (**4**), two large iron structures designed to provide some protection to CMS from beam losses in the long straight section leading to CMS.

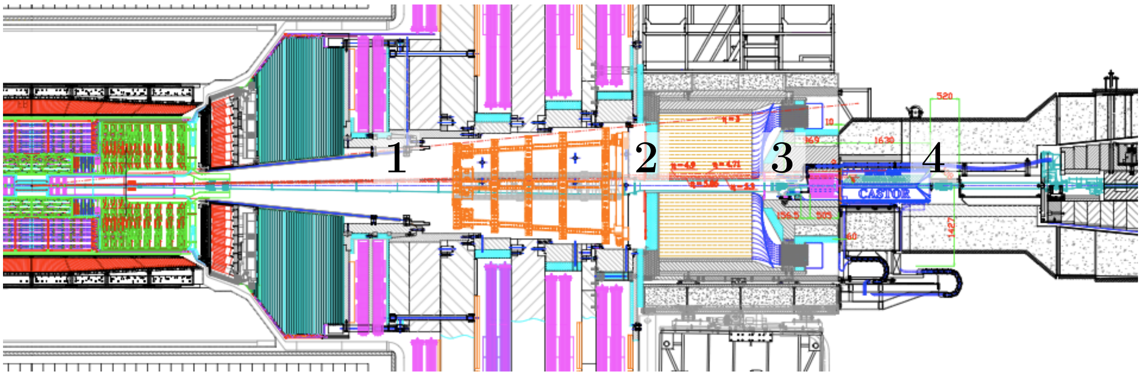

FIGURE 9.1: The longitudinal view of CMS. As well as the effects of radiation flux and magnetic fields, there are many mechanical issues to consider when planning a detector upgrade.

Additional to the mechanical constraints, consideration must be given to the time difference between incoming beam background particles and outgoing collision products if they are to be differentiated by their timing. At 25 bunch spacing, the beams cross at the I.P and every $\frac{25\text{ns}\cdot c}{2} = 3.75$ m in z. At these locations, it is impossible to differentiate the incoming (background) and outgoing (collision fragments + background) beams in terms of timing. As one moves away from these 'nodes', the time difference increases to a maximum of $\frac{25\text{ns}}{2} = 12.5$ ns. Figure 9.2 shows (red dashed line) the time difference between incoming and outgoing particles along z. Also shown are the *exclusion zones* due to mechanical restrictions and timing restrictions based on a minimum detector time resolution of 4 ns.* With these restrictions, there is very limited space to place a new detector.

After considering all possibilities, including placing the detector beyond the TAS in the Long Straight Sections, it was decided to stay with the current location of 10.86 m on the HF front face to reduce the cost and allow a system to be installed during the 2011 winter shutdown.

*The original BSC time resolution was 3 ns. This is expected to be matched in the upgrade and the figure of 4 ns allows for some safety margin.

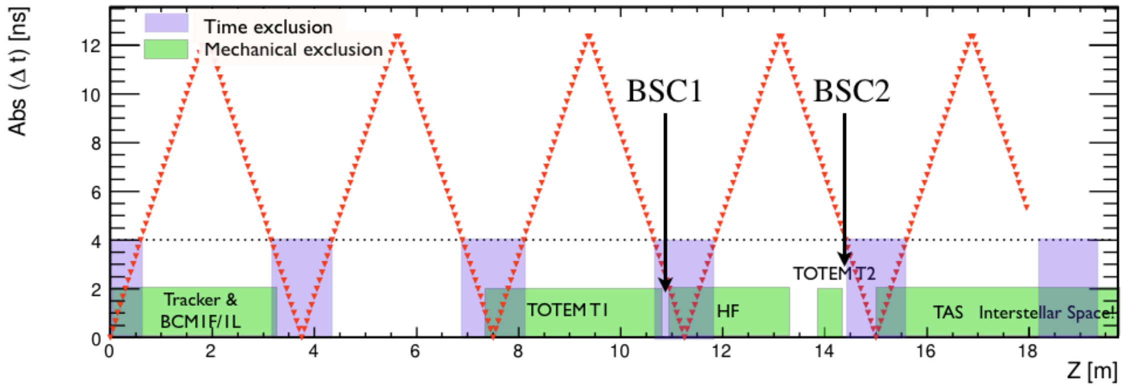

FIGURE 9.2: Δt and mechanical restrictions for the BHC location within the CMS cavern.

9.1.1 Radiation Environment

The radiation flux in the region of the BHC detector is the most intense in CMS. It has been calculated that the HF calorimeter will absorb 10 MGy of dose within 10 years of operation [27] mainly from charged hadrons and photons. The combined flux of all particles in the forward region is of the order of $10^7 \mathrm{cm}^{-2}\mathrm{s}^{-1}$. This includes thermal neutrons, photons, muons and charged hadrons of all energies [134]. The map of the expected particle flux at $\mathcal{L} = 10^{34}$ and $\sqrt{s} = 7$ TeV is shown in figure 9.3.

9.1.2 Considerations of Particle Flux

To serve as a beam background monitor, the detector must be able to distinguish between the signals generated from the charged particles stemming from the collision and those entering CMS as beam background. As figure 9.4 and table 9.1 both show, the ratio of collision flux to background flux is $\sim 10^5$ meaning that either the upgrade must be able to cope with the high collision rates and select the background signals based on the timing (by gating the signals), or it must be insensitive to the direction of the collision particles and sensitive only to the direction of background particles. The first is highly dependent on the sizes of the active area of the detector channels and their radial distance from the beam pipe where collision product rates are greatest. If they are too large, each channel will be hit by collision products every bunch crossing and may not be able to recover

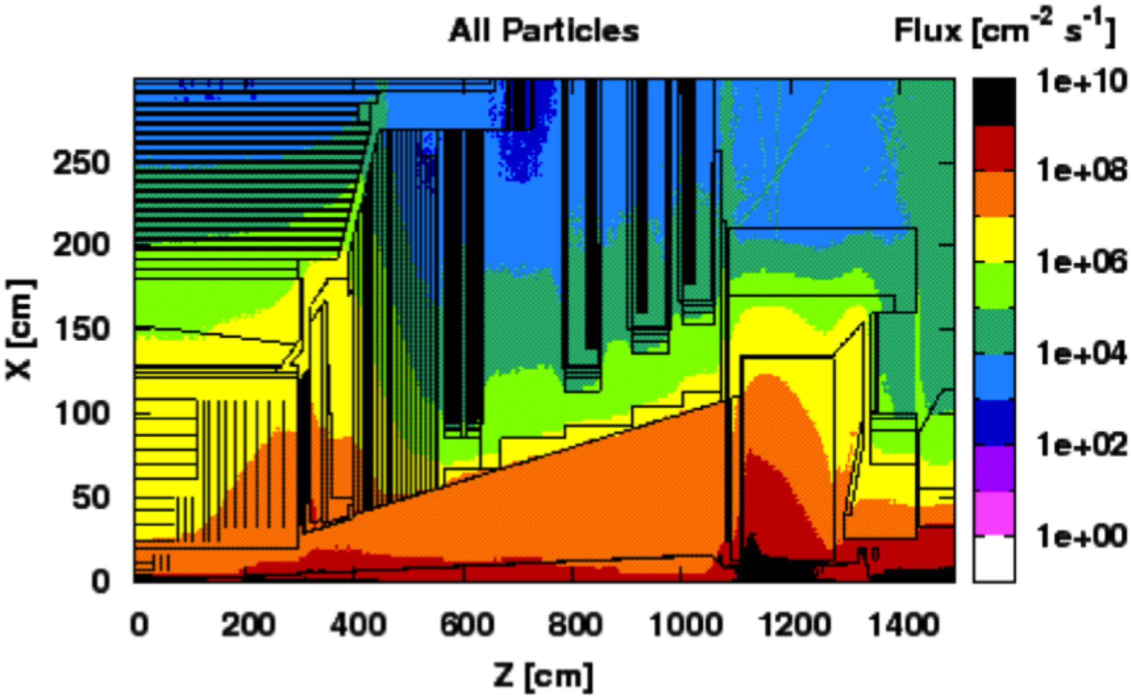

FIGURE 9.3: The radiation flux from all particles in the CMS cavern.

in time to measure the background associated with non-colliding bunches. Making the areas smaller will result in more channels and a more expensive sub-detector or a reduction in ϕ coverage and acceptance. The second option is more technically challenging and will require the exploitation of the Cěrenkov light cone to provide the directional sensitivity.

After several discussions with several CMS institutes and BRM members, two concepts emerged from several proposals. The first was a Cěrenkov detection method that uses the directional sensitivity to separate the detection of incoming background particles and the outgoing collision products. The second is a plastic scintillator gated system which uses the arrival time of the signals to discriminate between background and collision products. For the 2012 proton physics run, it was decided to pursue the simplest option of the time gated method using plastic scintillator tiles similar to those used in the BSC detector. This choice meant that the read-out system of the original BSC could be re-used with minimal reconfiguration and allow the original system to continue its use as a Minimum Bias trigger and luminosity monitor during the 2012 H.I runs.

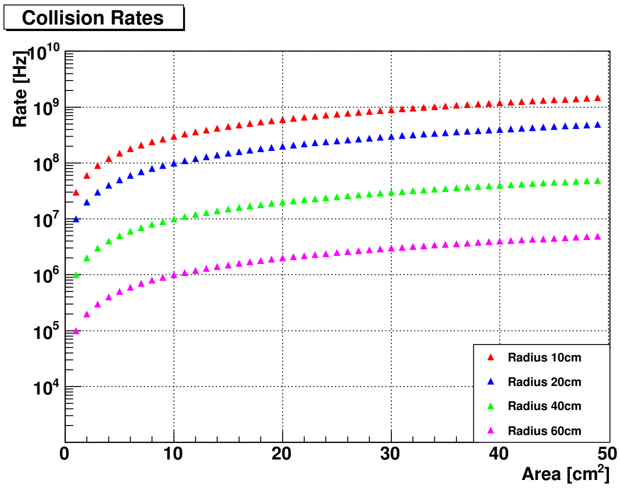

(a)

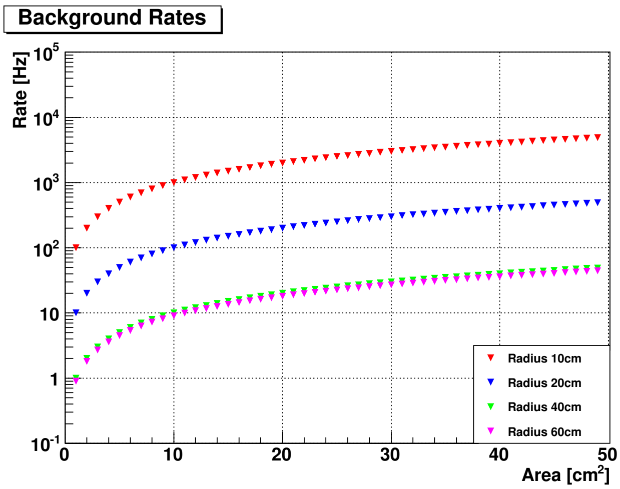

(b)

FIGURE 9.4: The predicted signal rates from charged hadrons from (a) collisions and (b) beam background. The charged particle rates per channel increase with the active area of the channel and decreases rapidly with radial distance.

9.2 Calculation of Channel Sizes

The BSC single channel rate measurements made during the VdM scan in June 2011 (see section 5) showed that the scintillator tiles used in the BSC saturated at luminosities in the order of 10^{32} cm^{2}s^{-1}. This, according to simulations [134], equates to a flux of 10^4cm^{-2}s^{-1} at the BSC 1 location. The approximate flux of charged hadrons from collisions and backgrounds are shown as a function of radial distance in figure 9.4. Table 9.1 gives the expected collision (background) flux for luminosities ranging from 10^{28} - 10^{34} cm^{-2}s^{-1} based on the simulations at

$R = 40$ cm from the beam. Also shown are the estimated particle rates for the current BSC tile sizes ($\sim$500 cm^2) and for a hypothetical tile sizes of 100 cm^2 and 2.5 cm^2 sized tile for the detector upgrade.

TABLE 9.1: The channel sizes of the upgrade can be estimated based on the luminosity limit of the current system and the expected flux at $\sim$40 cm radius, $\mathcal{L} = 10^{34}\text{cm}^{-2}\text{s}^{-1}$ and $\sqrt{s} = 7$ TeV.

$\mathcal{L}$ cm^{-2}s^{-1}	Φ cm^{-2}s^{-1}	Per 500 cm^2 s^{-1}	Per 100 cm^2 s^{-1}	Per 2.5 cm^2 s^{-1}
Collision Rates (Background Rates) [Hz]				
10^{28}	1 (10^{-5})	500 (10^{-3})	100 (10^{-3})	2.5 (10^{-5})
10^{29}	10 (10^{-4})	5×10^3 (10^{-2})	1×10^3 (10^{-2})	25 (10^{-4})
10^{30}	100 (10^{-3})	5×10^4 (10^{-1})	1×10^4 (10^{-1})	250 (10^{-3})
10^{31}	1×10^3 (10^{-2})	5×10^5 (10^{-0})	1×10^5 (10^{-0})	2.5×10^3 (10^{-2})
10^{32}	1×10^4 (10^{-1})	5×10^6 (10^1)	1×10^6 (10^1)	2.5×10^4 (10^{-1})
10^{33}	1×10^5 (10^0)	5×10^7 (10^2)	1×10^7 (10^2)	2.5×10^5 (10^0)
10^{34}	1×10^6 (10^1)	5×10^8 (10^3)	1×10^8 (10^3)	2.5×10^6 (10^1)

A scintillator tile size of 100 cm^2 at a larger radius could provide the acceptance required for beam background monitoring whilst keeping the collision induced signal down to a manageable rate. The following sections look in detail at the minimum bias and beam background event influence in the BSC plane.

9.2.1 Minimum Bias MC information

CMSSW simulations using minimum bias events were carried out on a MC dataset tuned to event pile-up of $\sim$10, as experienced during the Summer 2011 running. The analysis counts all particles passing through the HF front face plane, where the BSC is located, from approximately 20,000 events. The counts were taken from the reconstructed simulation of the HF calorimeter response. It should be noted that as the radius of the HF η rings increases, so too does the area coverage of each ring. This is however not true for the outer most ring (η ring 1) which is smaller due to mechanical constraints. See figure 2.5(a). For this reason, the data from the outer ring has been omitted. Figure 9.5 shows the hit rates for each HF η ring , normalised for pile-up. As expected, the flux of particles falls away at higher radii (smaller η) decreasing to 0.5 - 1 MHz at $|\eta| = 3$ resulting in an average of 1 hit/cm^2 every 2 - 4 bunch crossings at the 50 ns bunch spacing expected in 2012.

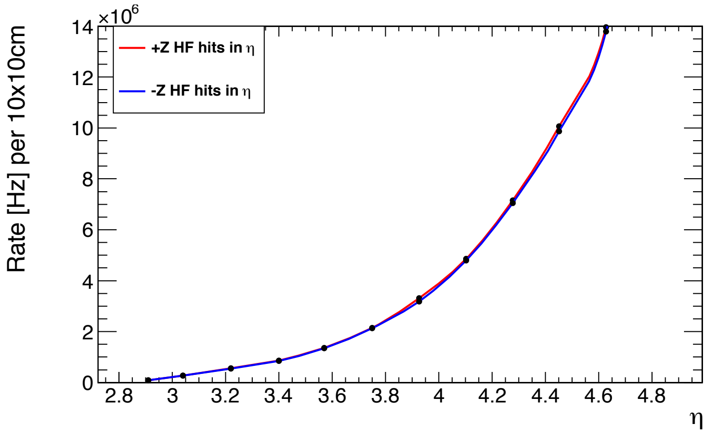

(a) All particles

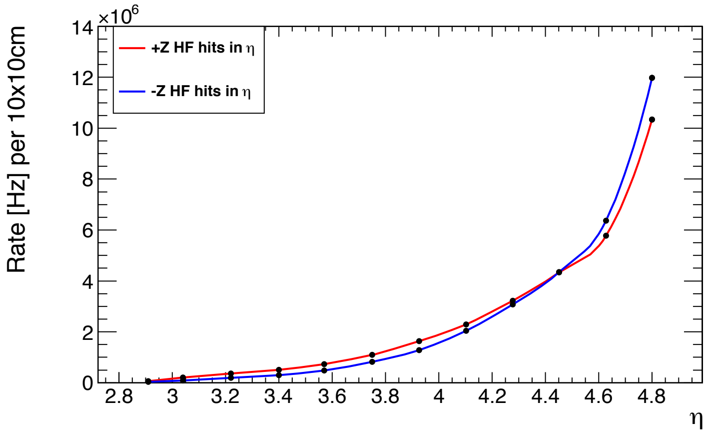

(b) Excluding photons and neutrons

FIGURE 9.5: The expected rate of detecting minimum-bias events with a 10×10 cm tile in various η locations on the HF front face. The inner tiles of the present system are located at 4.26< $|\eta|$ <4.76. The scintillators for the upgrade are to be located at $\sim$ 2.9 - 3.3 to prevent saturation at the expected $\mathcal{L} = 10^{33}$ cm^{-2}s^{-1} in 2012.

The data shown in figure 9.5(a) includes all particles at all energies. Not all particles will cause the scintillator tiles to respond. Low energy photons (<5 MeV) and neutrons for example, will barely interact with the scintillator. After applying a cut on particle type and energy, the effective flux through the scintillator tiles is slightly reduced, as shown in figure 9.5(b). Figure 9.6 shows the kinetic energies of the particles which are incident on the HF calorimeters between the pseudo-rapidity ranges of 2.85< $|\eta|$ <3.31 and would therefore pass through the region of interest for the BSC upgrade. Most of the signals induced into the BHC from collisions will be due to protons, charged pions and, indirectly from high energy photons. Thus, any hits to the tiles by particles stemming from the I.P are very likely to cause a signal.

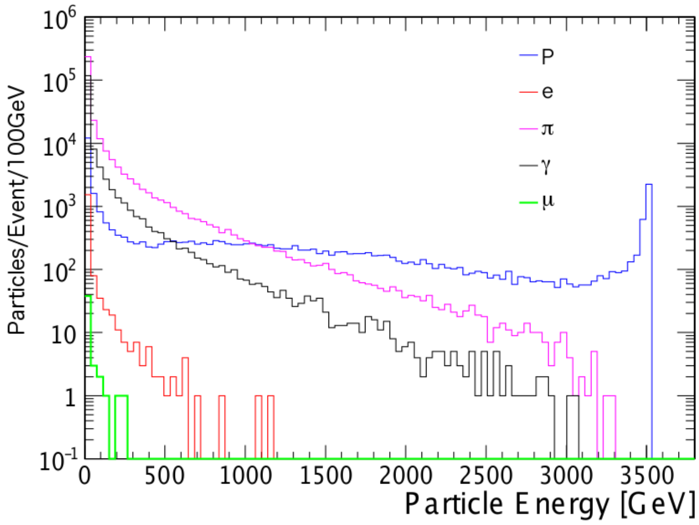

FIGURE 9.6: MC simulations of the energy of the minimum bias particles incident on the HF between 2.85< $|\eta|$ <3.31 per event. Pythia_6_Tune_ Z2 at 7TeV (Pile-up = 10) MC data used for this simulation.

9.2.2 Beam Halo Simulations

Simulations of the beam backgrounds were made with FLUKA [136]. The sources of beam backgrounds are inelastic and elastic interactions with residual gas nuclei inside the beam pipe, beam halo originating from cleaning inefficiencies where scattered protons are not absorbed by the collimators, and particles stemming from the collisions at neighbouring interaction points [137]. The quantities of beam gas vary, depending on the quality of the vacuum in the long-straight sections near CMS. The presence of beam halo is inevitable. As well as contaminating the data and impeding offline analysis, excessive beam halo rates can cause the Cathode Strip Chamber detectors of CMS to power trip. It also suggests poor beam dynamics with an increased likelihood of a total beam loss.

Figure 9.7 shows the results of the CMS beam halo simulations, where beam 1 halo particles, traveling from +Z to -Z have been tracked through the entire CMS detector. Only the muons of the beam halo are able to penetrate through the HF (+Z) to hit the BSC +Z tiles, shown as the green points in left of figure 9.7. As they pass through, the halo particles interact with the materials of the CMS

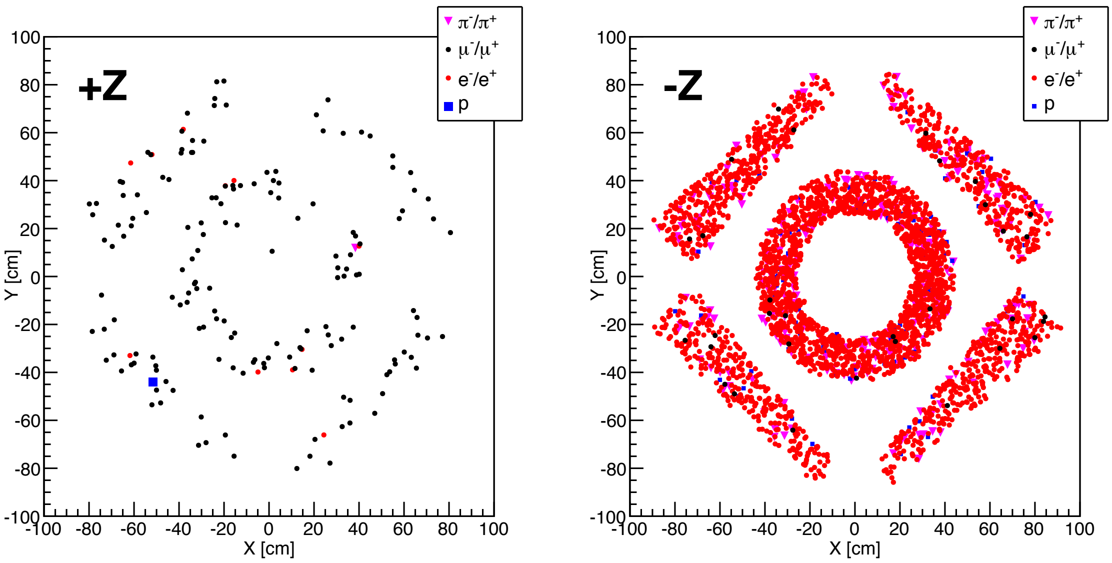

FIGURE 9.7: FLUKA driven background simulations processed in CMSSW show the particle spectra that hits the BSC scintillator tiles. The plots show the result of Beam 1 (+Z to -Z) halo particles interacting with the +Z BSC1 tiles (left) and the -Z BSC1 tile (right). Only $\mu^{\pm}$ are able to penetrate through the material to interact with the +Z BSC tiles. As they traverse, many electrons are produced through collisions which then interact with the -Z BSC tiles.

detector, causing showers of electrons to hit the opposite BSC detector (-Z). Many of the original muons also interact with the BSC -Z with a time-of-flight of ∼73 ns. The situation is the same for the beam 2 halo simulations. The outgoing beam background particles interacting with BHC detector will be accompanied by the collision products. At the expected interaction pile-up rates (>10) in 2012, the outgoing side of the detector will see particles from every collision, meaning there is little information to be gained by the Time-of-Flight approach used in the BSC system.

If beam halo is present, it is likely to accompany every bunch passing through CMS, including non-colliding bunches. Using the knowledge of the timing of the incoming bunches relative to the outgoing electron showers and collision products, it is possible to measure the beam halo during 2012 *pp* running. This is explained in section 9.3.5.

9.3 Scintillator based upgrade

Based on the results of the beam halo and minimum bias simulations, a tile size of 10×10 cm was chosen for the upgrade and a radial distance of approximately 80 - 90 cm ($3.18 < |\eta| < 3.3$) to detect the beam halo whilst keeping the collision detection to a minimum. An additional remit of the upgrade design was that it must be able to be installed and extracted with the minimum resources and risk to the CMS beam pipe. The mechanical design and the development and tests to the scintillator tiles are explained in the following sections.

9.3.1 Prototype Tiles

Two test tiles were produced using Eljan EJ-200 plastic scintillator which has an identical composition and performance to the Bicron BC-408 scintillator used in the original BSC detector. The tiles had the dimensions of 10×100×100 (D×W×H). Both tiles had four wavelength shifting fibres (WLS) embedded and glued into their surface; one with two fibres running along the centre of the top and bottom surfaces (known as the 'centre tile'); the other had four fibres embedded along one edge (known as the 'edge tile'). They are shown in figure 9.8. The edge tile (a) is slightly easier to manufacture but the center tile (b) was expected to give better performance due to the reduced distance between the WLS fibres and the farthest point of the tile (5 cm).

Both tiles were tested in the lab using muon particles generated from high energy cosmic ray interactions, as explained in the following section.

Prototype tile tests

Each tile was connected to a new ET9902KB photomultiplier and placed between two smaller (4cm × 10cm) scintillators whose signals were put through coincidence logic to act as a cosmic trigger. Any cosmic particle passing through both trigger scintillators must also pass through the test tile. 20,000 cosmic measurements were taken with the tiles connected to the PMT via a 1 m clear optical fibre. Another 20,000 measurements were taken with a 7 m clear fibre to measure the potential loss of signal from the tiles that are farther away from the PMTs.

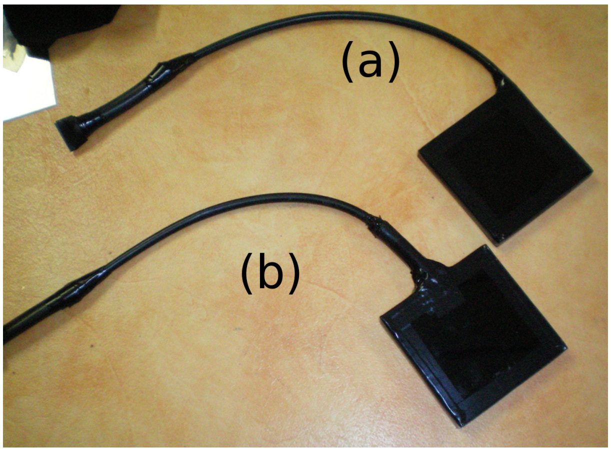

FIGURE 9.8: A photograph of the two upgrade test tiles. (a) with the wavelength shifting fibers running along the edge, (b) with the fibres running along the center of the top and bottom surfaces of the tile.

These measurements were made with a PMT voltage of 1100V and the signal being fed through a $\times 10$ LeCroy 612A PM amplifier before passing to the oscilloscope. An additional measurement was made with the PMT voltage increased to 1200V and the $\times 10$ amplifier removed. This latter measurement runs the PMT beyond the manufacturer's recommended voltage but gives a much better M.I.P detection efficiency without the need for additional amplification modules. Finally, measurements were made with a 2.5 m extension fibre connected in-line to quantify the losses due to additional optical connections.
A Matlab program was written to communicate with the Lecroy LT384 oscilloscope and retrieve information about the waveforms of each triggered acquisition. The whole waveform was sampled and integrated and the maximum amplitude also recorded. The results are shown in figures 9.10 to 9.13. Simultaneously, the efficiency was measured by counting the number of signals over a set threshold compared to the total number of triggers. The logic was set up such that the signal from the test tile would only be counted if the trigger coincidence fired *and* the signal was greater than the discriminator threshold (100 mV if the $\times 10$ amplifier was used; 30 mV if the signal was fed directly to the discriminator and the PMT voltage increased to 1200V).
Table 9.2 shows the results of the efficiency measurements.

The number of photoelectrons per minimum ionising particle ($N_{p.e}$) was calculated by fitting a Gaussian distribution to the pedestal and to the signal curves. By taking the mean of the pedestal and signal Gaussian distributions ($< x >_{ped}$

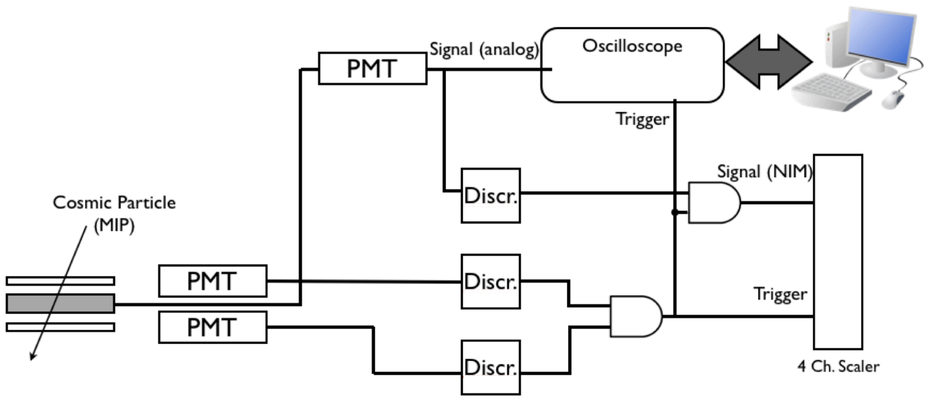

FIGURE 9.9: Schematic diagram of the scintillator tile efficiency measurement setup. The logic ensures that signals from the test tile are able to be counted only when there was a trigger from the coincidence of the smaller trigger scintillators. A PC running Matlab recorded the amplitudes and integrated signals which were used to calculate the number of photoelectrons per M.I.P.

TABLE 9.2: Results of the efficiency tests carried out on the prototype test tiles using the set up as described in the text.

Setup (Tile type / Discriminator threshold /Fibre Length)	H.V	Efficiency	±
Center Tile. 30mV. 1m clear fibre.	1200V	82.3%	4.7%
Edge Tile. 30mV. 1m clear fibre.	1200V	72%	4.7%
Center Tile. 30mV. 7m clear fibre.	1200V	79.2%	4.7%
Edge Tile. 30mV. 7m clear fibre.	1200V	76.2%	4.7%
Center Tile. 100mV. 1m clear fibre. ×10 amp	1100V	94%	4.7%
Edge Tile. 100mV. 1m clear fibre. ×10 amp	1100V	93.8%	4.7%
Center Tile. 100mV. 7m clear fibre. ×10 amp	1100V	91.6%	4.7%
Edge Tile. 100mV. 7m clear fibre. ×10 amp	1100V	90.4%	4.7%

and $< x >_{sig}$ respectively) and the standard deviation of the signal curve (σ_{sig}), the number of photoelectrons can be calculated by:

$$N_{pe} = \left(\frac{< x >_{sig} - < x >_{ped}}{\sigma_{sig}} \right)^2 \tag{9.1}$$

The integrated signal distributions with the results of the N_{pe} calculations are shown in the following figures. Both tiles performed almost equally well, with the 'center tile' having a slightly higher light yield ($N_{pe} = 15$ compared to $N_{pe} = 13$ for the 'edge tile'). Additionally, the center tile proved to be more mechanically suitable overall and was therefore the chosen design.

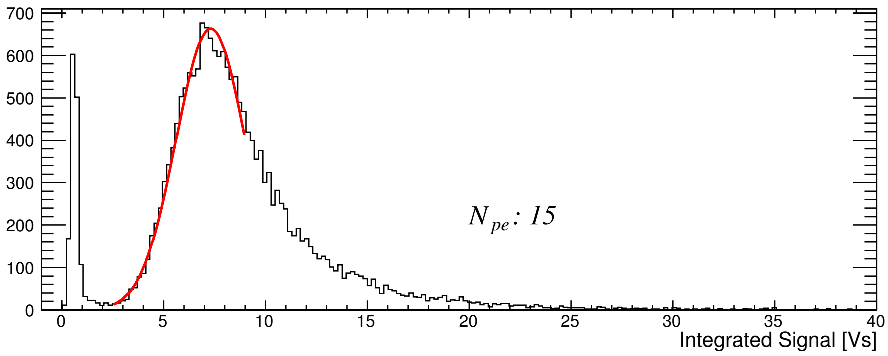

FIGURE 9.10: Center Tile. Integrated voltage from 20000 cosmic measurements triggered with small (4×10 cm) scintillators. PMT voltage @ 1100V. Raw signal amplified ×10.

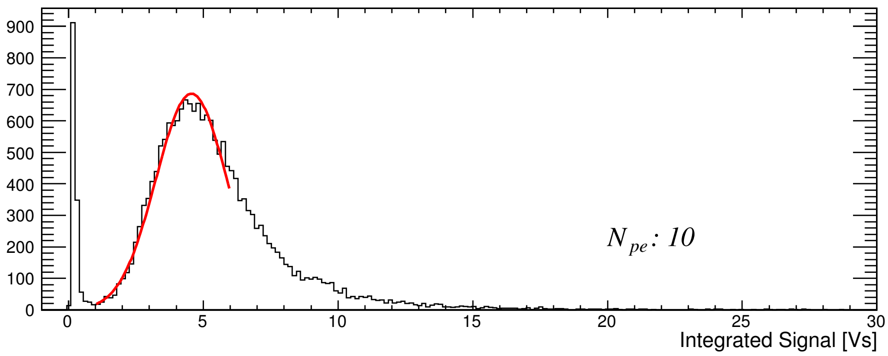

FIGURE 9.11: Center Tile. Integrated voltage from 20000 cosmic measurements triggered with small (4×10 cm) scintillators. PMT voltage @ 1100V. Raw signal amplified ×10. 2.5m pig-tail fibre in-line.

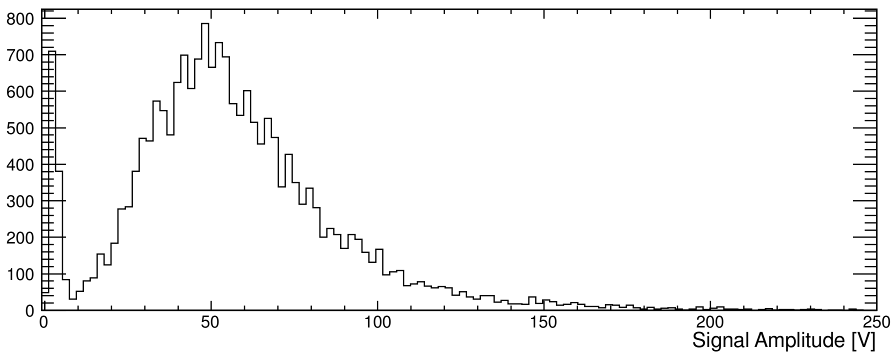

FIGURE 9.12: Center Tile. Amplitude spectrum from 20000 cosmic measurements triggered with small (4×10 cm) scintillators. PMT voltage @ 1200V. No amplification. 2.5m pig-tail fibre in-line.

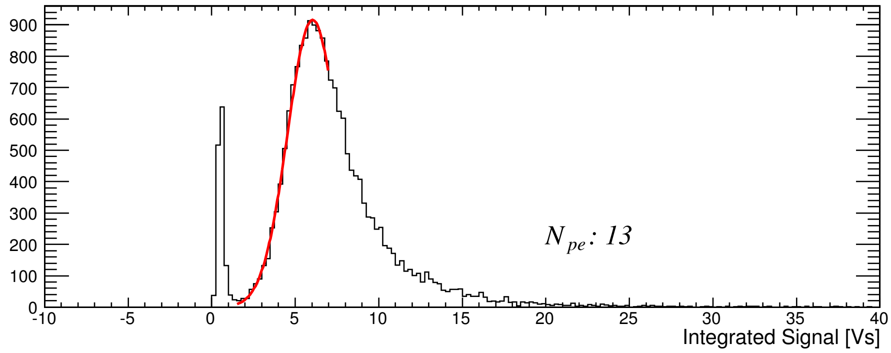

FIGURE 9.13: Edge Tile. Integrated voltage from 20000 cosmic measurements triggered with small (4×10 cm) scintillators. PMT voltage @ 1100V. Raw signal amplified ×10.

9.3.2 Albedo considerations

As a consequence of the compactness and large material budget of the CMS detector, short term activation and emission of low energy particles has been noticed in several sub-detectors during 2011, including the BSC. They are referred to as 'albedo' and are thought to consist mainly of thermal neutrons (<1 eV) and photons emitted after neutron capture. The thermal neutrons themselves do not induce a signal into the BSC, but the gamma photos emitted from their capture can indirectly cause ionisation through Compton scattering in the scintillator tile that subsequently causes scintillation which is detected. For each gamma photon, the mechanism of detection is very inefficient. However, there is a very large quantity of albedo during *pp* running and even a detection efficiency of $\ll$1% can lead to non-negligible signal production.
Figure 9.14 shows the expected neutron and photon energy ranges and their time-of-flight for studies relating to the BCM2. These ranges were used to determine the energy spectra to use in the following studies of albedo suppression.

A common method of suppressing undesirable signals in a M.I.P sensitive detector is to take the coincidence of two overlapping detector channels with an absorber material sandwiched in between. For low energy neutrons, high density borated polyethylene is commonly used in CMS. For the gamma photons, a higher density material such as lead needs to be used. The following simulations employed the use of BDSim [139], a command line interface to the standard GEANT 4 libraries. It provides a means to simulate the passage of particles through any

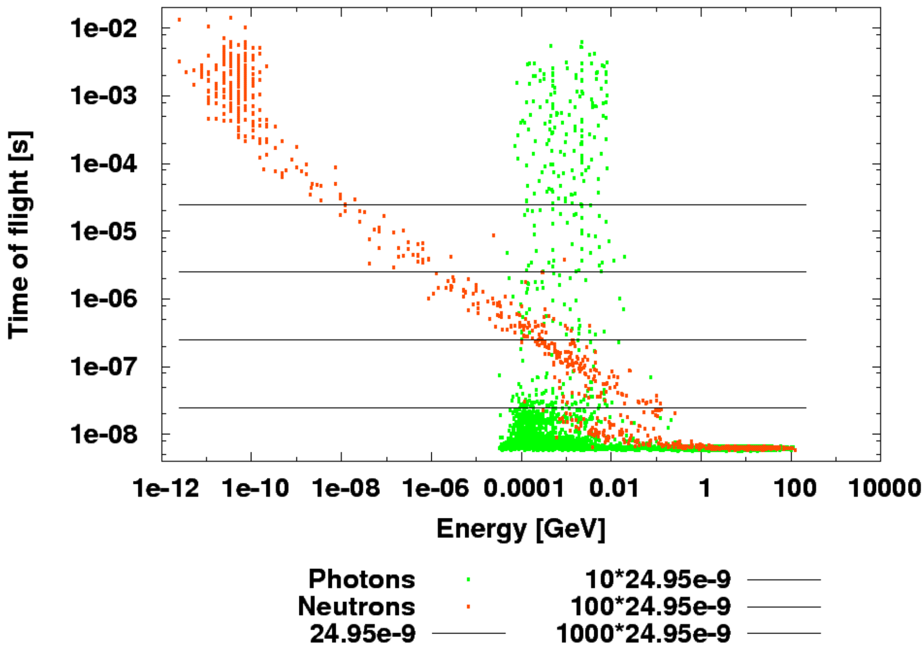

FIGURE 9.14: The time-of-flight of albedo particles as a function of their kinetic energie, measured at the BCM2 [138] detector. Time $t = 0$ refers to the time of the bunch crossing [134].

chosen material and geometry. For these studies, a high precision physics list, (QGSP_BERT_HP) was used. It incorporates all neutron interactions and the most up-to-date cross section data. Figure 9.15 is an example of a neutron (green line) passing through a model of the scintillator tiles (red) which are covered with 1 mm of aluminium (grey) and separated by 5 cm of polyethylene (blue). The light-elements in the polyethylene (PE) material have a large cross-section to neutron elastic scattering, slowing down the neutrons until they are finally thermalised or captured [140].

Using BDSim, a model of the PVT scintillator tiles was created. Each tile was 1 cm thick, 10×10 cm in width and height and covered with a 1mm layer of Aluminium, similar to the expected final design. Simulations were made with the tiles in various configurations, starting with the two tiles in contact; then with a 1 cm air gap between them. This was followed by filling the gap with PE of increasing thickness ranging from 1 cm to 5 cm in 1 cm steps. Additionally, for

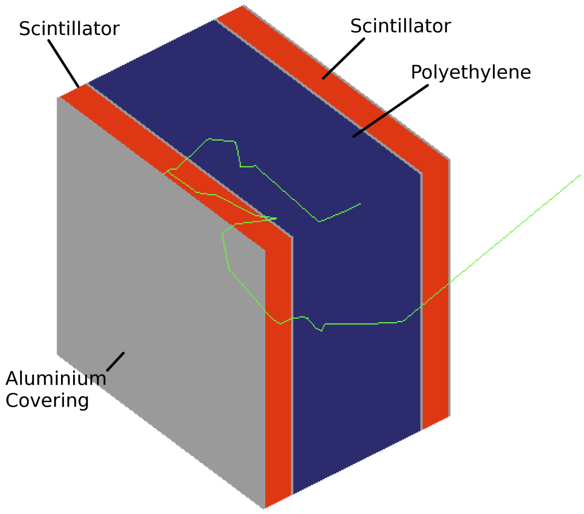

FIGURE 9.15: An example of a simulated 10 keV neutron passing through aluminium covered PVT scintillator tiles separated by 5 cm of polyethylene using BDSim [139]. BDSim is a command line interface for GEANT 4.

each configuration, the neutron energies varied from 100 eV, 1 keV, 10 keV and finally 100 keV.
Scoring planes (SP) were set in 5 Z-locations (see figure 9.15).

- SP1: First surface of the 1st Aluminum layer.
- SP2: First surface of the 1st Scintillator layer.
- SP3: First surface of the PE (Air) layer.
- SP4: First surface of the 2nd Scintillator layer.
- SP5. Back surface of the last Aluminum layer.

Particles passing these scoring planes in the +Z direction (the same direction as the primary neutron beam) were counted to see if the effects of a polyethylene layer between the tiles of the upgrade system would be beneficial. The results for 100 eV neutrons on to the scintillator tiles with 1 cm of air and 1 cm of PE are shown in figures 9.16 and 9.17 respectively. The first scintillator layer is between Sample Points 2 and 3, whereas the second scintillator layer is situated between Sample Points 4 and 5. The absorber (air) gap is between points 3 and 4. The complete set of results from the polyethylene absorption studies can be found in Appendix D.

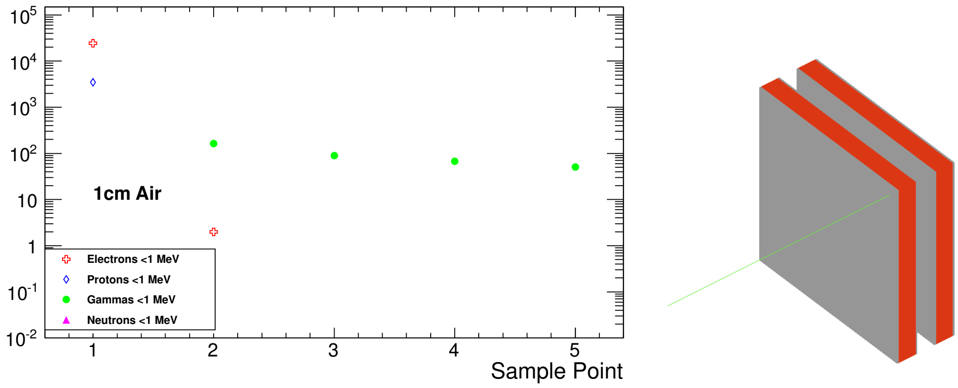

FIGURE 9.16: BDSim model showing 1 cm of air between two 10mm scintillator (red) tiles covered with 1mm Aluminium (grey).

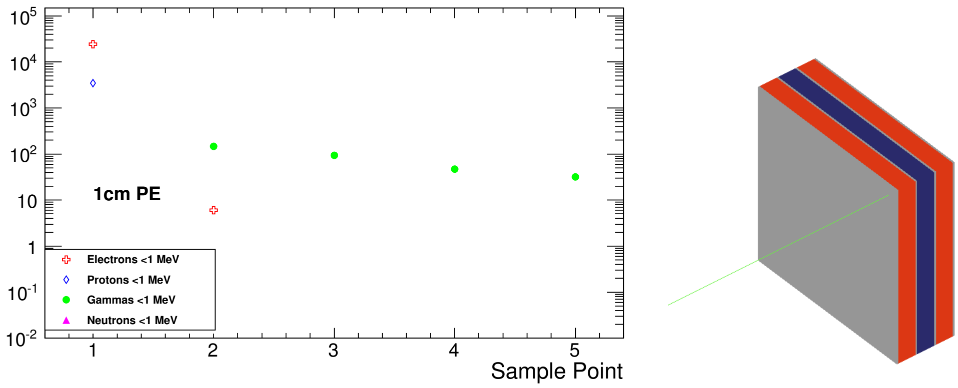

FIGURE 9.17: Neutron flux simulations. 1cm of PE between two 10mm scintillator tiles covered with 1mm Aluminium.

The studies show that there is practically no benefit gained by the use of a 1 cm thick PE absorber between tiles. The benefit of using PE only becomes apparent at thicknesses greater than 4 - 5 cm. As will be described later in this section, the mechanical limitations imposed on the design limited the PE thickness to 1 cm. There is therefore no benefit gained from using PE in the upgrade design to limit the effects of albedo. The method of suppressing the effects of albedo can be achieved by the requirement of a strict, high amplitude coincidence between overlapping tiles.

9.3.3 Light yield measurements

The final scintillator tiles to be used in the upgrade were cut at the CERN scintillator lab and transported to the INFN[†] laboratory in Bologne, Italy. 2.2mm grooves were cut and polished in to the tiles, running along the centre on both the upper and lower faces. Wavelength shifting fibres with a reflective aluminium coating on one end, were inserted and lightly glued into place. The scintillator was then wrapped in white Tyvek sheet (polyethylene) to reduce light loss and wrapped again in black Tedlar sheet (polyvinyl fluoride) to prevent light leaks. The non-aluminium coated ends of the four WLS fibres were glued into plastic connectors which interface with the clear plastic PMMA fibres that connect in turn to the PMTs. Each tile was then transported back to CERN and connected to the test set up shown in figure 9.9 to measure the amplitude and integrated signal spectra from cosmic rays. The number of photoelectrons were calculated as before (Eq 9.1). Table 9.3 gives the results of these measurements. The integrated signal spectra for all the tiles is given in Appendix E.

[†]Istituto Nazionale di Fisica Nucleare

TABLE 9.3: List of N_{pe} for each tile.

Tile Number	N_{pe}	Tile Number	N_{pe}
01	18	18	15
02	17	19	17
03	16	20	15
04	16	21	16
05	16	22	19
06	16	23	15
07	16	24	15
08	17	25	16
09	17	26	16
10	16	27	16
11	17	28	17
12	15	29	17
13	16	30	20
14	16	31	16
15	17	32	16
16	15	33	16
17	15		

9.3.4 Mechanical design

The BHC front end hardware was designed to be mounted to the I.P facing planes of the HF calorimeters. This region is usually inaccessible during short technical stops as it requires several days to lower the calorimeters to floor level. In situ, the calorimeters can be moved away from the CMS end-caps by up to 4 cm, the limitation coming from the nearby beam-pipe support mechanism. To allow the removal and installation of the BHC, the front-end structure was designed to fit through a 3 cm gap between the HF front face and the HE3 endcap. Figure 9.18 shows the prototype of the design with perspex plastic tiles and wavelength shifting fibres set out to aid in defining the exact layout of the active elements. Also shown is one section of the BHC structure with the plastic scintillators locked into place in the metal frame.

Four such quadrants were made for each end of the detector. Clear optical fibres were connected directly to the WLS fibres and taken away from the front face to the outer radial edge of HF via channels cut into the steel structure. Figure

FIGURE 9.18: (Top) Mock-up of the scintillator tile layout with the bending radius of the wavelength shifting fibres show. (Bottom) The wrapped scintillator tiles installed into the metallic frame.

9.19 shows the mechanical structure of the BHC with the channel names and a photograph of the fully installed system on the $+Z$ end of CMS.

CMS is a dense, compact detector with 12000T of iron return yoke surrounding the magnet. This large material budget combined with the high radiation levels from the unprecedented luminosity, causes *albedo* as explained in section 9.3.2. In order to veto on albedo, two overlapping tiles were installed as shown in figure 9.20. Only events in which both tiles fired in coincidence are counted in an attempt to reduce the effects of albedo on the muon halo count rates. The CAD drawing on the left of figure 9.20 shows the typical single tile as used by all other channels in the BHC system. On the right is shown the double layered *albedo veto* tile.

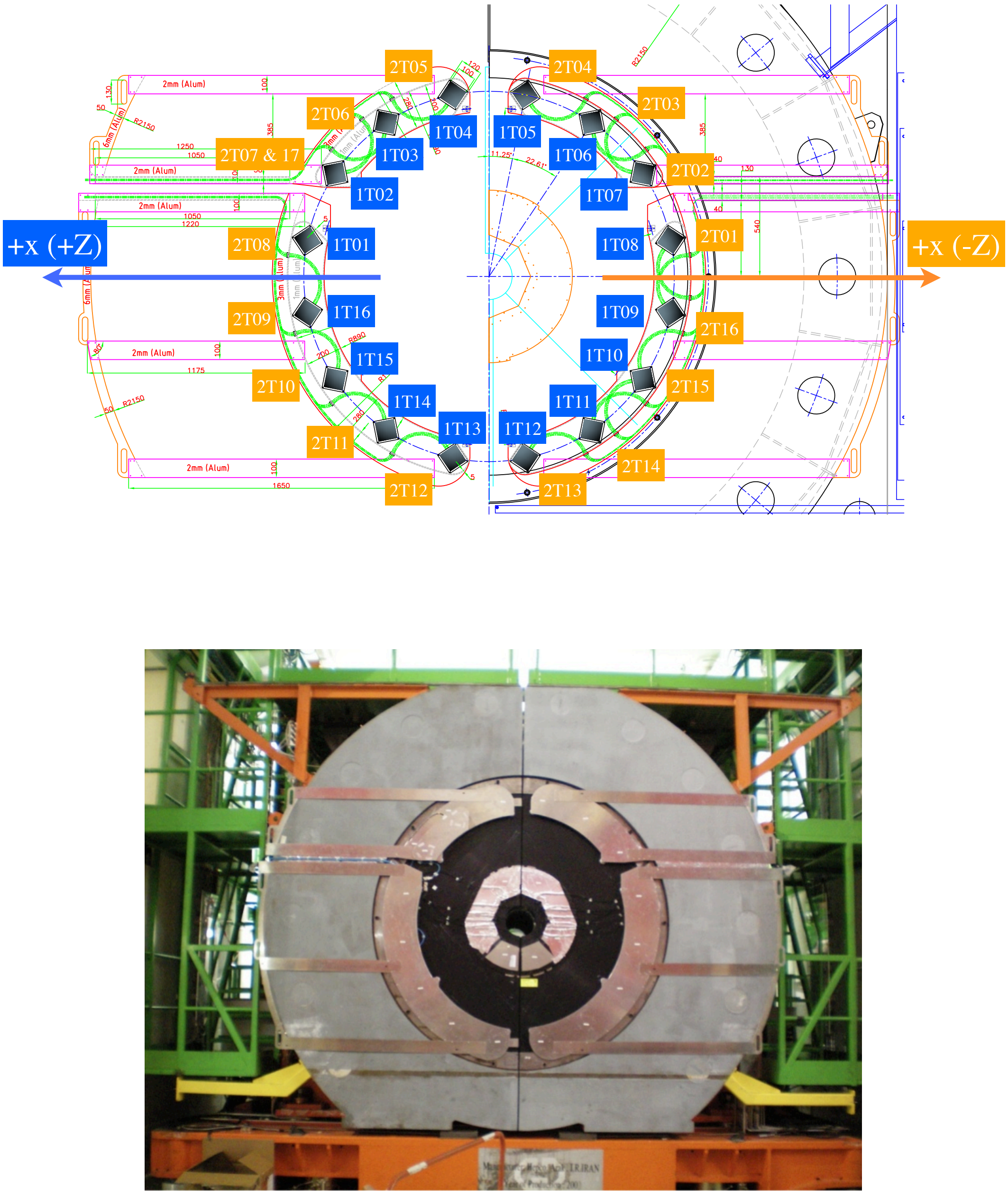

FIGURE 9.19: (Top) The final mechanical design of the BHC detector showing the 10×10 cm tiles around the periphery of the HF front face. One quadrant shown. (Bottom) The Beam Halo Counter installed on the Hadronic Forward Calorimeter in CMS.

These enter the readout system and pass through a 2-fold coincidence module, the output of which should fire only in the case of true, high energy muon halo events.

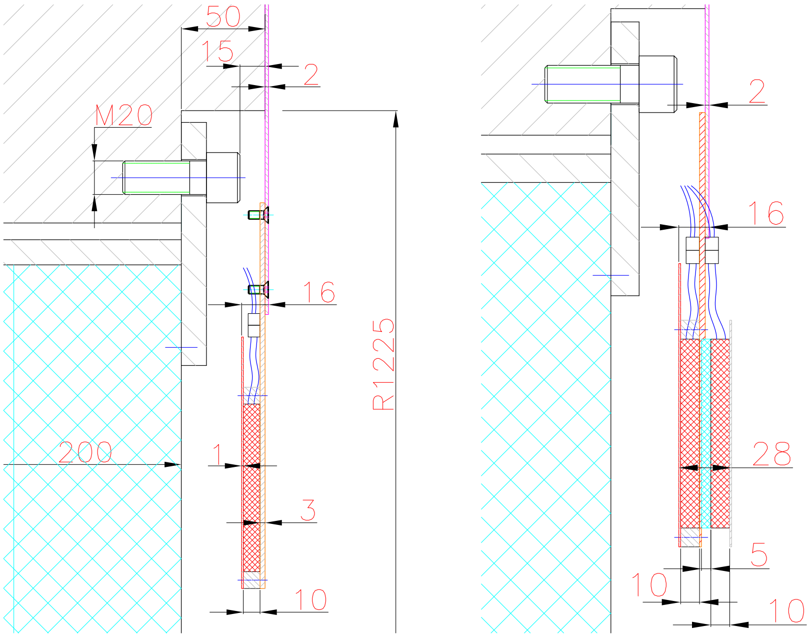

FIGURE 9.20: CAD drawings of the BHC albedo rejection tiles. (Left) The standard 'single tile' design. (Right) The overlapping 'albedo trigger' tiles.

9.3.5 Readout System

The BHC readout system was designed with two aims in mind. First, it must be capable of monitoring the muon halo rates with various degrees of sensitivity. The exceptional progress that has been made towards the understanding of the LHC behaviour means that most beam injections are very 'clean' with very low quantities of beam background. However, there are situations of vacuum problems, beam gas events and '*UFOs*' which cause halo rates to increase rapidly. Prior to collisions, the halo can be measured in the absence of collision products and their albedo. In this scenario, only one or two channels are expected to give a signal within the gating window. However, during collisions at high luminosities, more tiles will be hit and effected by albedo so a halo counter based on more channels is needed. Secondly, the readout must be adaptable for providing halo triggers to the Global Trigger (GT) system as its predecessor, the BSC did before. It must also be extendable to provide minimum bias triggers to the GT of various sensitivities during the 2012 Heavy Ion runs where Pb+Pb and Pb+p interactions will take place. Figure 9.21 shows the concept behind the monitoring of muon halo. It shows Beam 1 (Blue) passing from left to right while Beam 2 (Red) passes from right to left. At this time, the two incoming beams are passing through the centre of the BHC detector and their associated muon halo - shown as small red and blue dots - pass through and interact with the BHC tiles. A veto gate is opened (permitting the signal to propagate) as the incoming beam halo crosses the detector and closes N ns later and before the outgoing collision particles stemming from the previous collision reach the BHC tiles. This method is superior to using purely the Time-of-Flight method seen in the previous BSC detector as it focuses only on the halo particles by discriminating on their precise timing. Only late-arriving *albedo* particles can cause a signal within the $\overline{\text{veto}}$ window. The albedo contribution is measured in one scaler module. A second scaler is connected to a *post-quiet gate* signal. This gating signal opens N ns after the last colliding bunch - determined by the BPTX AND signal (i.e. Coincident incoming beams), and closes when the next colliding bunches are detected. N is adjustable depending on the bunch filling scheme and allows the albedo to decay before opening the post-quiet veto gate and measuring *only* the muon halo contribution. The BHC readout schematic is shown in figure 9.22.

The raw single channel signals enter from the left side into NIM linear fan-out modules which split the signals to go to the ADCs and to the halo logic. Next, each channel passes through a CAEN V256B discriminator with the threshold of 50 mV. The output of each channel is counted in two scalers, mostly for tuning and debugging purposes. The discriminators also have a 'summing' output, Σ which provides a current proportional to the number of input channels over threshold. With a 50 Ω load, this current equates to 75 mV per channel over threshold. The Σ signals (one for $+Z$, one for $-Z$) are taken to two channels of linear fan-out via small (100 pF) capacitors required to remove the large D.C offset. The linear fan-outs split each of the Σ signal four ways. The Σ copies are then fed into another pair of V258B discriminators with thresholds set for the desired sensitivity. For example, the most sensitive halo signal of $\geq$1 channel over threshold can be achieved by setting a threshold of $0 \geq Thr \geq 75$ mV. Lower sensitivities can be achieved by setting higher thresholds, thereby requiring more channels to respond in order to fire the halo trigger. The action of discrimination is only permissible when the veto gate is open - i.e. the signal connected to the veto input is low. There is a choice of two possible gating signals:

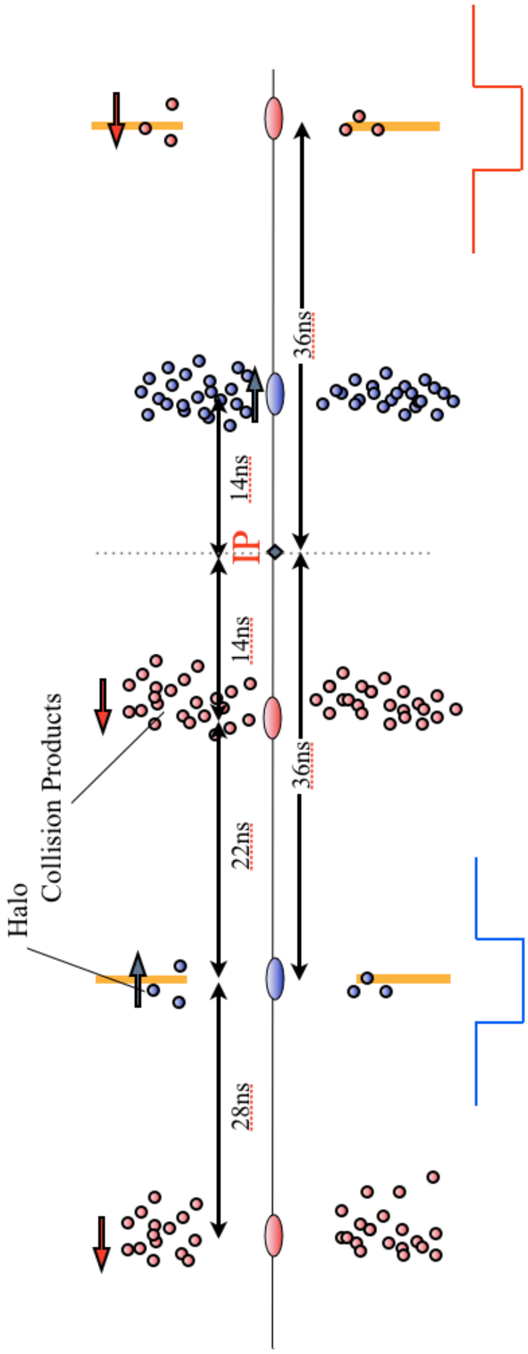

FIGURE 9.21: Detection of the muon halo relies on accurately timing of a veto gate in coincidence with the incoming beam. The gate is open as the halo passes through the BHC tiles, shown in orange, and closed before the passing of the outgoing collision products.

- B1 and B2 gates: Allows halo monitoring during colliding and non-colliding bunches. More prone to albedo effects.

- $\mathrm{B1\overline{B2}}$ and $\mathrm{B2\overline{B1}}$: Allows monitoring only during non-colliding bunches. This lessens effects from albedo but provides much lower count statistics due to the low fraction of non-colliding bunches in the 2012 fills.

After the discriminator, the outputs are counted in two V560E scalers, one of which is vetoed by the previously mentioned '*post-quiet gate*' signal to minimize the effects of post-collision albedo. All scalers publish their 1 Hz rates to DIP [51] and are displayed in the CMS control room.

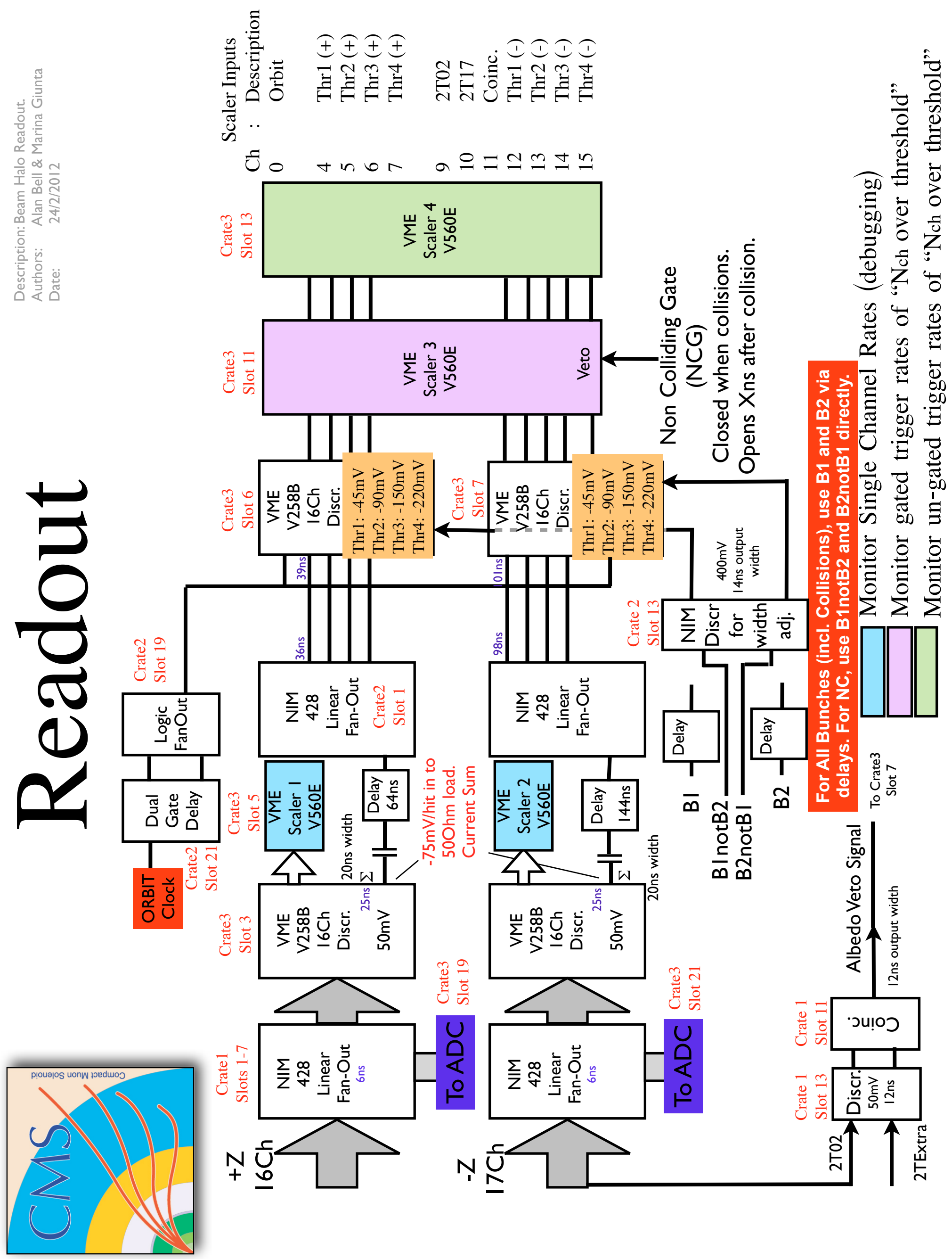

FIGURE 9.22: Schematic diagram of the BHC readout system using NIM logic modules and VME hardware to measure the muon halo in CMS. The system is capable of monitoring halo before and during collisions at bunch spacing of $\geq$50 ns.

9.3.6 Commissioning & Early Results

The Beam Halo Counter detector was commissioned during the first beams and collisions of 2012. The PMT voltages were scanned whilst measuring the average signal amplitude from each channel to produce a turn-on curve, providing an approximate baseline for the individual channel voltage settings. Further fine tuning was done with colliding beams and high luminosity ($\mathcal{L} \approx 10^{34}$ cm^{-2}s^{-1}). The Σ signals were timed in with the BPTX derived veto gating signals during collisions. As the collision rate is at least 10^5 more than the halo rate, expected from 2010 simulations, it was not possible to see the signals from the halo. Instead, the veto gating signals were brought into coincidence with their corresponding Σ signal (B1 with Σ +Z, B2 with Σ -Z), then retarded by 73 ns to coincide with the expected arrival time of the incoming halo. The oscilloscope screen captures shown in figure 9.23 show how the signals from collisions were used to determine the expected time of the muon halo.

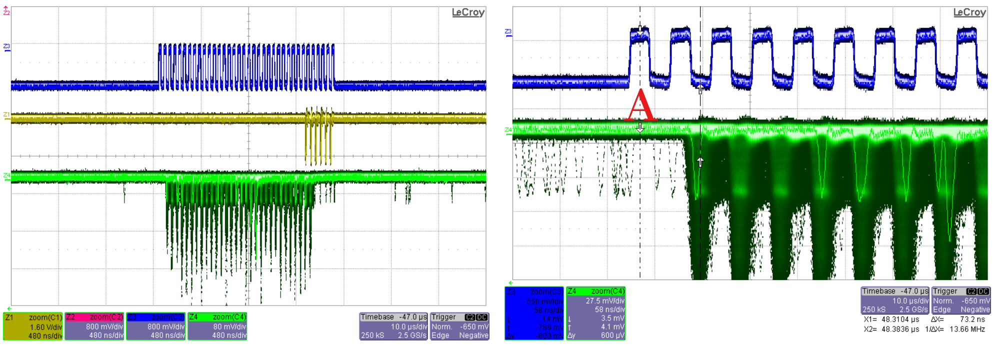

FIGURE 9.23: (Left) The BPTX B1 veto gate signal in blue (low = veto); BPTX B1$\overline{\text{B2}}$ in yellow and the BHC Σ (+Z) shown in green. Oscilloscope in trace persist mode. (Right) The Σ signal from collisions is set 73.2 ns after the corresponding $\overline{\text{veto}}$ signal. Halo is expected to pass through the detector at time *A*.

The width of the non-colliding beam gating signals (B1$\overline{\text{B2}}$ and B2$\overline{\text{B1}}$) were adjusted to optimise the counting of inter-bunch halo (with albedo) without allowing contamination of collision products. These rates were passed to the two scalers. One of the scalers was veto'd by the use of the 'post-quiet gate' which allowed only those non-colliding bunches arriving 900 ns after the previous collision. This minimizes the amount of albedo activity counted.

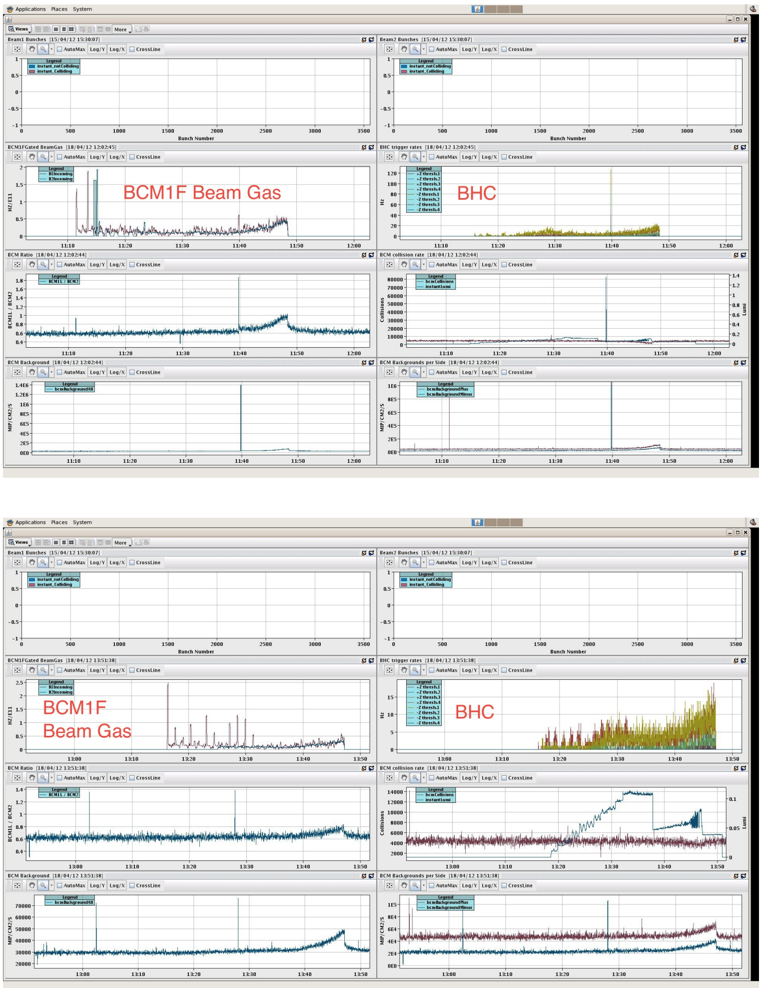

FIGURE 9.24: Signals from the Beams Conditions Monitor 1 - Fast (BCM1F) were in good agreement with the signals of the BHC after commissioning.

Figure 9.24 shows two examples of the correlation between the BHC signals with those of the independent BCM1F beam gas monitoring. The BHC, having a larger acceptance, is far more sensitive to beam backgrounds during injection and pre-collisions and provides important information for the CMS tracker and Cathode Strip Chambers which need ensured safety before switching on.

Further evidence that the BHC was able to detect beam losses in CMS came during the beginning of LHC fill 2911 when loss on Beam 2 occurred over a period of around 20 minutes. Figure 9.25(a) shows the LHC Page 1 information which clearly shows the rapid loss in Beam 2 (Red line) in the left hand plot as around $5{\times}10^{13}$ protons were lost. Figure 9.25(b) shows the response of the BHC.

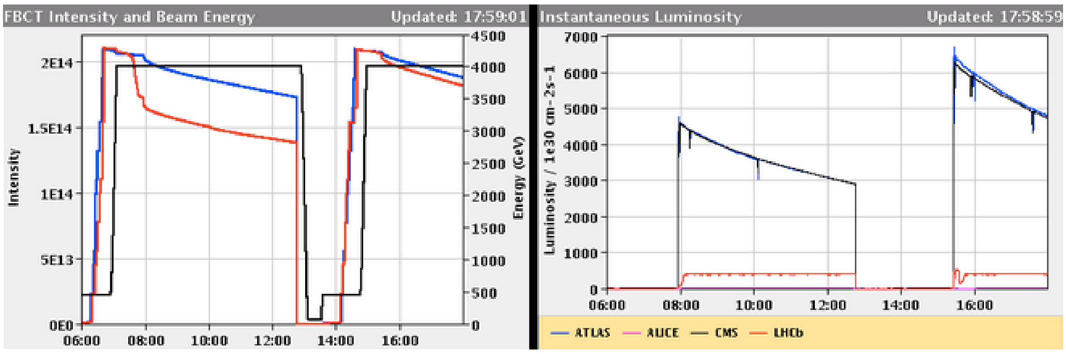

(a) The LHC Page 1 information showing the losses in Beam 2 (Red line, left-hand plot)

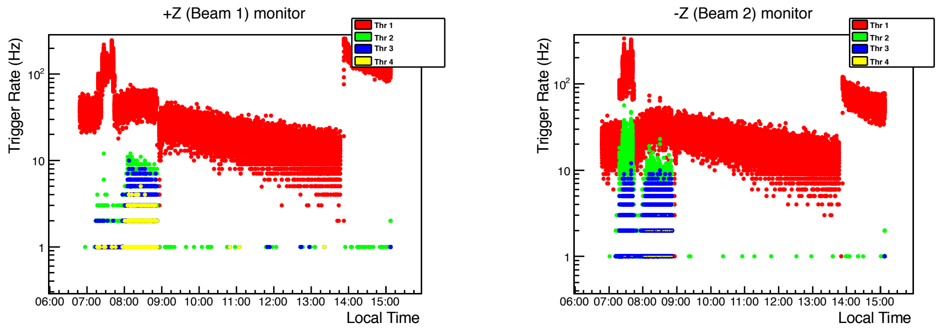

(b) The response of the BHC during the beam loss shows an increase in activity in the -Z side triggers.)

FIGURE 9.25: Beam Losses during fil 2911 and the BHC detector response.

Analysis of the BHC performance will continue through the 2012 - 2013 *pp* and Heavy Ion runs until the LHC Long Shutdown period.

Automatic voltage control with PVSS

When beams are injected into the LHC, several steps are followed. As far as the experiments are concerned, the steps are as follows:

- **Injection Probe Beam** This involves an initial, low intensity bunch injection during which a number of safety checks of the different accelerator sub-systems are carried prior to injecting higher beam intensities.
- **Injection Setup Beam**. An increased number of bunches allows for more precise measurements of the accelerator optimisation.
- Once the LHC has been optimised with stable circulating (low intensity) beams, the **Injection Physic Beam Mode** begins. During this mode, the

full bunch occupancy and intensities are injected in several steps until the full required bunch pattern is complete.

- At this point, the beam energies are 450 GeV. The **Ramp** mode then occurs, accelerating the beams from 450 GeV up to (currently) 4 TeV per beam.

- Once the target energy is reached, the **Flat Top** status is declared during which, more LHC system checks are carried out to test for stability and beam losses.

- At this stage, the two beams are crossing close each other, but kept separate in the vertical (horizontal) plane in the case of CMS (ATLAS), by magnets. The **Squeeze** mode refers to the point when the β function is reduced and the beams are made to cross.

- The penultimate state is **Adjust**. In this mode, the collimators are aligned and various beam adjustments are made until optimal collision rates are seen from each experiment. It is usually at this stage that collisions are first seen and particle rates in the sub-detectors of the experiments increases rapidly.

- Finally, **Stable Beams** mode is declared and data recording in the experiments can begin.

It is important for the BHC sub-detector to remain sensitive to beam backgrounds during the beam injection to adjust modes. To achieve this, higher voltages are applied to the BHC photo tubes to make each channel M.I.P sensitive. However, once collisions start to occur in the Adjust mode, the higher particle flux would cause several channels to trip due to over-current protection. It was thus decided to implement an automatic High Voltage switching mode using PVSS[‡] [141], a CERN developed software used for monitoring multichannel power supply voltages and currents and allowing simple GUI based control of complex power systems. PVSS code was written to monitor the LHC beam modes. From 'Injection Probe Beam' through to 'Squeeze', the high voltages of the BHC channels are set to a 'Low Intensity', or equivalently, 'High Voltage' mode in which each channel is sensitive to single M.I.Ps. When the beam mode reaches 'Adjust', the PVSS software switches all the voltages to a 'High Intensity' or 'Low Voltage' mode, reducing the

[‡]Prozessvisualisierungs- und Steuerungs-System. *translated* Process Visualization & Control System.

efficiencies of all channels and preventing them from tripping due to over-current once collisions commence. The voltages are returned to the 'Low Luminosity' setting when the 'Beam Dump' status is received. With this software in place, the BHC is capable of monitoring beam backgrounds through the entire lifetime of the LHC fill. There is a short time - typically 1 minute - when the BHC is insensitive to the LHC backgrounds in the time between Adjust and the onset of collisions.

Chapter 10

Conclusions

This thesis has been based primarily on the design and construction of two CMS sub-detectors; namely the Beam Scintillator Counter (BSC) and the Beam Halo Counter (BHC). The BSC sub-detector was very successful in providing highly sensitive and accurate trigger information for CMS in the first two years of running (December 2009 - August 2011) and helped in capturing minimum bias and almost zero bias event data for initial studies of the CMS detector response. It was the first sub-detector in CMS to respond to *pp* collisions and, as such, gave instant feedback to the LHC Control Center that the LHC was performing perfectly at Point 5, its most distant location. The data subsequently recorded with the BSC technical trigger bits were promptly displayed for physicists, the media and the general public to view, demonstrating without any ambiguity that the LHC and CMS were off to a hugely successful start and that soon, more precise measurements and new physics discoveries would be made.

The BSC was used in many early CMS papers [54, 55, 57, 58, 142–144] mainly to trigger on the few potential collision events in CMS at very low luminosities which, due to their clean, unobscured behaviour, help to understand the CMS detector performance as well as the event backgrounds that would increase in subsequent, higher intensity collisions.

Furthermore, the BSC provided real-time and full-time feedback on the beam conditions independent of the CMS data acquisition system, which was vital during the LHC commissioning phases. The system finally reached the end of its useful life in early 2011 when the LHC luminosities resulted in signal rates beyond the capabilities of the BSC individual channels. However, during those two years, it had served its purpose as a beam monitor, basic technical trigger and more. It was decided that a replacement detector should be designed and installed which would be capable of monitoring beam backgrounds and beam gas events in CMS for 2012. This was realised in the form of the Beam Halo Counter which, after a rapid 6 months of design, construction and installation, was commissioned with the first beams of 2012 and is providing real-time beam background information for CMS, again, independently of the CMS data acquisition status.

This thesis also presented a measurement of the *pp* inelastic cross-section in CMS at $\sqrt{s}$ = 7 TeV using low pile-up data from early 2010. The measurement was made using a kinematic cut of $\xi \equiv \frac{M_x^2}{s} = 5\times10^{-6}$ and for 4 GeV and 5 GeV energy thresholds applied to the reconstructed HF energy hits (recHits) in order to test the stability of the result in terms of HF energy scaling. The resulting measurement of σ_{inel} for $\xi = 5\times10^{-6}$ was found to be,

$$\sigma_{(\xi>5\times10^{-6})} = 60.2 \text{ mb } \pm\ 0.2\ (stat)\ \pm\ 1.1\ (syst) \text{ mb}$$

in excellent agreement with the similar measurement of ATLAS (60.3 mb ± 0.55 mb) [122] and the CMS pile-up counting method (58.7 mb ± 2.0 mb) [119].
The extrapolation to the total inelastic cross-section, σ_{inel} at $M_x \geq M_p$ used several Monte Carlo event generators (PYTHIA 8, PHOJET, SIBYLL, EPOS, EPOS LHC AND QGSJETII-4). The PYTHIA and PHOJET models were tested at generator level by searching for particles with energy $E > E_{\text{cut}}$ and within the geometrical acceptance of the HF calorimeters. The same calculations were made at the full detector simulation level by reading out the recHit energy values as was done with data. The results of the two methods were found to be comparable and justified the use of SIBYLL, EPOS, EPOS LHC and QGSJETII-4 at the generator levels to obtain predictions from some of the currently acceptable phenomenological models. All model predictions were compared with the $\sigma_{\xi>5\times10^{-6}}$ result and with results from the independent cross section analysis of FWD-11-001. EPOS LHC was found to give the most accurate predictions of data and was chosen as the primary model for the extrapolation. The extrapolation yielded a result of,

$$\sigma_{inel} = 68.1 \text{ mb} \pm 0.5 \text{ mb(stat.)}\ \pm 2.4 \text{ mb(syst.)}$$

which is compatible with the result from ATLAS (69.4±9.3 mb) and the CMS pile-up counting method (68 mb±7 mb) but a little lower than the result from TOTEM ($73.5^{+2.4}_{-1.9}$). Furthermore, the results from the LHC experiments at 7 TeV suggest that no new physics phenomenon relating to pp interactions, come into play at this energy. We eagerly await for the LHC to achieve even higher energies, including the design goal of $\sqrt{s} = 14$ TeV, to test the hypotheses of new processes, such as the Donnachie & Landshoff hard Pomeron exchange, which may enable theorist to develop a single, full and accurate model of high energy proton-proton interactions which are currently not truly understood.

Appendix A

Luminosity Limits

BSC1 Plus End Inner Tiles

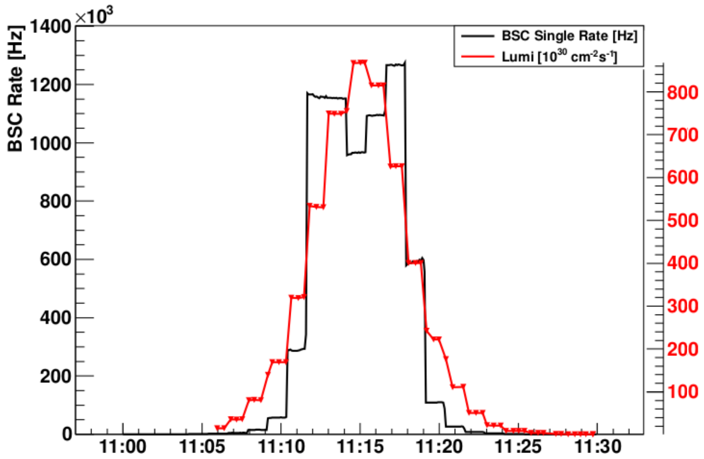

FIGURE A.1: Channel 1NBSC1D1. Lumi Limit = 800 $\times 10^{30}$cm^{-2}s^{-1}. High Voltage Setting: 900V. Max Rate: 1.2MHz.

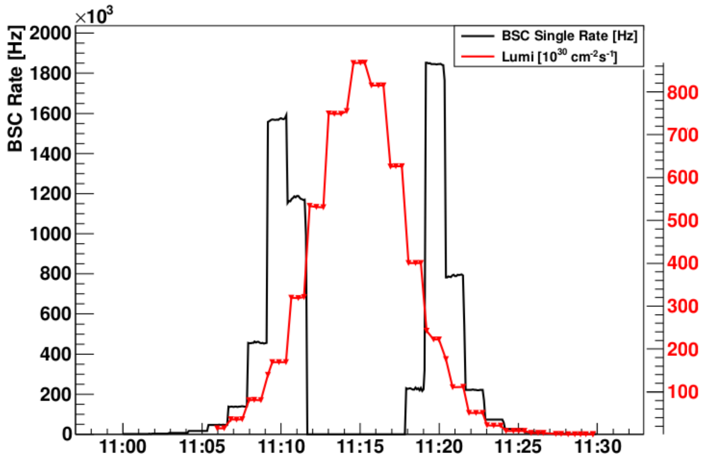

FIGURE A.2: Channel 1NBSC1D2. Lumi Limit = 430 $\times 10^{30}\mathrm{cm}^{-2}\mathrm{s}^{-1}$. High Voltage Setting: 950V. Max Rate: 1.8MHz.

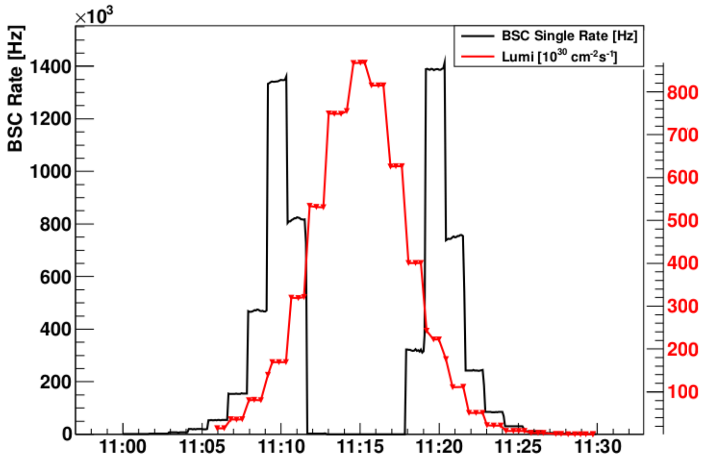

FIGURE A.3: Channel 1FBSC1D3. Lumi Limit = 420 $\times 10^{30}\mathrm{cm}^{-2}\mathrm{s}^{-1}$. High Voltage Setting: 925V. Max Rate: 1.4MHz.

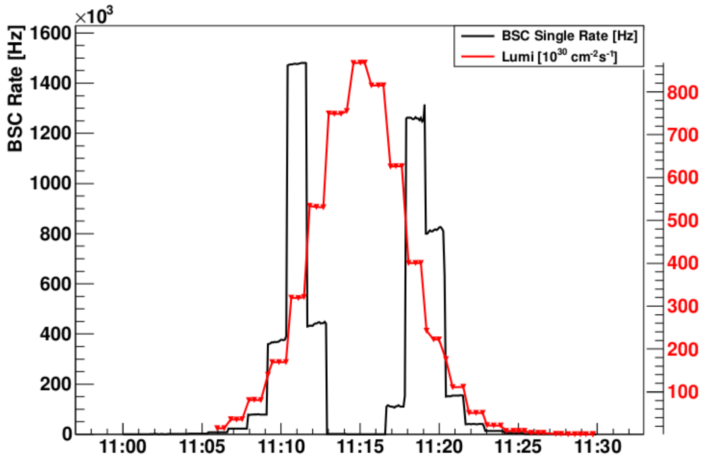

FIGURE A.4: Channel 1FBSC1D4. Lumi Limit = 420 $\times 10^{30}\text{cm}^{-2}\text{s}^{-1}$. High Voltage Setting: 860V. Max Rate: 1.5MHz.

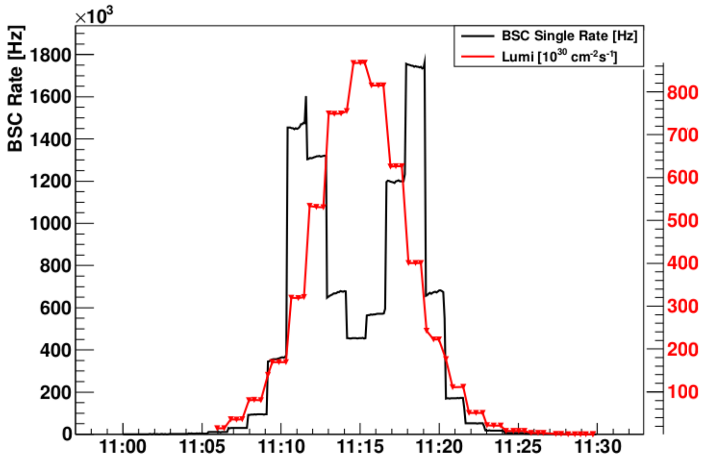

FIGURE A.5: Channel 1FBSC1D5. Lumi Limit = 640 $\times 10^{30}\text{cm}^{-2}\text{s}^{-1}$. High Voltage Setting: 930V. Max Rate: 1.8MHz.

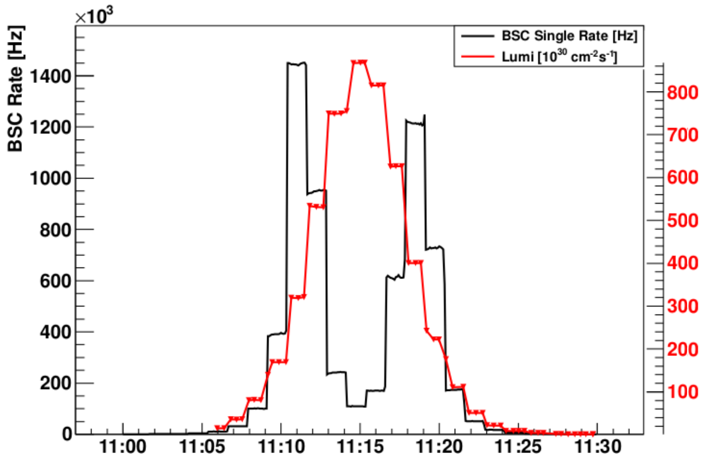

FIGURE A.6: Channel 1FBSC1D6. Lumi Limit = 550 $\times10^{30}$cm^{-2}s^{-1}. High Voltage Setting: 850V. Max Rate: 1.45MHz.

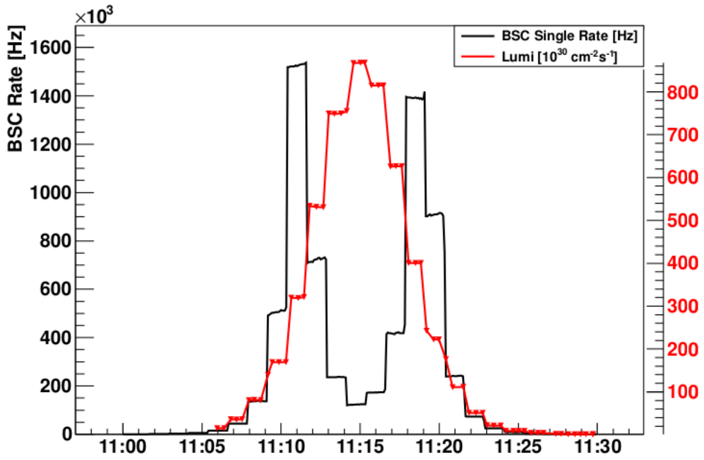

FIGURE A.7: Channel 1NBSC1D7. Lumi Limit = 480 $\times10^{30}$cm^{-2}s^{-1}. High Voltage Setting: 900V. Max Rate: 1.55MHz.

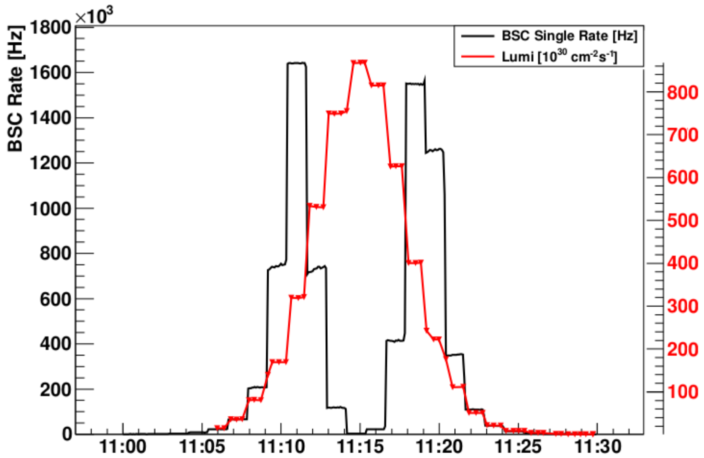

FIGURE A.8: Channel 1NBSC1D8. Lumi Limit = 480 $\times 10^{30}\text{cm}^{-2}\text{s}^{-1}$. High Voltage Setting: 1210V. Max Rate: 1.65MHz.

BSC1 Minus End Inner Tiles

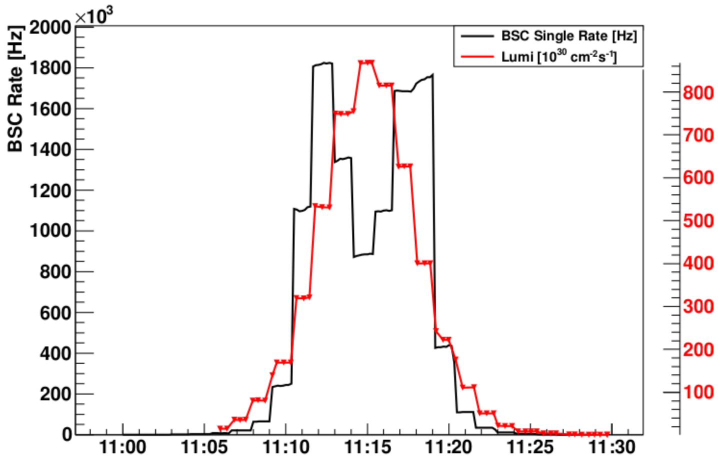

FIGURE A.9: Channel 2NBSC1D1. Lumi Limit = 700 $\times 10^{30}\text{cm}^{-2}\text{s}^{-1}$. High Voltage Setting: 1100V. Max Rate: 1.8MHz.

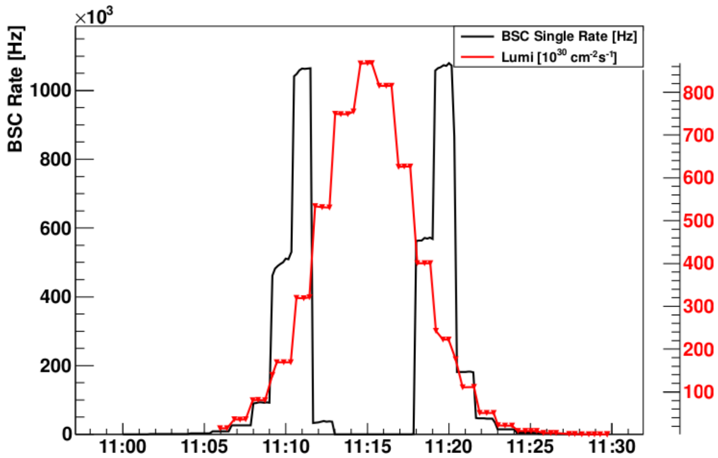

FIGURE A.10: Channel 2NBSC1D2. Lumi Limit = 460 $\times 10^{30}\text{cm}^{-2}\text{s}^{-1}$. High Voltage Setting: 800V. Max Rate: 1.4MHz.

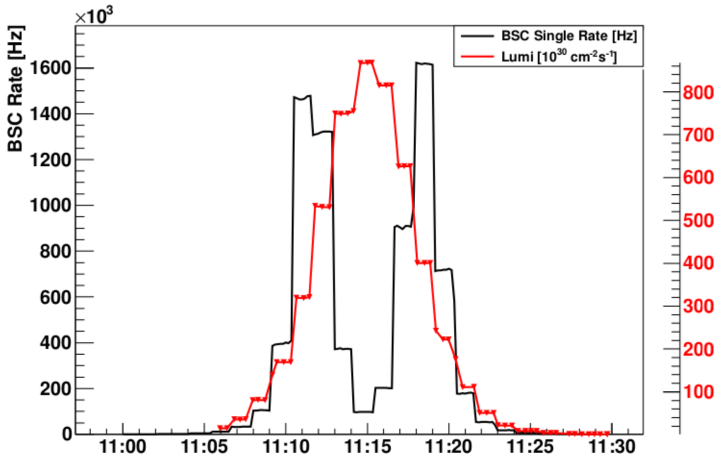

Figure A.11: Channel 2FBSC1D3. Lumi Limit = 640 $\times 10^{30}\text{cm}^{-2}\text{s}^{-1}$. High Voltage Setting: 900V. Max Rate: 1.6MHz.

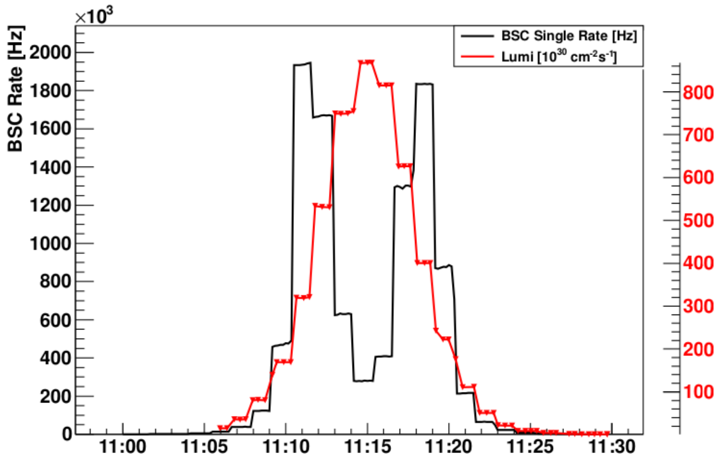

Figure A.12: Channel 2FBSC1D4. Lumi Limit = 650 $\times 10^{30}\text{cm}^{-2}\text{s}^{-1}$. High Voltage Setting: 1000V. Max Rate: 1.9MHz.

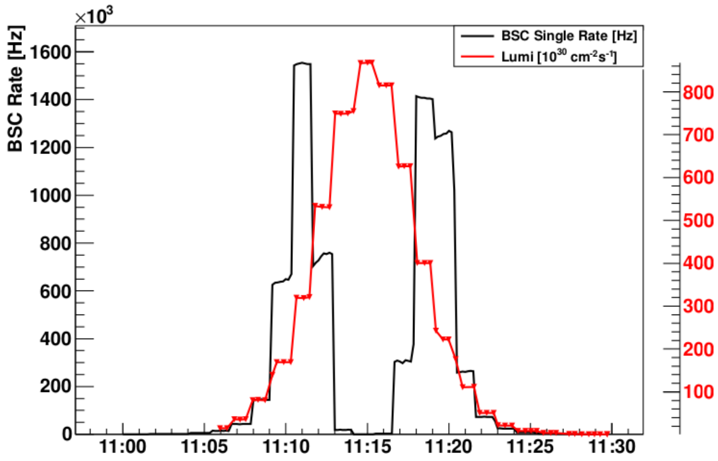

FIGURE A.13: Channel 2FBSC1D5. Lumi Limit = 450 $\times 10^{30}$cm^{-2}s^{-1}. High Voltage Setting: 870V. Max Rate: 1.5MHz.

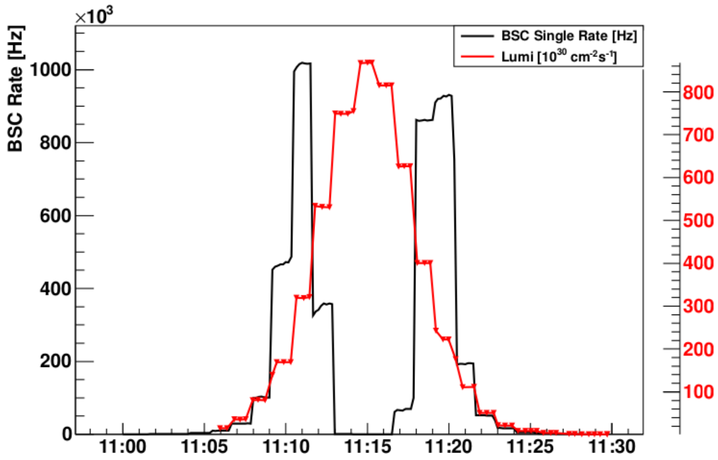

FIGURE A.14: Channel 2FBSC1D6. Lumi Limit = 400 $\times 10^{30}$cm^{-2}s^{-1}. High Voltage Setting: 800V. Max Rate: 1.0MHz.

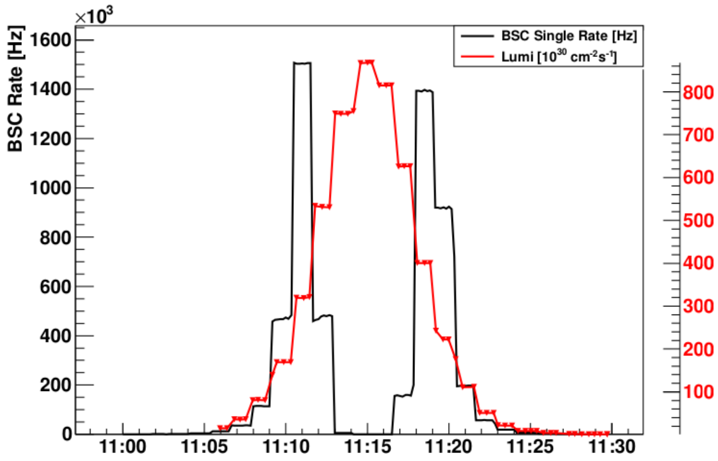

FIGURE A.15: Channel 2NBSC1D7. Lumi Limit = 420 $\times 10^{30}$cm^{-2}s^{-1}. High Voltage Setting: 870V. Max Rate: 1.5MHz.

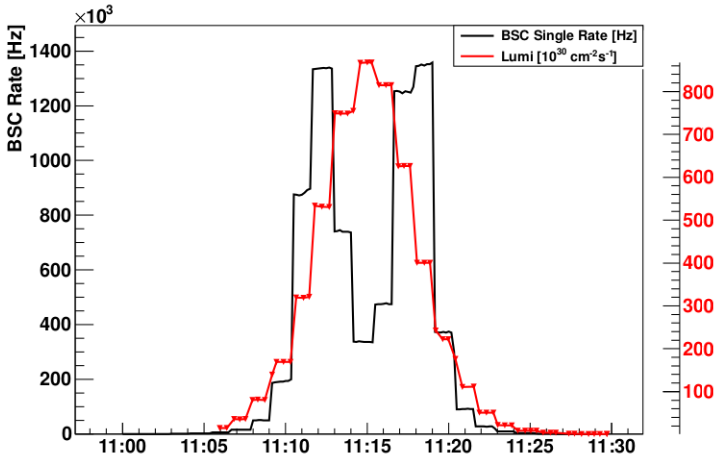

FIGURE A.16: Channel 2NBSC1D8. Lumi Limit = 650 $\times 10^{30}$cm^{-2}s^{-1}. High Voltage Setting: 930V. Max Rate: 1.35MHz.

BSC1 Plus End Outer Tiles

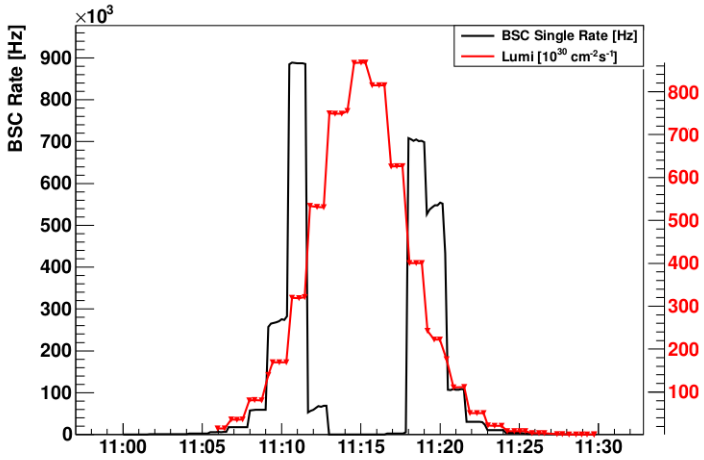

FIGURE A.17: Channel 1NBSC1P1. Lumi Limit = 420 $\times 10^{30}$cm^{-2}s^{-1}. High Voltage Setting: 910V. Max Rate: 900kHz.

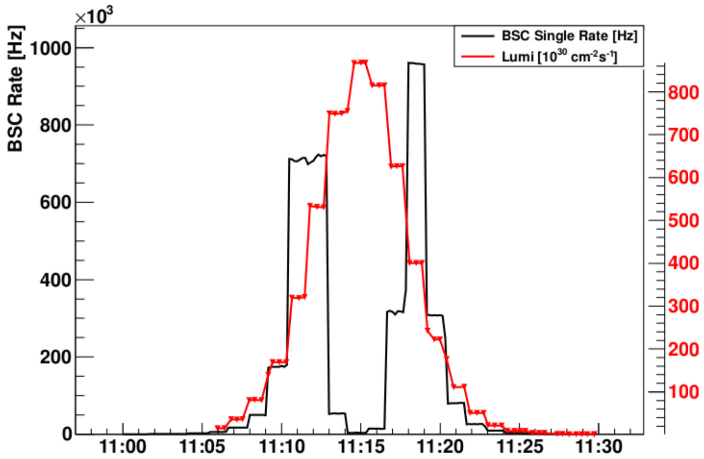

FIGURE A.18: Channel 1NBSC1P2. Lumi Limit = 600 $\times 10^{30}$cm^{-2}s^{-1}. High Voltage Setting: 1000V. Max Rate: 1.0MHz.

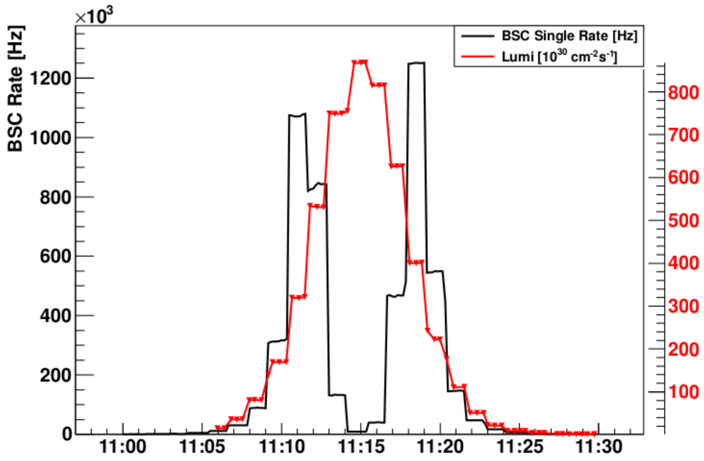

FIGURE A.19: Channel 1FBSC1P3. Lumi Limit = 560 $\times 10^{30}\text{cm}^{-2}\text{s}^{-1}$. High Voltage Setting: 980V. Max Rate: 1.2MHz.

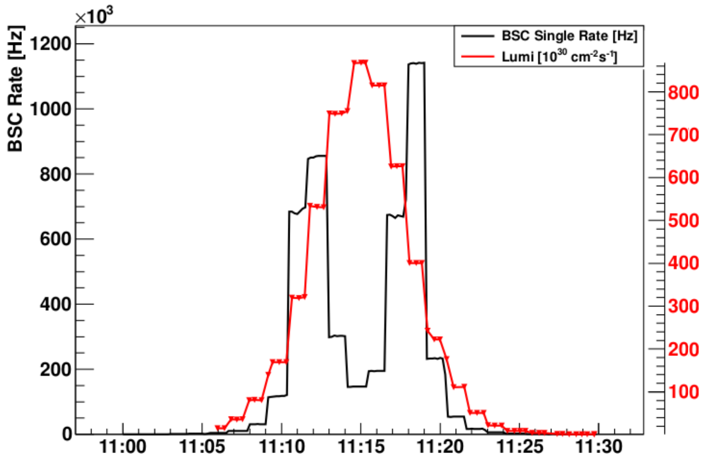

FIGURE A.20: Channel 1FBSC1P4. Lumi Limit = 620 $\times 10^{30}\text{cm}^{-2}\text{s}^{-1}$. High Voltage Setting: 875V. Max Rate: 1.1MHz.

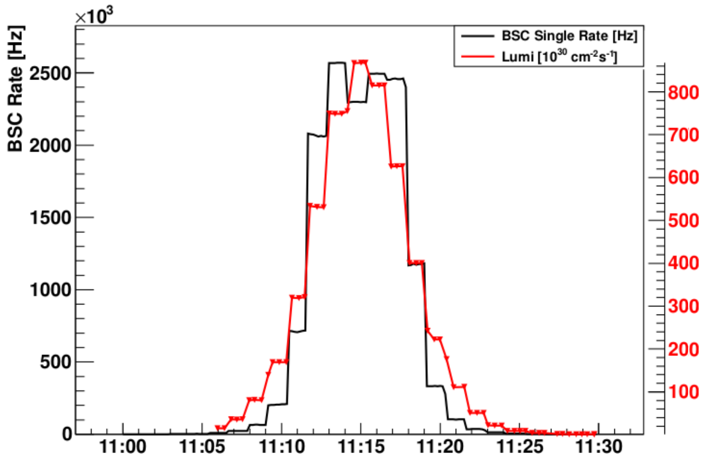

Figure A.21: Channel 1FBSC1P5. Lumi Limit = 800 $\times 10^{30}\mathrm{cm}^{-2}\mathrm{s}^{-1}$. High Voltage Setting: 1430V. Max Rate: 2.55MHz.

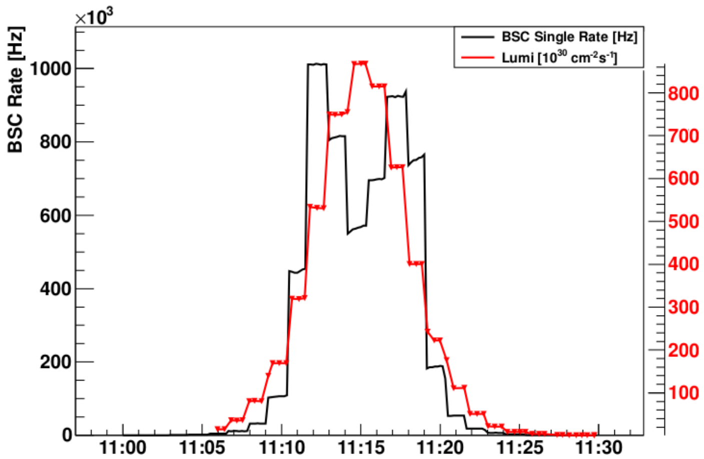

Figure A.22: Channel 1FBSC1P6. Lumi Limit = 760 $\times 10^{30}\mathrm{cm}^{-2}\mathrm{s}^{-1}$. High Voltage Setting: 880V. Max Rate: 1.0MHz.

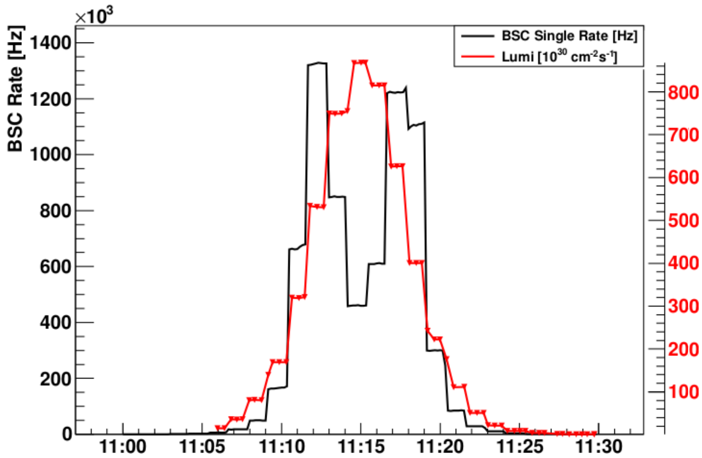

FIGURE A.23: Channel 1NBSC1P7. Lumi Limit = 700 $\times 10^{30}$cm^{-2}s^{-1}. High Voltage Setting: 1000V. Max Rate: 1.3MHz.

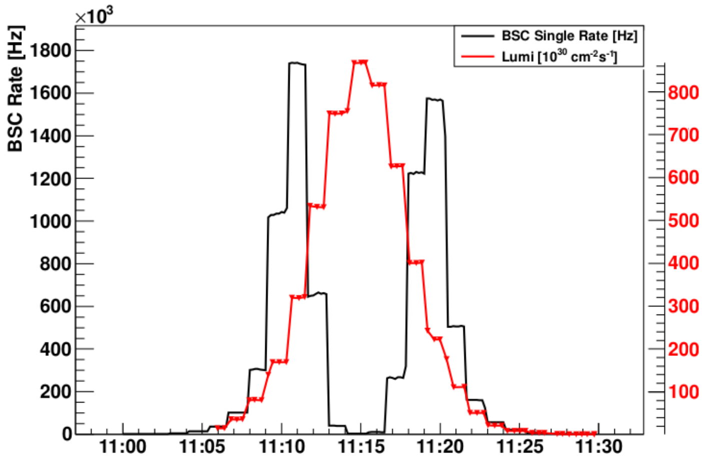

FIGURE A.24: Channel 1NBSC1P8. Lumi Limit = 460 $\times 10^{30}$cm^{-2}s^{-1}. High Voltage Setting: 1000V. Max Rate: 1.7MHz.

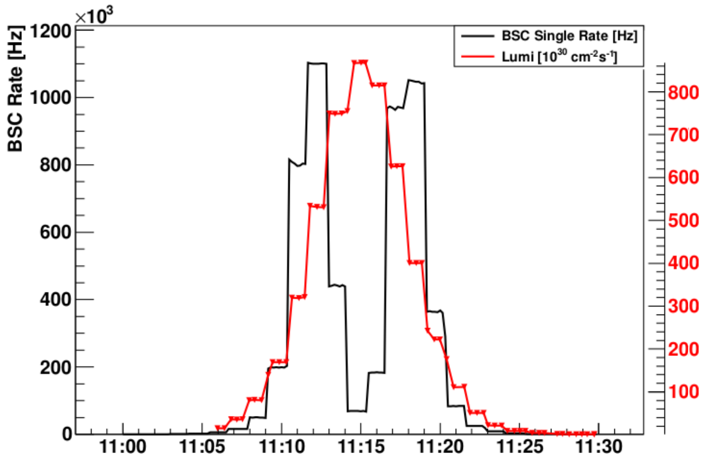

Figure A.25: Channel 2NBSC1P1. Lumi Limit = 650 $\times 10^{30}\mathrm{cm}^{-2}\mathrm{s}^{-1}$. High Voltage Setting: 900V. Max Rate: 1.1MHz.

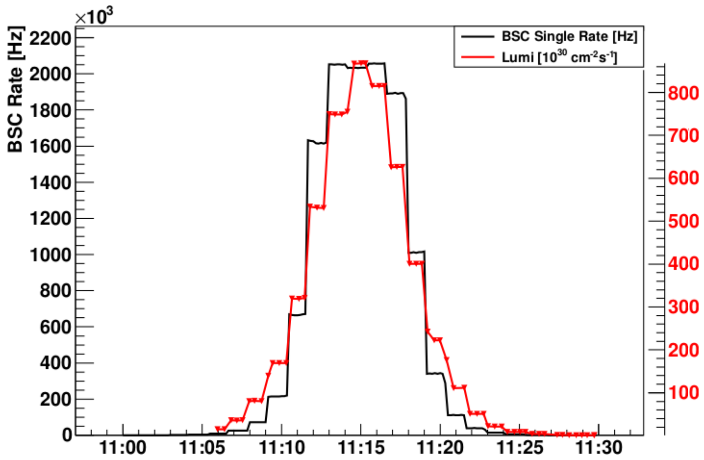

Figure A.26: Channel 2NBSC1P2. Lumi Limit = 860 $\times 10^{30}\mathrm{cm}^{-2}\mathrm{s}^{-1}$. High Voltage Setting: 1200V. Max Rate: 2.0MHz.

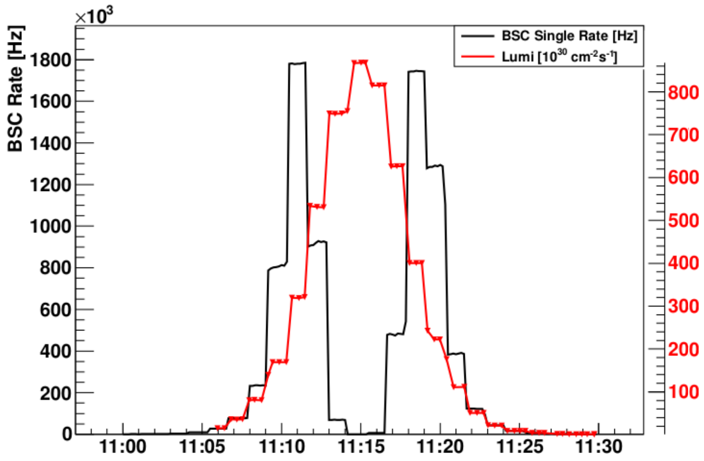

FIGURE A.27: Channel 2FBSC1P3. Lumi Limit = 500 $\times 10^{30}$cm^{-2}s^{-1}. High Voltage Setting: 900V. Max Rate: 1.8MHz.

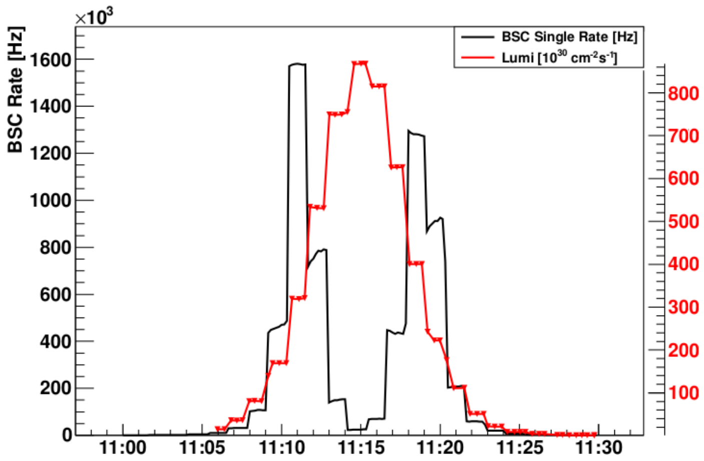

FIGURE A.28: Channel 2FBSC1P4. Lumi Limit = 450 $\times 10^{30}$cm^{-2}s^{-1}. High Voltage Setting: 875V. Max Rate: 1.6MHz.

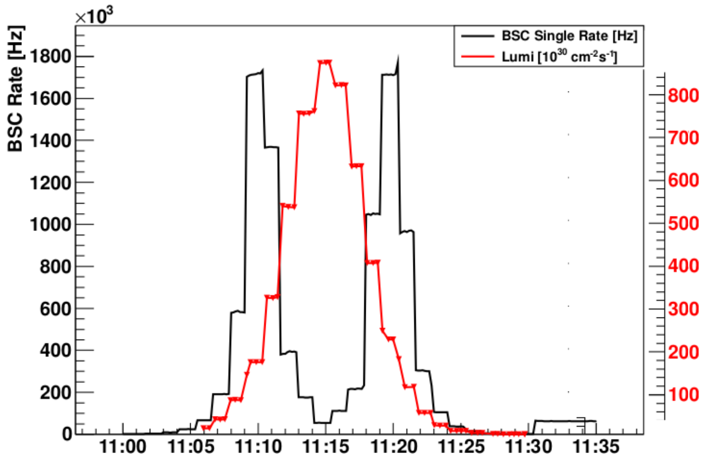

FIGURE A.29: Channel 2FBSC1P5. Lumi Limit = 400 $\times 10^{30}\mathrm{cm}^{-2}\mathrm{s}^{-1}$. High Voltage Setting: 1050V. Max Rate: 1.7MHz.

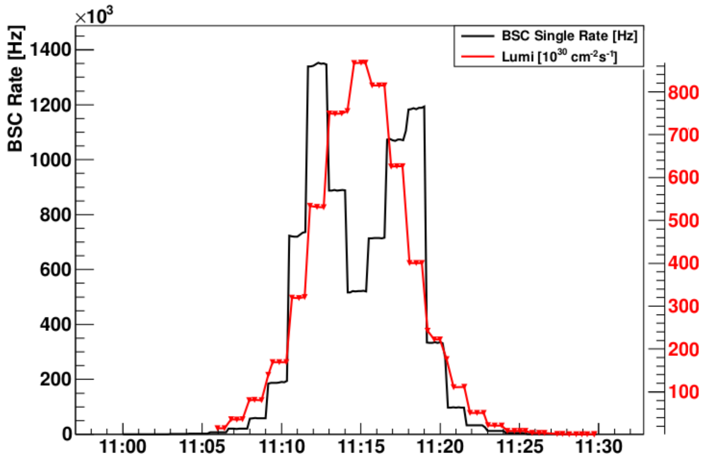

FIGURE A.30: Channel 2FBSC1P6. Lumi Limit = 660 $\times 10^{30}\mathrm{cm}^{-2}\mathrm{s}^{-1}$. High Voltage Setting: 960V. Max Rate: 1.35MHz.

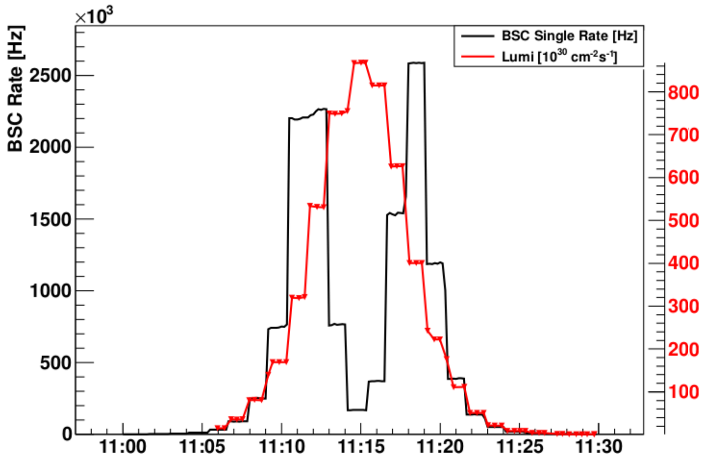

FIGURE A.31: Channel 2NBSC1P7. Lumi Limit = 650 $\times 10^{30}\mathrm{cm}^{-2}\mathrm{s}^{-1}$. High Voltage Setting: 1320V. Max Rate: 2.5MHz.

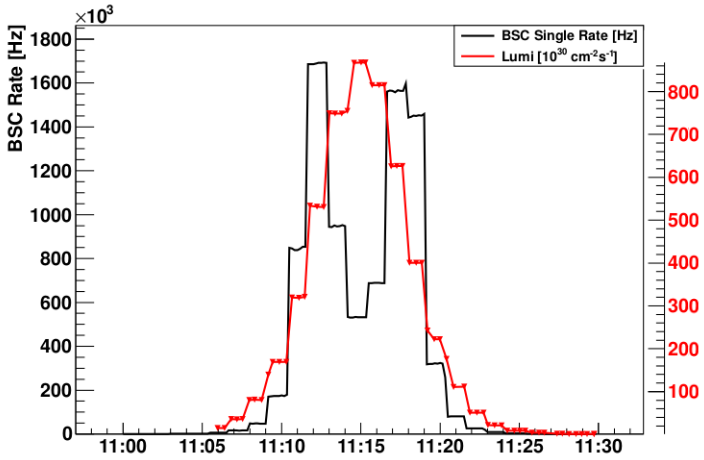

FIGURE A.32: Channel 2NBSC1P8. Lumi Limit = 660 $\times 10^{30}\mathrm{cm}^{-2}\mathrm{s}^{-1}$. High Voltage Setting: 1000V. Max Rate: 1.7MHz.

HV Channel	Rate (kHz)	$\mathcal{L}_{inst}(10^{30}\mathrm{cm}^{-2}\mathrm{s}^{-1})$	Volts
1NBSC1D1	1200	800	900
1NBSC1D2	1800	430	950
1FBSC1D3	1400	420	925
1FBSC1D4	1500	420	860
1FBSC1D5	1800	640	930
1FBSC1D6	1450	550	850
1NBSC1D7	1500	480	900
1NBSC1D8	1650	480	1210
0 1NBSC1P1	900	420	910
1NBSC1P2	1000	600	1000
1FBSC1P3	1200	560	980
1FBSC1P4	1100	620	875
1FBSC1P5	2550	800	1430
1FBSC1P6	1000	760	880
1NBSC1P7	1300	700	1000
1NBSC1P8	1700	460	1000
2NBSC1D1	1100	700	1100
2NBSC1D2	1400	460	800
2FBSC1D3	1600	640	900
2FBSC1D4	1900	650	1000
2FBSC1D5	1500	450	870
2FBSC1D6	1000	400	800
2NBSC1D7	1500	440	870
2NBSC1D8	1350	650	930
2NBSC1P1	1100	650	900
2NBSC1P2	2000	860	1200
2FBSC1P3	1800	500	900
2FBSC1P4	1600	450	875
2FBSC1P5	1700	400	1050
2FBSC1P6	1350	660	960
2NBSC1P7	2500	650	1320
2NBSC1P8	1700	660	1000

Appendix B

Poisson Mean

The expectation value of a discrete random variable i is defined as:

$$\lambda = \Sigma_{i=1}^{\infty} iP(i, \lambda) \tag{B.1}$$

$$= e^{-\lambda}\Sigma_{i=1}^{\infty} i\frac{\lambda^i}{i!} \tag{B.2}$$

$$= \lambda e^{-\lambda}\Sigma_{i=1}^{\infty} \frac{\lambda^{i-1}}{(i-1)!} \tag{B.3}$$

$$\tag{B.4}$$

Letting $k = (i - 1)$,

$$= \lambda e^{-\lambda}\Sigma_{i=1}^{\infty} \frac{\lambda^k}{k!} \tag{B.5}$$

$$= \lambda e^{-\lambda} e^{\lambda} \tag{B.6}$$

$$= \lambda \tag{B.7}$$

Appendix C

ξ Comparisons

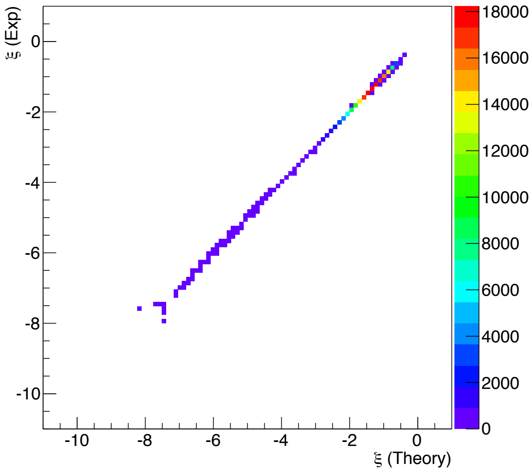

(a) EPOS 1.99 COMPARISON OF ξ CALCULATIONS

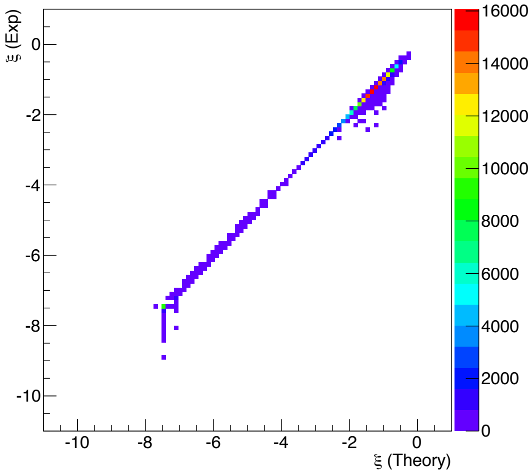

(b) EPOS LHC COMPARISON OF ξ CALCULATIONS

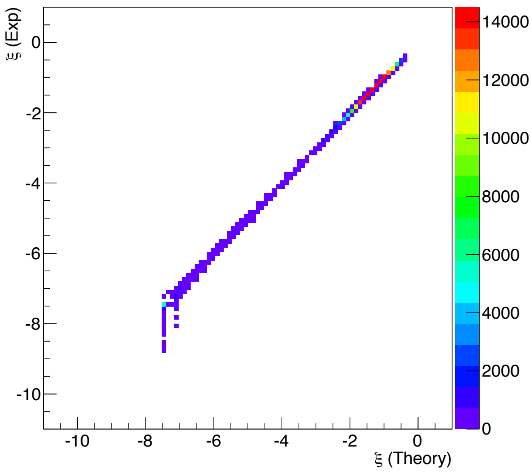

(c) QGSJETII-4 COMPARISON OF ξ CALCULATIONS

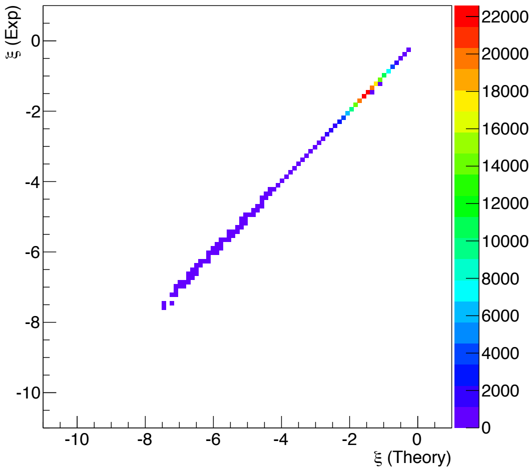

(d) PHOJET COMPARISON OF ξ CALCULATIONS

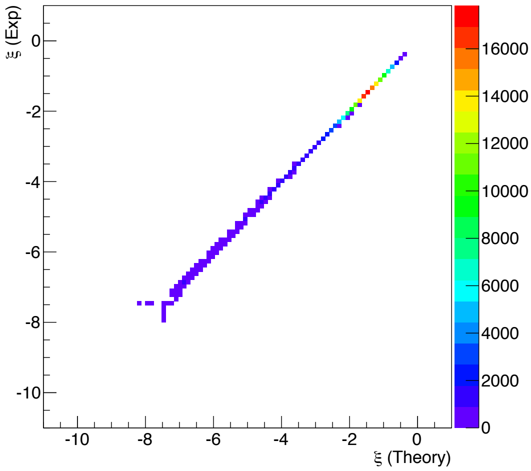

(e) PYTHIA COMPARISON OF ξ CALCULATIONS

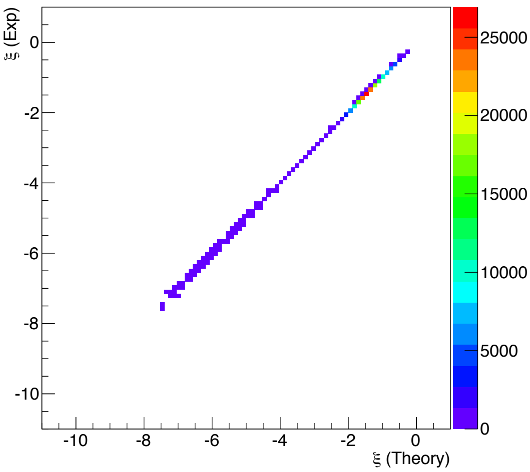

(f) SIBYLL COMPARISON OF ξ CALCULATIONS

Appendix D

Polyethylene Absorption Studies

100 eV. $\sigma = 1$ keV.

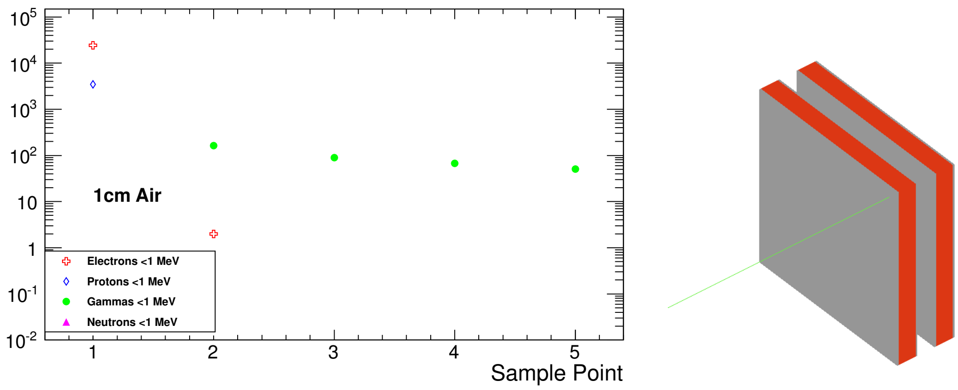

FIGURE D.1: BDSim model showing 1cm of air (not visible) between two 10mm scintillator (red) tiles covered with 1mm Aluminium (grey).

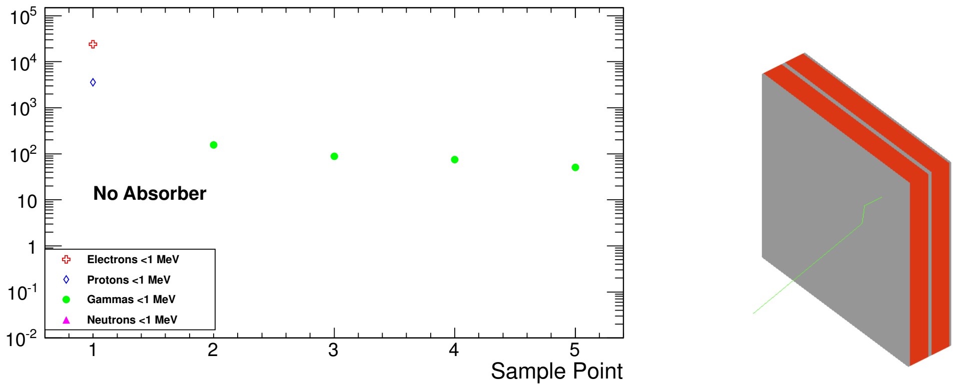

FIGURE D.2: BDSim model showing no absorber between two 10mm scintillator (red) tiles covered with 1mm Aluminium (grey).

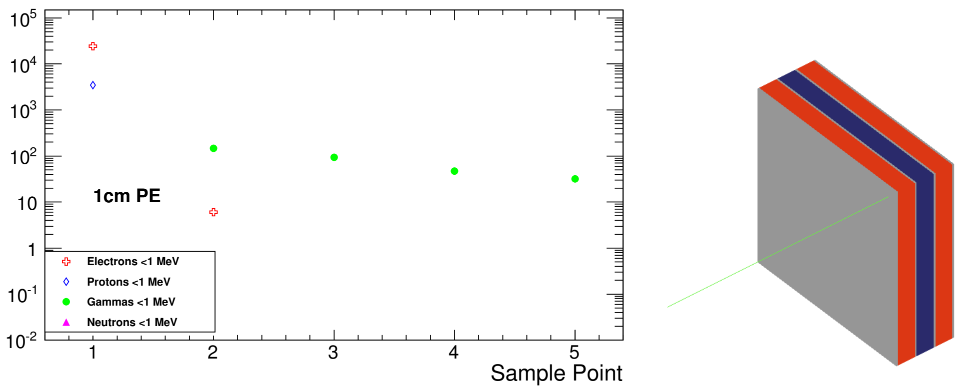

FIGURE D.3: Neutron flux simulations. 1cm of PE between two 10mm scintillator tiles covered with 1mm Aluminium.

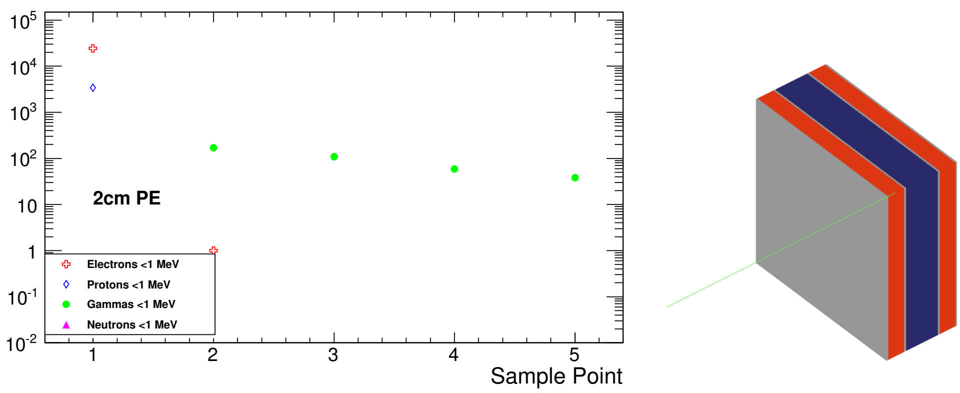

FIGURE D.4: Neutron flux simulations. 2cm of PE between two 10mm scintillator tiles covered with 1mm Aluminium.

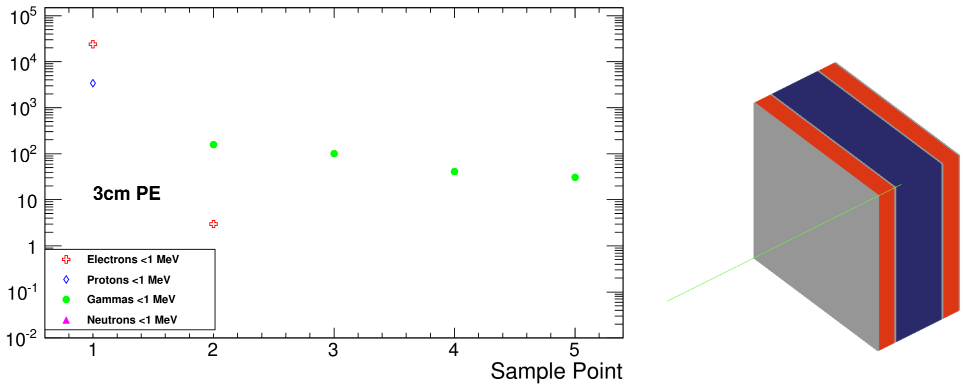

FIGURE D.5: Neutron flux simulations. 3cm of PE between two 10mm scintillator tiles covered with 1mm Aluminium.

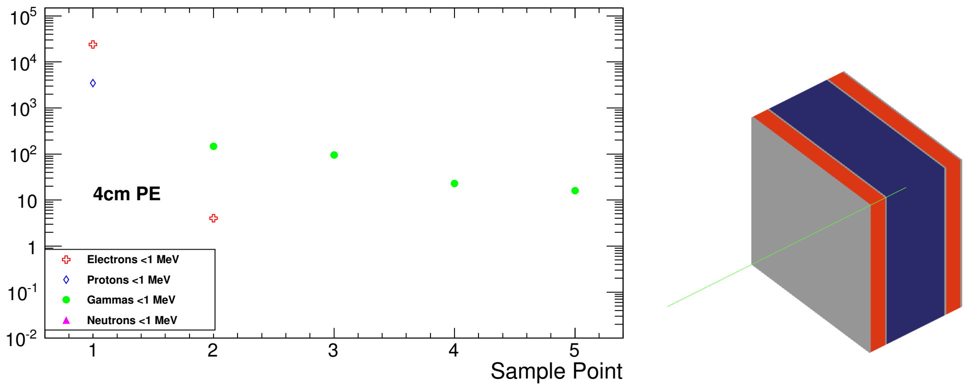

FIGURE D.6: Neutron flux simulations. 4cm of PE between two 10mm scintillator tiles covered with 1mm Aluminium.

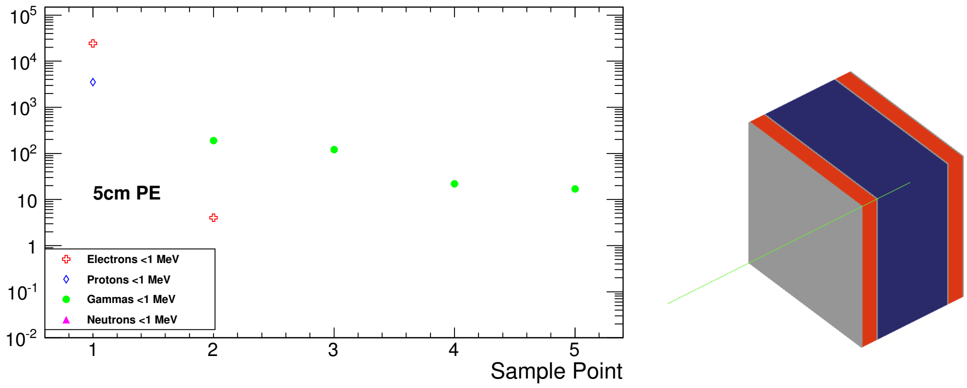

FIGURE D.7: Neutron flux simulations. 5cm of PE between two 10mm scintillator tiles covered with 1mm Aluminium.

1 keV. $\sigma = 1$ keV.

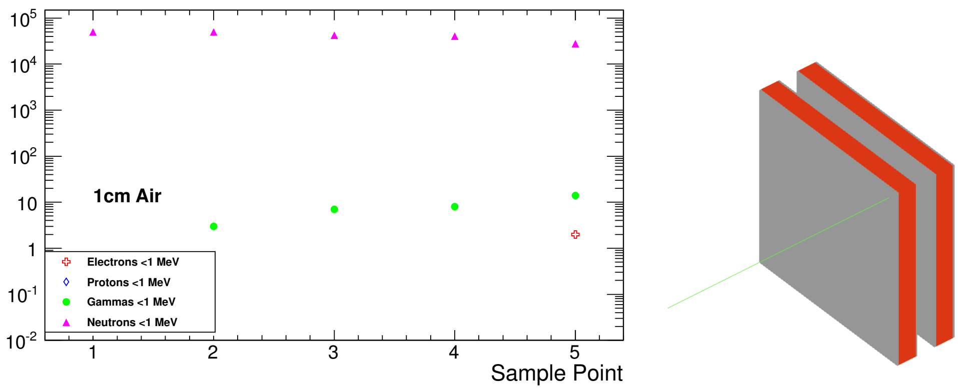

FIGURE D.8: BDSim model showing 1cm of air (not visible) between two 10mm scintillator (red) tiles covered with 1mm Aluminium (grey).

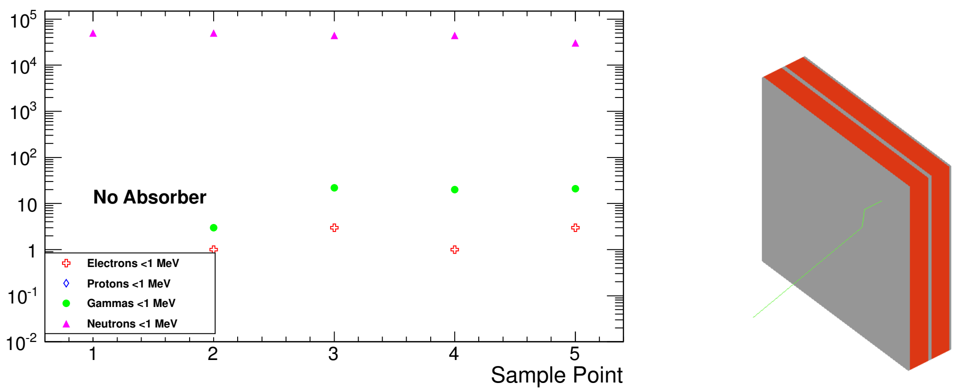

FIGURE D.9: BDSim model showing no absorber between two 10mm scintillator (red) tiles covered with 1mm Aluminium (grey).

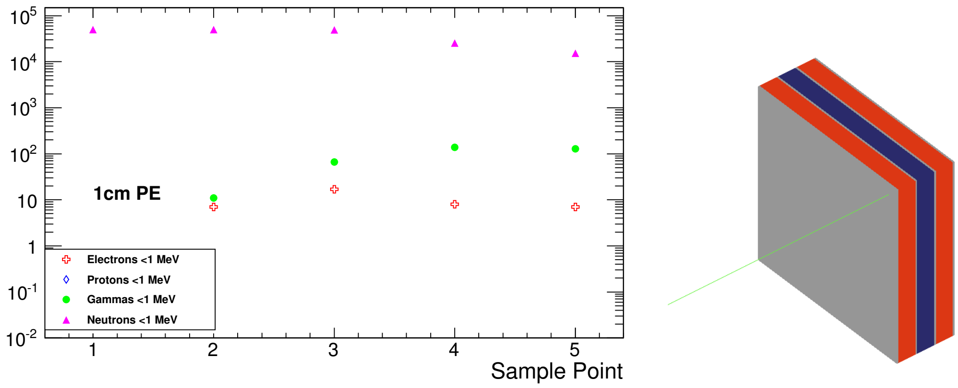

FIGURE D.10: Neutron flux simulations. 1cm of PE between two 10mm scintillator tiles covered with 1mm Aluminium.

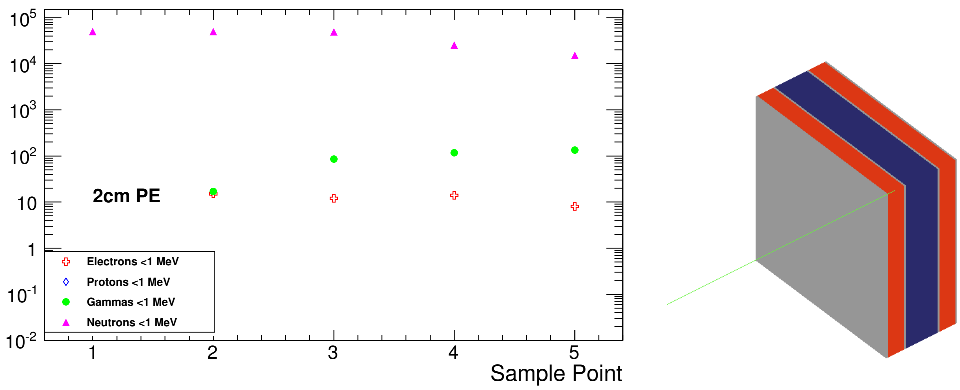

FIGURE D.11: Neutron flux simulations. 2cm of PE between two 10mm scintillator tiles covered with 1mm Aluminium.

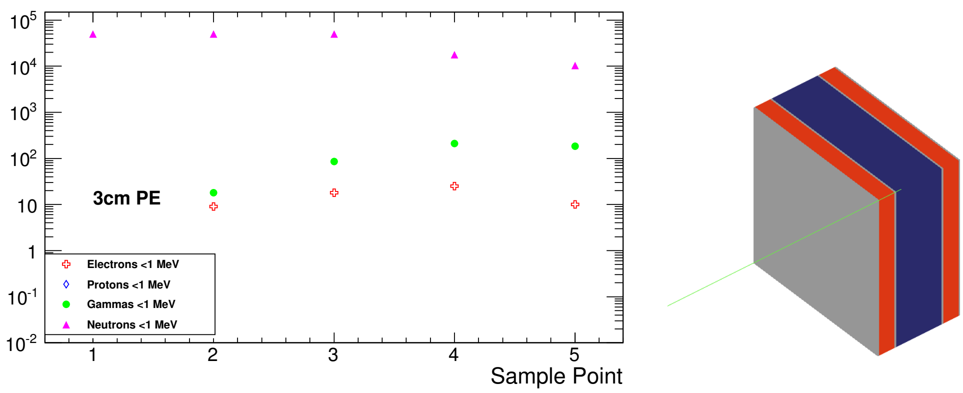

FIGURE D.12: Neutron flux simulations. 3cm of PE between two 10mm scintillator tiles covered with 1mm Aluminium.

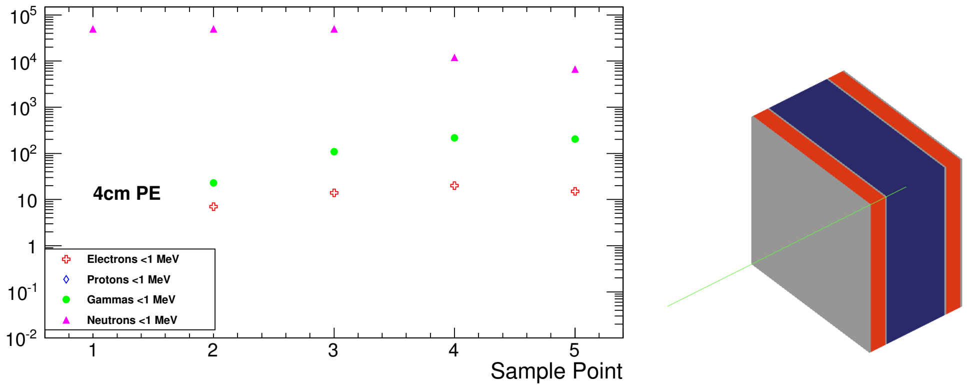

FIGURE D.13: Neutron flux simulations. 4cm of PE between two 10mm scintillator tiles covered with 1mm Aluminium.

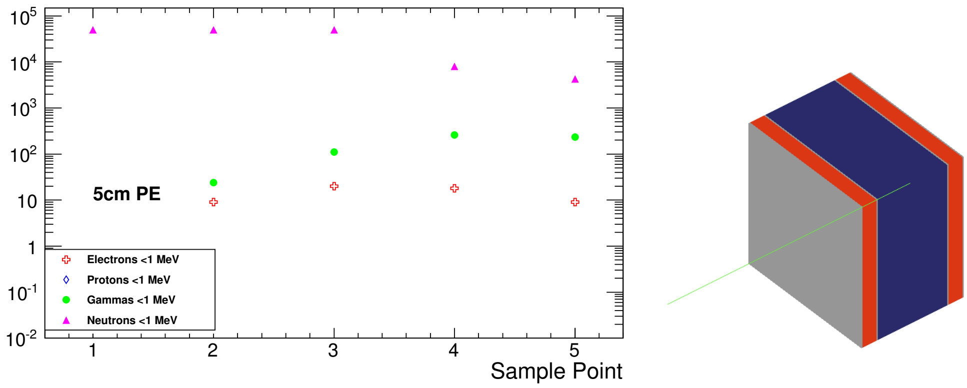

FIGURE D.14: Neutron flux simulations. 5cm of PE between two 10mm scintillator tiles covered with 1mm Aluminium.

10 keV. $\sigma = 1$ keV

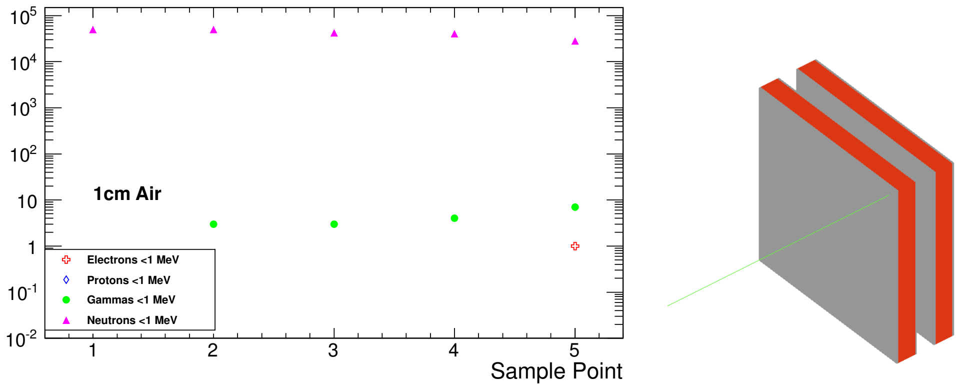

FIGURE D.15: BDSim model showing 1cm of air (not visible) between two 10mm scintillator (red) tiles covered with 1mm Aluminium (grey).

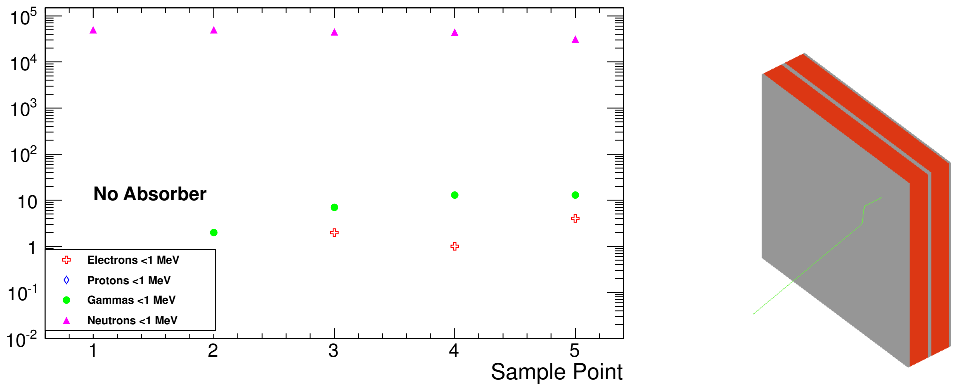

FIGURE D.16: BDSim model showing no absorber between two 10mm scintillator (red) tiles covered with 1mm Aluminium (grey).

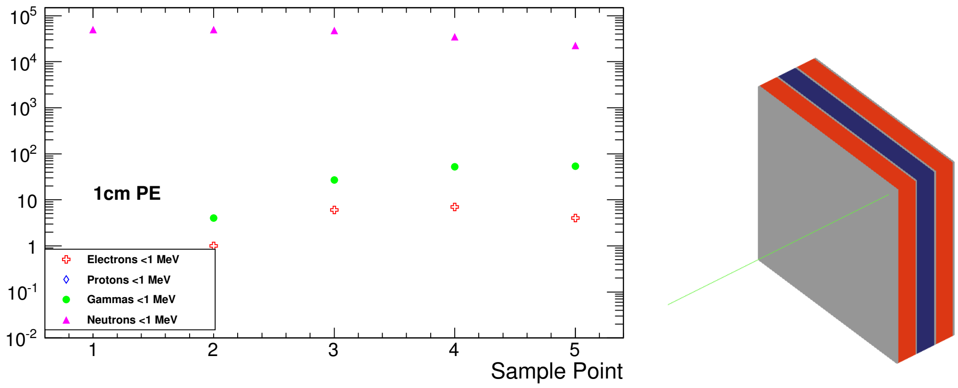

FIGURE D.17: Neutron flux simulations. 1cm of PE between two 10mm scintillator tiles covered with 1mm Aluminium.

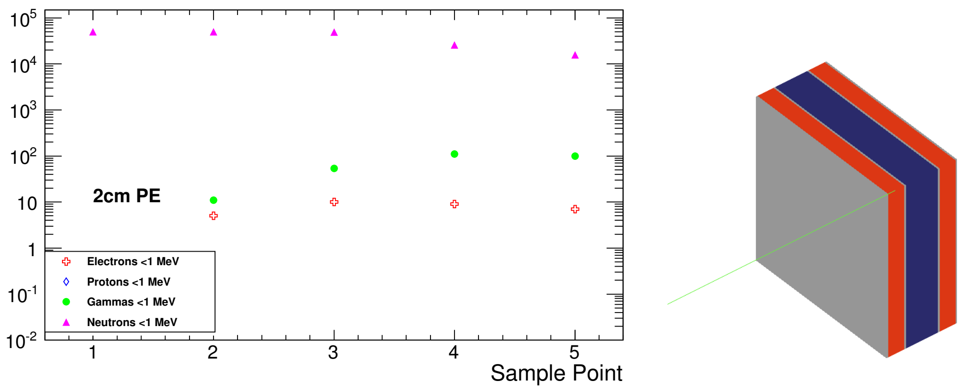

FIGURE D.18: Neutron flux simulations. 2cm of PE between two 10mm scintillator tiles covered with 1mm Aluminium.

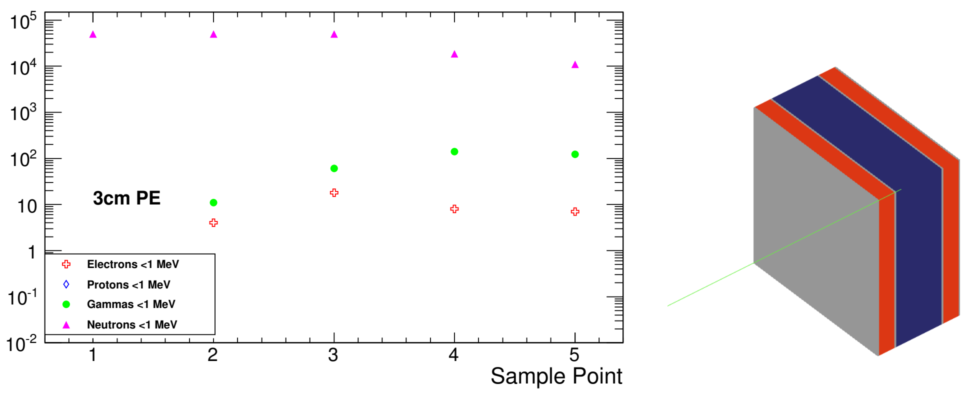

FIGURE D.19: Neutron flux simulations. 3cm of PE between two 10mm scintillator tiles covered with 1mm Aluminium.

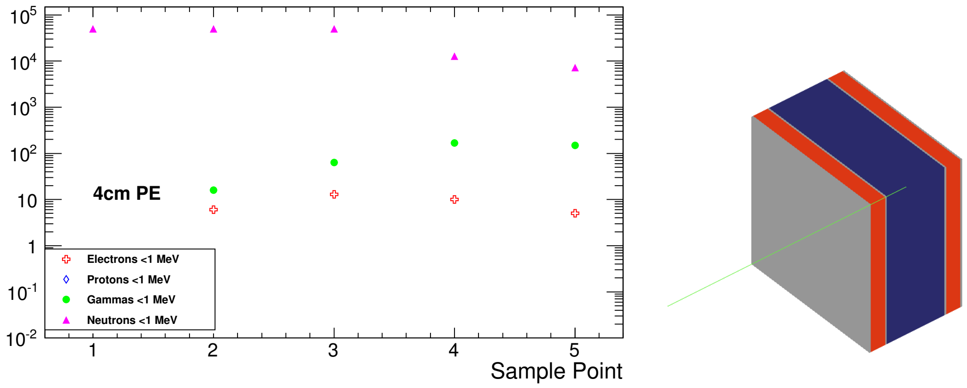

FIGURE D.20: Neutron flux simulations. 4cm of PE between two 10mm scintillator tiles covered with 1mm Aluminium.

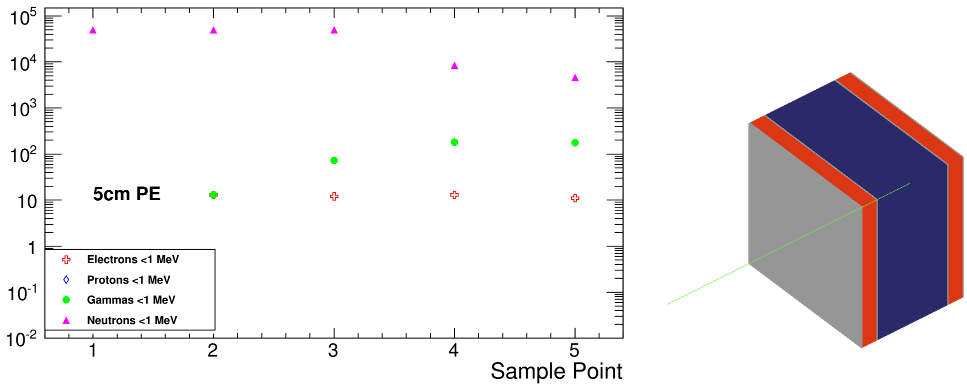

FIGURE D.21: Neutron flux simulations. 5cm of PE between two 10mm scintillator tiles covered with 1mm Aluminium.

100 keV. σ = 1 keV

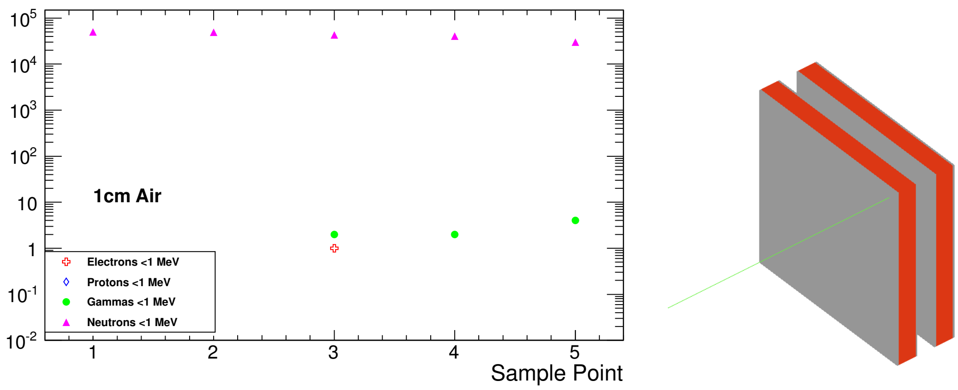

FIGURE D.22: BDSim model showing 1cm of air (not visible) between two 10mm scintillator (red) tiles covered with 1mm Aluminium (grey).

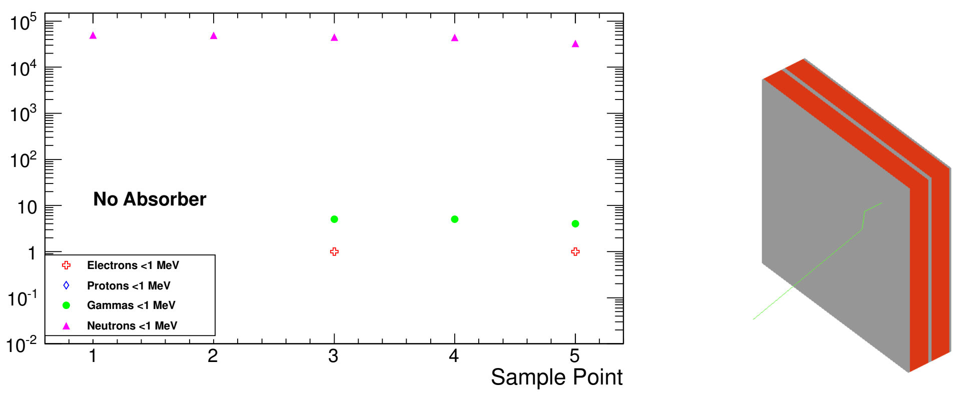

FIGURE D.23: BDSim model showing no absorber between two 10mm scintillator (red) tiles covered with 1mm Aluminium (grey).

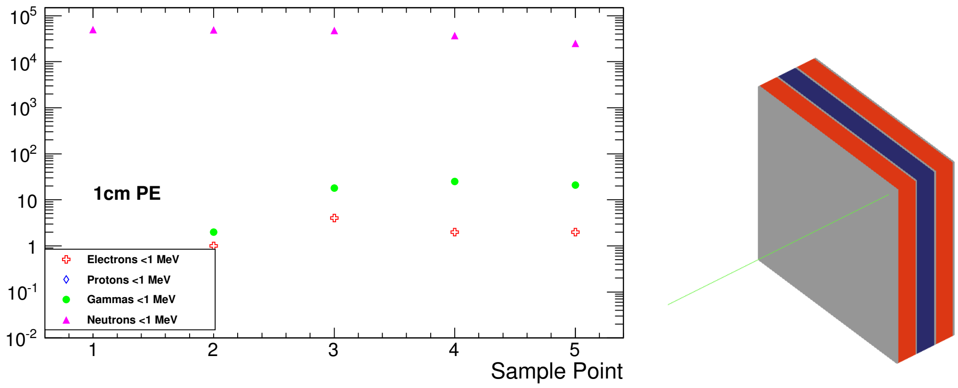

FIGURE D.24: Neutron flux simulations. 1cm of PE between two 10mm scintillator tiles covered with 1mm Aluminium.

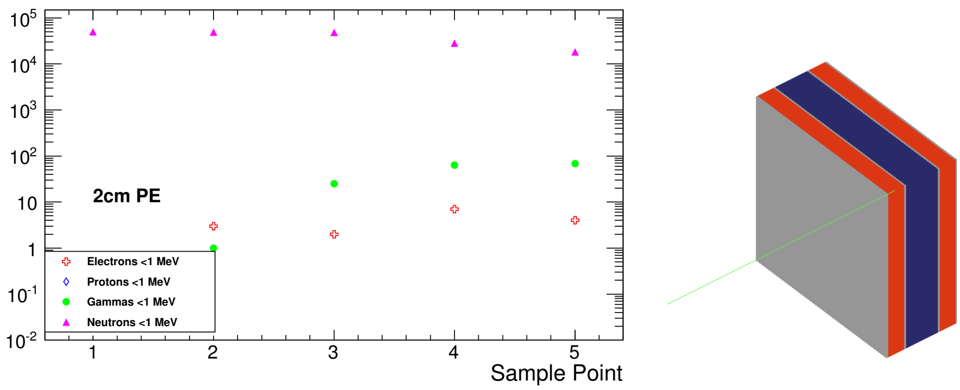

FIGURE D.25: Neutron flux simulations. 2cm of PE between two 10mm scintillator tiles covered with 1mm Aluminium.

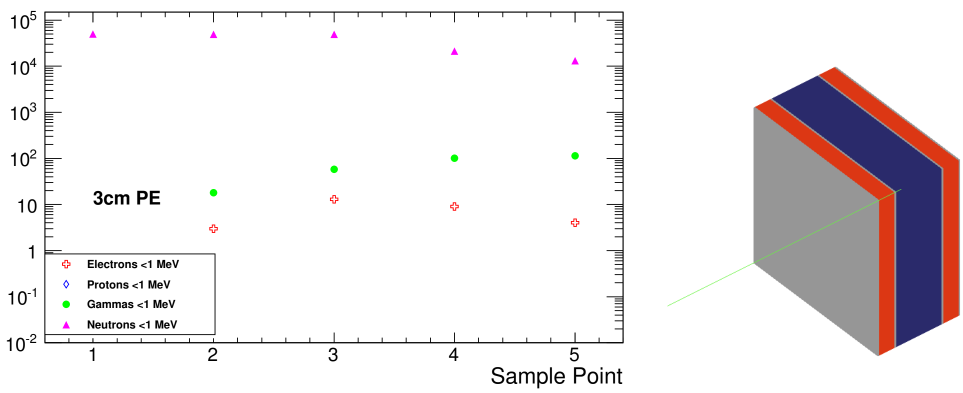

FIGURE D.26: Neutron flux simulations. 3cm of PE between two 10mm scintillator tiles covered with 1mm Aluminium.

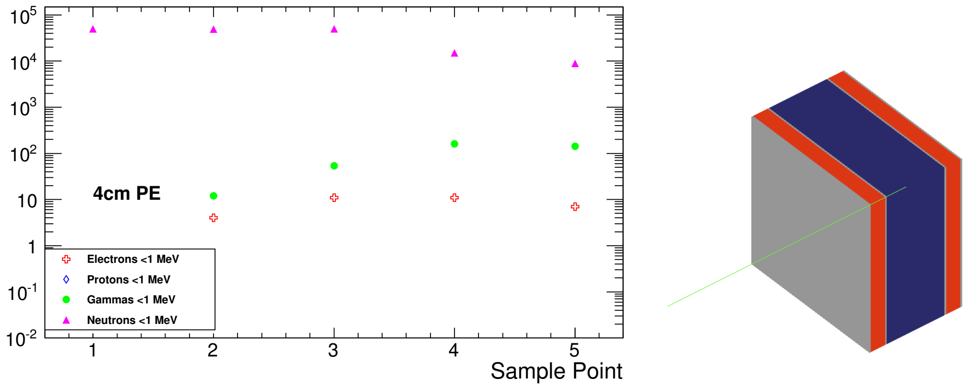

Figure D.27: Neutron flux simulations. 4cm of PE between two 10mm scintillator tiles covered with 1mm Aluminium.

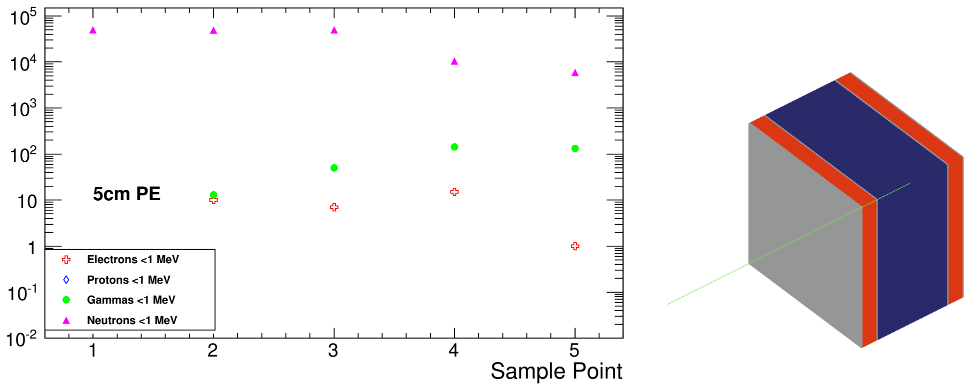

Figure D.28: Neutron flux simulations. 5cm of PE between two 10mm scintillator tiles covered with 1mm Aluminium.

Appendix E

Tile Test Results

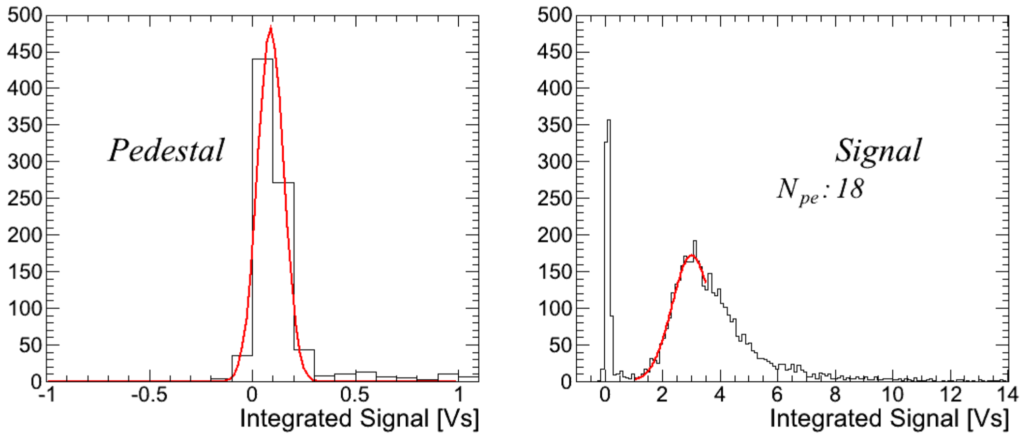

FIGURE E.1: Tile 01. $N_{p.e}$ per M.I.P measurement using signals from cosmics.

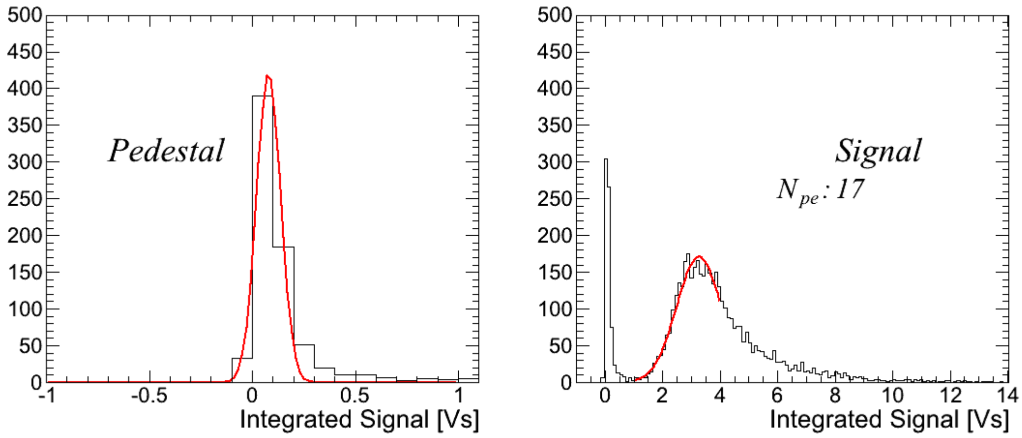

FIGURE E.2: Tile 02. $N_{p.e}$ per M.I.P measurement using signals from cosmics.

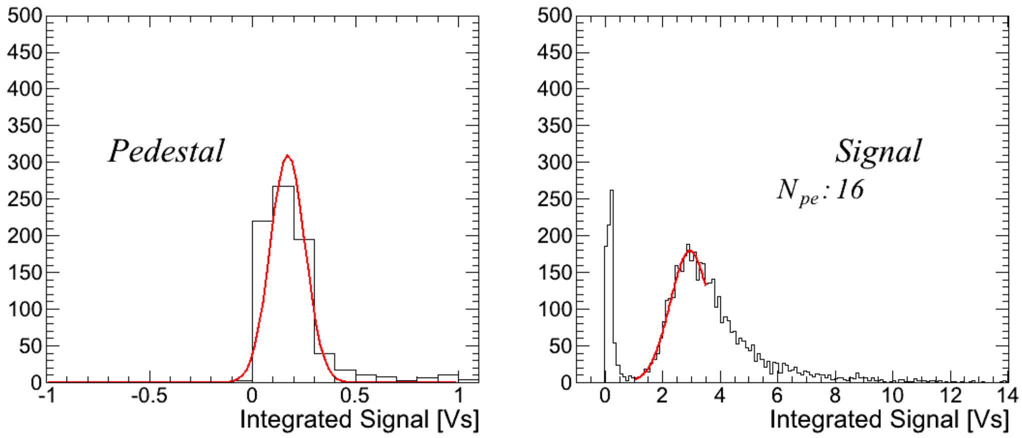

FIGURE E.3: Tile 03. $N_{p.e}$ per M.I.P measurement using signals from cosmics.

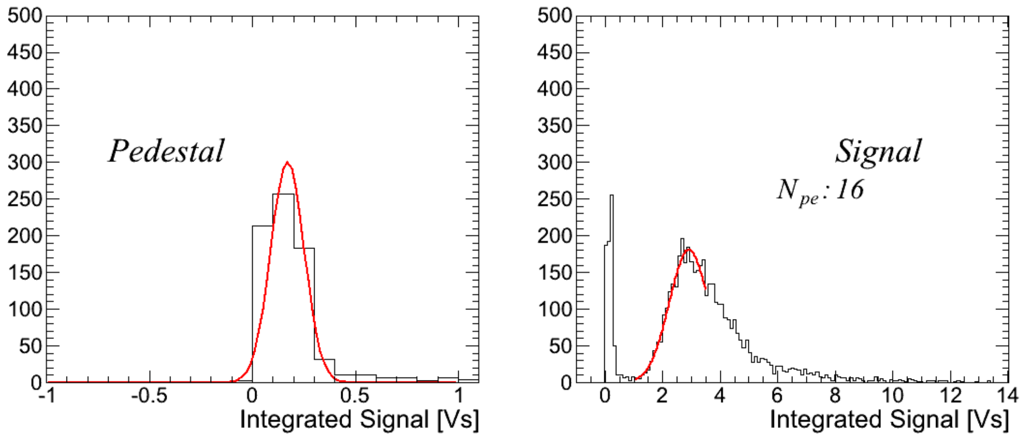

FIGURE E.4: Tile 04. $N_{p.e}$ per M.I.P measurement using signals from cosmics.

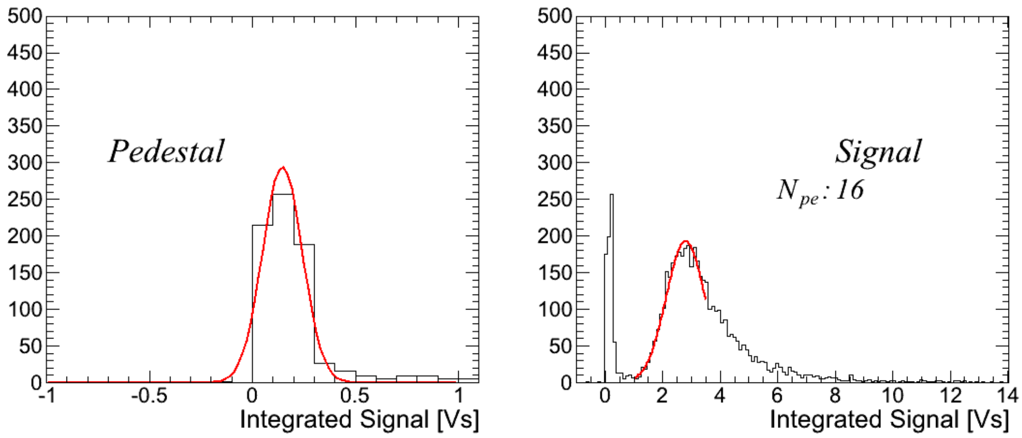

FIGURE E.5: Tile 05. $N_{p.e}$ per M.I.P measurement using signals from cosmics.

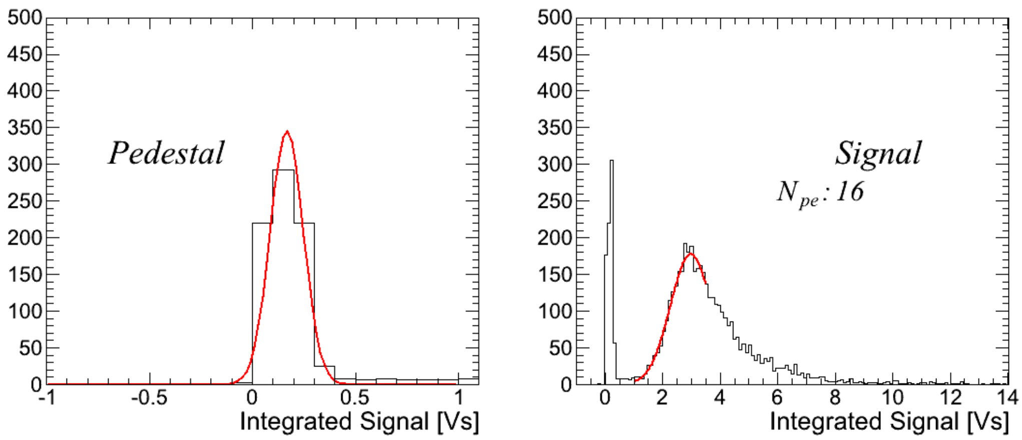

FIGURE E.6: Tile 06. $N_{p.e}$ per M.I.P measurement using signals from cosmics.

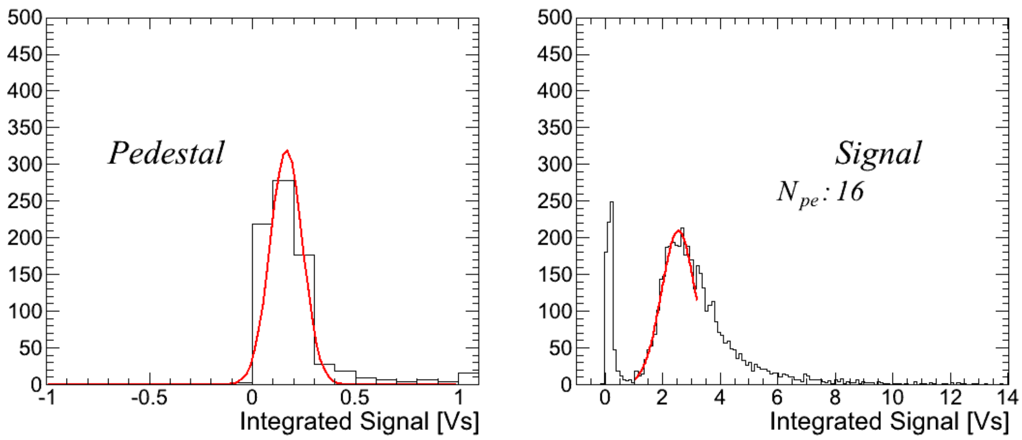

FIGURE E.7: Tile 07. $N_{p.e}$ per M.I.P measurement using signals from cosmics.

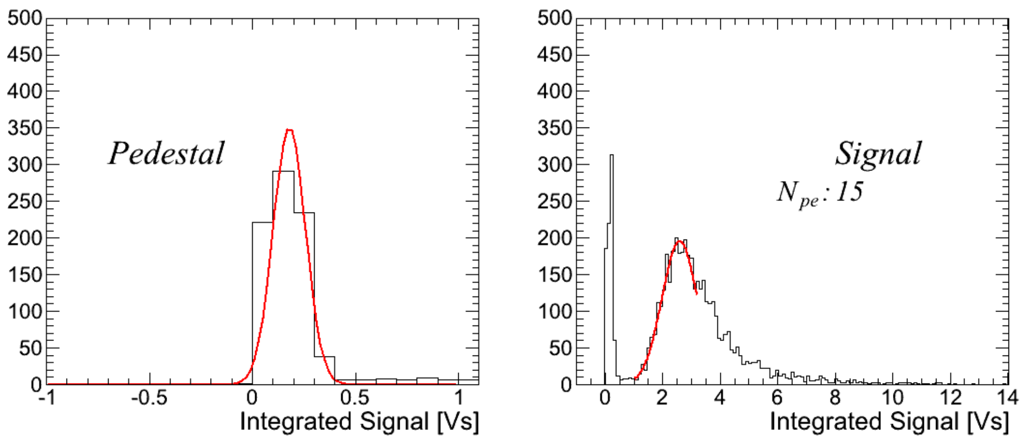

FIGURE E.8: Tile 08. $N_{p.e}$ per M.I.P measurement using signals from cosmics.

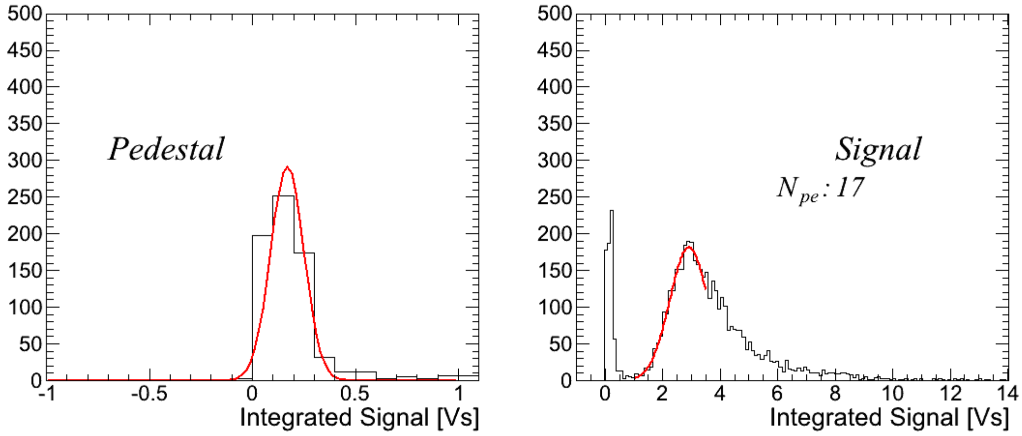

FIGURE E.9: Tile 09. $N_{p.e}$ per M.I.P measurement using signals from cosmics.

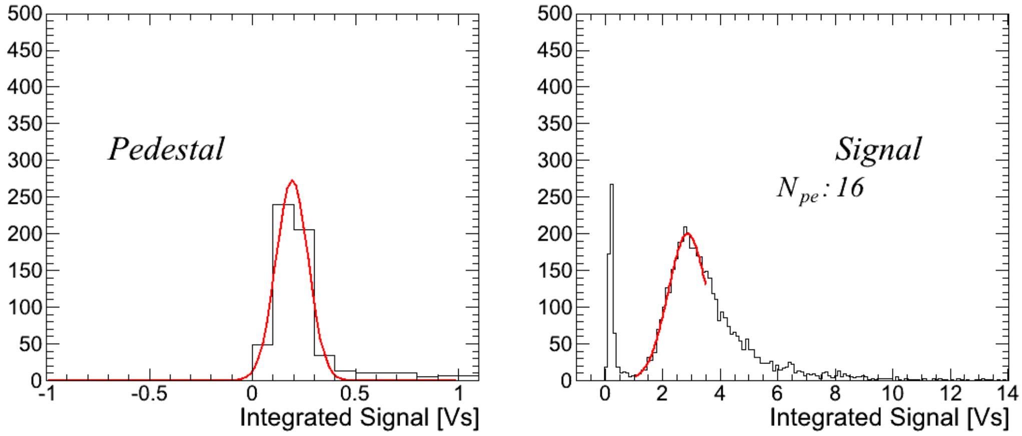

FIGURE E.10: Tile 10. $N_{p.e}$ per M.I.P measurement using signals from cosmics.

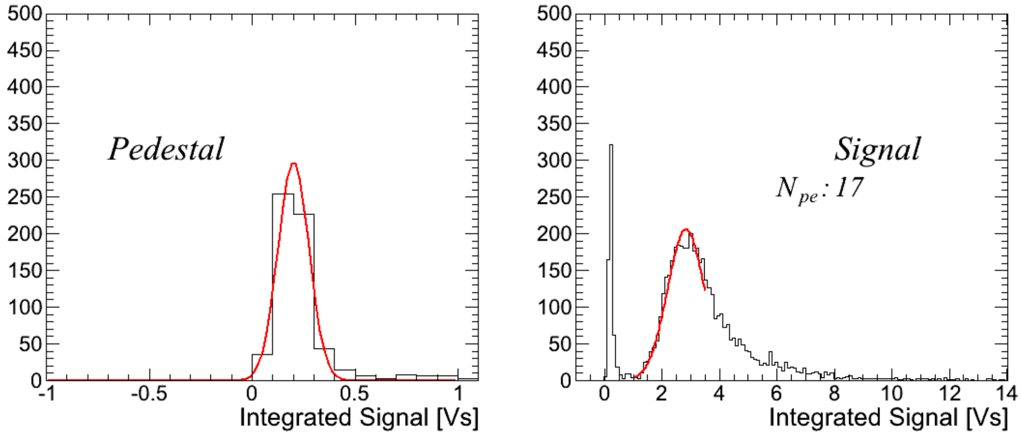

FIGURE E.11: Tile 11. $N_{p.e}$ per M.I.P measurement using signals from cosmics.

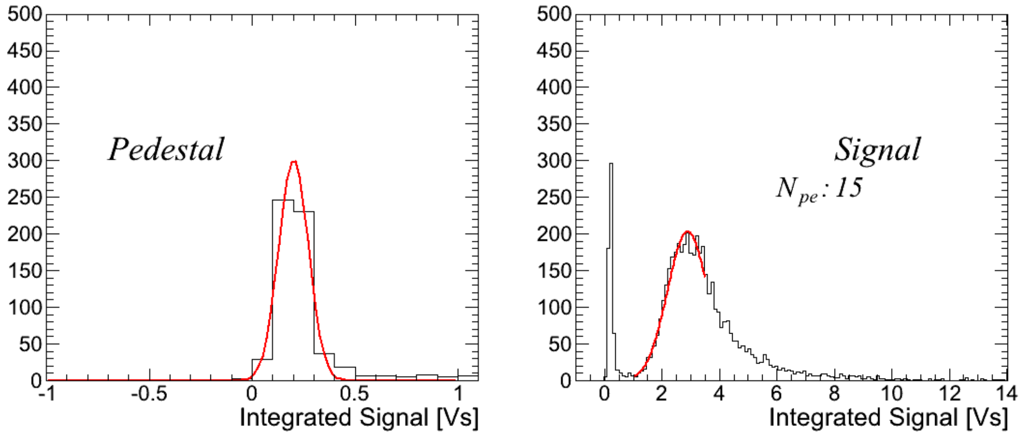

FIGURE E.12: Tile 12. $N_{p.e}$ per M.I.P measurement using signals from cosmics.

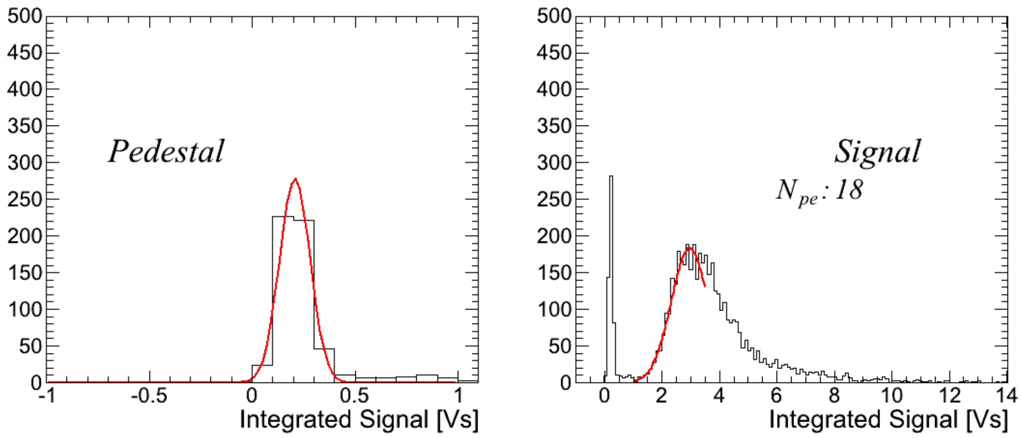

FIGURE E.13: Tile 13. $N_{p.e}$ per M.I.P measurement using signals from cosmics.

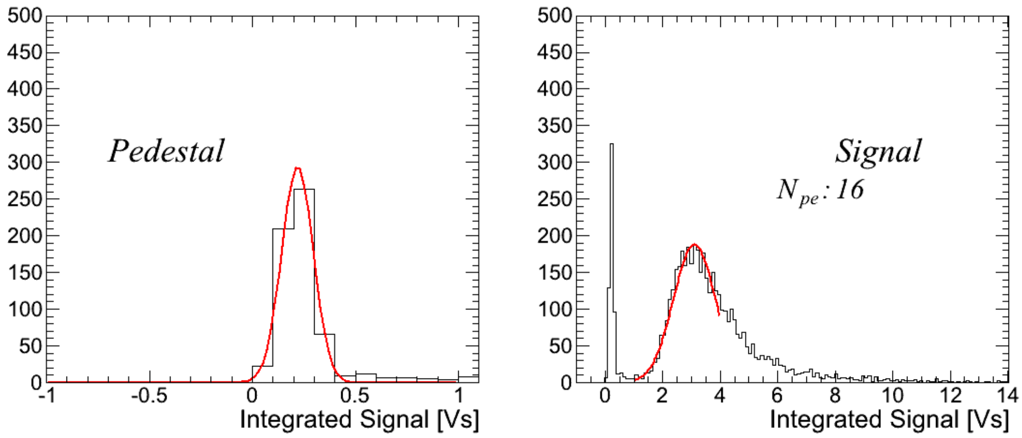

FIGURE E.14: Tile 14. $N_{p.e}$ per M.I.P measurement using signals from cosmics.

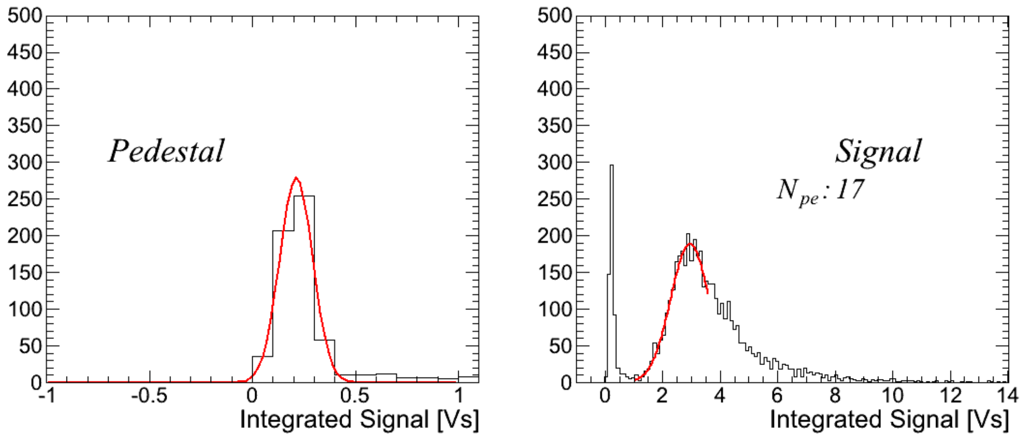

FIGURE E.15: Tile 15. $N_{p.e}$ per M.I.P measurement using signals from cosmics.

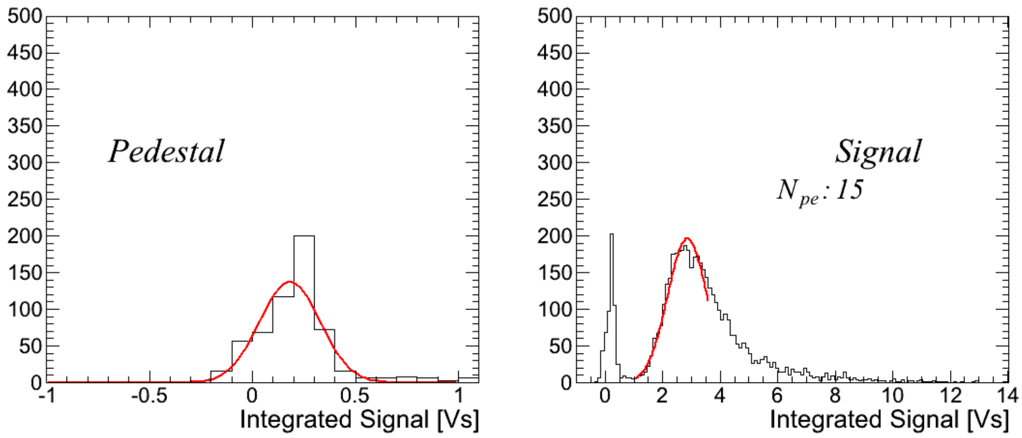

FIGURE E.16: Tile 16. $N_{p.e}$ per M.I.P measurement using signals from cosmics.

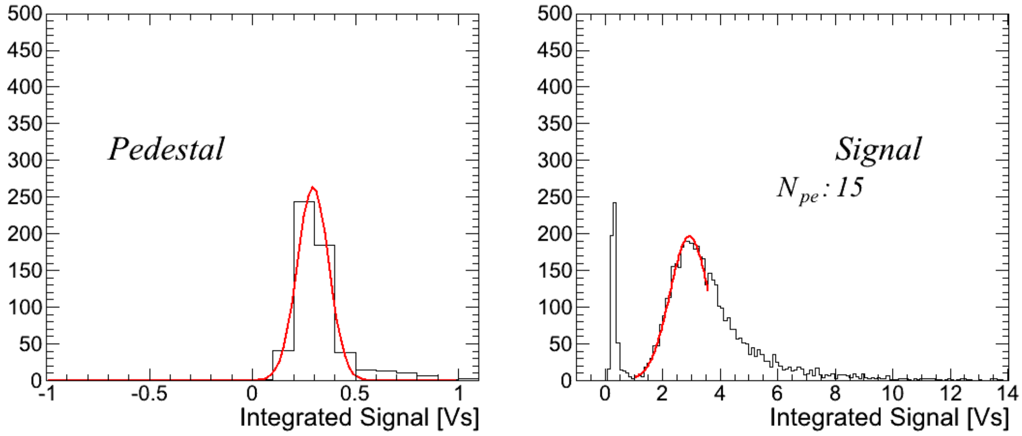

FIGURE E.17: Tile 17. $N_{p.e}$ per M.I.P measurement using signals from cosmics.

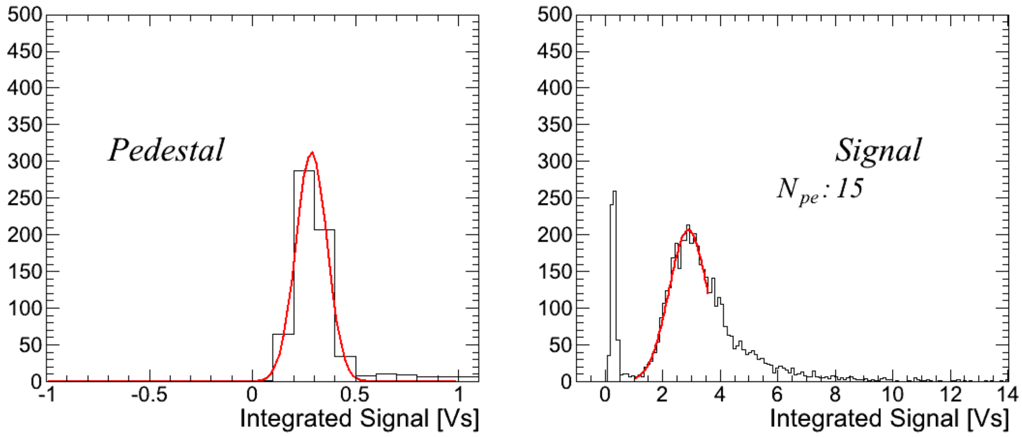

FIGURE E.18: Tile 18. $N_{p.e}$ per M.I.P measurement using signals from cosmics.

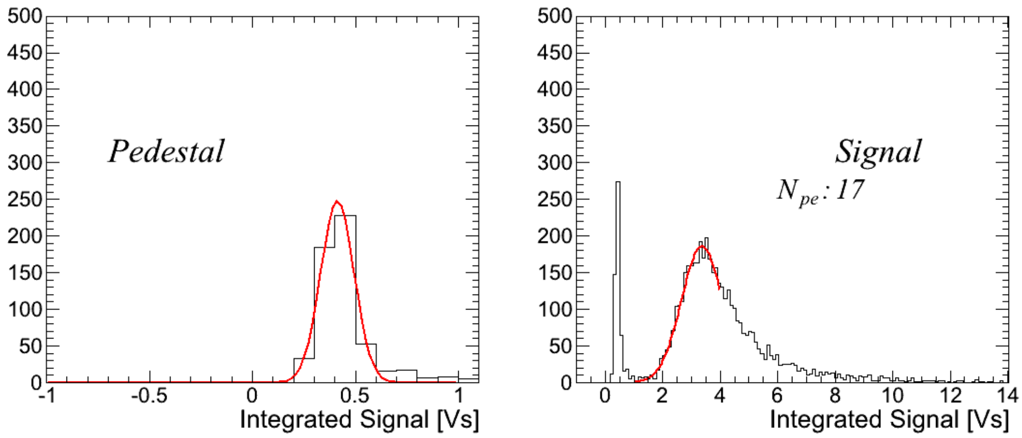

FIGURE E.19: Tile 19. $N_{p.e}$ per M.I.P measurement using signals from cosmics.

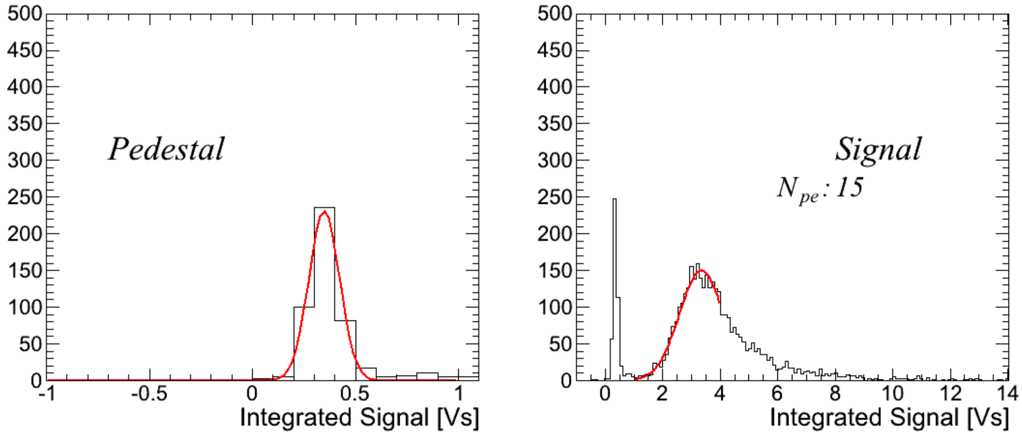

FIGURE E.20: Tile 20. $N_{p.e}$ per M.I.P measurement using signals from cosmics.

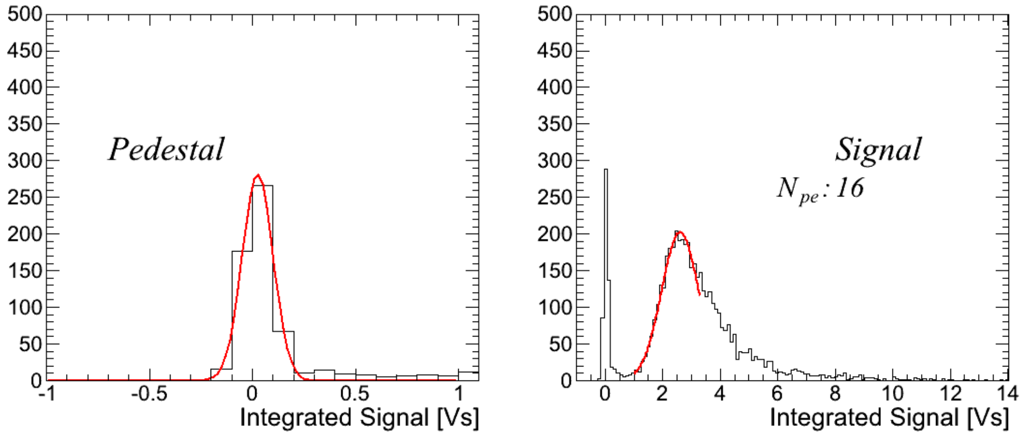

FIGURE E.21: Tile 21. $N_{p.e}$ per M.I.P measurement using signals from cosmics.

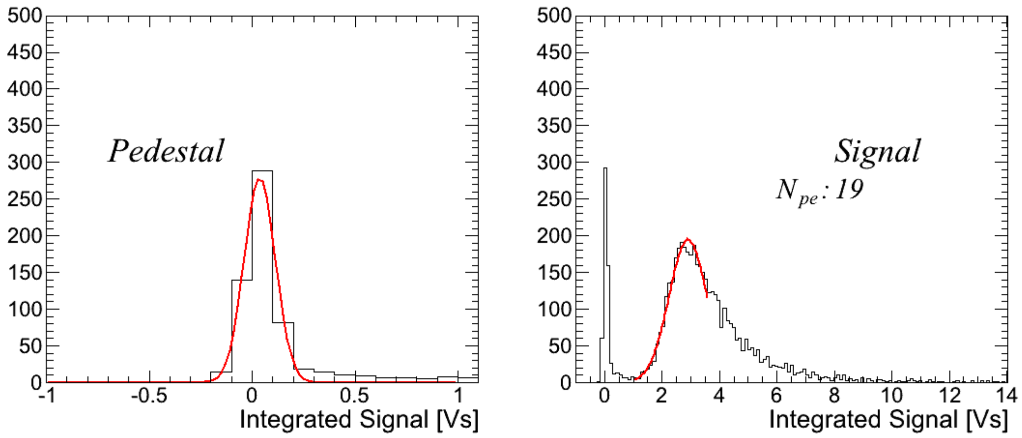

FIGURE E.22: Tile 22. $N_{p.e}$ per M.I.P measurement using signals from cosmics.

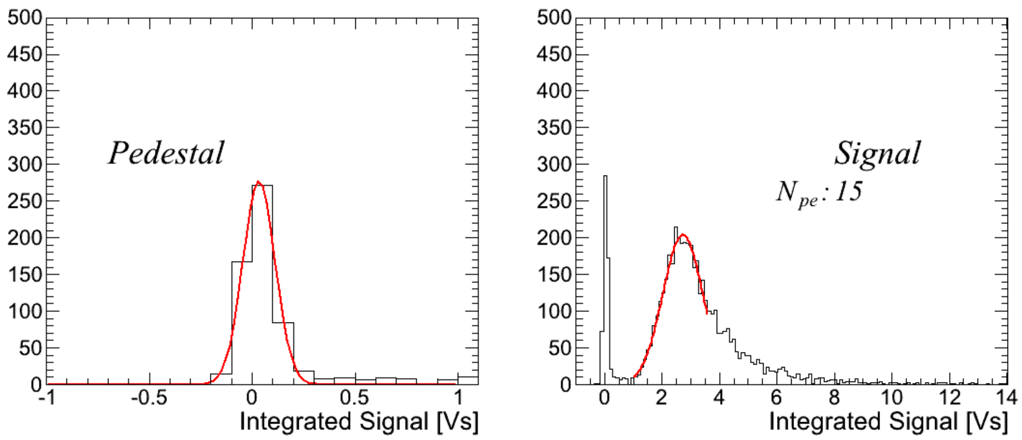

FIGURE E.23: Tile 23. $N_{p.e}$ per M.I.P measurement using signals from cosmics.

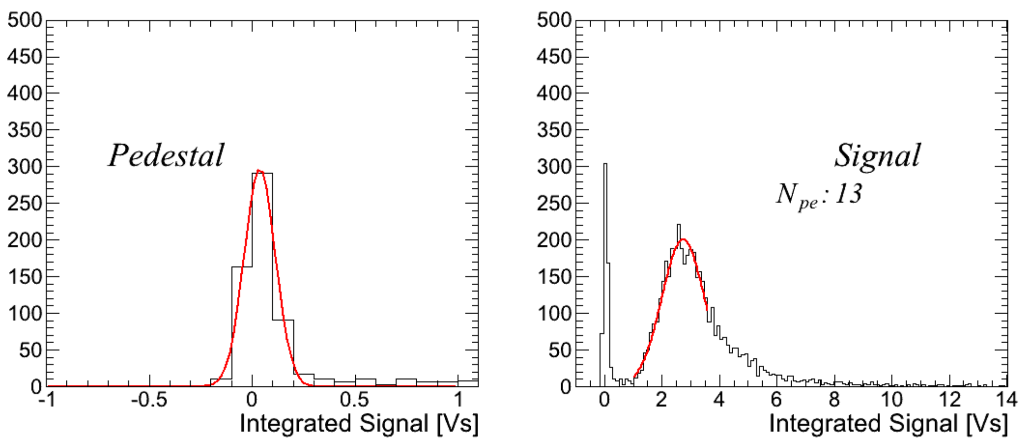

FIGURE E.24: Tile 24. $N_{p.e}$ per M.I.P measurement using signals from cosmics.

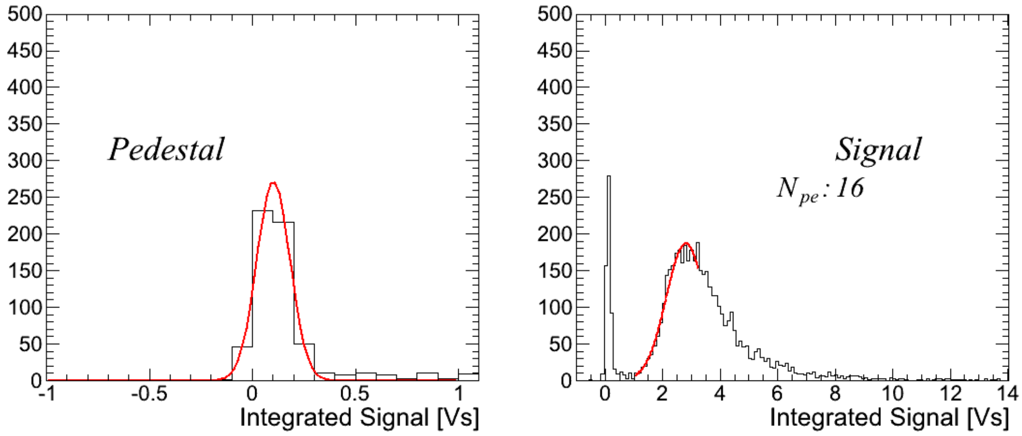

FIGURE E.25: Tile 25. $N_{p.e}$ per M.I.P measurement using signals from cosmics.

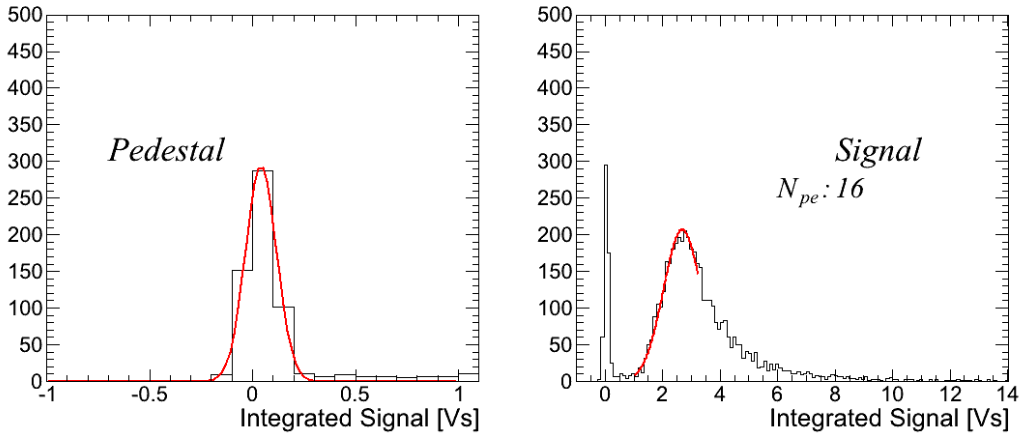

FIGURE E.26: Tile 26. $N_{p.e}$ per M.I.P measurement using signals from cosmics.

Appendix F

Optical Theorem

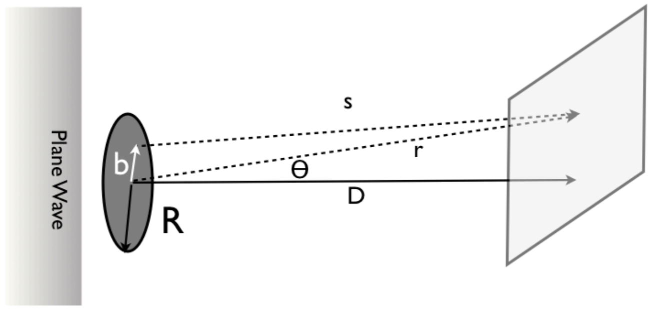

FIGURE F.1: The principles of Fraunhofer scattering are applicable to deriving the total cross-section of particle scattering.

The full version of this proof can be found in [145].
Figure F.1 shows a plane wave incident on an opaque disk of radius R. If the condition $kR^2 \ll D^*$ is satisfied, the priciples of Fraunhoffer diffraction apply. The differential cross section $d\sigma$ is the ratio of the outgoing (scattered) energy in the solid angle $d\Omega$ to the incident energy flux of the plane wave.

$$d\sigma = \frac{I_{\text{scat}} r^2 d\Omega}{I_{\text{inc}}} \tag{F.1}$$

where $I_{\text{inc}} = |U_0|^2$ is the square of the incident wave amplitude and $I_{\text{scatt}} = |U_o|^2 \frac{|T^{ab}|^2}{r^2}$, with T^{ab}, the scattering amplitude defined as:

$$T^{ab} = \frac{ik}{2\pi} \int d^2\mathbf{b}|1 - S(\mathbf{b})|e^{-i\mathbf{q}\cdot\mathbf{b}} \tag{F.2}$$

$^*k$ being the wavenumber, $\frac{2\pi}{\lambda}$.

$S(\mathbf{b})$ is the profile function whose value ($0 \geq S(\mathbf{b}) \leq 1$) varies depending on the position of incidence of the plane wave with the opaque disk. The two extreme cases are:

$$S(\mathbf{b}) = \begin{cases} 1, & \text{if plane wave is fully incident on the disk} \\ 0, & \text{if plane wave is fully outside the disk} \end{cases}$$

In the first case, the wave is incident on the totally opaque disk and no transmission occurs. In the second case, there is no disk in the path of the wave, and therefore, no diffraction occurs. $\mathbf{q}$ ensures we deal only with the transverse momentum-transfer, $\mathbf{q} \equiv (\frac{kx}{r}, \frac{ky}{r}, 0)$. Then,

$$\frac{d\sigma}{d\Omega} = \frac{I_{\text{scat}} r^2}{I_{\text{inc}}} \tag{F.3}$$

$$= \frac{|U_0|^2 \; |T^{ab}|^2 \; r^2}{|U_0|^2 \; r^2} \tag{F.4}$$

$$= |T^{ab}|^2 \tag{F.5}$$

Integrating eq. F.5 gives us the scattering cross-section:

$$\sigma_{\text{scat}} = \int \frac{d\sigma}{d\Omega} d\Omega \tag{F.6}$$

$$= \frac{1}{k^2} |T^{ab}|^2 d^2\mathbf{q} \tag{F.7}$$

$$= \int d^2\mathbf{b} |1 - S(\mathbf{b})|^2 \tag{F.8}$$

The absorption cross-section σ_{abs} is given by the difference of the absorbed energy, $|S(\mathbf{b})|^2$, and the incident energy:

$$\sigma_{abs} = \int d^2\mathbf{b} (1 - |S(\mathbf{b})|^2) \tag{F.9}$$

The Total Cross-Section is the sum of the scattering and the absorption cross-sections, namely;

$$\sigma_{total} = \sigma_{scat} + \sigma_{abs} \tag{F.10}$$

$$= \int d^2\mathbf{b}|1 - S(\mathbf{b})|^2 + \int d^2\mathbf{b}(1 - |S(\mathbf{b})|^2) \tag{F.11}$$

$$= \int d^2\mathbf{b}(1 - 2S(\mathbf{b}) + |S(\mathbf{b})|^2) + \int d^2\mathbf{b}(1 - |S(\mathbf{b})|^2) \tag{F.12}$$

$$= 2\int d^2\mathbf{b}[1 - S(\mathbf{b})] \tag{F.13}$$

The part in the square brackets is just $\frac{2\pi}{ik}T^{ab}e^{i\mathbf{q}\cdot\mathbf{b}}$ (see eq. F.2). Combining eq. F.13 with eq. F.2 and setting the scattering angle $= 0$ and therefore, the momentum transfer $\mathbf{q} = 0$, we obtain the total cross-section;

$$\sigma_{total} = \frac{4\pi}{k}\mathbb{I}m\ T^{ab} \tag{F.14}$$

Bibliography

[1] J. Allday. *Quarks, Leptons and the Big Bang*. Taylor & Francis: 2nd Edition, 2001.

[2] L. Evans and P. Bryant. LHC Machine. *Journal of Intsrumentation doi:10.1088/1748-0221//3/08/S08001*, 3, 2008.

[3] CERN. LHC Working Group. The LHC design report Vol1. *CERN Webserver*, Vol 1(5):1–1001, July 2004. URL `http://lhc.web.cern.ch/lhc/LHC-DesignReport.html`.

[4] M. Spiropulu and S. Stapnes. *Perspectives on LHC Physics - Chapter 3. LHC's ATLAS and CMS Detectors*. World Scientific, 2008.

[5] *Early Particle Accelerators*. The American Institute of Physics, 2002. URL `http://www.aip.org/history/lawrence/epa.html`.

[6] LHC Data Group. Beam parameters & definitions. Technical report, CERN, https://edms.cern.ch/file/445830/5/Vol_1_Chapter_2.pdf, 2007.

[7] The ALICE Collaboration. The ALICE experiment at the CERN LHC. *Journal of Instrumentation doi:10.1088/1748-0221//3/08/S08002*, 3, 2008.

[8] The LHCb Collaboration. The LHCb experiment at the CERN LHC. *Journal of Instrumentation doi:10.1088/1748-0221//3/08/S08005*, 3, 2008.

[9] The TOTEM Collaboration. The LHCb experiment at the CERN Large Hadron Collider. *Journal of Instrumentation doi:10.1088/1748-0221//3/08/S08007*, 3, 2008.

[10] CMS Collaboration. The CMS experiment at the CERN LHC. *Journal of Instrumentation doi:10.1088/1748-0221/3/08/S08004*, 3, 2008.

[11] The ATLAS Collaboration. The ATLAS experiment at the CERN Large Hadron Collider. *Journal of Instrumentation doi:10.1088/1748-0221/3/08/S08003*, 3, 2008.

[12] LHC Machine Outreach, 2010. URL `http://lhc-machine-outreach.web.cern.ch/lhc-machine-outreach/`.

[13] The CDF II Collaboration. The CDF II detector techncial design report. Technical report, Fermilab, Chicago, IL, 2001. URL `http://www-cdf.fnal.gov/upgrades/tdr/tdr.html`.

[14] The CMS Collaboration. CERN Document Server, 2012. URL `http://cdsweb.cern.ch/`.

[15] The CMS Collaboration. Combined results of searches for the standard model Higgs boson in pp collisions at $\sqrt{s} = 7$ TeV. *Physics Letters B*, 710, 2012.

[16] J. Incandela on behalf of the CMS collaboration. Status of the CMS SM Higgs search. In *Presented at CERN Higgs Update Seminar*, 4 July 2012.

[17] P. Wells. Trackers and the effect of material on impact parameter and momentum resolution. In *Presented at the Excellence in Detector and Instrumentation Technologies conference*, 5 May 2011.

[18] Herwig Schopper. *Landolt-Börnstein Series - Detectors for Particles and Radiation, Volume 21, Part 2*, pages 5–48. Springer, group i. subvolume b edition, 2010.

[19] LHCC CERN LHC Experiments Committee. The CMS magnet project: Technical design report. Technical report, CERN, 1997.

[20] *The CMS Tracker*. http://cms-tracker.web.cern.ch/cms-tracker/, 2011.

[21] The CMS Collaboration. CMS tracking performance results from early LHC operation. *Eur. Phys. Journal C*, 70:1165 – 1192, 2010.

[22] The CMS Collaboration. Performance and operation of the CMS electromagnetic calorimeter. *arXiv:0910.3423v3 Physics.ins-det*, 2010.

[23] The ECAL Detector Performance Group. Ecal dpg results, 2012. URL `https://twiki.cern.ch/twiki/bin/view/CMSPublic/EcalDPGResults-(RestrictedAccess)`.

[24] P. Adzic et al. Energy resolution of the barrel of the CMS electromagnetic calorimeter. *Journal of Instrumentation*, 2, 2007.

[25] The CMS Collaboration. Electromagnetic calorimeter calibration with 7 TeV data. *CMS Physics Analysis Summary - EGM-10-003*, 2010.

[26] The CMS Collaboration. Electron reconstruction and identification at $\sqrt{s} = 7$ TeV. *CMS Physics Analysis Summary - EGM-10-004*, 2010.

[27] CMS Collaboration. The CMS experiment at the CERN LHC - hadron calorimeter. *Journal of Instrumentation doi:10.1088/1748-0221/3/08/S08004*, 3, 2008.

[28] Sunanda Banerjee. Simulation geometry for the CMS hcal. Technical report, CERN, 2005.

[29] M. F. García. CMS muon system status. In *The 2007 Europhysics Conference on High Energy Physics*, 2008.

[30] *The Level-1 Global Trigger for the CMS Experiment at LHC*, 2007. Presented at the 12th Workshop on Electronics for LHC Experiments and Future Experiments.

[31] CMS Trigger Group. *External Conditions at L1: Definitions and Additional Info*, 2010. URL `https://twiki.cern.ch/twiki/bin/view/CMS/L1ExternalConditions`.

[32] Michael Padrta. Global trigger hardware. Technical report, Austrian Acadamy of Sciences, Vienna, 2007. URL `http://wwwhephy.oeaw.ac.at/p3w/electronic1/GlobalTrigger/GlobalTriggerCrate.htm`.

[33] The CMS Collaboration. The triDAS project technical design report, volume 1. Technical report, CERN, CERN/LHCC 2000 - 38. CMS TDR 6.1, December 2000.

[34] The CMS Collaboration. The triDAS project technical design report, data acquisition and high-level trigger. *CERN/LHCC 2006-001 CMS TDR 8.1*, Volume 2, 2006.

[35] R. Schmidt, R. Assmann, E. Carlier, et al. Protection of the CERN large hadron collider. *New Journal of Physics*, 8, 2006.

[36] Mika Huhtinen. *The Radiation Environment at the CMS Experiment at the LHC*. PhD thesis, Helsinki University of Technology, Finland, 1996.

[37] A. Ball, A. J. Bell, A. Butler, et al. Design, implementation and first measurements with the Medipix2-MXR detector at the compact muon solenoid experiment. *Journal of Instrumentation*, 6, 2011.

[38] R. Hall-Wilton, E. Castro, W. Lange, W. Lohman, A. Macpherson, M. Ohlerich, V. Ryjov, R.S. Schmidt, and R.L. Stone. Fast beam conditions monitor bcm1f for the CMS experiment. *arXiv:0911.2480v3*, 2009.

[39] B. Dehning et al. The beam loss monitoring system. In *Proceedings of the XIII LHC Project Chamonix Workshop*, , Chamonix France, 2004.

[40] A.J. Bell. The design & construction of the beam scintillation counter for CMS. Master's thesis, Dept. of Physics & Astronomy, University of Canterbury, Christchurch, New Zealand, 2007. URL `http://ir.canterbury.ac.nz/handle/10092/1588`.

[41] G. Aguillion, B. Anderson, A. H Ball, et al. Thin scintillating tiles with high light yield for the opal encaps. *Nucl. Instrum and Methods. in Physics Research A*, 417, 1998.

[42] *BC408 Specifications*. www.detectors.saint-gobain.com/.../BC400-404-408-412-416-Data-Sheet.pdf, 2007.

[43] L.Bagby, A.J.Bell, G.Veres, and Y.-J Lee. The beam scintillation counter trigger system for CMS. Technical Report CMS DN -2010/018, CERN, 2010.

[44] F. Ferro, A Sobol, and J.P Guillaud. Similation of diffractive and non–diffractive processes at the LHC energy with the pythia and phojet mc event generators. *TOTEM NOTE 2004-05*, 2004.

[45] The CMS Collaboration. Ridge correlation structure in high multiplicity pp collisions with CMS. *arXiv:1107.2196v1*, 2011.

[46] E. Wenger. BSC2 PKAM triggers. Personal Communication, Oct 2010.

[47] E.Wenger. Cluster shape based event selection, April 2010. URL `https://twiki.cern.ch/twiki/bin/viewauth/CMS/DNDEtaClusterShapeEvtSel`.

[48] CAEN Electronics Instrumentation. *CAEN V560N 16 Channel VME Scaler*, 2000. URL `http://www.caen.it/nuclear/product.php?mod=V560`.

[49] CAEN Electronics Instrumentation. *CAEN V767 128 Channel VME TDC*, 2000. URL `http://www.caen.it/nuclear/product.php?mod=V767`.

[50] CAEN Electronics Instrumentation. *CAEN V1721 500MHz Digitizer*, 2000. URL `http://www.caen.it/nuclear/product.php?mod=V1721`.

[51] *DIP and DIM*, 2011. URL `http://j2eeps.cern.ch/wikis/display/EN/DIP+and+DIM`.

[52] Web based monitoring, 2010. URL `https://cmswbm.web.cern.ch/cmswbm/brm/snapshots/index.html`.

[53] The CMS Collaboration. Observation of Long-Range Near-Side Angular Correlations in Proton-Proton Collisions at the LHC. *Jounal of High Energy Physics*, 2010(9):1 – 38, September 2010.

[54] The CMS Collaboration. Transverse-momentum and pseudo-rapidity distributions of charged hadrons in pp collisions at $\sqrt{s} = 0.9$ and 2.36 TeV. *Journal of High Energy Physics. JHEP02 (2010) 041*, 2010.

[55] The CMS Collaboration. First measurement of the underlying event activity at the LHC with $\sqrt{s} = 0.9$ TeV. *European Physics Journal C. arXiv:1006.2083v1.*, 2010.

[56] The CMS Collaboration. CMS tracking performance results from early LHC operation. *European Physics Journal C*, 2010.

[57] The CMS Collaboration. Charged particle transverse momentum spectra in pp collisions at $\sqrt{s} = 0.9$ and 7 TeV. *Jounal of High Energy Physics - arXiv:1104.3547v1*, 2010, April 2011.

[58] Sercan Sen. Measurement of the energy flow in a large η range and forward jets at LHC at $\sqrt{s} = 0.9$ TeV, 2.36 TeV and 7 TeV. *Proceedings of Science - arXiv:1102.2867v1*, February 2011.

[59] G. R. Martinez. Measurement of forward jets, forward energy flow and diffractive events with CMS. *Nucl Phys A*, 855:478–481, 2011.

[60] E. Wenger. Early measurements of bulk observables in CMS. *Journal of Physics: Conference Series*, 270, 2011.

[61] D. Volyanskyy. Observation of diffraction with the CMS experiment at the large hadron collider. *arXiv:1102.0708v1*, February 2011.

[62] R.S Hollis A. Iordanova and D.J Hofman. Level-1 triggering studies for heavy-ion collisions at $\sqrt{s_{NN}} = 5$ TeV in CMS. CMS Analysis Note - AN-2007/053, 2007.

[63] *ROOT - An Object Oriented Data Analysis Framework*, volume 389, 1997. Proceedings AIHENP'96 Workshop, Lausanne, Sept. 1996.

[64] I. Antcheva, M. Ballintijn, B. Bellenot, M. Biskup, R. Brun, et al. Root - a c++ framework for petabyte data storage, statistical analysis and visualization. *Computer Physics Communications*, 180:2499–2512, December 2009.

[65] *Luminosity Optimization*, Evian Proc., 2009.

[66] *First Luminosity Scans in the LHC*, IPAC proc. Kyoto, Japan, 2010.

[67] N. Adam, V. Halyo andJ. Jones, D. Marlow, S. Schnetzer, Y. Guo, L. Lueking, K. Maeshima, W. Badgett, L. Sexton-Kennedy, I.M De Abril, and M.M De Abril. The CMS luminosity system. Technical Report CMS IN-2007/030, CERN, 2007.

[68] The CMS Collaboration. Measurement of CMS luminosity. CMS PAS EWK-10-004, 2010.

[69] The CMS Collaboration. Measurement of CMS luminosity in the 2010 run. *Available on the CERN CDS information server - AN-10-175*, 2010.

[70] The CMS Collaboration. Absolute Calibration of the CMS Luminosity Measurement: Summer 2011 Update. CMS PAS EWK-11-001, 19 Aug 2011.

[71] David Griffiths. *Introduction to Elementary Particles.* John Wiley & Sons, Inc., 1987. ISBN 0-471-60386-4.

[72] K. Nakamura et al. Particle data group. *Journal of Physics G*, 37, 075021, 2010.

[73] The weak interaction - warwick university lecture series, 2011. URL `http://www2.warwick.ac.uk/fac/sci/physics/current/teach/module_home/px435/weak.pdf`.

[74] T. D Lee and C. N Yang. Question of parity conservation in weak interactions. *Physical Review*, 104(1), 1956.

[75] C. S. Wu et al. Experimental test of parity conservation in beta decay. *Phys Rev.*, 105, 1957.

[76] F. J Hassert et al. Observation of neutrino-like interaction without muon or electron in the gargamelle neutrino experiment. *Physics Letters*, 46B(1), 1973.

[77] The UA1 Collaboration, 1978 - 1993.

[78] L. Reina. Tasi 2004 lecture notes on Higgs boson physics. *arXiv:hep=ph/0512377v1*, 30 Dec 2005.

[79] David J. Gross. Asymptotic freedom and qcd - a historical perspective. *Nuclear Physics B*, 135:193–211, 2004.

[80] M. Deile et al. Diffraction and total cross-section at the Tevatron and the LHC. *arXiv:hep-ex/0602021v1*, February 2006.

[81] K. Goulianos. Diffractive cross sections and event final states at the LHC. In *Presented at Forward Physics at LHC Workshop, Elba Island, Italy.*, May 27 - 29 2010.

[82] D. d'Enterria. Forward physics a the LHC: within and beyond the Standard Model. *Brazilian Journal of Physics*, 38(3B), 2008.

[83] M. Froissart. Asymptotic behavior and subtractions in the mandelstam representation. *Physical Review*, 123, 1961.

[84] T. Regge. Regge theory. *Nuovo Cimento*, 14, 1959.

[85] A. Donnachie and P.V Landshoff. Elastic scattering and diffraction dissociation. *Nuclear Physics B*, 244, 1984.

[86] The WA91 Collaboration. $p\bar{p}$ cross section at wa91. *Phys. Letters B*, 321, 1994.

[87] V. N. Gribov. *Soviet Physics: Journal of Experimental and Theoretical Physics*, 41, 1961.

[88] N. Cartiglia. Diffraction at hera. *arXiv:hep-ph/9703245v1*, May 1997.

[89] F.E Low. Model of the bare Pomeron. *Physical Review D*, 12(1), July 1975.

[90] Nussinov. Colored-Quark Version of Some Hadronic Puzzles. *Physical Review Letters*, 34(20), May 1975.

[91] J.F Gunion and D.E Soper. Quark-counting and hadron-size effects for total cross sections. *Physical Review D*, 15, May 1977.

[92] O. Nachtmann. Pomeron Physics and QCD. In *Contribution to the Ringberg Workshop on HERA physics*, 2003.

[93] Landshoff Donnachie, Dosch and Nachtmann. *Pomeron Physics and QCD*. Cambridge University Press, 2002.

[94] H Cheng, J.K. Walker, and T.T Wu. Impact picture of pp, $\bar{p}p$, $\pi^{\pm}p$ and $k^{\pm}p$ elastic scattering from 20 to 5000 GeV. *Physics Letters B*, 44B, 1973.

[95] C. Bosio U. Amaldi, R. Biancastelli et al. The energy dependence of the proton-proton total cross-section for centre-of-mass energies between 23 and 52 GeV. *Physics Letters*, 44B, 1973.

[96] C. Augier. Prediction on the total cross section and real part at LHC and ssc. *Physics Letters B*, 315:503–506, 1993.

[97] G. Matthiae. Diffractive physics at the LHC. *Brazilian Journal of Physics*, 2000.

[98] The TOTEM Collaboration. Proton-Proton Elastic Scattering at the LHC Energy of $\sqrt{s} = 7$ TeV. *EPL - 41001*, 95(4), August 2011.

[99] P. Collins. *An Introduction to Regge Theory and High Energy Phyics*. Cambridge University Press, 1977.

[100] Michele Arneodo and Markus Diehl. Diffraction for non-believers. *arXiv:hep-ph/05110467v1*, Nov 2005.

[101] M. Albrow. XIth international conference on elastic and diffractive scattering. In *arXiv:hep-ph/0509292v1*, Sept. 2005.

[102] R. Engel et al. PHOJET. *Phys. C*, 66, 1995.

[103] Sergey Ostapchenko. Monte Carlo treatment of hadronic interactions in enhanced Pomeron scheme: I. QGSJET-II model. *Phys.Rev.*, D83:014018, 2011. doi: 10.1103/PhysRevD.83.014018.

[104] P. Skands T. Sjostrand, S. Mrenna. PYTHIA6: Physics and Manual. *arXiv:hep-ph/0603175v2*, 2006.

[105] P. Skands T. Sjostrand, S. Mrenna. PYTHIA8. *Compt. Phys. Commun*, 178, 2008.

[106] G. A. Schuler and T. Sjöstrand. Towards a complete description of high energy photoproduction. *Nuclear Physics*, B407:539–605, 1993.

[107] Bo Andersson. *The Lund Model*. Cambridge University Press, 1998.

[108] P. Bruni and G. Ingelman. Diffractive W and Z production at $p\bar{p}$ colliders and the Pomeron parton content. *Phys. Lett B*, 311:317–323, 1993.

[109] E. L Berger, J. C Collins, et al. Diffractive hard scattering. *Nuclear Physics*, B286:704 – 728, 1987.

[110] Sparsh Navin. Diffraction in pythia. Technical report, The University of Birmingham, United Kindom, arXiv:1005.389v1, May 2010.

[111] A. Capella, U. Sukathme, C-I Tan, and J.Tran Thanh Van. Dual parton model. *Physics Reports*, 236:225 – 329, 1994.

[112] F. Abe et al. Measurement of the $p\bar{p}$ total cross section at $\sqrt{s} = 546$ and 1800 GeV. *Phys Rev D.*, 1993.

[113] N. Amos et al. A luminosity-independent measurement of the $p\bar{p}$ total cross section at $\sqrt{s}$ =1.8 TeV. *Phys. Lett. B*, 243, 1990.

[114] Tanguy Pierog, Karlsruhe Institute of Technology. Personal Communications, 20 September 2012.

[115] S.R. Amendolia, G. Bellettini, P.L. Braccini, C. Bradaschia, R. Castaldi, et al. Total cross-section measurement at the ISR. *Nuovo Cim.*, A17:735–755, 1973. doi: 10.1007/BF02786846.

[116] The ARGO-YBJ Collaboration. Proton-air cross section measurement with the ARGO-YBJ. *arXiv:0904.4198v1 [hep-ex]*, 27 April 2009.

[117] A.A. Arkhipov. Proton-Proton Total Cross-Sections from the Window of Cosmic Ray Experiments. *arXiv:hep-ph/0108118v3*, 20 Dec 2002.

[118] G. Corcella, I.G. Knowles, G. Marchesini, S. Moretti, K. Odagiri, et al. HERWIG 6: An Event generator for hadron emission reactions with interfering gluons (including supersymmetric processes). *JHEP*, 0101:010, 2001.

[119] The CMS Collaboration. Measuring the inelastic pp cross section at $\sqrt{s} = 7$ TeV with the CMS detector. *Available on the CERN CDS information server - PAS FWD-11-001*, June 2011.

[120] Ralf Ulrich, Ralph Engel, and Michael Unger. Hadronic Multiparticle Production at Ultra-High Energies and Extensive Air Showers. *Phys.Rev.*, D83: 054026, 2011. doi: 10.1103/PhysRevD.83.054026.

[121] Michael L. Miller, Klaus Reygers, Stephen J. Sanders, and Peter Steinberg. Glauber modeling in high energy nuclear collisions. *Ann.Rev.Nucl.Part.Sci.*, 57:205–243, 2007. doi: 10.1146/annurev.nucl.57.090506.123020.

[122] The ATLAS Collaboration. Measurement of the Inelastic Proton-Proton Cross-Section at $\sqrt{s} = 7$ TeV with the ATLAS Detector. *arXiv.org hep-ex*, 2011. URL `http://arxiv.org/abs/1104.0326v1`.

[123] Edmund Berry, HCal. Personal Communications, 31 March 2011.

[124] Eun-Joo Ahn, Ralph Engel, Thomas K. Gaisser, Paolo Lipari, and Todor Stanev. Cosmic ray interaction event generator SIBYLL 2.1. *Phys.Rev.*, D80:094003, 2009. doi: 10.1103/PhysRevD.80.094003. 33 pages, 13 figures.

[125] Klaus Werner, Fu-Ming Liu, and Tanguy Pierog. Parton ladder splitting and the rapidity dependence of transverse momentum spectra in deuteron-gold collisions at RHIC. *Phys.Rev.*, C74:044902, 2006. doi: 10.1103/PhysRevC.74.044902.

[126] S. Ostapchenko. QGSJET-II: Towards reliable description of very high energy hadronic interactions. *Nucl. Phys. Proc. Suppl.*, 151:143–146, 2006. doi: 10.1016/j.nuclphysbps.2005.07.026.

[127] David d'Enterria, Ralph Engel, Tanguy Pierog, Sergey Ostapchenko, and Klaus Werner. Constraints from the first LHC data on hadronic event generators for ultra-high energy cosmic-ray physics. *Astropart.Phys.*, 35:98–113, 2011. doi: 10.1016/j.astropartphys.2011.05.002.

[128] Kenneth Oesterberg. Personal Communications, 20 September 2012.

[129] The ALICE Collaboration. Inelastic cross section measurement in ALICE. Minimum Bias and Underlying Event Working Group, June 2011.

[130] G. Antchev, P. Aspell, I. Atanassov, V. Avati, J. Baechler, et al. First measurement of the total proton-proton cross section at the LHC energy of $\sqrt{s}$ =7 TeV. *EPL*, 95(4), 2011.

[131] G. Ingelman and P.E Schlein. Jet structures in high mass diffractive scattering. *Physics Letters*, 152B, 1985.

[132] R. Bindel, E. Garcia, A.C. Mignerey, and L.P. Remsberg. Array of scintillator counters for phobos at RHIC. *Nucl. Instrum. and Methods in Physics Research A*, 474:38 – 45, 2001.

[133] A. Iordanova, R.S. Hollis, and D.J Hofman. Level-1 triggering studies for heavy ion collisions at $\sqrt{S_{NN}}$ = 5.5TeV in CMS. *CMS Internal Analysis Note AN-2007/053*, 2007.

[134] Steffen Müller. *Design, Commissioning and Performance of the CMS Beam Condition Monitor 2 and Simulation Studies of the Radiation Environment near CMS at LHC*. PhD thesis, Fakultät für Physik de Universität Karlsruhe, 2010.

[135] M. Guthoff. Expected particle flux for various possible BSC positions. Contribution to the BSC Upgrade workshop, August 2011.

[136] S. Viret. Beam background studies with the bsc. Contribution to the BSC Upgrade workshop, August 2011.

[137] *Aspects of Machine Induced Backgrounds In The LHC Experiments*, 2006. LHC Project Workshop - Chamonix XV.

[138] A. J Bell on behalf of the CMS BRM Group. Beam & radiation monitoring for CMS. In *IEEE Nucl. Sci. Symp. Conf. Rec.(2008) 2322.*, 2008.

[139] I. Agapov, G. A. Blair, S. Malton, and L. Deacon. BDSIM: A particle tracking code for accelerator beam-line simulations including particle-matter interactions. *Nucl. Instrum. Meth.*, A606:708–712, 2009. doi: 10.1016/j.nima.2009.04.040.

[140] P. Rinard. Neutron interactions with matter. Los Alamos Technical Report, 1997. URL `http://www.fas.org/sgp/othergov/doe/lanl/lib-www/la-pubs/00326407.pdf`.

[141] PVSS Service, 2012. URL `http://j2eeps.cern.ch/wikis/display/EN/PVSS+Service`.

[142] The CMS Collaboration. Measurement of the energy flow at large pseudorapidities in pp collisions at $\sqrt{s} = 0.9$ TeV, 2.36 TeV and 7 TeV. *Journal of High Energy Physics*, November 29 2011.

[143] Lea Caminada. Results of first collisions at $\sqrt{s} = 900$ GeV and $\sqrt{s} = 2.36$ TeV. In *Study of the Inclusive Beauty Production at CMS and Construction and Commissioning of the CMS Pixel Barrel Detector*, pages 75–84. Springer Berlin Heidelberg, 2012. 10.1007/978-3-642-24562-6_5.

[144] The CMS Collaboration. First measurement of the underlying event activity at the LHC with $\sqrt{s} = 7$ TeV and comparison with $\sqrt{s} = 0.9$ TeV. *Journal of High Energy Physics*, 109(9), 2011.

[145] V. Barone and E. Predazzi. *High-Energy Particle Diffraction.* Springer, 2001. ISBN 0172-5998.